ALMA MATER STUDIORUM
UNIVERSITÀ DEGLI STUDI DI BOLOGNA

SCUOLA DI SCIENZE

Dipartimento di Fisica e Astronomia

Dottorato di ricerca in Astrofisica
Ciclo XXX

Cluster-scale radio emission: analysis of a mass-selected sample of galaxy clusters

Tesi di Dottorato

Supervisore:
Dott.
Gianfranco Brunetti

Candidata:
Virginia Cuciti

Co-supervisore:
Chiar.mo Prof.
Daniele Dallacasa

Coordinatore Dottorato:
Chiar.mo Prof.
Francesco Rosario Ferraro

Esame finale anno 2018

Settore concorsuale: 02/C1–Astronomia, Astrofisica, Fisica della Terra e dei Pianeti
Settore scientifico–disciplinare: FIS/05–Astronomia e Astrofisica

This Thesis work was done as part of the research activity of the Istituto di Radioastronomia - Istituto Nazionale di Astrofisica (INAF) in Bologna.

Ai miei genitori
per tutto quello che hanno sempre fatto
e continuano a fare per me

Contents

List of acronyms

ACT	Atacama Cosmology Telescope
AGN	Active Galactic Nucleus
AIPS	Astronomical Image Processing System
CASA	Common Astronomy Software Applications
CDM	Cold Dark Matter
CFF	Control Field Flux densities
CMB	Cosmic Microwave Background
CR	Cosmic Ray
DSA	Diffusive Shock Acceleration
GMRT	Giant Meterwave Radio Telescope
GRHS	GMRT Radio Halo Survey
HM	High Mass
HT	Head-Tail
IC	Inverse Compton
ICM	Intra Cluster Medium
IR	Infrared
IRA	Institute of Radioastronomy
LAS	Largest Angular Size
LLS	Largest Linear Size
LM	Low Mass

MCXC	Meta-catalog of X-ray detected Clusters of Galaxies
MHD	Magneto-Hydro Dynamic
NVSS	NRAO VLA Sky Survey
RDF	Residual Diffuse Flux density
RM	Rotation Measure
RXTE	Rossi X-ray Timing Explorer
SDSS	Sloan Digital Sky Survey
S/N	Signal-to-noise ratio
SPAM	Source Peeling and Atmospheric Modelling
SPT	South Pole Telescope
SZ	Sunyaev-Zel'dovich
UL	Upper Limit
USSRH	Ultra Steep Spectrum Radio Halos
VLA	Very Large Array
WENSS	Westerbork Northern Sky Survey
WISE	Wide-field Infrared Survey Explorer
WSRT	Westerbork Synthesis Radio Telescope

Abstract

Clusters of galaxies occupy an exclusive position in the cosmic hierarchy, since they are the most massive gravitationally bound structures in the Universe. They form and grow through the accretion of matter and smaller systems driven by the gravitational field dominated by the dark matter. Mergers between clusters are the most energetic events in the Universe. Although most of the energy released during cluster mergers is dissipated to heat the Intra Cluster Medium (ICM) up to the observed temperatures ($10^7 - 10^8 K$), a fraction of it is channelled into the acceleration of particles and amplification of magnetic fields in the ICM. The most spectacular evidence for this non-thermal activity in the ICM is the formation of diffuse cluster scale synchrotron sources observed in a large number of clusters of galaxies. According to their morphology, size and location, these sources are commonly classified as radio relics, radio halos and mini halos. Being probes of the dissipation of energy into the ICM in different forms, the relevance of cluster-scale radio sources goes well beyond the physics of magnetic field amplification and particle acceleration. In fact, they provide crucial information on the microphysics of the ICM, including the way energy is transported at different scales throughout this medium. For this reason, the study of cluster-scale radio sources is a central topic in the key science programs of the new generation of radio and X-ray facilities, including LOFAR, Athena and SKA.

Radio relics are elongated or arc-like shaped sources located at the periphery of dynamically disturbed clusters. They are considered as tracers of merger-driven shocks propagating through the ICM. Radio halos are centrally located sources and their emission roughly coincides with the X-ray emission of the host clusters. Mini halos, are smaller sources found at the center of some relaxed clusters, they usually surround the central elliptical galaxy, but extend to larger scales, almost filling the core of the host cluster. The mechanisms responsible for the formation of mini halos are still debated: one possibility is that they are connected to the sloshing of the core in the cluster potential well.

The main focus of this PhD Thesis is the formation and evolution of radio halos. According to the current theoretical picture, radio halos form via the re-acceleration of electrons in the ICM by means of turbulence, injected during cluster mergers. In this scenario, the formation history of radio halos and their properties depend on the clusters merging rate throughout cosmic epochs and on the mass of the host clusters, which ultimately sets the amount of energy available for particle acceleration. Basic predictions on the statistical properties of radio halos have been derived in the framework of turbulent re-acceleration models. In particular, radio halos are expected to be preferentially found in massive and merging systems and they are expected to be increasingly rarer in less massive clusters and/or less energetic merging events. These less energetic events are expected to generate radio halos with steep spectra that should glow up at low radio frequencies. The unique way to test these expectation is the analysis of large samples of galaxy clusters with adequate radio and X-ray data.

A first observational step in this direction has been achieved trough the GMRT radio halo follow up of X-ray selected samples of clusters. These studies showed that the radio properties of clusters on the Mpc scale have a bimodal behaviour, either they host radio halos, whose radio powers increase with the X-ray luminosity of the hosting clusters, or they do not show diffuse emission at the sensitivity level of those observations. An observational milestone achieved with the GMRT surveys is the connection between the bimodality and the dynamics of galaxy clusters, with systems hosting radio halos being dynamically more active than non-radio halo systems. These statistical studies allowed fundamental information on the origin of radio halos in clusters to be obtained, and made it possible to test the basic predictions of the theoretical scenario, triggering an intense discussion in the community.

One of the main limitations of those studies was the selection of the clusters samples for radio follow-up. In fact, a necessary step forward in these studies is the selection of clusters on the basis of their mass, since it is the key parameter of models for the formation of radio halos. The recent advent of cluster surveys via the Sunyaev-Zel'dovich (SZ) effect (e.g. with the *Planck* satellite), has enabled the construction of cluster samples that are as close as possible to be mass-selected, owing to the tight relation between the SZ signal and the cluster mass. Early studies revealed that the fraction of radio halos in SZ-selected clusters appears larger than the one derived in X-ray selected clusters. The analysis of a sample of 30-40 galaxy clusters a posteriori selected in mass (SZ) have recently found a bimodal behaviour similar, although less evident, to that derived in the X-rays. However, those samples did not have the completeness and purity necessary to properly evaluate the occurrence of radio halos and, in particular, to study the dependence of such occurrence on the cluster mass.

The main goal of this Thesis is to achieve a major step forward in this direction. We aim at studying, in the radio and in the X-rays, the first complete large sample of mass (SZ)-selected galaxy clusters to obtain solid statistical constraints on the connection between radio halos and the dynamics and mass of the host clusters. To this purpose, we used the Planck SZ catalogue to select a sample of 75 massive galaxy clusters ($M_{500} \gtrsim 6 \times 10^{14} M_{\odot}$) in the redshift range $z = 0.08 - 0.33$ and we collected information on the presence or absence of diffuse emission from

the literature, from archival data and from a large observational campaign that we carried out during this PhD project. We complemented the radio information with the analysis of X-ray *Chandra* and *XMM-Newton* data, available for the great majority of the sample, to investigate the dynamical properties of clusters.

The project is ambitious and intended to derive constraints on the evolution of radio halos and their connection with cluster dynamical properties that will be a long-standing reference for theoretical and interpretative efforts in the field.

Focusing on the results of the statistical study of the link between thermal and non-thermal properties, we anticipate the following highlights:

- we found that the radio power-mass scaling relation for radio halos shows an increased scatter with respect to previous studies. This is a natural consequence of the superposition of different radio halo states, generated by the complex hierarchy of merger events.

- Once the scatter induced in the correlation by the redshift distribution and by the different sizes of radio halos in the sample is removed, we find clear evidence for a bimodal behaviour of clusters in both the radio power-mass plane and, for the first time, in the radio emissivity-mass diagram, with radio halos and non-radio halo clusters following two distinct distributions. This opens the way to unprecedented constraints on the time evolution and origin of radio halos.

- Similarly to previous studies, we find that this bimodality is clearly connected to the cluster dynamics. Still, we find that an increasing fraction of merging clusters with relatively low mass do not show radio halos, pinpointing a prominent interplay of mass and energetics in the mechanisms that lead to the formation of radio halos

- For the very first time, we measured the occurrence of radio halos as a function of the cluster mass in a complete mass-selected sample. We found that the observed increase of the radio halo fraction with the cluster mass is remarkably in agreement with theoretical models. An unavoidable consequence of these models is that a large fraction of merging systems without radio halos detected in our GMRT and JVLA observations will glow up in LOFAR, MWA (or future SKA-Low) observations as halos with very steep spectra.

In addition to the study of the the statistics of radio halos, the amount of data available in this Thesis led to the discovery of new radio relics, mini halos and head tail radio galaxies in our clusters.

The structure of this Thesis is outlined below.

- In **Chapter 1** we introduce the general properties of galaxy clusters. We describe their X-ray thermal emission and how it is connected to their dynamical properties. Then we focus on the non-thermal components in the ICM, magnetic fields and relativistic particles, that give rise to the diffuse synchrotron emission in the ICM. The main characteristics of radio halos, relics and mini halos and the scenarios proposed for their formation are discussed.

- **Chapter 2** is focused on radio halos. First, we describe the model proposed by Cassano & Brunetti (2005) and Cassano et al. (2006) to derive basic predictions on the statistics of radio halos in the framework of the turbulent re-acceleration scenario. Then we review the main observational results, prior to this work, on the statistical properties of radio halos.

- In **Chapter 3** the selection of our sample from the Planck SZ cluster catalogue is presented. We built a total sample of 75 clusters with $M_{500} \gtrsim 6 \times 10^{14} M_\odot$ and $0.08 < z < 0.33$. We report on the early radio and X-ray analysis carried out on a subsample of clusters that had available information about the possible presence of radio halos. We analyse the occurrence of radio halos as a function of the cluster mass and the connection between the presence of radio halos and the disturbed dynamical state of the the host clusters.

- In **Chapter 4** we describe the radio GMRT and JVLA data reduction carried out to complete the radio information about the presence/absence of diffuse emission for all the clusters of the sample. The general methods to calibrate the datasets and image the cluster fields are discussed. Moreover, we describe the technique to place upper limits to the diffuse emission of clusters without radio halos.

- In **Chapter 5** we report the results of the radio data analysis. We detected diffuse radio emission in form of radio halos or mini halos in a number of clusters. For clusters without radio halos we report the values of the upper limits.

- **Chapter 6** focuses on two interesting galaxy clusters: Abell 1451 and Zwcl 0634.1+4750. We discovered that they both host radio halos that are underluminous with respect to the known correlation between the radio halo power and the cluster mass. In addition, Abell 1451 hosts a radio relic located at large distance from the cluster center, which might be the result of an accretion/external shock passing through some ghost plasma and Zwcl 0634.1+4750 hosts a peculiar head tail radio galaxy which shows clear evidence for the interaction with a merger-shock based on the combination of the brightness and spectral index profiles along the tail.

- In **Chapter 7** we discuss the statistical properties of the total sample. We characterize the dynamical properties of clusters using X-ray data. Then we focus on the properties of radio halos. We investigate the distribution of clusters in the radio power mass diagram and in the radio emissivity-mass diagram. We analyse the occurrence of radio halos as a function of the cluster mass and we compare our results with the expectations of the turbulent re-acceleration scenario.

- We summarize and discuss the main results of this Thesis in **Chapter 8** and we give some future perspectives to expand our understanding of the non-thermal emission in galaxy clusters.

Chapter 1

Galaxy clusters

Clusters of galaxies are the largest and most massive gravitationally bound systems in the Universe. They include hundreds to thousands of galaxies in a spherical volume with a radius of $\sim 1-3$ Mpc. Being large concentrations of galaxies, clusters have been discovered in the optical band first and catalogues were based on the visual inspection of photographic plates (e.g. Abell 1957). However, galaxies constitute only a small fraction ($\sim$few %) of the total mass of clusters, which is typically of the order of $10^{14}-10^{15}M_{\odot}$. The majority of the clusters mass is in the form of dark matter ($70-80\%$), which exhibits itself only through dynamical activity and lensing effects. The volume between galaxies is filled with hot ($10^{7}-10^{8}K$) and rarefied ($n_{gas} \sim 10^{-1}-10^{-4}\text{cm}^{-3}$) gas, the so-called Intra Cluster Medium (ICM), which accounts for the $\sim 15-20\%$ of the total mass.

According to the current standard cosmological model (ΛCDM, where Λ refers to the cosmological constant and CDM stays for Cold Dark Matter), cosmic structures form via a hierarchical process of accretion of smaller substructures. In this framework, galaxy clusters form and grow at the intersection of cosmic filaments where matter is channelled as a consequence of the gravitational collapse driven by the dark matter (Fig. 1.1). Clusters of galaxies can be used as cosmological probes of the physics leading to the formation of large scale structures, and, at the same time, they are laboratories to study the microphysics of barions. Therefore, they are excellent crossroads between cosmology and astrophysics (e.g. Borgani et al. 2004).

As for all astrophysical systems, a complete view of galaxy clusters requires a multi-wavelength approach. The different components of clusters are visible in different ways: galaxies can be observed mainly in the optical and infrared (IR) bands, while Active Galactic Nuclei (AGNs) and the ICM can be studied by means of X-ray and radio observations. To investigate the non-visible component of clusters (the dark matter) dynamical and lensing effects need to be investigated. As an example, we show a multi-wavelength view of the famous Coma cluster in Fig. 1.2. In this Chapter we review the main observational characteristics of galaxy clusters and some of the properties that can be inferred from observations.

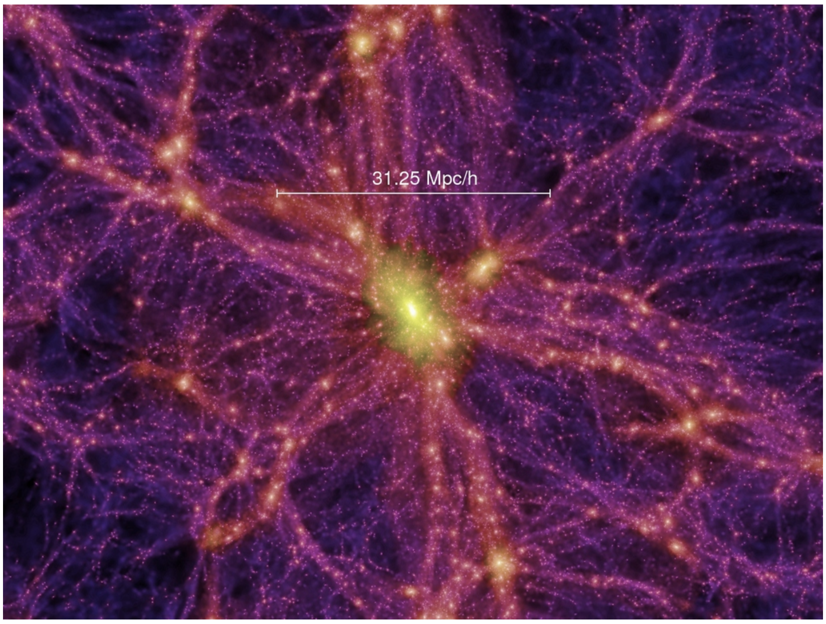

Figure 1.1: The Millennium simulation: a slice through the density field of the dark matter at $z = 0$ (t=13.6 Gyr). Galaxy clusters represent the node at the intersection of cosmic filaments. A massive forming clusters is located at the center of the panel (Springel et al. 2006).

1.1 Mass estimates

Under the assumption of virial equilibrium, the cluster mass can be estimated by knowing the position and redshift of a high enough number of member galaxies:

$$M \propto \frac{3\sigma_r^2 R_V}{G} \tag{1.1}$$

where σ_r is the radial velocity dispersion of galaxies and R_V is the virial radius of the cluster. This approach is simplified and based on the assumption of virial equilibrium, which is often not completely satisfied. Nevertheless, from an historical point of view, it led to the first estimate of the mass of the Coma cluster by Zwicky (1937), who also noted that the mass inferred from the motions of galaxies within the cluster exceeded (by a factor of ~ 10) the sum of the mass of all the visible galaxies, providing the first evidence of the presence of dark matter in galaxy clusters.

Another method to estimate the cluster mass is based on the assumption of hydrostatic equilibrium (which is not always fully satisfied, as well), i.e. the pressure force is balanced by the gravitational force: $\bigtriangledown P_{gas} = -\rho_{gas} \bigtriangledown \phi$, where P_{gas} and ρ_{gas} are the gas pressure and density and ϕ is the gravitational potential. If we assume the gas distribution to be spherically symmetric, this becomes:

$$\frac{dP_{gas}}{dr} = -\rho_{gas}\frac{d\phi}{dr} = -\rho_{gas}\frac{GM(< r)}{r^2} \tag{1.2}$$

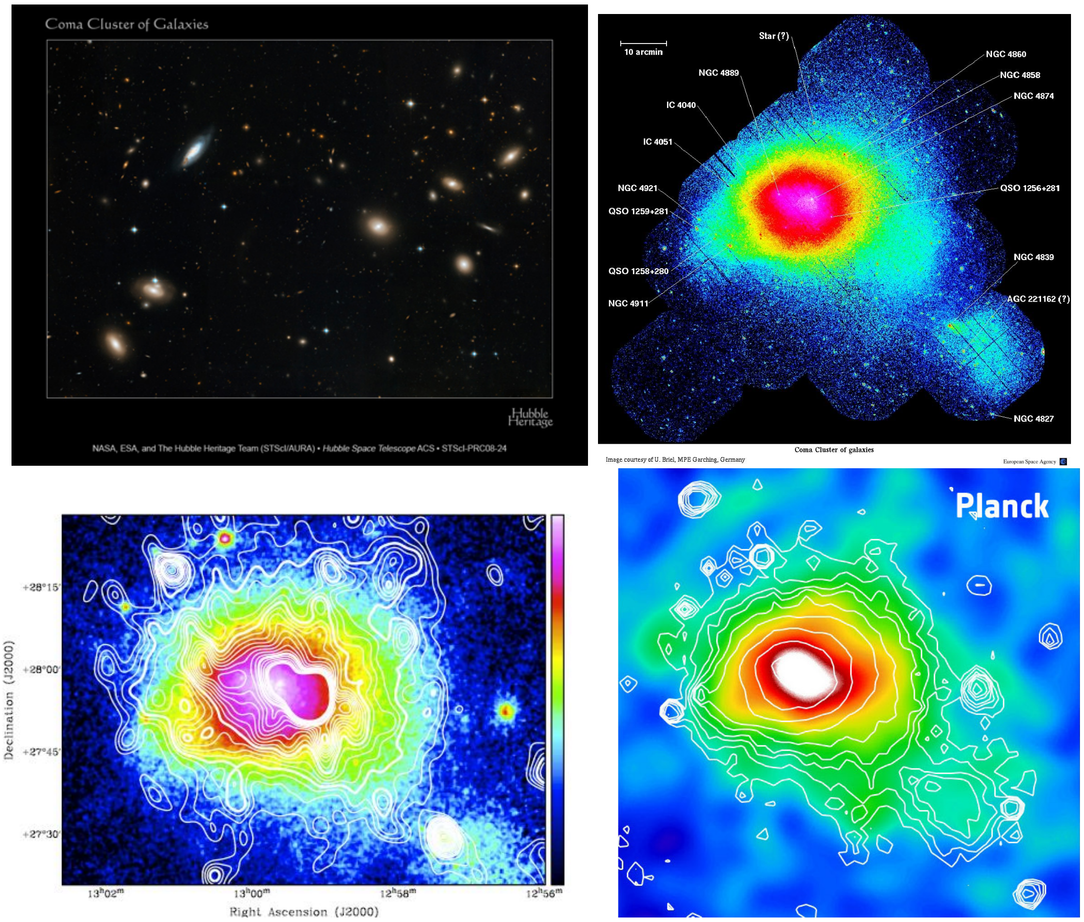

Figure 1.2: A multi-wavelength view of the Coma cluster. *Top left*: Hubble Space Telescope image revealing the emission from galaxies. *Top right*: Thermal ICM emitting in the X-ray as seen by the *XMM-Newton* satellite. *Bottom left*: radio contours (WSRT 350 MHz) overlaid on the X-ray image. *Bottom right*: X-ray contours overlaid on the *Planck* SZ image.

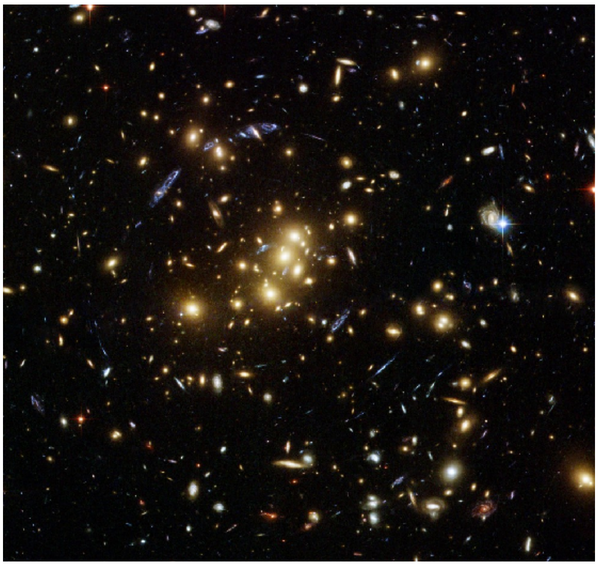

Figure 1.3: Gravitational lensing around the galaxy cluster CL0024+17. Yellow elliptical galaxies are cluster members. The elongated blue objects are much more distant galaxies, lying behind the cluster. Gravitational lensing has distorted their apparent images into a series of tangential arcs (strong lensing) Other background galaxies appear distorted (weak lensing). Credit: NASA/ESA.

where r is the distance from the cluster centre and $M(<r)$ is the mass contained within r. Considering the equation of state of a perfect gas $P = (K_B \rho T)/\mu m_p$, the mass is given by:

$$M(<r) = \frac{r K_B T}{G \mu m_p} \left(\frac{\mathrm{d}\ \ln\ \rho_{gas}}{\mathrm{d}\ \ln\ r} + \frac{\mathrm{d}\ \ln\ T}{\mathrm{d}\ \ln\ r} \right) \tag{1.3}$$

where μ is the mean molecular weight of the gas and m_p is the proton mass. $T(r)$ and $\rho(r)$ can be estimated from deprojection analysis of X-ray observations.

Cavaliere & Fusco-Femiano (1976) proposed that, if the gravitational potential supports both the gas and the galaxies distribution, the gas density radial profile can be written as:

$$\rho_{gas}(r) = \frac{\rho_0}{[1 + (r/r_c)^2]^{3\beta/2}} \tag{1.4}$$

where r_c is the core radius and $\beta = \mu m_p \sigma_v^2/(k_B T)$. The parameter β can be obtained by fitting the surface brightness radial profile, thus Eq. 1.4 gives another independent method to evaluate the density profile.

A third way to measure the mass of clusters is based on the effects of gravitational lensing. Being the most massive systems in the Universe, galaxy clusters are excellent gravitational lenses. As a result of the deflection of light due to the cluster gravitational potential, background objects appear distorted, sometimes elongated, sometimes fragmented, with shape and intensity different from the original ones (Fig. 1.3). All these effects can be used to infer the mass of the lens.

Gravitational lensing events are generally divided into strong and weak lensing, depending on the geometry of the event and on its manifestation. In case of strong lensing, a simple spherical model provides a good estimate of the cluster mass within the radius r_{arc} that is the distance between the cluster center and the arc-like image of the lensed object (Bartelmann et al. 2003):

$$M_{lens}(< r_{arc}) \approx \pi r^2 \Sigma_{crit} \tag{1.5}$$

where

$$\Sigma_{crit} = \frac{c^2}{4\pi G} \frac{D_S}{D_{LS} D_L} \tag{1.6}$$

D_L, D_{LS} and D_S are the distances from the observer to the lens, from the lens to the source and from the observer to the source, respectively. Observations of weak lensing aim at reconstructing the cluster mass distribution from the weak ellipticity that the cluster gravity induces on (faint) background galaxies. This method is complicated because galaxies are intrinsically elliptic, therefore it requires several source images to be averaged, under the assumption of intrinsically random orientation of galaxies.

In addition, if a large number of redshift measurements is available, the mass of a cluster of galaxies can be inferred from the dynamical analysis of member galaxies. One method is to fit the velocity dispersion data to the solution of the Jeans equations (e.g. Sanchis et al. 2004; Łokas et al. 2006a,b). Another method is the "caustic technique". In the line of sight velocity – projected radius diagram, cluster galaxies distribute in a characteristic trumpet shape. The edges of the trumpet are called caustic and, under the assumption of spherical symmetry, they trace the escape velocity profile of the cluster and can thus be used to determine the cluster mass profile (e.g. Diaferio 1999; Diaferio et al. 2005; Geller et al. 2013; Maughan et al. 2016).

Finally, the mass of clusters can be inferred from the total energy of the gas combined with other observational constraints. This energy budget can be measured directly via scaling relations with other observational properties, such as the X-ray luminosity or the Sunyaev-Zel'dovich effect (see Sect. 1.4)

1.2 The Sunyaev-Zel'dovich effect

The Sunyaev-Zel'dovich (SZ) effect is a small distortion of the Cosmic Microwave Background (CMB) spectrum caused by the Inverse Compton (IC) scattering of the CMB photons with the electrons of a hot plasma. The Intra Cluster Medium (ICM) is a hot and ionised gas, hence it is a reservoir of energetic electrons. When a "cold" CMB photon encounters a "hot" ICM electron, the former gains energy via IC process, its frequency increases an it is blue-shifted. The characteristic spectral signature of the SZ effect is a decrease in the CMB intensity at frequencies $\leq$ 218 GHz and an increase at higher frequencies (Fig. 1.4). In practice, given the combination of the photon cross section and the electron column density of the ICM, only the $\sim 1\%$ of the CMB photons undergoes IC scattering as they travel through a massive cluster (Rephaeli et al. 2005).

The Comptonization parameter, y, is defined as:

$$y \propto \int_0^\infty n_e T_e dl \tag{1.7}$$

where n_e and T_e are the electron density and temperature and the integration is done along the line of sight. Expressed in unit of intensity, the SZ effect can be written as:

$$\Delta I_{SZ} \propto I_0 y \tag{1.8}$$

where I_0 is the CMB intensity unaffected by IC scattering. The integrated Compton parameter, corresponding to the CMB intensity decrement due to the SZ effect, can be obtained by integrating the y-parameter over the solid angle Ω subtended by the cluster:

$$\text{SZ flux} \propto Y \equiv \int_\Omega y \; d\Omega \propto \frac{1}{D_A^2} \int_0^\infty dl \int_A n_e T_e dA \tag{1.9}$$

where A is the area of the cluster in the plane of the sky and D_A is the angular diameter distance.

The SZ signal integrated over the solid angle of the cluster provides the sum of the electrons weighted by temperature (Eq. 1.9), which is a measure of the total thermal energy of the cluster. Therefore, an useful characteristic of the SZ effect is its correlation with the cluster mass, that we will discuss in Sec. 1.4.

1.3 X-ray thermal emission

With typical luminosities $L_X \sim 10^{43-45}$erg/s, galaxy clusters, together with quasars, are the most luminous X-ray sources in the sky. They have been clearly detected as bright diffuse X-ray sources since the early high energy experiments carried out with balloons. The first all sky survey in the X-ray band, built up with the Uhuru satellite in the '70s, revealed that the majority of galaxy clusters are X-ray luminous objects and, even today, the X-ray selection is one of the easiest ways to search for galaxy clusters. Their radiation is from bremsstrahlung emission coming from the ICM. The bremsstrahlung emissivity at the frequency ν in a plasma with ion density n_i, electron density n_e and temperature T is:

$$J_{br}(\nu, T) \propto n_e n_i g(\nu, T) T^{-1/2} e^{-\frac{h\nu}{k_B T}} \;\; [\text{erg cm}^{-3}\text{s}^{-1}\text{Hz}^{-1}] \tag{1.10}$$

where $g(\nu, T) \propto ln\left(\frac{k_B T}{h\nu}\right)$ is the Gaunt factor and accounts for quantum mechanical effects and effects of distant collisions. The spectral shape of the emissivity provides

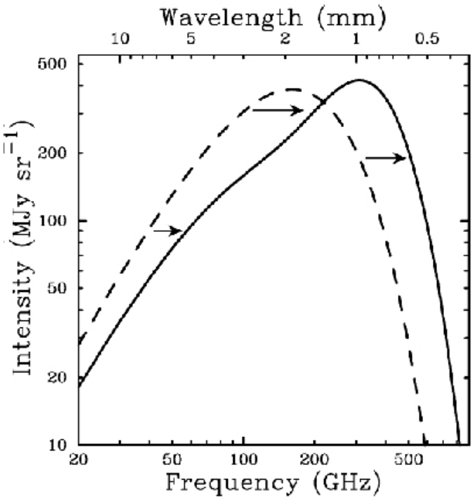

Figure 1.4: The CMB spectrum, undistorted (dashed line) and distorted by the SZ effect (solid line). This is derived for a fictional cluster 1000 times more massive than a typical massive cluster, the real distorsion is much smaller.

a measure of $T(r)$, while its normalization gives a measure of $n_e(r)$, with r being the distance from the cluster center. The bolometric emissivity can be obtained integrating Eq. 1.10 over the entire spectrum:

$$J_{br}(T) \propto n_e n_i g(T) T^{1/2} \text{ [erg cm}^{-3}\text{s}^{-1}] \tag{1.11}$$

and Eq. 1.11 can be written as:

$$J_{br}(T) \propto \Lambda(T) n_e n_i \text{ [erg cm}^{-3}\text{s}^{-1}] \tag{1.12}$$

where $\Lambda(T)$ is the cooling function (Raymond & Smith 1977; Sutherland & Dopita 1993).

X-ray observations reveal that galaxy clusters show a variety of morphologies, connected to the cluster dynamical status. We can identify two main extreme cases: **cool-core** clusters, which are dynamically relaxed clusters with peaked X-ray emission and low specific entropy at their centres, and **merging** clusters, characterised by irregular morphologies, substructures in their X-ray brightness distribution and high central entropy (Fig. 1.5). In practice, clusters are much more complex than this. In fact, the presence of the cool core or the regular morphology of the cluster X-ray emission do not directly imply the absence of dynamical activity. For instance, merging events happening along the line of sight may lead to a fairly regular X-ray brightness distribution and enhance the X-ray surface brightness in the central region. In these cases, optical spectroscopy of the galaxies of the subclusters is needed to investigate the dynamics of the system (e.g. Andersson & Madejski 2004). Moreover, there could be minor merging events that do not destroy the cool core, but still perturb the system and induce large-scale motions. We will briefly

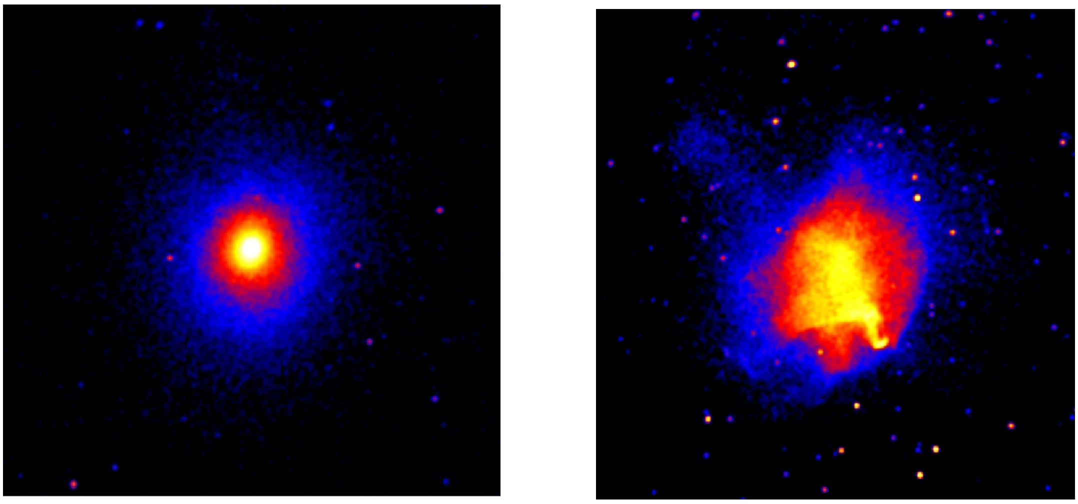

Figure 1.5: *Left panel*: X-ray *Chandra* image of the cool core cluster Abell 1835. *Right panel*: X-ray *Chandra* image of the merging cluster Abell 520.

describe the main characteristics of cool-cores and merging clusters in the following subsections.

1.3.1 Cool-core clusters

As we discussed above, the ICM primarily looses energy via thermal bremsstrahlung, emitting X-ray radiation. The cooling time for this process is (Sarazin 1988):

$$t_{cool} \simeq 8.5 \times 10^{10} \left(\frac{n}{10^{-3}\mathrm{cm}} \right)^{-1} \left(\frac{T}{10^{8}\mathrm{k}} \right)^{1/2} \ [\mathrm{yr}] \tag{1.13}$$

and it is generally longer than the Hubble time. However, in relaxed clusters, not disturbed by merging activity, the gas density rises towards the center (see eq. 1.4), implying that, in some cases, the cooling time can become shorter than the cluster age in the central region. In absence of any balancing heating, as the gas cools down it is compressed by the surrounding ICM, further increasing the central density and thus the X-ray emissivity. In order to balance the pressure of the overlying ICM, a slow inflow of gas is expected to take place, the so called *cooling flow* (Fabian 1994). However, X-ray observations with *XMM-Newton* and *Chandra* revealed that the expected cooling flow rates were overestimated (Peterson & Fabian 2006, for a review). Actually, the temperature in the central region of cool core clusters is lower (2-3 kev) with respect to the surrounding regions, but no evidence of "flow" has been found (Bauer et al. 2005). This triggered the discussion on the possible phenomena that could contribute to slow down the *cooling flow*. Without going into the many processes that have been proposed to balance the catastrophic cooling in the cluster centres (McNamara & Nulsen 2012, for a review), the most accredited mechanism to solve the *cooling flow* problem is the AGN feedback (e.g. McNamara

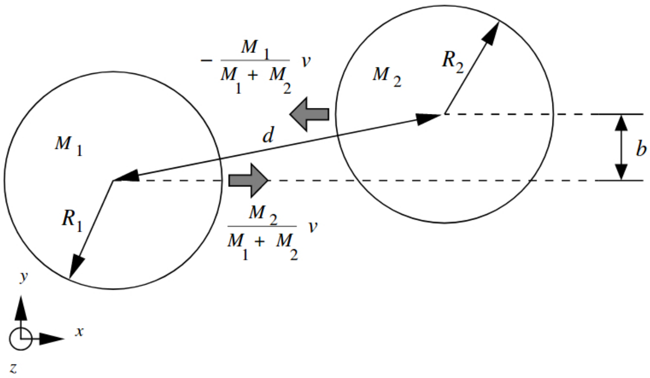

Figure 1.6: A schematic diagram of the kinematics for a merger between two subclusters of masses M_1 and M_2 and radii R_1 and R_2. The distance of the cluster centres is d and the impact parameter is b. v is the relative velocity.

& Nulsen 2007). In fact, a high fraction of cD (central dominant) galaxies in cool-core clusters show signatures of AGN activity, such as jets and lobes (Best et al. 2007). Some cool-core cluster hosts cavities in the X-ray emission, filled with radio emitting plasma inflated by the central AGN (Bîrzan et al. 2004; McNamara & Nulsen 2007). The huge amount of energy released by the AGN in the surrounding ICM could be able to provide heat and support the pressure of the cooling flow.

1.3.2 Merging clusters

Mergers between clusters of galaxies are the most energetic events in the Universe. They release energies up to $\sim 10^{63-64}$ erg during one cluster crossing time (~ 1 Gyr) and they have a fundamental role in determining the observed characteristics and dynamical properties of galaxy clusters (Markevitch et al. 1999). This huge amount of kinetic energy is mostly converted into heat by large scale shock waves travelling through the ICM. Moreover, part of this energy is dissipated through large scale turbulent motions of the gas.

The impact velocity, v, of two subclusters with masses M_1 and M_2, can be estimated from simple dynamical arguments (Sarazin 2002):

$$v = 2930\left(\frac{M_1+M_2}{10^{15}M_\odot}\right)^{\frac{1}{2}}\left(\frac{d}{1\mathrm{Mpc}}\right)^{\frac{1}{2}}\left[\frac{1-\frac{d}{d_0}}{1-\left(\frac{b}{d_0}\right)^2}\right]^{\frac{1}{2}} \quad [\mathrm{km/s}] \qquad (1.14)$$

where b is the impact parameter, d is the distance from the cluster centres and d_0 is the initial separation (Fig. 1.6). This lunches shock waves into the ICM with moderate Mach number. Numerical simulations confirm this expectations at least in the central Mpc-scale region where the temperature of the gas is not far from the virial equilibrium, whereas in the external regions or within cold clumps accreted into the main cluster higher Mach numbers may be generated (Ryu et al. 2003;

Pfrommer et al. 2006; Vazza et al. 2009). During their propagation, shock waves compress and heat the gas producing an increase in the X-ray surface brightness in correspondence of the shock front. Nevertheless, shock waves are difficult to detect from an observational point of view for many reasons. However, shocks with such low Mach numbers are expected to produce relatively small density jumps, implying that they can be visible only if they have not moved yet to the very external regions of the cluster where the X-ray emission is dominated by the background. Furthermore, shocks are detectable only if they are moving at large angle with respect to the line of sight, otherwise their observable effects can be smoothed by projection effects. In this respect, the high angular resolution of *Chandra* has been crucial to detect the unequivocal signature of shock fronts in galaxy clusters (Markevitch et al. 2002, 2005; Macario et al. 2011; Russell et al. 2011; Owers et al. 2014; Dasadia et al. 2016; Botteon et al. 2016a, 2017).

The supersonic interaction between clusters is expected to generate turbulent motions in the ICM (Cassano & Brunetti 2005; Subramanian et al. 2006). Numerical simulations allow the generation and evolution of turbulence in clusters to be studied in some detail (Dolag et al. 2005; Vazza et al. 2006, 2011; Miniati 2014; Vazza et al. 2017), however, a direct observation of the turbulent motions in the ICM is challenging with current instruments. The rotation measure (RM, see Section 1.5.1) can be used as a probe of turbulence in the ICM because it is related to the tangling of the magnetic field that is driven by the motions of the gas. The unique direct measure of the line broadening in excess with respect to the thermal broadening has been achieved with Hitomi for the Perseus cluster (Hitomi Collaboration et al. 2016), unfortunately, the Hitomi spacecraft lost its ground contact a month after its launch on March 2016. Nevertheless, gas density fluctuation, measurable from X-ray observations, can be used as tracers of velocity fluctuations in the ICM (Zhuravleva et al. 2014; Eckert et al. 2017). This method has been shown to be consistent with the direct measurement available for the Perseus cluster (Hitomi Collaboration et al. 2016).

1.4 Scaling relations

The simplest way to predict the observable properties of the ICM is assuming that gravity alone determines the thermodynamical properties of the hot diffuse plasma (Kaiser 1986). Since gravity does not have preferred scales, it is expected that clusters of different sizes are scaled version of each other. In this sense, the ICM model is said to be *self-similar*. Under this assumption, simple scaling relations between different global properties, such as mass, temperature, X-ray luminosity, velocity dispersion of galaxies, can be derived.

The relation between the total mass M and the temperature T, can be derived

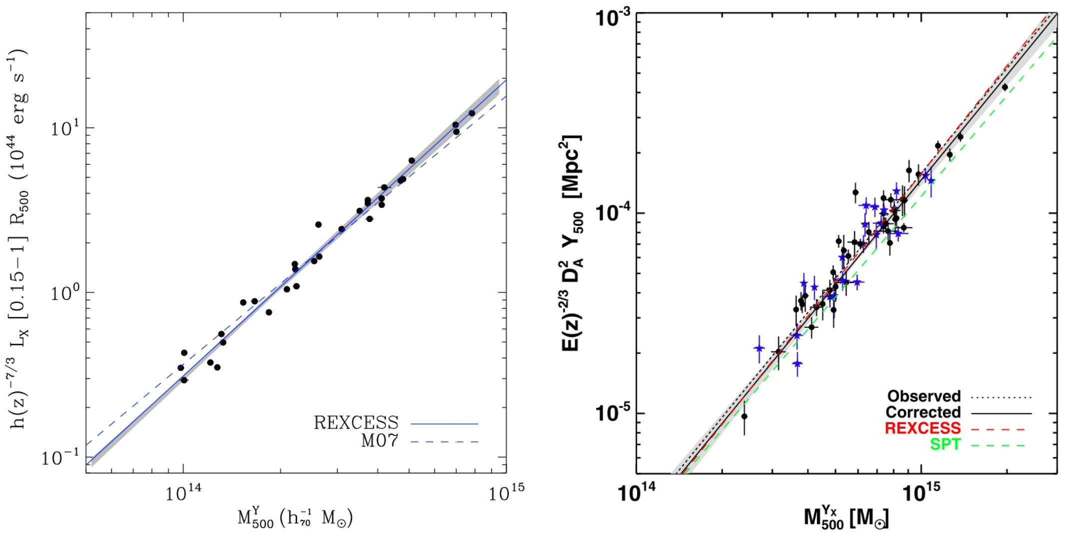

Figure 1.7: *Left panel*: $L_X - M_{500}$ relation for emission in the $[0.15-1]R_{500}$ aperture, for the REXCESS sample (Pratt et al. 2009). *Right panel*: $Y_{500} - M_{500}$ scaling relation for clusters in the *Planck-XMM-Newton* archive sample (Planck Collaboration et al. 2011b)

from the virial equilibrium $\frac{3K_BT}{2\mu m_p} = \frac{GM}{R}$:

$$K_BT = 3.23\left(\frac{\mu}{0.6}\right)\left(\frac{\delta}{500}\right)^{1/3}\left(\frac{M}{10^{14}h^{-1}\,M_\odot}\right)^{2/3}\quad[\mathrm{kev}] \tag{1.15}$$

Here δ is the average over-density of the cluster with respect to the critical density of the Universe at the cluster redshift, defined as $\rho_{cr} = \frac{3H(z)^2}{8\pi G}$. Quantities in Eq. 1.15 are normalised to typical values observed in clusters. Similarly, we can write the X-ray luminosity as:

$$L_X = 1.33\times10^{43}\left(\frac{f_{gas}}{0.1h^{-3/2}}\right)^2\left(\frac{0.6}{\mu}\right)\left(\frac{n}{10^{-3}h^2\mathrm{cm}^{-3}}\right)\left(\frac{T}{\mathrm{keV}}\right)^{0.4}\times$$
$$\times\left(\frac{M}{10^{14}h^{-1}\,M_\odot}\right)h^{-2}[\mathrm{erg\ s}^{-1}] \tag{1.16}$$

Eq. 1.16 shows that the X-ray luminosity linearly correlates with the total mass of clusters. X-ray observations of large samples of galaxy clusters confirm this relation (e.g. Pratt et al. 2009, Fig.1.7, left panel), despite some scatter, indicating that the self-similar picture is an idealised, but still reasonable, description of the galaxy clusters population.

As we mentioned in Sect. 1.2, an important property of the SZ effect, induced in the CMB spectrum by the ICM electrons, is its tight relation with the cluster mass. Indeed, if the gas is isothermal, the integrated Compton parameter, Y, can be written as:

$$Y_{500}D_A^2 \propto T_e\int n_e dV = M_{gas}T_e = f_{gas}M_{tot}T_e \tag{1.17}$$

where f_{gas} is the fraction of mass in form of ICM. Y_{500} is the Compton parameter integrated within R_{500}, i.e. the radius within which the average density is 500 times the critical density of the Universe at the cluster redshift. From the combination of Eq. 1.15 and Eq. 1.17, we obtain:

$$Y_{500}D_A^2 \propto f_{gas}M_{tot}^{5/3}E(z)^{2/3} \tag{1.18}$$

with $E^2(z) = \Omega_{m0}(1+z)^3 + \Omega_\Lambda + \Omega_{k0}$. Fig. 1.7, right panel, shows that this correlation has been found observationally and thus the SZ effect can be successfully used as a proxy of the mass of clusters.

1.5 Non-thermal components

The evidence of the presence of non-thermal phenomena in galaxy clusters comes from radio observations. In addition to the individual radio sources associated to member galaxies, many clusters show spectacular diffuse synchrotron emission arising from the ICM. Depending on their size, morphology and location, these sources are generally referred to as **radio halos**, **radio relics** and **mini-halos**. These synchrotron sources prove that the ICM is permeated by relativistic particles and magnetic fields. The non-thermal components of the ICM reveal themselves mainly in the radio band, but they are expected to generate radiation also in the hard X-ray and γ-ray bands. Further diffuse radio emission is expected from cosmic filaments connecting galaxy clusters, but no clear detection has been claimed so far. For observational and theoretical reviews on the subject we refer to Feretti et al. (2012) and Brunetti & Jones (2014).

Non-thermal emission on cluster scales is an important research topic for the new generation radio facilities, such as LOFAR (Röttgering et al. 2011), MWA (Duchesne et al. 2017) and SKA precursors (Norris 2010; Scaife et al. 2015; Bernardi et al. 2016)

1.5.1 Magnetic fields in galaxy clusters

Even though a direct measure of the magnetic field strength in galaxy clusters is not a trivial task, different estimates converge on similar values of $\approx \mu$G. Since the magnetic pressure in galaxy clusters is about 10-100 times below the thermal gas pressure, magnetic fields are not dynamically important, but they have a significant effect on energy transport in the ICM (Sarazin 1988; Tribble 1989; Narayan & Medvedev 2001; Ruszkowski & Begelman 2002; Asai et al. 2004, 2007; Keshet et al. 2010; Lecoanet et al. 2012; ZuHone et al. 2013, 2015) and relevant implications for the life-times of relativistic particles in the ICM.

The reference method to measure the magnetic field in galaxy clusters is the Faraday RM. When a linearly polarized radiation passes through a magnetised plasma, the left and right handed components which it can be split into, propagate with different velocities. This leads to a rotation of the polarization plane that is proportional to the wavelength λ such that $\Delta\Phi = \mathrm{RM}\lambda^2$, with:

$$\mathrm{RM} = 812 \int_0^L n_e B_{\|} \times dl \ [\mathrm{rad\ m^{-2}}] \tag{1.19}$$

where L is the depth of the screen, $B_{\|}$ is the component of the magnetic field along the line of sight and n_e is the electron density. The Faraday RM can be derived by measuring the position angle of the polarised radiation at different frequencies. If n_e is known this gives an estimate of $B_{\|}$. The available studies of RM in galaxy clusters report values for the central magnetic field of $\sim 1-$ few μG (Vogt & Enßlin 2005; Govoni et al. 2006; Vacca et al. 2012; Bonafede et al. 2010, 2013). Radio observations indicate that the magnetic field strength in clusters declines with radius, from the core to the outskirts (Dolag et al. 2001; Murgia et al. 2004; Bonafede et al. 2010).

Another method to estimate the magnetic field strength in galaxy clusters is from their hard X-ray emission, if interpreted as the result of IC scattering between CMB photons and ICM electrons. The synchrotron emissivity is proportional to the energy density of the magnetic field, $U_B = (B^2/8\pi)$, while the IC emissivity is proportional to the energy density in the photon field, U_{ph}. Thus the magnetic field strength can be derived by comparing the synchrotron and the IC emission. In galaxy clusters, U_{ph} is dominated by the CMB (T=2.73 K, $U_{CMB} = 0.26$ eV cm^{-3}), with an "equivalent magnetic field" strength $B_{CMB} = 3.25(1+z)^2$ μG. While the first IC searches yielded to the detection of several clusters (Rephaeli et al. 1999; Rephaeli & Gruber 2002; Fusco-Femiano et al. 1999), although with marginal significance, the new generation of hard X-ray satellites, *Suzaku* and *Swift*, failed to confirm IC detections at similar levels (Ajello et al. 2009, 2010; Wik et al. 2012; Ota et al. 2014). These observations suggest a lower limit for the magnetic field strength in the ICM $B \gtrsim 0.2$ μG (e.g. Wik et al. 2011, 2012).

It is worth mentioning that a procedure that is commonly adopted to estimate magnetic fields in the ICM is based on equipartition arguments for radio halos/relics (Feretti et al. 2012, for a review). However the assumption of energy equipartition between electrons and magnetic field is not justified for radio sources with life-time much longer than the electrons radiative lifetime.

The origin and evolution of the magnetic fields in clusters of galaxies are still poorly understood. Three main classes of model has been proposed for the origin: *i)* magnetic field are produced at relatively low redshift ($z \sim 2-3$) from the ejecta of galaxies and/or AGNs feedback; *ii)* they have origin at higher redshift, before the cluster formation and then they are amplified; *iii)* merger-driven shocks, resulting from the process of formation of clusters, produce the magnetic fields. All these models require a substantial amplification process to reproduce the main properties of the observed magnetic fields. Magneto-Hydro dynamic (MHD) simulations have been carried out to study the amplification process (e.g. Dolag et al. 2005; Brüggen et al. 2005). These works suggest that the kinetic dynamo activated in the ICM by the hierarchical process of formation of galaxy clusters is the main driver of magnetic field amplification.

1.5.2 Relativistic particles in the ICM

Several sources in galaxy clusters (Supernovae, AGNs, powerful galactic winds) are able to inject relativistic particles (protons and/or electrons) into the ICM. Shock waves, produced during the process of formation of large scale structures, are able to supply the ICM with cosmic rays, as well (Ryu et al. 2003). Once particles have been accelerated in the ICM, they are subject to energy losses that determine their life-time. The life-time of electrons is set by Coulomb losses at lower energies (typically below few×100 MeV) and radiative losses at higher energies :

$$\tau_{sync+IC} \simeq \frac{2.5 \times 10^{13}}{[\frac{B}{\mu G}^2 + \frac{B_{CMB}}{\mu G}^2]\gamma} \ [\mathrm{yr}] \tag{1.20}$$

where γ is the Lorentz factor (typically $\gamma \sim 10^4$ for relativistic electrons), B is the intensity of the magnetic field and B_{CMB} is the equivalent magnetic field of the CMB ($B_{CMB} = 3.25(1+z)^2$). The life-time of CRp is set by Coulomb collisions (CRp-p, CRp-e) and inelastic CRp-p collisions at higher energies, the latter channel occurs above a threshold kinetic energy of CRp = 300 MeV and generates secondary particles. The lifetime set by this channel is :

$$\tau_{pp} \simeq \frac{1}{c n_{th} \sigma_{pp}} \tag{1.21}$$

where σ_{pp} is the cross section of CRp-p encounters.

Fig. 1.8 shows the (total) time-scales for CRe and CRp energy losses. CRp with energy 1 GeV-1 TeV are long-living particles with life-times in the core of galaxy clusters of several Gyrs. At higher energy the CRp time-scale gradually drops below 1 Gyr, while at very high energy, in the regime of ultra high energy CRp (not shown in the figure), the life-time is limited by inelastic collisions between CRp and CMB photons. On the other hand, CRe are short-living particles due to unavoidable IC and synchrotron losses. The maximum life-time of CRe ($\sim$ 1 Gyr) is reached at energies $\sim$ 100 Mev, where radiative losses are roughly equivalent to Coulomb losses. CRe emitting synchrotron radiation in the radio band ($\sim$ several GeV), have shorter life-times, $\sim$ 0.1 Gyrs. CRe IC life-times scale strongly and inversely with cluster redshift according to $(1+z)^{-4}$ (Eq. 1.20).

The diffusion time of CRs is substantially larger than the Hubble time (Fig. 1.8), implying that they remain confined within the cluster volume. As a consequence, CRp are expected to accumulate in the ICM, increasing the probability of having

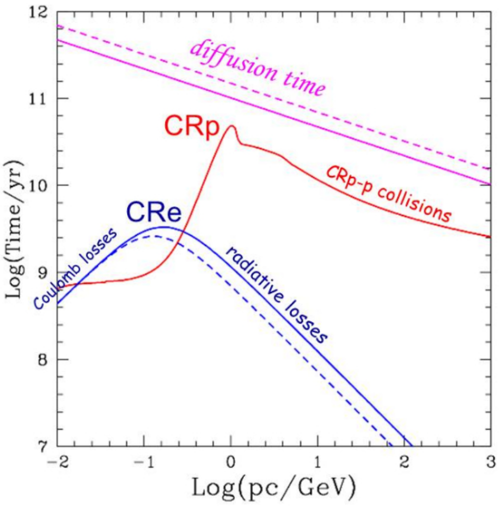

Figure 1.8: Life-time of CRp (red line) and CRe (blu line) in the ICM at $z = 0$ compared with the CR diffusion time on Mpc scales (magenta) for different values of the magnetic field intensity (the solid line is for 1μG and the dashed line for 3μG, Brunetti & Jones 2014).

inelastic hadronic collisions that generate CRe as secondary particles. Indeed the decay chain of a p-p collision is:

$$\begin{gathered} p + p \longrightarrow \pi^0 + \pi^+ + \pi^- + \text{ anything} \\ \pi^0 \longrightarrow \gamma\gamma \\ \pi^\pm \longrightarrow \mu^\pm + \nu_\mu \\ \mu^\pm \longrightarrow e^\pm \nu_\mu \nu_e \end{gathered}$$

1.5.3 Radio halos

Giant radio halos are extended (~1 Mpc) synchrotron sources located at the center of many merging galaxy clusters. They exhibit regular morphologies, fairly coincident with the X-ray brightness distribution of the cluster. Typically, radio halos have luminosities of the order of $10^{23} - 10^{25}$ W/Hz and low surface brightness ($\sim \mu$Jy/arcsec^2). The radio halo emission is usually unpolarised ($< 10\%$), although significant level of polarization has been found in a few cases (Govoni et al. 2005; Bonafede et al. 2009a) that however may be contaminated by relics/extended radio galaxies embedded/projected in the diffuse emission (e.g. Pizzo et al. 2009; Bonafede et al. 2012)

The prototype of this class of objects is the radio halo in the Coma cluster (Fig. 1.2), which has been discovered by Willson (1970) and, given its vicinity ($z = 0.023$) it has been extensively studied at many different frequencies (Venturi et al. 1990; Giovannini et al. 1993; Thierbach et al. 2003; Brown & Rudnick 2011). The Coma radio spectrum, shown in Fig. 1.9, represents an unique case in terms of the broad range of frequencies over which it has been measured. Remarkably, it shows a

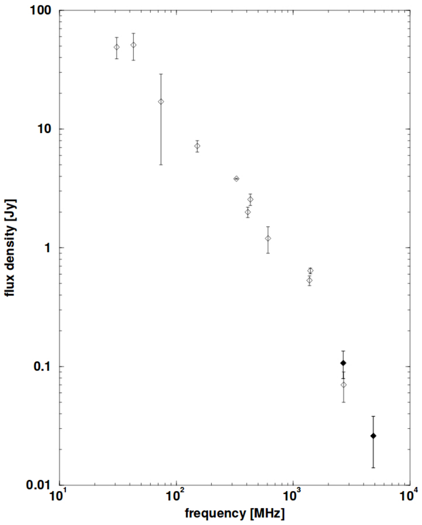

Figure 1.9: Total observed radio spectrum of the radio halo in the Coma cluster (Thierbach et al. 2003).

steepening at high radio frequencies that can be interpreted as the signature of a break in the spectrum of the emitting electrons (Schlickeiser et al. 1987; Reimer et al. 2004; Donnert et al. 2010; Brunetti et al. 2013).

Apart from the case of Coma, radio halo spectra are usually determined with two or three data points and the values that have been found so far range from $\alpha \sim -1.2$ to $\alpha \sim -2$ (with $J(\nu) \propto \nu^{\alpha}$, e.g. Venturi et al. 2013), indicating that the synchrotron spectrum of radio halos is not an universal power law. Reference values for the spectral index of typical radio halos are $\alpha \approx -1.2, -1.3$, but there are radio halos with extremely steep spectra $\alpha \leq -1.5$, the so called Ultra Steep Spectrum Radio Halos (USSRH). Given their spectral properties, the majority of USSRHs is expected to be detected at low frequencies (Brunetti et al. 2008; Macario et al. 2010; Venturi et al. 2017). In fact, new low frequency instruments, such as LOFAR and MWA are discovering many steep spectrum radio sources that where previously undetectable (Shimwell et al. 2016; Duchesne et al. 2017; Wilber et al. 2018). The analysis of the spectral index distribution of a few well studied radio halos reveals the presence of inhomogeneities on small scales, that may reflect the complexity of the energy distribution of the emitting electrons (e.g. Feretti et al. 2004; Orrú et al. 2007; Shimwell et al. 2016). At the same time, in other radio halos the spectral index is fairly constant throughout a large fraction of the radio halo area (van Weeren et al. 2016; Rajpurohit et al. 2018; Hoang et al. 2017).

Since radio halos are the main focus of this Thesis, Chapter 2 will be devoted to describe their statistical properties, both from a theoretical and an observational point of view.

1.5.3.1 Models for the formation of radio halos

The main difficulty in explaining the origin of radio halos arises from the combination of their Mpc size and the relatively short radiative lifetime of the radio emitting electrons (Fig. 1.8, see also Sect. 1.5.2). Indeed, the diffusion time necessary for the electrons to cover such distances is much larger than their radiative life-time; quantitatively, radio emission at ~ 1 GHz is typically due to electrons of $\approx 10B_{\mu G}^{-1/2}$ GeV, which have a radiative life-time of $\sim 10^8$ yrs. During this time, electrons can reach at most a diffusion distance of few tens of kpc (Blasi 2001; Brunetti 2003), which is ~ 2 orders of magnitude smaller than the typical size of radio halos. This argument, known as the *diffusion problem*, leads to the requirement that the emitting particles in radio halos are continuously accelerated or generated *in situ* in the emitting regions (Jaffe 1977). We give an overview of the main models proposed to solve the *diffusion problem* and explain the origin of radio halos below.

Secondary models

According to this class of models, the radio emitting electrons are continuously injected in the cluster volume as secondary products of inelastic hadronic collisions between CRp and thermal protons in the ICM (Dennison 1980; Blasi & Colafrancesco 1999). Secondary models would solve the *diffusion problem* because CRe are generated *in situ* throughout the ICM. They would also explain the connection between the radio and X-ray emission in galaxy clusters because the X-rays trace thermal matter that provides the targets for hadronic collisions. However, there is general consensus that current observations strongly disfavour a pure hadronic origin for radio halos (Jeltema & Profumo 2011; Brunetti et al. 2012, 2017).

The strongest constrain against secondary models comes from the non detection of galaxy clusters in the γ-rays. Indeed, an unavoidable consequence of p-p interactions in the ICM is the decay of neutral pions (π_0) that are produced by the same decay chain responsible for the injection of secondary CRe (Sect. 1.5.2). Only upper limits to the γ-ray emission of clusters of galaxies have been obtained so far with the Fermi-LAT satellite (Ackermann et al. 2010, 2014, 2015, 2016) putting stringent constraints on the CR content and in fact disfavouring a pure "secondary" origin for radio halos.

On one hand, these challenges from gamma-ray limits could be circumvented if magnetic fields in galaxy clusters were much larger than those constrained from Faraday RM, say $\geq$ few $\times 10$ μG. On the other hand, however, hadronic models face challenges from additional and independent observables. One basic expectation of these models is that, since CRp are long-living particles and accumulate on Hubble times in galaxy clusters, there is no obvious reason to expect that some clusters host luminous radio halos and some other clusters appear radio quiet at the sensitivity level of current observations (Brunetti et al. 2007, 2009; Cassano et al. 2013). In order to avoid this contradiction it should be assumed that the presence/absence of radio halos is due to the CRp dynamics in the ICM considering the possibility that CRp can stream on large scales in a relatively short timescale (e.g. Enßlin et al. 2011).

Another point that challenges pure secondary models is connected to the observed spectrum of radio halos. The most striking evidence comes from the spectrum of the Coma halo, which shows a steepening at high frequency (Brunetti et al. 2013) and that, in the context of hadronic models, would require an unrealistic break at about 10 GeV in the spectrum of the CRp that generate the secondary electrons. Although the Coma cluster is an unique case, more recently a similar problem has arisen from the discovery of USSRHs, whose steep spectra would require an energy run-away in the spectrum of CRp in the case of a secondary origin of the emitting electrons (e.g. Brunetti et al. 2008; Dallacasa et al. 2009; Macario et al. 2010; Wilber et al. 2018).

Although secondary models are nowadays disfavoured by several observables, it should be stressed that it is still unclear whether CRp and their secondary electrons play a role in the origin of radio halos, for example one possibility is that these particles are re-accelerated by other mechanisms in the ICM (e.g. Brunetti & Blasi 2005).

Re-acceleration models

The currently favoured scenario for the origin of RH is the re-acceleration model. In this model, the radio emitting electrons are continuously re-accelerated by MHD turbulence. In fact, large scale turbulent motions are generated in the ICM during mergers (e.g. Vazza et al. 2006; Miniati 2014; Vazza et al. 2017). These motions dissipate part of the merger energy throughout the cluster volume in ~ 1 Gyr. The largest motions generate random and turbulent velocity fields and may eventually cascade into electromagnetic fluctuations at smaller scales where they scatter and accelerate CR (Brunetti & Jones 2014, for a theoretical review).

Numerical simulations suggest that turbulence accounts for a considerable fraction of the thermal energy (15-20%, Dolag et al. 2005; Vazza et al. 2006, 2012; Miniati 2015; Vazza et al. 2017, see also Sect. 1.3.2). This turbulence can potentially trigger several mechanisms of particle acceleration (Brunetti & Jones 2014). The basic mechanism is the second order Fermi acceleration, where particles are stochastically accelerated as a consequence of random interactions with the perturbations in the structure of the magnetic field. Actually, acceleration of CRs directly from the thermal pool to relativistic energies by MHD turbulence in the ICM is very inefficient and faces serious problems associated to energy arguments (Petrosian & East 2008; Chernyshov et al. 2012). Consequently turbulent acceleration in the ICM is a matter of re-acceleration of pre-existing CRs rather than *ab initio* acceleration (Brunetti et al. 2001; Petrosian 2001).

Not only turbulent re-acceleration models solve the *diffusion problem*, because particles are accelerate *in situ*, directly on the cluster-scale, but also explain the

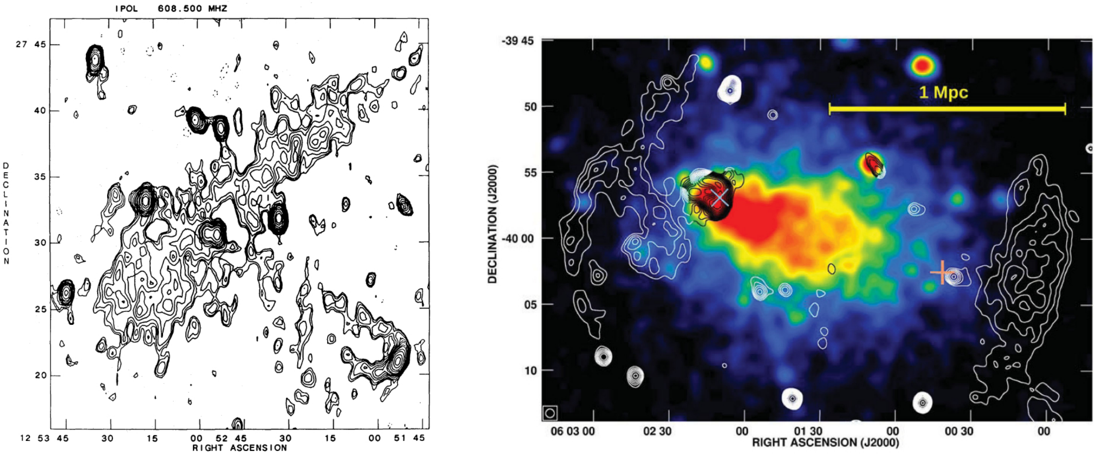

Figure 1.10: *Left panel*: 608 MHz WSRT map of the relic in the Coma cluster (Giovannini et al. 1993). *Right panel*: GMRT 325 MHz contours (white) superimposed on the ROSAT soft X-ray band image of the cluster Abell 3376 (colour) hosting double radio relics (Kale et al. 2012).

connection between radio halos and cluster mergers in a straightforward way. In this context, radio halos as expected to be transient phenomena during the entire cluster life-time that originate as a consequence of a merger event. The time scale of the radio halo phenomenon depends on the combination of the time necessary for turbulence to cascade from large to small scales (relevant for particle acceleration), of the time-scale for dissipation of turbulence and of the cluster-cluster crossing time. As we mentioned above, current results suggest that the typical life-time of radio halos is $\sim 1 - 2$ Gyr.

Further support to the re-acceleration scenario comes from the observed spectral properties of radio halos. Indeed, the predicted maximum Lorentz factor of the re-accelerated electrons is $\gamma \leq$few$\times 10^4$, producing a high energy cut off in the radio halo spectrum. This explains the variety of the observed spectra of radio halos, including the steepening observed in some halos and the USSRHs, that, conversely, challenge secondary models, as discussed above.

1.5.4 Radio relics

Similarly to radio halos, radio relics are giant ($\sim$Mpc) low surface brightness synchrotron sources found in some merging clusters. Unlike radio halos, relics are located at the cluster periphery and they have elongated or arc-like shapes. The emission of radio relics is polarized up to levels of $\sim 30\%$. Their spectra are steep, with typical spectral indices $\alpha \sim -1.2$ (Feretti et al. 2012). The prototype of this class of sources is the relic 1253+275 detected in the Coma cluster (Giovannini et al. 1991, 1993, Fig. 1.10, left panel). Spectacular cases of clusters with double radio relics, symmetrically located with respect to the cluster center, have been observed (e.g. Röttgering et al. 1997; Bonafede et al. 2009b; Kale et al. 2012; de Gasperin et al. 2014; Riseley et al. 2017).

There is consensus on the fact that radio relics are generated by the acceleration or re-acceleration of electrons at cosmic shocks (Ensslin et al. 1998; Brunetti & Jones 2014). The association between relics and peripheral shocks finds its origin in the characteristic shape of relics and in the fact that sometimes they appear in pairs, as expected for emerging merger shocks. In fact, some radio relics have been found to spatially coincide with merger shocks, detected in X-ray observations as jumps in temperature and/or density profiles (Giacintucci et al. 2008; Macario et al. 2011; Akamatsu & Kawahara 2013; Bourdin et al. 2013; Botteon et al. 2016a,b). Additionally, polarization studies show that the magnetic field is aligned with the long axis of the relic, suggesting that they form in regions where the magnetic field is compressed in the shock plane (Clarke & Ensslin 2006; van Weeren et al. 2010; Brüggen et al. 2012). The shock scenario is supported also by the evidence for a spectral steepening along the minor axis of the relic, from the shock front to the back, because the oldest population of electrons is also the most distant from the shock (e.g. Clarke & Ensslin 2006; van Weeren et al. 2016).

On the other hand, the mechanisms responsible for the origin of the emitting particles are still under discussion. One possibility to explain the formation of relics is the Diffusive Shock Acceleration DSA of thermal electrons (Krymskii 1977; Bell 1978a,b; Drury 1983), which is essentially a first order Fermi process, where particles are scattered up and downstream and they gain energy at each passage across the shock front. However, the commonly used DSA model is challenged by the low Mach number of shocks associated with cluster mergers (see Sect. 1.3.2). Indeed, the DSA of thermal particles is expected to generate very steep energy spectra in the case of weak shocks, as those observed in galaxy clusters ($\delta > 2$ with $\delta = 2\frac{\mathcal{M}^2+1}{\mathcal{M}^2-1}$). In several cases the observed spectra are much flatter than those expected from the observed shock Mach numbers, therefore the re-acceleration of a population of "fossil" relativistic electrons might be required to explain the properties of some relics (Markevitch et al. 2005; Kang et al. 2012; Vazza & Brüggen 2014; Bonafede et al. 2014a; Shimwell et al. 2015; Eckert et al. 2016; Botteon et al. 2016a; van Weeren et al. 2016, 2017).

A correlation between the radio power of relics and the mass of the host clusters has been recently found, together with the trend of larger relics to be located at larger distances from the cluster center (de Gasperin et al. 2014). This suggests that merger shocks become larger and larger as they move outwards from the cluster center.

It is worth mentioning that, in addition to merger shocks, external/accretion shocks are expected to form as the result of the continuous accretion of matter at large distance from the cluster center (Miniati et al. 2001). External shocks are typically much stronger than merger shocks, since they develop in regions where the medium is (much) cooler than in clusters. On the other hand, they propagate in regions with extremely low gas densities, therefore the energy dissipated by ex-

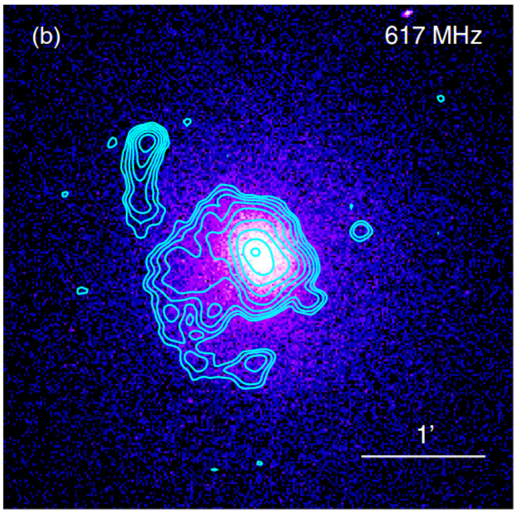

Figure 1.11: GMRT 617 MHz contours of the central ∼ 500 kpc of the cluster RX J1720.1. overlayed on the *Chandra* X-ray image. The central diffuse source in a mini-halo, while the elongated source in the North-East is a head-tail radio galaxy (Giacintucci et al. 2014a).

ternal shocks is much smaller than that dissipated at merger shocks that are faster and propagate through relatively dense environments (energy flux across the shock surface S is $\propto \rho V_{sh}^3 S$, where V_{sh} is the shock front speed, Ryu et al. 2003; Vazza et al. 2009). Therefore, external shocks are usually very difficult to detect, unless they encounter some cloud of relativistic plasma during their propagation.

1.5.5 Mini halos

Mini halos are diffuse sources located at the center of a number of cool-core clusters that extend on scales smaller than the cluster cores (e.g. smaller than $0.2 \times R_{500}$; Giacintucci et al. 2014b, 2017). They usually embed the radio emission of the central elliptical galaxy often detected in relaxed clusters (Fig. 1.11). The prototype of this class of objects is the mini halo in the Perseus cluster (Burns et al. 1992; Sijbring 1993), whose emission fills the cool core of the cluster and extends much beyond the central AGN radio emission (Fabian et al. 2000). The combination of high and low resolution images with high dynamic range is necessary to map the diffuse emission and to disentangle the emission of the central AGN from the mini halo emission. Nevertheless, the number of known mini halos has been considerably increasing in the past years (Hlavacek-Larrondo et al. 2013; Giacintucci et al. 2014b; van Weeren et al. 2014; Kale et al. 2015; Giacintucci et al. 2017) allowing to perform the first statistical studies (Giacintucci et al. 2014b; Bravi et al. 2016; Giacintucci et al. 2017). These studies confirm that mini halos are associated to relaxed clusters and that there is the tendency to find mini halos preferentially in the most massive cool core clusters (Giacintucci et al. 2014b). Moreover, there is evidence for a connection between the thermal properties of cool cores and non-thermal properties of mini halos (Bravi et al. 2016) suggesting that the mechanisms responsible for the formation of mini halos are sustained by the thermal energy budget and might contribute to balance the radiative cooling in the cluster cores (Zhuravleva et al. 2014).

Although to less extent than for radio halos, mini halos face the *diffusion problem* as well. Therefore mini halos require some mechanism of acceleration or injection of particles *in situ*. One possibility is that the synchrotron emission arises from a population of pre-existing electrons (for instance injected by past AGN activity) re-accelerated from turbulence (Gitti et al. 2002, 2004). The origin of turbulence is still unclear. The mini halo-cool core connection tells that, contrary to radio halos, turbulence in mini halos is not associated to major merger events. The fact that mini halos are often confined between cold fronts (Mazzotta & Giacintucci 2008; Hlavacek-Larrondo et al. 2013; Giacintucci et al. 2014a) resulting from sloshing of the cold gas in the core (Ascasibar & Markevitch 2006), suggests that such sloshing may generate turbulence in cluster cores (Mazzotta & Giacintucci 2008). Numerical simulations support this scenario, showing that sloshing motions can amplify magnetic fields and develop turbulence in the region between cold fronts (ZuHone et al. 2013). The unique direct measurement of the gas velocities in the cool core of Perseus has been performed with the Hitomi X-ray satellite and revealed the presence of turbulence sufficient for accelerating particles, and possibly for balancing the radiative cooling in the core (Hitomi Collaboration et al. 2016).

Another possibility to explain the origin of mini halos is the hadronic model, where the electrons are continuously injected in the central ICM as by-products of p-p collisions (Pfrommer & Enßlin 2004; Zandanel et al. 2014; ZuHone et al. 2015). In this scenario, relativistic protons could be naturally provided by the central AGN and then diffused across the cluster core. Simulations show that secondary electrons in a sloshing core can generate diffuse radio emission, although it does not seem to be completely confined within the cold fronts, as observed in typical mini halos (ZuHone et al. 2015). Unlike the case of giant radio halos, hadronic models for mini halos are not challenged by gamma-ray observations because the emitting volumes are much smaller (e.g. Fujita et al. 2014; Pfrommer et al. 2017). The instabilities generated by the streaming of the same CRp that are responsible for the secondaries in the cool core may provide a rate of heating that could balance gas cooling, thus accounting for the origin of mini halos and the *cooling flow* problem, at the same time.

1.5.6 High energy emission

Thermal emission from the ICM is dominant in the ∼kev energy range, but it is expected to decline rapidly at higher energies, allowing the detection of non-thermal emission in the $\sim 10-20$ keV band. Non thermal emission at high energies is un-

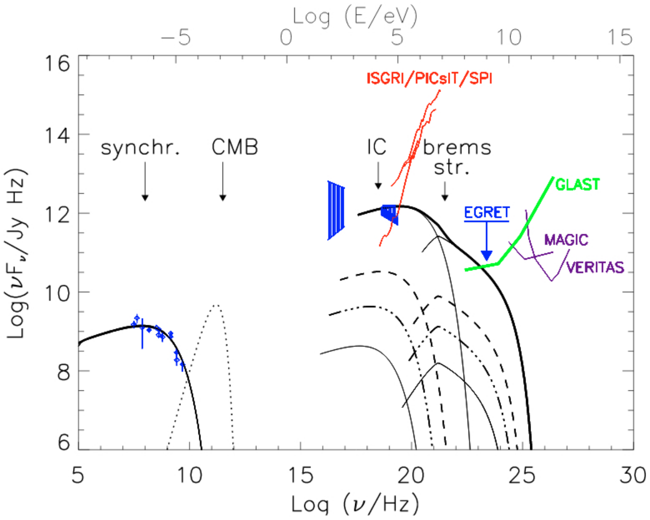

Figure 1.12: Expected spectrum of the Coma cluster from the radio to the gamma ray band (Reimer et al. 2004).

avoidably expected in the theoretical framework explaining the origin of radio halos and radio relics. Supra-thermal particles generate non-thermal bremsstrahlung, higher energy particles generate IC emission in the hard X-rays and the decay of the neutral pions from CRp-p interactions generate gamma-ray emission at some level (Fig. 1.12 Reimer et al. 2004; Brunetti & Jones 2014).

Hard X-ray emission has been claimed for Coma by Rephaeli et al. (1999) and Rephaeli & Gruber (2002) with observations from the Rossi X-ray Timing Explorer (RXTE) and by Fusco-Femiano et al. (1999, 2004) with BeppoSAX observations. However, these detections remain controversial (Rossetti & Molendi 2004; Fusco-Femiano et al. 2007). More recent observations with Swift and Suzaku have failed to confirm the detection of IC from galaxy clusters (Wik et al. 2011; Ota et al. 2014). Not even the Hard X-ray spectrum of the Bullet and the Coma clusters observed with the unprecedented focusing capability of NuSTAR need to invoke IC emission (Wik et al. 2014; Gastaldello et al. 2015).

The emission of γ-rays in clusters of galaxies is a natural by-product of the CRp confinement and consequent decay chain of p-p collisions (Sect. 1.5.2). In the last decades, numerical simulations have provided estimates of the expected γ-ray emission from clusters, predicting that they would be potentially detected by the Fermi-LAT satellite (Miniati et al. 2001; Miniati 2003; Pfrommer et al. 2008). However, the most recent limits, derived from 6 years of Fermi-LAT observations, are not consistent with those expectations (Ackermann et al. 2016). To date, no detection of galaxy clusters in the γ-rays has been reported, still, the absence of gamma-rays provides important information on the physics of particle acceleration and transport in the ICM.

Chapter 2

Statistical properties of radio halos

Radio halos are the main focus of this PhD Thesis. The statistical analysis of the properties of radio halos is a powerful tool to understand the physical processes involved in their origin and evolution. Statistical models have a fundamental role because they provide expectations that can be tested with observations of a large number of galaxy clusters. On the other hand, statistical studies of the observed properties of radio halos provide a solid and unavoidable basis for theoretical models. Clearly, this kind of interplay between theory, observations and statistics requires huge efforts, both in terms of calculations and simulations and in terms of observations and data analysis and interpretation. In fact, the present PhD Thesis is devoted to obtain a solid assessment of the statistical properties of radio halos and a first comparison with model expectations. In Chapters 5 and 6 we will discuss our observational findings, in Chapter 7 we will show a first comparison of our findings with theoretical expectations from Cassano & Brunetti (2005) and Cassano et al. (2006).

In this Chapter, we briefly describe the statistical model proposed by Cassano & Brunetti (2005) and Cassano et al. (2006) to describe the evolution of the non-thermal emission in galaxy clusters in the framework of the turbulent re-acceleration scenario. We summarize the main expectations on the observable properties of radio halos and we recall the main observational results found in the last decade.

2.1 A statistical model for the formation of radio halos

The semi-analytical calculations proposed by Cassano & Brunetti (2005) and Cassano et al. (2006) are based on a self- consistent approach: the evolution of the thermal properties of the ICM in the host cluster and the generation of non-thermal phenomena are both taken into account at the same time. The main ingredients of this model can be summarised as follows.

- **Cluster formation**
  The model is based on the hierarchical theory of structure formation, according to which galaxy clusters form via subsequent mergers of smaller substructures. This complex process is computed following the extended Press-Schechter theory (Press & Schechter 1974) developed by Lacey & Cole (1993). Given the mass and temperature of a cluster at redshift $z = 0$, its formation history is built up with Monte Carlo simulations. The present properties of a cluster can be the result of different merging histories, hence a large number of merger trees is needed to describe the cosmological evolution of clusters from a statistical point of view (Fig. 2.1, top panel).

- **Turbulence in the ICM**
  Turbulence is assumed to be injected in the ICM during each merger event leading to the formation of a cluster. Hence, turbulence is considered as a transient phenomenon in clusters, tightly connected to the merging activity. The rate of energy density that is injected into turbulence is basically calculated from the PdV work done by the infalling subcluster when passing through the most massive one. This is:

  $$\frac{E_t}{\tau_{cross} \times V_H} \simeq \frac{\bar{\rho}_{max,s}}{R_{max}} v_i^3 \left(\frac{V_t}{V_H} \right) \tag{2.1}$$

  where $V_H = (4\pi R_H^3)/3$ and R_H are the volume and the radius of the radio halo, respectively. $E_t = \bar{\rho}_{max,s} v_i^2 V_t$ and $\bar{\rho}_{max}$ is the density of the ICM averaged on the volume swept by the infalling subcluster.
  Turbulence is then dissipated throughout the cluster volume on time-scales of the order of the crossing time. A turbulent cascade from large to small scales is developed and eventually a fraction of the turbulent energy is channelled into magneto-sonic waves that in turns accelerate particles. We stress that the amount of turbulent energy and thus the efficiency of turbulent reacceleration, depends on the energetics of the merger, i.e. major mergers have higher energy budget available for particle acceleration.

- **Particle acceleration**
  The model assumes a pre-existing population of relativistic electrons, injected in the ICM by e.g. AGNs, powerful galactic winds and/or Supernovae. The process of particle re-acceleration starts when the turbulent cascade reaches the small scales and the time needed for particles to be significantly boosted in energy is inversely proportional to the efficiency of turbulent acceleration. The model assumes Transit Time Damping (Brunetti & Lazarian 2007, for details on the physics of the mechanism) with magnetosonic/fast turbulent modes

as the mechanisms of re-acceleration. For each merger tree, the acceleration efficiency as a function of redshift (2.1, bottom right panel), represented by the acceleration coefficient $\chi(z) = \frac{1}{\tau_{acc}} = D_{pp}/4p^2$ where D_{pp} is the diffusion coefficient in the particles momentum space due to the stochastic acceleration mechanisms, can be obtained by combining all the merger events that contribute to the injection of turbulence at a given redshift. An example of the time evolution of the electron spectrum during the re-acceleration process is shown in Fig. 2.1 (bottom left panel). Electrons, initially accumulated at $\gamma \sim 10^3$, are efficiently accelerated up to $\gamma \sim 10^4 - 10^5$ (Cassano & Brunetti 2005).

This describes the complex picture of the formation and evolution of radio halos in a relatively simple form and involves several poorly constrained parameters, such as the magnetic field intensity, the fraction of turbulent energy, the fraction of energy converted into magneto-sonic waves. Nevertheless, it allows to derive basic and unavoidable predictions on the statistical properties of radio halos that can be investigated with observational studies.

2.1.1 Main expectations

Acceleration of CRe from MHD turbulence is a a rather inefficient mechanism (Brunetti & Jones 2014) that boosts the energies of electrons only up to ~10 Gev, due to the competition with radiative (IC and synchrotron) losses. This implies that a high frequency cut off in the synchrotron spectra of radio halos, with ν_b being the break frequency. Consequently, the possibility to detect a radio halo is related to the observing frequency, ν_{obs} and, in particular, the spectral steepening challenges the detection of radio halos with $\nu_s \sim$ few $\times\ \nu_b < \nu_{obs}$, where we have defined ν_s as the frequency at which the steepening becomes severe. A crucial prediction of the model proposed by Cassano & Brunetti (2005) and Cassano et al. (2006) is the existence of radio halos with different spectral properties. As a reference, if we assume a simplified homogeneous model (i.e. typical acceleration efficiency and magnetic field in the ICM), the break frequency of radio halos is expected to be proportional to the electron acceleration coefficient:

$$\nu_b \propto \langle B\rangle \gamma_{max}^2 \propto \frac{\langle B\rangle \chi^2}{(\langle B\rangle^2 + B_{CMB}^2)^2} \tag{2.2}$$

where γ_{max} is the maximum energy of the emitting electrons. χ, in turns, is related to the energetics of the merger event, and thus to the mass of the clusters involved and to the kind of merger (major or minor merger). Therefore, high values of ν_b are expected for massive clusters and in connection with major mergers. Consequently, radio halos with $\nu_b >$GHz are expected to form only in the most massive clusters, undergoing energetic merger events, that however are rare in the Universe (Fig. 2.2). At the same time, an unique prediction of this model is the existence of

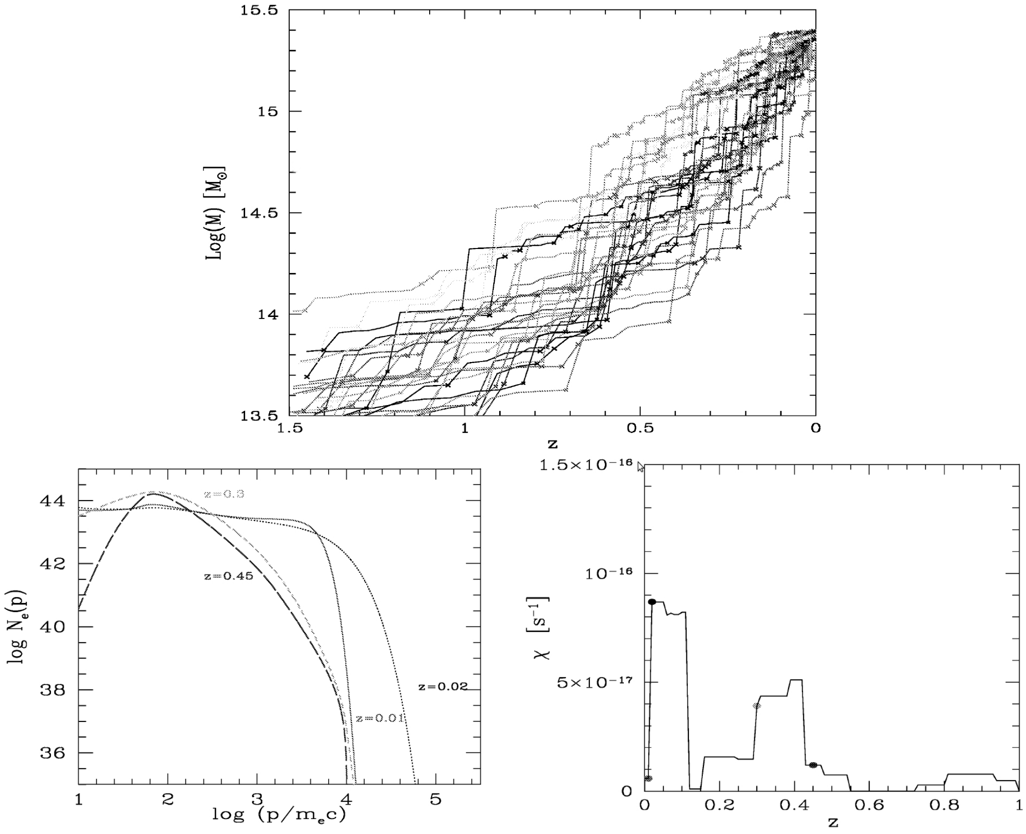

Figure 2.1: *Top*: merger trees obtained from Monte Carlo simulations for clusters with present-day mass $M_0 = 2.5 \times 10^{15}\, M_\odot$. *Bottom left*: electron spectra calculated at different redshift for the same cluster. *Bottom right*: Evolution with redshift of the electron-acceleration coefficient resulting from the combination of the merger events that contribute to the ICM turbulence at a given redshift.

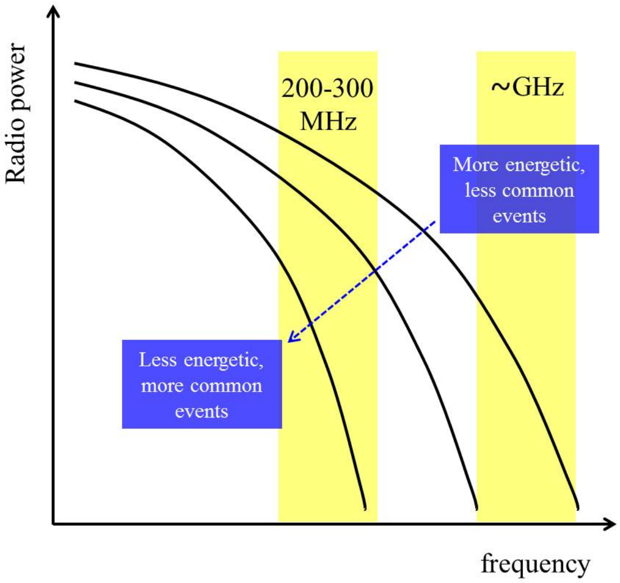

Figure 2.2: Cartoon of radio halo spectra expected in the framework of turbulent re-acceleration models. Yellow regions represent two possible observing frequency bands.

radio halos with ν_b <GHz, generated in less massive clusters and/or minor mergers. These radio halos, when observed at ∼GHz frequencies should show extremely steep spectra ($\alpha < -1.5$) and they are expected to constitute the class of USSRHs. Less energetic merger events, involving clusters of smaller masses, are more common in the Universe, therefore, given the existence of USSRHs, the number of radio halos is expected to increase at low observational frequencies (Fig. 2.2, see Sect. 2.1.1.1) .

2.1.1.1 Probability of forming radio halos

Since the break frequency depends on the electron acceleration coefficient, the above-mentioned condition for the detectability of radio halos becomes a condition on the acceleration coefficient: $\chi \geq \chi_{min}(\nu_{obs})$. Each merger tree of each cluster in the model, has a corresponding $\chi(z)$ (Fig. 2.3) that reflects the formation history of the cluster. We can calculate the fraction of time that the cluster spends with $\chi \geq \chi_{min}$ in a given mass and redshift range (ΔM and Δz in Fig.2.3). The total probability of forming a radio halo is obtained from the combination of all the contributions of the merger trees relevant for that mass and redshift bins. This probability is then weighted with the Press & Schechter mass function to take into account the number density of clusters as a function of mass.

The basic prediction of the model is that the probability of forming radio halos increases with the mass of the host cluster (Fig.2.4, left panel, Cassano et al. 2006). Even though these calculations are complex and based on a number of unknown

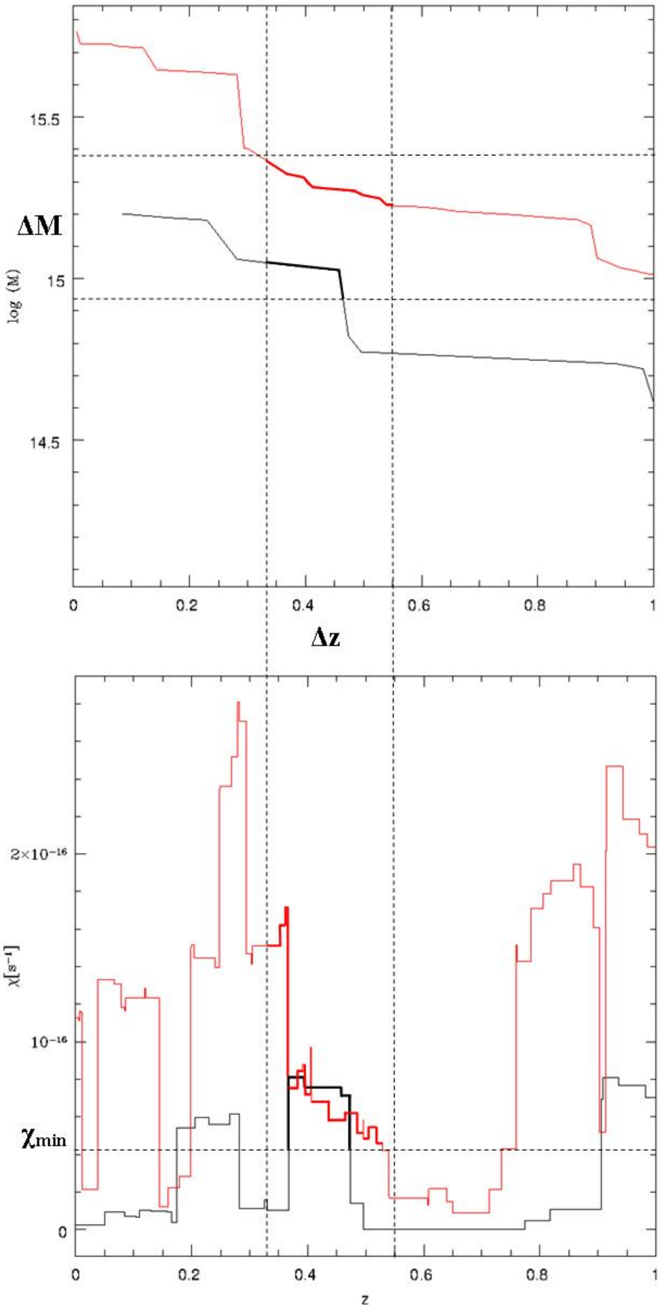

Figure 2.3: *Top*: example of two merger trees (black and red lines) of the same cluster. *Bottom*: evolution of the electron acceleration coefficient, $\chi(z)$, associated with the two merger trees reported above. For a given ΔM (and Δz) selected on the merger trees (bold face lines in the upper panel), we selected the fraction of time that each cluster spends with $\chi \geq \chi_{min}$ (bold face lines in the lower panel). For example, we report a value of $\chi_{min} \sim 4 \times 10^{-17}$ s^{-1}.

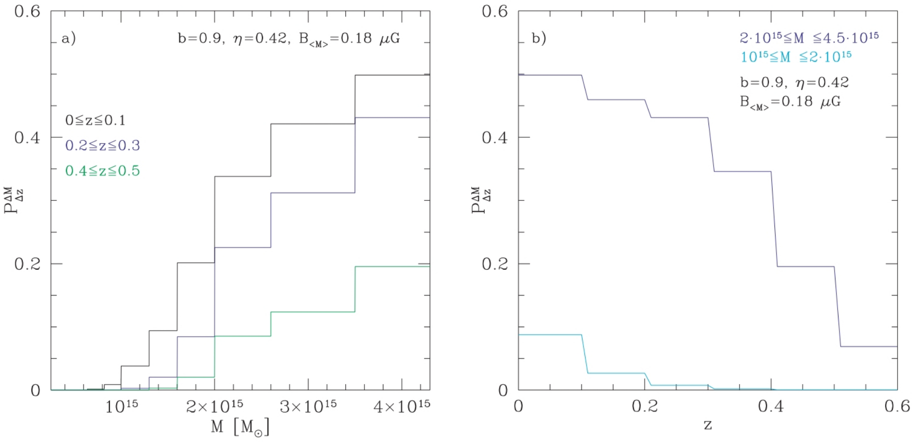

Figure 2.4: *Left panel*: probability of forming radio halos as a function of the cluster mass in three redshift bins: $z = 0 - 0.1$ (black line), $z = 0.2 - 0.3$ (blue line) and $z = 0.4 - 0.5$ (green line). *Right panel*: Probability of forming radio halos as a funtion of redshift in two mass bins: $M = 1 - 2 \times 10^{15} M_{\odot}$ (cyan line) and $M = 2 - 4 \times 10^{15} M_{\odot}$ (blue line).

parameters, this is a clear prediction of the re-acceleration model, because the mass, which defines the energetic of the merger events, sets the amount of energy available for particle acceleration. On the other hand, the probability of forming radio halos is expected to decrease with redshift due to the increasing IC losses (Fig. 2.4, right panel). Indeed, at high redshift, the electron energy losses via IC largely prevail the synchrotron energy losses ($B_{CMB} \simeq 3.28 \times (1+z)^2$ μG).

Another crucial expectation of turbulent re-acceleration models is that the fraction of clusters with radio halos should increase at low frequencies (Fig. 2.5, Cassano et al. 2010a, 2012). In particular, such increase is expected to be more significant for relatively low mass systems and at higher redshift (Fig. 2.5). This is due to the presence of a population of USSRHs, that are only visible at low radio frequency. In fact, USSRHs are expected to be generated in smaller systems and/or at relatively higher z with respect to radio halos emitting up to GHz frequencies. In low mass clusters, the merger driven turbulence is not sufficient to accelerate particles up to the energy necessary to emit synchrotron radiation at GHz frequencies, and at high redshift IC losses limit the maximum energy of the accelerated electrons and thus decrease the break frequency. This prediction is particularly relevant for radio telescopes such as the LOFAR (Röttgering et al. 2011; van Haarlem et al. 2013; Röttgering et al. 2013) and the MWA (Tingay et al. 2013; Wayth et al. 2015) that are opening a new observational window, at low frequencies.

2.2 Observational results

Pioneering studies based on Arecibo observations and radio surveys like the NRAO VLA Sky Survey (NVSS) and the Westerbork Northern Sky Survey (WENSS) re-

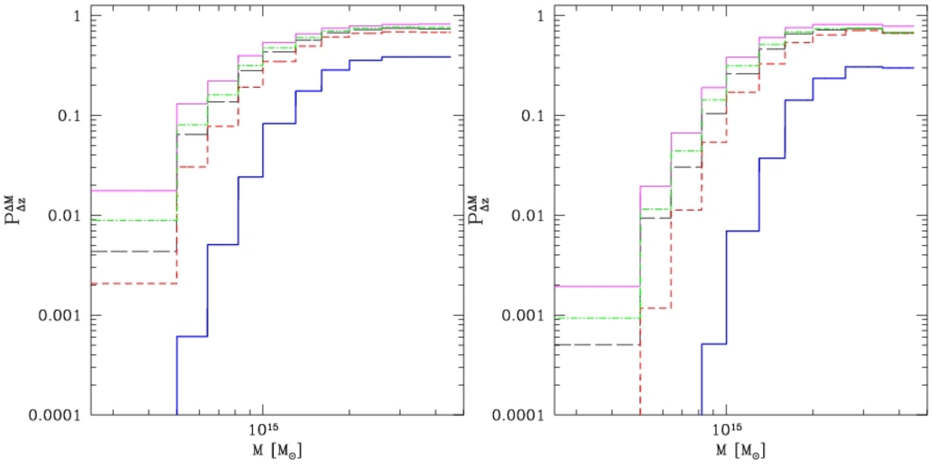

Figure 2.5: Probability of forming radio halos with $\nu_s \geq \nu_{obs}$ as a function of the cluster mass at $z = 0 - 0.1$ (*left panel*) and at $z = 0.4 - 0.5$ (*right panel*). $\nu_{obs} = (1400, 240, 150, 120, 74)$ MHz (solid blue, red, dashed blue, green and pink lines, respectively). From Cassano et al. (2010a).

vealed that radio halos are not ubiquitous in galaxy clusters (Hanisch 1982; Giovannini et al. 1999; Kempner & Sarazin 2001). In particular, Giovannini et al. (1999) suggested that the occurrence of radio halos increases with increasing the X-ray luminosity of the parent clusters. However, that conclusion was at least partly driven by the fact that the radio luminosity of halos increases with the cluster X-ray luminosity, which was discovered a couple of years later.

An important step forward in these studies has been made with the GMRT Radio Halo Survey (GRHS, Venturi et al. 2007, 2008), a sample of X-ray selected galaxy clusters observed with the Giant Meterwave Radio Telescope (GMRT) at 610 MHz in order to search for extended emission. Clusters were selected from the combination of two X-ray catalogues, the REFLEX (Böhringer et al. 2004) and the eBCS (Ebeling et al. 2000), with the following selection criteria:

- L_X (0.1-2.4 keV)$\geq 5 \times 10^{44}$ erg/s
- $0.2 \leq z \leq 0.4$
- $-30^\circ < \delta < +2.5^\circ$ for the REFLEX sample and $-15^\circ < \delta < +60^\circ$ for the eBCS sample.

The sample built up by Venturi et al. (2007, 2008) included 50 clusters. That sample has been then extended by Kale et al. (2013, 2015) by using a declination limit $\delta > -30^\circ$ both for the REFLEX and the eBCS catalogues, leading to a final sample of 64 clusters that we refer to as the Extended GRHS (EGRHS). This survey led to the detection of $\sim$ 10 new radio halos, $\sim$ 10 new mini halos and $\sim$ 5 new relics (Kale et al. 2015). Most of the clusters of the GRHS and its extension do not host diffuse emission, however, from a statistical point of view, they potentially provide useful information. Venturi et al. (2008) developed a procedure to place upper limits

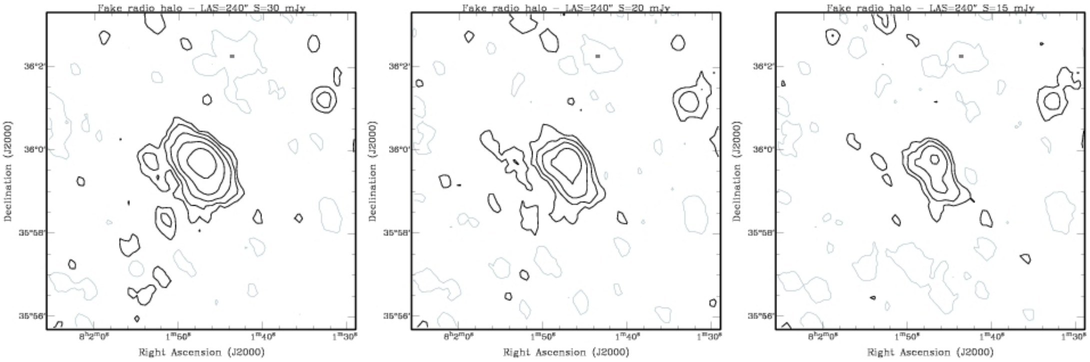

Figure 2.6: GMRT 610 MHz contours of a sequence fake radio halos with decreasing flux densities: 30 mJy (*left*), 20 mJy (*center*) and 15 mJy (*right*). Adapted from Venturi et al. (2008).

to the diffuse flux density of clusters that do not show hints of diffuse emission. This procedure was thought to derive meaningful values of the radio upper limits taking into account the interferometric response of the observations. Specifically, they injected a set of simulated (fake) halos with decreasing flux densities in the datasets and then re-imaged the data in order to determine the minimum flux density that would be detectable as a possible radio halo for any specific observation. They set the diameter of the fake radio halo to 1 Mpc and they modelled its brightness distribution with a set of concentric spheres with different radii and flux densities in order to match the typical profile of known radio halos. The model was added to the *uv* dataset and the modified dataset was imaged to evaluate the detection of the fake radio halo. They started injecting fake radio halos with flux density of ~ 30 mJy and they iterated the process decreasing the injected flux density until the diffuse emission resulted only in positive residuals that would lead to the suspect of diffuse emission. An example of this procedure is shown in Fig. 2.6.

2.2.1 Ultra-steep spectrum radio halos

Statistical studies of galaxy clusters in the radio band, including the GRHS and its extension, allowed a census of the spectral properties of radio halos. The detailed spectral analysis of radio halos is a challenging task because it requires reliable and comparable measurements in a broad frequency range. Nevertheless, the spectral properties of radio halos are fundamental to constrain their origin. Radio halos have spectral indices in the range $\alpha \approx -1, -2$ (Feretti et al. 2012; Venturi 2011; Venturi et al. 2013), indicating that their synchrotron spectrum is not an universal power law and this provides an important constrain for models. Particularly stringent constraints, however, come from radio halos with very steep spectra, the USSRHs. This class of radio halos has integrated spectral indices $\alpha < -1.5$, in comparison with the spectral indices of "typical" radio halos $\alpha \approx -1.2, -1.3$. The prototype of USSRH has been found in the galaxy cluster Abell 521 with GMRT

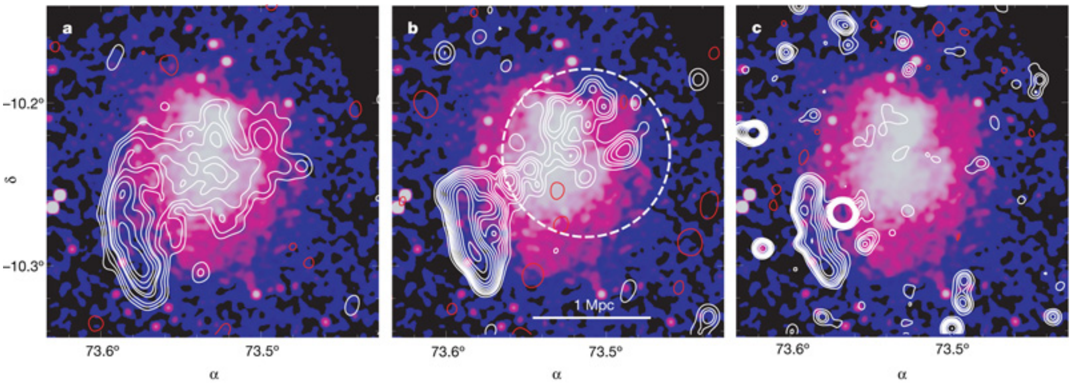

Figure 2.7: A521 GMRT 240 MHz (*left*), GMRT 610 MHz (*center*) and VLA 1.4 GHz (*right*) contours overlaid on the X-ray *Chandra* image (Brunetti et al. 2008).

240, 330 and 610 MHz observations (Fig. 2.7, Brunetti et al. 2008). Deep VLA 1.4 GHz follow-up observations were carried out by Dallacasa et al. (2009) who constructed the spectrum of the radio halo and measured the average spectral index $\alpha = -1.86 \pm 0.08$. The spectrum of the emitting electrons is $\delta = 2\alpha + 1$ (with $S \propto \nu^{-\alpha}$) implying that for $\alpha > 1.5$ a spectrum of electrons $\delta > 4$ is necessary, leading to a unavoidable runaway of the energetics associated to these particles (in particular to the lower energy part of the spectrum). For this reason, the spectrum of electrons should flatten at lower energies (or steepen at higher energies) in line with the expectations from re-acceleration models (see discussion in Brunetti et al. 2008). At the same time, these sources also challenge hadronic models due to energy arguments requiring a spectrum of the primary CRp $\delta_p > 3.0$ (see Section 1.5.3 and references therein).

Until a few years ago, only few USSRHs and candidate USSRHs were known in the literature (Brunetti et al. 2008; Macario et al. 2010; Venturi et al. 2013). Given their steep spectra, the bulk of these sources is expected to be discovered at low frequencies (Cassano et al. 2012). In this respect, we are living an exciting era for radio astronomy with new facilities operating at low frequencies with unprecedented sensitivity. In fact, new USSRHs has been recently detected with LOFAR (Shimwell et al. 2016; Venturi et al. 2017; Wilber et al. 2018, Savini et al. in prep.) and MWA (Duchesne et al. 2017).

2.2.2 Radio power-X-ray luminosity correlation

The existence of a correlation between the radio power of radio halos and the X-ray luminosity of the host clusters is known from the first studies of collections of radio halos (e.g. Liang et al. 2000; Enßlin & Röttgering 2002; Bacchi et al. 2003; Cassano et al. 2006; Rudnick & Lemmerman 2009). This correlation has been confirmed also for the clusters of the GMRT Surveys (Fig.2.8, Brunetti et al. 2009; Kale et al. 2015). Moreover, the sensitivity of the observations carried out with the GMRT allowed to place deep upper limits to the diffuse flux density of clusters without radio halos (Sect. 2.2). This led to the discovery of the "radio bimodality" of galaxy clusters in the radio-X-ray luminosity diagram, with giant radio halos lying on the well-known correlation and clusters without diffuse emission lying well below the correlation (Brunetti et al. 2007, 2009). Most importantly, the bimodality can be highlighted by combining the information on the distribution of radio halos in the radio-X-ray luminosity diagram with the dynamical properties of the hosting systems: radio halos are found in merging clusters, while clusters with upper limits are typically relaxed systems (Cassano et al. 2010b, see Sect. 2.2.4 for details). In the context of turbulent re-acceleration models, the radio bimodality of clusters can be explained in terms of different evolutionary stages, in connection with the dynamical activity. The idea is that, during merger events, the synchrotron emission evolves with the cluster dynamics: it increases in the early stage of the merger, when turbulence accelerates electrons, and then it declines along with the dissipation of turbulence at later merger stages. In the absence of additional sources of turbulence/particles, this induces a migration of radio halos from the region of the upper limits to the correlation and back to the upper limits, or below. A solid estimate of the lifetime of radio halos and of the time necessary to migrate from the correlation to the upper limits is challenging as it depends on the details of cluster dynamics and the ICM microphysics. Still, a first look at these timescales has been obtained from idealised simulations, including turbulent re-acceleration of primary electrons. It has been shown that merger-induced turbulence has the potential to light up the radio emission, lifting the clusters from the region of the upper limits up to the region spanned by the correlation in the radio power-X-ray luminosity diagram (Donnert et al. 2013). Within $\sim 1-2$ Gyr the radio luminosity is expected to decrease and clusters go back to the upper limits level. According to these simulations, clusters are expected to spend ≤ 0.5 Gyr in the region between the correlation and the current level of the upper limits, thus it is not surprising that this region is statistically less populated. In this framework, the transition region should be populated either by young systems, where the synchrotron emission is "switching on" (moving upwards) or by systems in the late phase of merging, where the radio halo is fading away (moving downwards). This implies that a number of radio halos in the transition region between the correlation and the upper limits is expected to be found with the increase of the statistics. In the cosmological framework, the situation can be much more complicated than this, not only because the the observed population of radio halos is the combination of different intermediate radio halo stages, but also because radio halos are generated from a complex hierarchy of merging events and each merger is different in terms of energetics and impact in the ICM. For this reason, statistical studies of galaxy clusters are crucial to understand the evolution of the radio diffuse emission. This point will be discussed in more detail in the interpretation of the observations in Chapter 6.

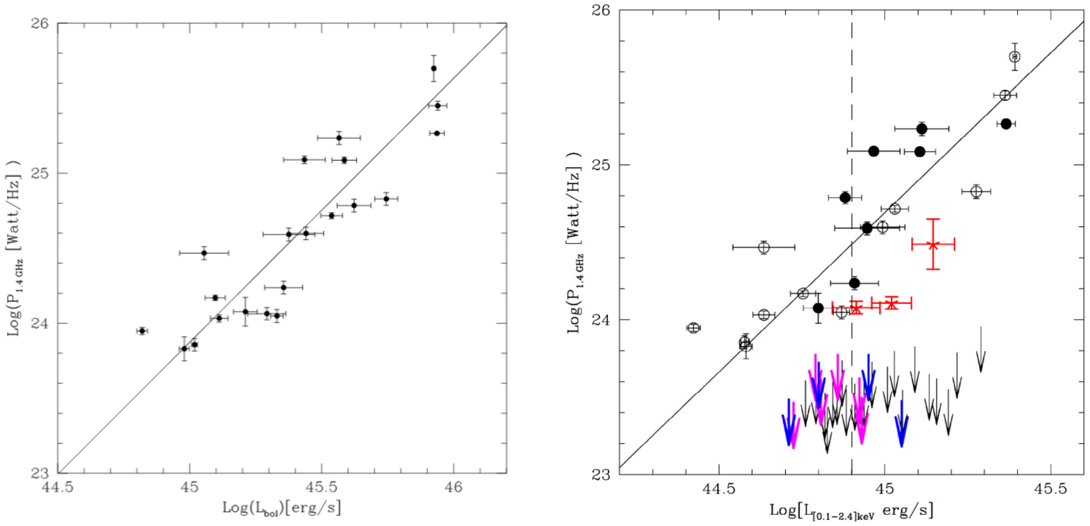

Figure 2.8: *Left panel*: distribution of clusters (GRHS+literature) in the radio power-X-ray luminosty diagram. The solid line is the best fit of the distribution (Brunetti et al. 2009). *Right panel*: Upper limits to the diffuse emission of cluster without radio halos (arrows) are shown on the radio power-X-ray luminosity diagram together with the correlation for giant radio halos (Kale et al. 2015).

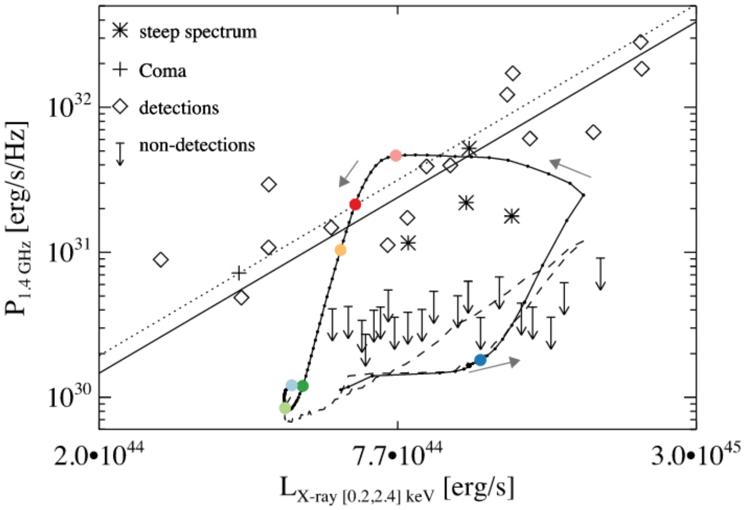

Figure 2.9: Evolution of a cluster experiencing a merger event in the radio-X-ray luminosity diagram (black line). Coloured dots mark the time evolution every 25 Myr. Overplotted are the radio halo clusters and the uper limits from Brunetti et al. (2009) together with the correlation. From Donnert et al. (2013).

2.2.3 Occurrence of radio halos

Early studies of the occurrence of radio halos in galaxy clusters suggested that the fraction of radio halos increases with the X-ray luminosity of the host cluster (Giovannini et al. 1999; Kempner & Sarazin 2001; Rudnick et al. 2006). An important step forward in this sense has been made by Cassano et al. (2008) who presented a statistical analysis of the occurrence of radio halos in an X-ray-selected sample of galaxy clusters accounting for both radio and X-ray selection biases. They combined the NVSS-XBAC sample at $z < 0.2$ (Giovannini et al. 1999) and the GRHS at $0.2 \leq z \leq 0.4$ and they calculated the fraction of clusters with radio halos in the populations of low luminosity and high luminosity clusters. $L_X = 10^{44.9}$ erg/s was chosen as the transition value for the luminosity because it ensures a good statistic in both the luminosity bins. Their main finding was that the fraction of clusters hosting radio halos increases with increasing the X-ray luminosity of the clusters, in particular they claimed that the fraction of clusters hosting radio halos in the low luminosity bin is $7.5 \pm 3.8\%$, while it is $40.6 \pm 11.2\%$ in the high luminosity bin.

The increase of the probability of forming radio halos with increasing the cluster mass is an unique expectation of the turbulent re-acceleration scenario, since a more efficient particle acceleration is triggered in massive (X-ray luminous) systems during major mergers (Sec 2.1.1.1). Therefore, the jump in the occurrence of radio halos from low luminosity to high luminosity clusters gives support to the model of turbulent re-acceleration. The limitation of this result lies in the fact that the correlation between the X-ray luminosity and the cluster mass needs to be assumed in order to compare the observational results with the theoretical expectations (see Section 2.2.5 and Chapter 3).

2.2.4 Radio halo-merger connection

There is general consensus that radio halos are preferentially found in clusters with evidence of ongoing dynamical activity [1]. The first quantitative evaluation of the dynamical status of clusters with radio halos has been performed by Buote (2001) using the multiple decomposition of the X-ray surface brightness distribution. In particular, they found a correlation between the radio halo luminosity and the dipole ratio P_1/P_0, which gives an estimate of the dynamical disturbance of clusters. Venturi et al. (2008) extended the analysis of the dipole ratios to the P_3/P_0 parameter, which is related to the presence of multiple peaks in the X-ray surface brightness distribution and to the P_2/P_0 that can be considered as a measurement of the cluster ellipticity. They found a separation in the $P_1/P_0 - P_3/P_0$ diagram between relaxed and disturbed clusters, with radio halos in the disturbed region and clusters without diffuse emission in the relaxed one.

---

[1] Only three radio halos have been found so far in relaxed clusters: CL1821+643 (Bonafede et al. 2014b), A2261 and A2390 (Sommer et al. 2017).

The GRHS has been of fundamental importance also in this respect, providing the first solid statistical assessment of the radio halo-merger connection. Cassano et al. (2010b) analysed the *Chandra* X-ray surface brightness distribution of the clusters belonging to the GRHS and derived three morphological parameters that have been largely used in the literature to characterise the dynamical status of clusters (e.g. Buote & Tsai 1995; Böhringer et al. 2010; Poole et al. 2006; Maughan et al. 2008; Santos et al. 2008): the centroid shift, w, the concentration parameter, c and the power ratios P_3/P_0. The centroid shift is a measure of the shift between the peak and the centroid of the X-ray emission, the concentration parameter measures how much the X-ray surface brightness is concentrated in the core of the cluster, and the power ratios measure the presence of substructures in the X-ray surface brightness distribution. Since the parameters and the method to derive them will be extensively discussed in Chapter 3, here we only mention that high values of c imply relaxed clusters, while high values of w and P_3/P_0 mean dynamically disturbed clusters.

Cassano et al. (2010b) found a clear anti-correlation between the concentration and the centroid shift parameters (c, w), and between the concentration parameter and the power ratio $(c, P_3/P_0)$, while they found a correlation between the centroid shift and the power ratio parameters $(w, P_3/P_0)$(Fig. 2.10). Most importantly, radio halo clusters (red filled dots) can be well separated from clusters without radio halos (black open dots) in all diagrams, confirming the hypothesis that radio halos form in dynamically disturbed clusters, while clusters without diffuse radio emission are relaxed systems. To test quantitatively this result, Cassano et al. (2010b) used Monte Carlo simulations on the $c - w$ plane, finding that the probability to have such segregation between radio halos and non-radio halo clusters by chance is of the order of $(3 - 4) \times 10^{-5}$, thus ensuring, from a statistical point of view, the connection between radio halos and cluster mergers.

2.2.5 Radio-SZ correlations

The main parameter of the models for the origin and evolution of radio halos is the cluster mass (Section 2.1). The X-ray luminosity can be used as a proxy of the cluster mass, however, the mass-X-ray luminosity correlation may be affected by biases, mainly introduced by the presence of cool-core clusters (see Chapter 3). In order to have a prompt comparison between observations and model expectations, large mass-selected sample of galaxy clusters with adequate radio and X-ray data are necessary. One possibility to build cluster samples that are as close as possible to be mass-selected is to use SZ surveys, such as the one carried out with the *Planck* satellite (Planck Collaboration et al. 2011c,b, 2014a, 2015). The SZ signal indeed is a more robust indicator of the cluster mass with respect to the X-ray luminosity (Carlstrom et al. 2002; Motl et al. 2005; Nagai 2006).

First studies based on the Planck early SZ cluster catalogue (ESZ, Planck Col-

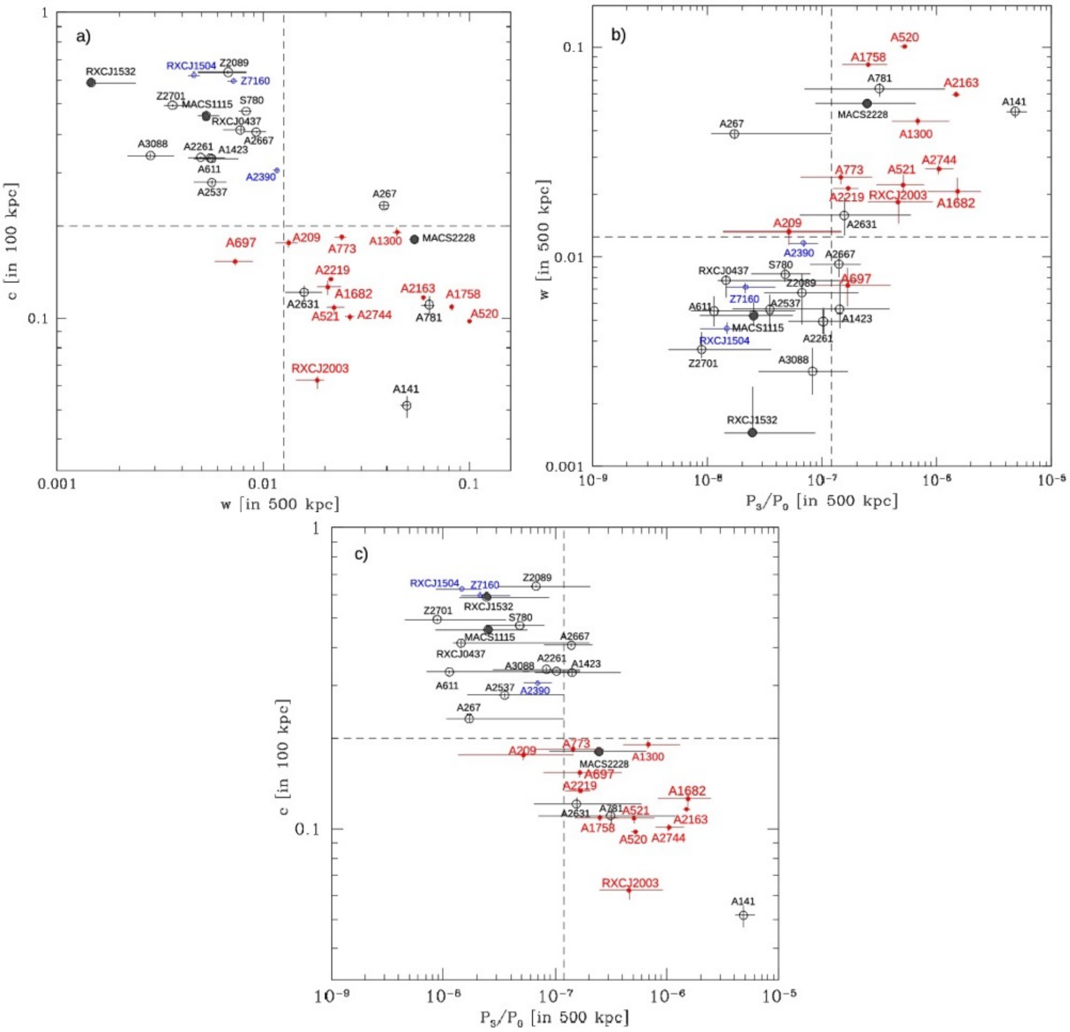

Figure 2.10: (a) Concentration parameter, c, vs. centroid shift, w; (b) w vs. power ratio parameter, P_3/P_0; (c) c vs. P_3/P_0. Symbols: radio halos (red filled dots), non-radio halo (black open dots), mini-halos (blue open dots), and clusters at $z > 0.32$ (grey filled dots). Vertical and horizontal dashed lines represent the median value of each parameter: $c = 0.2, w = 0.012$ and $P_3/P_0 = 1.2 \times 10^{-7}$ (Cassano et al. 2010b).

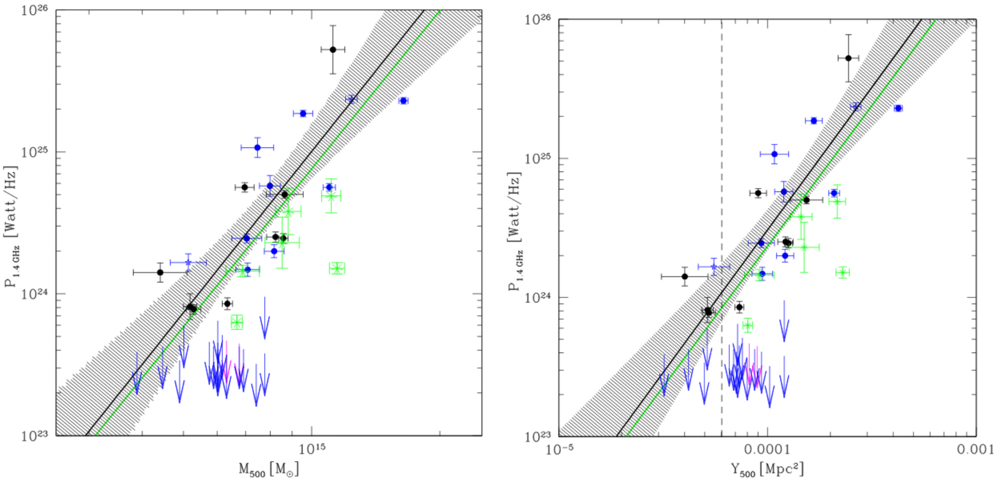

Figure 2.11: *Left panel*: distribution of clusters in the $P_{1.4} - M_{500}$ plane. *Right panel*: distribution of clusters in the $P_{1.4} - Y_{500}$ plane. In both panels different symbols indicate: EGRHS halos (blue filled dots), halos from literature (black open dots), USSRHs (green asterisks). The black lines represent the best fit relation to giant radio halos. The dashed line in the right panel marks the value $Y_{500} = 6 \times 10^{-5}$ Mpc^2. Form Cassano et al. (2013)

laboration et al. 2011a) confirmed the expected existence of a correlation between the radio power of clusters and their mass, however they did not find any evidence of bimodality (Basu 2012). These initial studies did not have the necessary statistics and sample purity to investigate the bimodality in detail. Follow-up studies based on NVSS observations of SZ-selected samples claimed a higher fraction of radio halos with respect to X-ray-selected samples (Sommer & Basu 2014). Cassano et al. (2013) analysed an updated version of the Planck catalogue (PSZ1 Planck Collaboration et al. 2014a). They found clear correlations between the radio power of radio halos and both the integrated Compton parameter and the mass of the clusters 2.11. Specifically, the latter can be written as:

$$log\left(\frac{P_{1.4}}{10^{24.5} Watt/Hz}\right) = B\ log\left(\frac{M_{500}}{10^{14.9}\ M_{\odot}}\right) + A \qquad (2.3)$$

where the slope of the correlation, B, is 3.77 ± 0.57 in the reference case of BCES-bisector fitting method (Akritas & Bershady 1996). The statistics of this sample allowed, for the first time, to look at the bimodal split of clusters in the radio power-mass diagram. Cassano et al. (2013) found a clear bimodality for clusters with $Y_{500} \geq 6 \times 10^{-5}$ (corresponding to $M_{500} \geq 5.5 \times 10^{14} M_{\odot}$), indeed radio halo clusters follow the correlation between the SZ signal and the radio luminosity, while clusters without diffuse emission (upper limits) lie well below the 95% confidence level of the scaling relations (Fig. 2.11).

More recently, Martinez Aviles et al. (2016) and Duchesne et al. (2017) updated the $P_{1.4GHz} - M_{500}$ correlation with a larger number of radio halos. While the slope of the correlation is remarkably consistent with the findings from Cassano et al. (2013), the scatter seems to be larger (Duchesne et al. 2017). The scatter in the radio power-mass correlation contains fundamental information on the physics of non-thermal components and on the evolution of radio halos. On one hand, a fairly large intrinsic scatter of this correlation is expected because of the superposition of different intermediate radio halo evolutionary states that are generated by the complex merging history of clusters (see Section 2.2.2). On the other hand, the increased scatter in the $P_{1.4GHz} - M_{500}$ correlations may be also induced by the extrapolation of the 1.4 GHz power of some radio halos from lower frequency measurements, assuming $\alpha = -1.3$, that is likely not always accurate.

A fair evaluation of the scatter of the $P_{1.4GHz} - M_{500}$ correlation in a large mass-selected sample of galaxy clusters is one of the goals of this PhD Thesis.

Chapter 3

Sample selection and early results

As discussed in Chapter 2, one of the main limitations of the statistical studies on radio halos performed so far is the selection of clusters on the basis of their X-ray luminosity. In fact, the mass is the key parameter of theoretical models for the formation of radio halos, because it sets the energy budget available for particle acceleration. The mass of clusters can be derived from the well known $L_X - M$ relation (Pratt et al. 2009), however, it has been shown that this correlation is affected by biases, especially introduced by the presence of cool-core clusters. Indeed, the presence of a bright core with high X-ray emissivity may enhance the X-ray luminosity, resulting in an overestimate of the cluster mass. Moreover, cool core clusters are more luminous than non-cool core clusters, and their prominent surface brightness peak makes their detection easier with respect to clusters with shallower profiles. Therefore, the ratio between cool core and non cool core clusters in X-ray flux limited sample of galaxy clusters is likely overestimated (Eckert et al. 2011).

One possibility to overcome these problems is to use SZ-selected samples of galaxy clusters. Given the tight correlation between the SZ signal and the cluster mass, SZ selected samples of clusters are as close as possible to be mass-selected (Motl et al. 2005; Nagai 2006; Angulo et al. 2012). In the last decade, catalogues of clusters observed via the SZ effect have been produced by the South Pole Telescope (SPT, Bleem et al. 2015), the Atacama Cosmology Telescope (ACT, Hasselfield et al. 2013) and *Planck* satellite (Planck Collaboration et al. 2011a, 2014a), containing hundreds to thousands of galaxy clusters. These catalogues constitute a powerful tool to select large nearly mass-selected samples of clusters.

The possibility of building a meaningful (i.e. complete and large enough) sample of clusters selected on the basis of their mass and to follow-up these clusters with adequately deep radio observations motivated this PhD project. In this Thesis we used the Planck SZ catalogue (Planck Collaboration et al. 2014a) to select a sample of massive galaxy clusters ($M_{500} \gtrsim 6\times10^{14}\, M_{\odot}$) in the redshift range $0.08 < z < 0.33$ aimed at studying the statistical properties of radio halos as a function of the cluster mass.

In this Chapter we present the selection of the sample studied in this work (Section 3.2). A first attempt to extract information on the statistical properties of radio halos in a subsample with adequate radio data already available in the literature is reported in Section 3.5. The results of this Chapter have been published in Cuciti et al. (2015).

Throughout this Thesis we assume a ΛCDM cosmology with $H_0 = 70$ km s^{-1}Mpc^{-1}, $\Omega_\Lambda = 0.7$ and $\Omega_m = 0.3$.

3.1 The Planck SZ cluster catalogue

The catalogue we used to select our sample consists of 1227 objects (861 confirmed clusters and 366 cluster candidates) derived from SZ effect detections using the first 15.5 months of the *Planck* satellite observations (PSZ1, Planck Collaboration et al. 2014a). This selection was chosen in 2014, at the beginning of the PhD project, therefore, although a new catalogue is nowadays available (PSZ2, Planck Collaboration et al. 2015) we will use the Planck Collaboration et al. (2014a) catalogue for self consistency. When we selected our sample, the Planck catalogue was the largest and deepest SZ-selected cluster all-sky catalogue. It spanned the broadest cluster mass range from 0.1 to $1.6 \times 10^{15}\, M_\odot$, with redshift up to about one. The SZ sources classified as cluster candidates undergo a process of validation that permits to identify previously known clusters and to collect the available information. The association with known clusters is performed in steps, first using X-ray (Meta-catalog of X-ray detected Clusters of Galaxies, MCXC), then optical (Abell, Zwicky and the Sloan Digital Sky Survey, SDSS) and then SZ catalogues (SPT and ACT), and finally NED and SIMBAD. At the same time, follow-up observations of the newly discovered cluster candidates are carried out with *Chandra* and *XMM-Newton* to derive their X-ray properties.

The mass of the clusters is obtained from the SZ signal assuming the scaling relation between M_{500} and Y_{500} (Planck Collaboration et al. 2014b,a):

$$E^{-\frac{2}{3}}(z)\left[\frac{D_A^2(z)Y_{500}}{10^{-4}\mathrm{Mpc}^2}\right] = 10^{-0.19}\left[\frac{M_{500}}{6\times 10^{14} M_\odot}\right] \tag{3.1}$$

where $E^2(z) = \Omega_m(1+z)^3 + \Omega_\Lambda$ computed in the ΛCDM cosmology and D_A is the angular diameter distance. This scaling relation has an intrinsic scatter of $\sigma_{logY} = 0.075$. The mass-redshift distribution of the Planck clusters is shown in Fig. 3.1, together with the limiting mass corresponding to the 20-50-80% completeness. The regions of the diagram where we extracted our sample are highlighted. The selection criteria, described in the following Section, have been chosen in order to reach a good compromise between the completeness of the PSZ1 catalogue, the availability of radio information and the number of selected objects. We point out that we selected our sample in mass and redshift ranges where the PSZ1 catalogue is more than 80 % complete (Fig. 3.1)

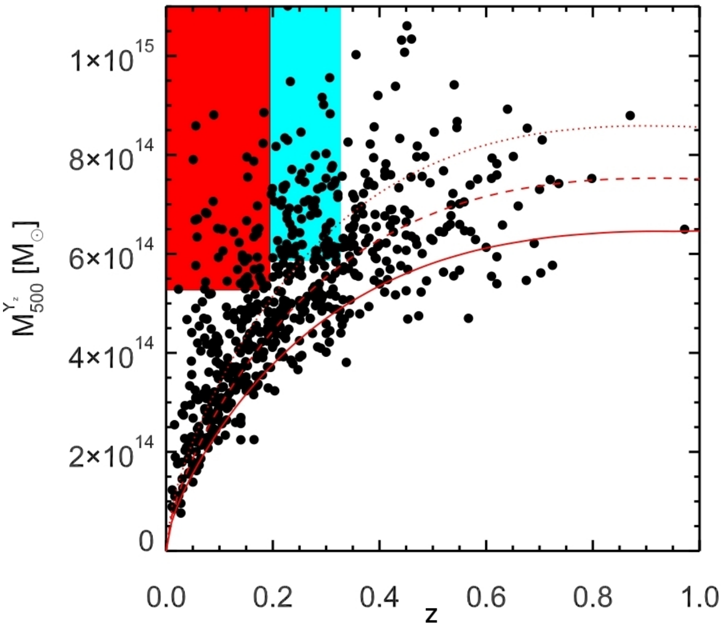

Figure 3.1: Distribution of the Planck clusters in the $M_{500} - z$ plane. The lines show the Planck mass limit at 20% (solid), 50% (dashed) and 80% (dotted) completeness level. The coloured rectangles show the region where we selected our sample: the red rectangle stands for the low redshift sample, while the cyan rectangle stands for for the high redshift one.

3.2 Sample selection

From the PSZ1 catalogue we extracted all the clusters with $M_{500} \gtrsim 6 \times 10^{14}\, M_\odot$ and redshift $0.08 < z < 0.33$. Our selection criteria are outlined below, for two redshift bins:

- at redshift $0.08 < z < 0.2$ we adopted $M_{500} \geq 5.7 \times 10^{14} M_\odot$ and we selected clusters visible in the NVSS ($\delta > -40°$, Condon et al. 1998). The lower redshift limit ($z > 0.08$) is driven by the fact that radio interferometers suffer from the lack of sampling at short baselines, resulting in decreased sensitivity to emission on large spatial scales, such as the typical scales of radio halos. For example, Farnsworth et al. (2013) showed that, for emission on scales larger than $\sim 11'$ (corresponding to 1 Mpc at $z = 0.08$), less than 50% of the the total flux density is recovered with an NVSS snapshot observation; at even larger scales ($\sim 15'$), only the 10% of the flux density is recovered.

- at redshift $0.2 < z < 0.33$ we selected clusters with $M_{500} \geq 6 \times 10^{14}\, M_\odot$ and we adopted a declination limit $\delta > -31°$ and $|b| \geq 20°$ ($|b|$ is the galactic latitude), which coincides with that of the GRHS (Venturi et al. 2007, 2008; Kale et al. 2013, 2015). The upper redshift limit ($z < 0.33$) is mainly related to the unsatisfactory completeness of the PSZ1 catalogue at higher redshift

(Fig. 3.1).

With these selection criteria, we obtained a total sample of 75 clusters: 21 at $0.08 < z < 0.2$ and 54 at $0.2 < z < 0.33$. The mass-completeness of the sample is $> 80\%$ (Fig. 3.1). Among the 54 clusters at $z > 0.2$, 34 belong to the EGRHS, thus they have deep radio observations. Two additional clusters (PSZ1 G205.07-62.94 and PSZ1 G171.96-40.64) have literature information. As a first step, for targets at $z < 0.2$, we collected data from the literature (14 clusters) and re-analysed data from the NVSS survey for the remaining 7 clusters. In the following Sections, we present the analysis and the statistical results based on the 57 clusters (21 at low-z and 36 at high-z) with available radio information. The mass-completeness of this sub-sample is $\sim 90\%$ at $z = 0.08 - 0.2$ and $\sim 53\%$[1] at $z = 0.2 - 0.33$. These clusters and their properties are listed in Tab. 3.1. The next step, i.e. the total sample, including the radio follow-up of clusters without deep/pointed radio data will be presented and discussed in Chapter 7.

3.3 The low redshift sample and the NVSS data analysis

Thanks to previous studies, mainly related to the GRHS, all the 54 clusters of the high-redshift sample have information about the possible presence of diffuse emission. Fo the low-redshift sample we collected radio information from the literature and from the NVSS.

The low-z sample consists of 21 clusters at $z = 0.08 - 0.2$. For 14 of these clusters we found literature information on the presence/absence of diffuse emission based on Very Large Array (VLA) and/or Westerbork Synthesis Radio Telescope (WSRT) pointed observations. Seven clusters (marked with an asterisk in Tab. 3.1) lack literature radio information. As a first step, we searched for hints of diffuse emission in the NVSS images of these seven cluster. The NVSS is a radio survey performed with the VLA at 1.4 GHz in D and DnC (for negative declination pointings) configuration (Condon et al. 1998). It has an angular resolution of 45” and an rms noise of ~ 0.45 mJy/beam. None of these clusters show clear evidence of diffuse emission in the NVSS images. To improve the quality of the available radio images, obtained via a pipeline, we reprocessed the NVSS fields of these clusters. Data were analysed using the NRAO Astronomical Image Processing System (AIPS). We calibrated the NVSS dataset and we obtained the images of the pointings containing the cluster, then we combined them with the task FLATN. This procedure, known as the mosaic technique, is fundamental especially when the cluster falls at the border of the primary beam, because the S/N decreases with the

---

[1] This estimate considers both the completeness in mass of the Planck catalogue in those mass and redshift ranges and the availability of radio information: $0.8 \times \frac{36}{54} = 0.53$.

Table 3.1: Properties of the clusters analysed in this Chapter

cluster name	RA	Dec	z	M_{500} ($10^{14}\,M_{\odot}$)	Radio info	X-ray info
A1437	12 00 22.3	+03 20 33.9	0.134	5.69	no RH*	M ✓
A2345	21 27 06.8	−12 07 56.0	0.176	5.71	Relics^4	M ✓
A2104	15 40 08.2	−03 18 23.0	0.153	5.91	no RH*	M ✓
Zwcl 2120.1+2256	21 22 27.1	+23 11 50.3	0.143	5.91	no RH*	M ✓
RXC J0616.3-2156	06 16 22.8	−21 56 43.4	0.171	5.93	no RH*	M ✓
A1413	11 55 18.9	+23 24 31.0	0.143	5.98	MH ^{5}	R ✓
A1576	12 37 59.0	+63 11 26.0	0.302	5.98	UL^6	R^{26}
A2697	00 03 11.8	−06 05 10.0	0.232	6.01	UL^2	R ^{x}
Z5247	12 33 56.1	+09 50 28.0	0.229	6.04	RH^7	M ✓
Zwcl 0104.9+5350	01 07 54.0	+54 06 00.0	0.107	6.06	RH^8	–
RXC J0142.0+2131	01 42 02.6	+21 31 19.0	0.280	6.07	UL^6	R ^{26}
A1423	11 57 22.5	+33 39 18.0	0.214	6.09	UL^2	R^{25}
RXC J1314.4-2515	13 14 28.0	−25 15 41.0	0.244	6.15	RH^1	M^x
A2537	23 08 23.2	−02 11 31.0	0.297	6.17	UL^2	R^{25}
A68	00 37 05.3	+09 09 11.0	0.255	6.19	UL^7	M ✓
A1682	13 06 49.7	+46 32 59.0	0.226	6.20	RH^2	M^{25}
A1132	10 58 19.6	+56 46 56.0	0.134	6.23	no RH^3	M ✓
RXJ1720.1+2638	17 20 10.1	+26 37 29.5	0.164	6.34	MH^9	R ✓
A781	09 20 23.2	+30 26 15.0	0.295	6.36	UL^2	M^{25}
A2218	16 35 51.6	+66 12 39.0	0.171	6.41	RH^3	M^{28} ✓
A3411	08 41 55.6	−17 29 35.7	0.169	6.48	RH^{10}	M ✓
Zwcl 0634.1+4750	06 38 02.5	+47 47 23.8	0.174	6.52	suspect*	M ✓
A3888	22 34 26.8	−37 44 19.1	0.151	6.67	suspect*	M?^{x,29}
A3088	03 07 04.1	−28 40 14.0	0.254	6.71	UL^2	R^{26}
A2667	23 51 40.7	−26 05 01.0	0.226	6.81	UL^2	R^{25}
A521	04 54 09.1	−10 14 19.0	0.248	6.91	RH^{11,US}	M^{25}
A2631	23 37 40.6	+00 16 36.0	0.278	6.97	UL^2	M^{25}
A1914	14 26 03.0	+37 49 32.0	0.171	6.97	RH^{12}	M ✓
RXC J1504.1-0248	15 04 07.7	−02 48 18.0	0.215	6.98	MH^{13}	R^{25}
A520	04 54 19.0	+02 56 49.0	0.203	7.06	RH^{14}	M^{25}
A478	04 13 20.7	+10 28 35.0	0.088	7.06	MH^{15}	R ✓
A773	09 17 59.4	+51 42 23.0	0.217	7.08	RH^{14}	M^{25}
A1351	11 42 30.8	+58 32 20.0	0.322	7.14	RH^{16}	M ✓
A115	00 55 59.5	+26 19 14.0	0.197	7.21	Relic^{14}	M ✓
A1451	12 03 16.2	−21 32 12.7	0.199	7.32	suspect*	M ^{x}
PSZ1 G205.07-62.94	02 46 27.5	−20 32 5.29	0.310	7.37	no RH^p	M^x
A2261	17 22 17.1	+32 08 02.0	0.224	7.39	UL^6	R^{25}
RXCJ2003.5-2323	20 03 30.4	−23 23 05.0	0.317	7.48	RH^1	M^{25}
A2552	23 11 26.9	+03 35 19.0	0.300	7.53	RH?^{7}	R? ✓
A3444	10 23 50.8	−27 15 31.0	0.254	7.62	MH^7	R ✓
S780	14 59 29.3	−18 11 13.0	0.236	7.71	MH^7	R^{25}
A2204	16 32 45.7	+05 34 43.0	0.151	7.96	MH^{15}	R ✓
A1758a	13 32 32.1	+50 30 37.0	0.280	7.99	RH^{17}	M^{25}
A209	01 31 53.0	−13 36 34.0	0.206	8.17	RH^1	M^{25}
A665	08 30 45.2	+65 52 55.0	0.182	8.23	RH^3	M ✓
A1763	13 35 17.2	+40 59 58.0	0.228	8.29	no RH^2	M ✓
RXC J1514.9-1523	15 14 58.0	−15 23 10.0	0.223	8.34	RH^{18,c}	M ✓
A1835	14 01 02.3	+02 52 48.0	0.253	8.46	MH^{19}	R ✓
A2142	15 58 16.1	+27 13 29.0	0.089	8.81	RH^{24}	M^{30} ✓
A1689	13 11 29.5	−01 20 17.0	0.183	8.86	RH^{20}	M^{27} ✓
A1300	11 31 56.3	−19 55 37.0	0.308	8.83	RH^{21,c}	M^{25}
A2390	21 53 34.6	+17 40 11.0	0.234	9.48	MH^{12}	R^{25}
A2744	00 14 18.8	−30 23 00.0	0.307	9.56	RH^{14}	M^{25}
A2219	16 40 21.1	+46 41 16.0	0.228	11.01	RH^{12}	M^{25}
PSZ1 G171.96-40.64	03 12 57.4	+08 22 10	0.270	11.13	RH^{22,c}	M^x
A697	08 42 53.3	+36 20 12.0	0.282	11.48	RH^{32,US}	M^{25,31}
A2163	16 15 46.9	−06 08 45.0	0.203	16.44	RH^{23}	M^{25}

RH = Radio Halo, MH = Mini-Halo, UL = Upper Limit, M=merger, R= relaxed. [1] Venturi et al. (2007), [2] Venturi et al. (2008), [3] Giovannini & Feretti (2000), [4] Bonafede et al. (2009), [5] Govoni et al. (2009), [6] Kale et al. (2013), [7] Kale et al. (2015) , [8] van Weeren et al. (2011), [9]Giacintucci et al. (2014b), [10]van Weeren et al. (2013), [11]Brunetti et al. (2008), [12]Bacchi et al. (2003), [13]Giacintucci et al. (2011a), [14]Govoni et al. (2001), [15] Giacintucci et al. (2014a), [16] Giacintucci et al. (2009), [17]Giovannini et al. (2006), [18]Giacintucci et al. (2011b), [19]Murgia et al. (2009), [20]Vacca et al. (2011), [21]Venturi et al., 2013, [22]Giacintucci et al. (2013), [23]Feretti et al. (2001), [24]Farnsworth et al. (2013), [25]Cassano et al. (2010), [26]Cassano et al. (2013), [27]Andersson & Madejski (2004), [28]Pratt et al. (2005), [29]Weißman et al. (2013a), [30]Owers et al. (2011), [31]Girardi et al. (2006), [32]Macario et al., 2010, [US] Ultra Steep Spectrum RH, [c] candidate USSRH, [p]Ferrari et al. (private communication), [x] visual inspection of *XMM-Newton* image, [*]NVSS data analysed in this Chapter, ✓ X-ray *Chandra* data analysed in this Thesis.

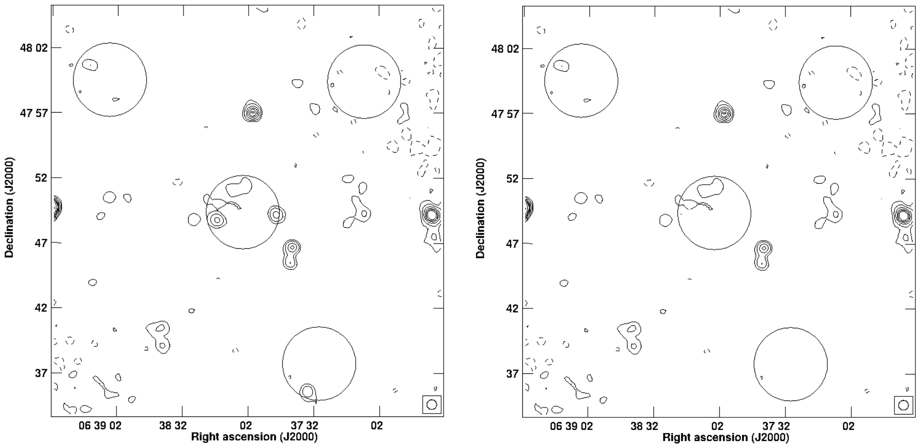

Figure 3.2: Zwcl0634.1+4750 NVSS reprocessed image. The contour levels are $0.66 \times (-1, 1, 2, 4, 6, 8...)$ mJy b^{-1}. The 1σ level is 0.22 mJy b^{-1}. In both panels the region where we extracted the flux densities are shown (solid circles). The central region has a diameter of 1 Mpc and is centred on the centroid of the X-ray emission; the other three areas are the control fields. With the task BLANK we masked the discrete sources in the central region and the one that falls in the lower control field (left panel).

distance from the pointing position. For the seven reprocessed clusters we reached an average rms$\approx$ 0.25 mJy/beam, which is $\sim$ 2 times better than the nominal NVSS noise.

We did not obtain any clear detection of cluster-scale radio emission in these objects. Nonetheless, we further investigated the possible presence of residual emission in the central region of these clusters. Specifically, we selected a circle with diameter 1 Mpc, centred on the centroid of the cluster X-ray emission, on each image. With the task BLANK, we masked the discrete sources in the cluster that show contours at least at the 6σ level, then we measured the residual diffuse flux density (RDF) in the circular region. We compared the RDF with the flux densities measured in other areas of the same size taken around the cluster (three for each cluster), i.e. "control fields". In order to make a consistent comparison we normalized both the RDF and the control field flux densities (CFF) to the number of pixels enclosed in a circle of 1 Mpc diameter after masking the discrete sources. An example of this procedure is shown in Fig. 3.2.

To test the reliability of this procedure, we also applied it to three known radio halo clusters (A3411, A2218, and Zwcl 0104.9+5350) and to the mini-halo in RXJ1720.1+2638 that belong to our sample and have information from the literature. We note that, since few NVSS beams correspond to $100 - 300$ kpc at these redshifts, the use of the task BLANK in the case of relatively bright sources at the cluster center, is also expected to remove possible diffuse emission on those scales. Therefore this procedure does not allow to properly assess the presence of mini-halos, which, however, are not the main focus of this work.

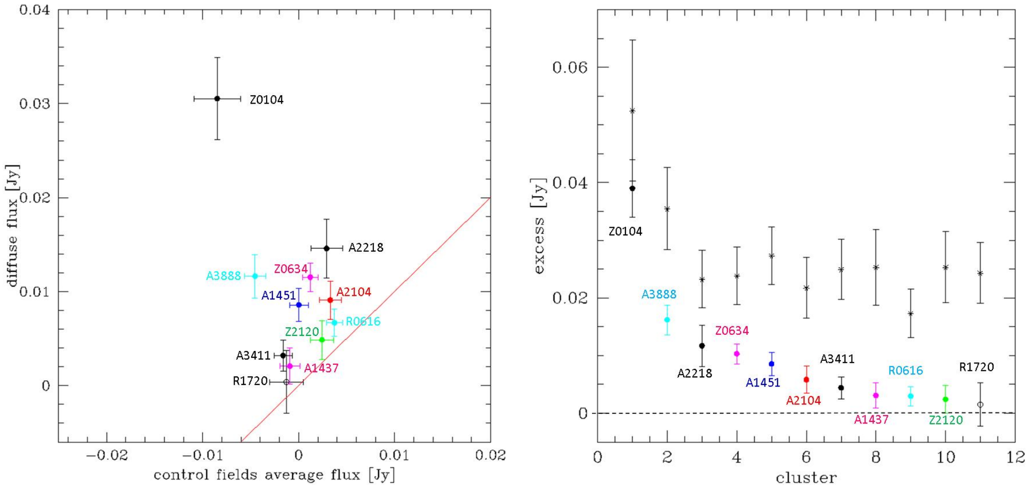

Figure 3.3: *Left panel*: Diffuse flux density vs. control fields average flux density. Symbols: colored dots are clusters with reprocessed NVSS datasets; black filled dots are known radio halo clusters; and the black open dot is the mini-halo. The red line is the 1:1 line. *Right panel*: Excess of diffuse flux with respect to the average control fields flux densities. Black asterisks represent the expected radio power of the radio halo on the basis of the $P_{1.4} - M_{500}$ correlation (Cassano et al. 2013).

In Fig. 3.3 (left panel) we compare the average value of the CFF with the RDF for each cluster, whereas the offset between the RDF and the average CFF are given in Fig. 3.3 (right panel). Four clusters (A3888, Zwcl0634.1+4750, A1451, and A2104) and the clusters with already known radio halos (A2218, Zwcl 0104.9+5350, and A3411) show an excess at $> 2\sigma$ level. We consider this as the threshold level to identify clusters with the possible presence of a radio halo. We note that all the clusters show a positive offset (at least a few mJy) between the RDF and the CFF (Fig. 3.3, right panel). This is likely due to residual contamination from faint cluster radio galaxies that are below the NVSS detection limit, rather than to diffuse flux on cluster scales (e.g. Farnsworth et al. 2013). For the sake of completeness, in Fig. 3.3 (right panel, black asterisks) we also show the expected level of radio halo emission according to the $P_{1.4} - M_{500}$ correlation (Cassano et al. 2013, Eq. 4.10). We note that the mini-halo in RXJ1720.1+2638 does not show any excess of diffuse emission because, as explained above, a large fraction of the diffuse emission associated to the mini-halo is masked with the central radio galaxy.

3.4 X-ray data analysis

In this Section we describe the analysis of the dynamical properties of the clusters of our sample. Among the 57 clusters of the sub-sample with available radio information, 50 have archival X-ray *Chandra* data. 24 of them already have literature information on their dynamical status (Cassano et al. 2010b, 2013). We produced and analysed the *Chandra* images of the remaining 26 clusters (marked with $\surd$ in Tab.3.1). *Chandra* X-ray data were reprocessed with CIAO 4.5 using calibration files from CALDB 4.5.8. Standard techniques to correct time-dependent issues were applied[2], the screening of the events file was applied to filter out strong background flares, cosmic rays and soft protons. We adopted an automatic algorithm for the identification of point sources which were then removed from images. We normalised the image for the exposure map of the observation, which provides the effective exposure time as a function of the sky position exposed on the CCD. We did not correct for the background emission to treat the exposure-corrected images without introducing negative values in correspondence of pixels with zero counts. This procedure is sufficiently safe both because we are dealing with integrated quantities and because the images are largely dominated by the cluster signal inside the aperture radius we are interested in (see below)[3].

Following (Cassano et al. 2010b, 2013), we made use of the *Chandra* images, derived in the 0.5-2 keV band, to study the clusters dynamical properties on the typical radio halo scale. For each cluster, we analysed the surface brightness inside an aperture radius R_{ap} = 500 kpc, centred on the cluster X-ray peak. 500 kpc is the typical radius of radio halos, in this way we evaluate the dynamics within the region where energy is dissipated and generates visible non-thermal activity. To provide a quantitative measure of the level of dynamical disturbance of the clusters, we used three methods, widely used in the literature to investigate the dynamics of cluster: the power ratios, P_3/P_0 (e.g. Buote & Tsai 1995; Jeltema et al. 2005; Ventimiglia et al. 2008; Böhringer et al. 2010; Cassano et al. 2016; Lovisari et al. 2017), the centroid shift, w (e.g. Mohr et al. 1993; Poole et al. 2006; O'Hara et al. 2006; Ventimiglia et al. 2008; Maughan et al. 2008; Böhringer et al. 2010; Cassano et al. 2016; Lovisari et al. 2017) and the concentration parameter, c (e.g. Santos et al. 2008; Cassano et al. 2016; Rossetti et al. 2017).

- The power ratio method is based on the idea that the X-ray surface brightness is a good representation of the projected mass distribution of the cluster. It is the two-dimensional multipole decomposition of the mass distribution within an aperture of radius R_{ap}. It describes the radial fluctuations of the surface brightness, with higher order moments being sensitive to smaller and smaller scales. The power ratio can be defined as:

$$P_0 = [a_0 \; ln(R_{ap})] \tag{3.2}$$

  where a_0 is the total intensity inside the aperture radius: $a_0 = S(< R_{ap})$,

---

[2] http://cxc.harvard.edu/ciao/threads/index.html

[3] Using the background values provided in the *Chandra* proposers' observatory guide we estimated that $\sim 95\%$ (both in ACIS I and ACIS S) of the total counts in the $0.5 - 2$ Kev band are from the cluster.

$S(x)$ is the X-ray surface brightness, and

$$P_m = \frac{1}{2m^2 R_{ap}^{2m}}(a_m^2 + b_m^2) \tag{3.3}$$

where the moments a_m and b_m are given by:

$$a_m(R) = \int_{R' \leq R_{ap}} S(x')(R')cos(m\phi')d^2x' \tag{3.4}$$

and

$$b_m(R) = \int_{R' \leq R_{ap}} S(x')(R')sin(m\phi')d^2x' \tag{3.5}$$

Here we only use the third moment P_3/P_0, which is the lowest providing a clear substructure measure (Böhringer et al. 2010). High values of P_3/P_0 indicate the presence of substructures that can be interpreted in terms of ongoing dynamical activity in the ICM.

- The centroid shift is a geometrical parameter. It is computed in a series of circular apertures centred on the cluster X-ray peak. Starting from $R_{ap} = 500$ kpc, the radius of the aperture is decreased of 5% at every step until $0.05R_{ap}$, and the centroid shift, w, is defined as the standard deviation of the projected separation between peak and the centroid in unit of R_{ap}, i.e.:

$$w = \left[\frac{1}{N-1}\sum(\Delta_i - \langle\Delta\rangle)^2\right]^{1/2} \times \frac{1}{R_{ap}} \tag{3.6}$$

where Δ_i is the distance between the X-ray peak and the centroid of the *ith* aperture. The shift between the centroid and the X-ray peak is very sensitive to the dynamical status of the cluster (Poole et al. 2006). High values of w are usually found for merging clusters, with irregular shapes and surface brightness distributions.

- The concentration parameter is the ratio between the peak and the “ambient” surface brightness. In particular, we define:

$$c = \frac{S(r < 100 \text{ kpc})}{S(r < 500 \text{ kpc})} \tag{3.7}$$

The concentrations parameter is effective in distinguishing cool core clusters from clusters where the core have been disrupted by merging events. Clearly, high values of c indicate relaxed clusters, showing a peaked surface brightness in the central region.

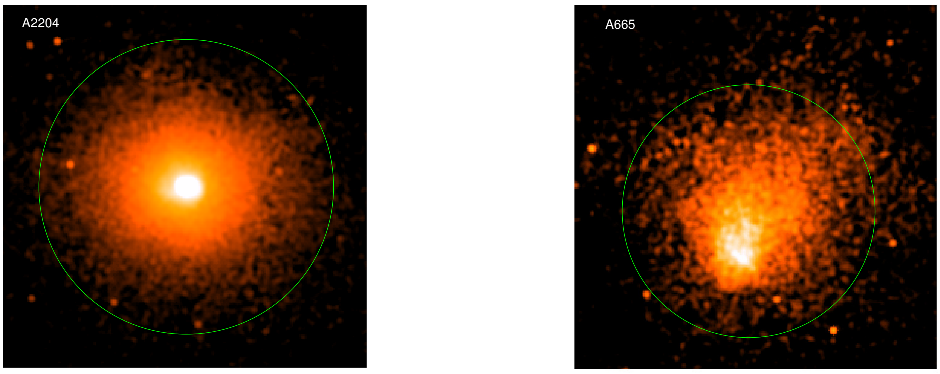

Figure 3.4: X-ray *Chandra* image of the relaxed cluster A2204 (*left*) and the merging cluster and A665 (*right*). The green circles have radii of 500 kpc and represent the region where the morphological parameter are measured.

We show, as an example, the X-ray *Chandra* images of a relaxed (A2204) and a merging (A665) clusters in Fig. 3.4. The concentration parameter is high for A2204, while it is relatively low for A665, whereas the power ratios and the centroid shift have low values for A2204 and high values for A665.

Other morphological parameters are used in the literature to define the merging or relaxed status of clusters (e.g. Wen & Han 2013; Yuan et al. 2015; Parekh et al. 2015; Rossetti et al. 2016; Lovisari et al. 2017). For simplicity, in the following work we will consider only the three parameters described above.

Morphological parameters are powerful tools to characterise the dynamical status of clusters, however, given that they rely on two-dimensional analysis of the X-ray surface brightness, they are insensitive to mergers happening along, or close to, the line of sight. Indeed, mergers happening along the line of sight would have low values of w and P_3/P_0 and intermediate or relatively high values of c, because the X-ray surface brightness in the central region may be boosted by projection effects. Moreover, morphological parameters depend on the aperture radius where they are calculated and are insensitive to the possible X-ray surface brightness features on larger scales.

3.5 Results

3.5.1 Occurrence of radio halos

Among the sample of 57 clusters with radio information (from the EGRHS and Section 3.3), 24 host radio halos and 4 show residual emission in a Mpc-scale region that is a possible indication of the presence of a radio halo. The aim of this Section is to study the occurrence of radio halos as a function of the mass of the host clusters. To do that, we split this sample into two mass bins and derived the fraction of clusters with radio halos, f_{RH}, in the low-mass bin (LM, $M < M_{lim}$) and in the high-mass bin (HM, $M > M_{lim}$) for different values of the limiting mass, M_{lim} (as detailed below). In general we found that f_{RH} is lower in the LM bins ($f_{RH} \approx 20 - 30\%$), while it is higher ($f_{RH} \approx 60 - 80\%$) in the HM bins (Fig. 3.6).

This difference is systematic and thus we attempted to identify the value of M_{lim} that provides the most significant jump between low- and high-mass clusters. We performed Monte Carlo simulations considering both the cases in which the four objects in the low-z sample with suspect diffuse emission are included (i) as non-radio halo clusters and (ii) as radio halo clusters. Considering case *(i)*, we randomly assigned 24 radio halos among the 57 clusters of the sample and obtained the distributions of radio halos in the two mass bins (after 10^5 Monte Carlo trials). These represent the expected distributions if radio halos were distributed independently of the cluster mass.

We consider five different values of the transition mass between the two bins, specifically $M_{lim} = (6, 7, 8, 9, 10) \times 10^{14}\, M_{\odot}$. An example of the expected distribution of the number of radio halos in the HM bin is shown in Fig. 3.5 for the case $M_{lim} = 8 \times 10^{14}\, M_{\odot}$. Each distribution can be fitted by a Gaussian function. The results of the Monte Carlo simulations are given in Tab. 3.2 for cases *(i)* (upper panel) and *(ii)* (lower panel). Specifically, we list the number of clusters ($N_{clusters}$), the number of radio halos (N_{RH}), and the fraction of clusters hosting radio halos (f_{RH}) in the two mass bins for each value of M_{lim}. In Tab. 3.2 we also show the significance of our result in units of σ, $Z = (N_{RH} - \mu)/\sigma$ (where μ is the Gaussian median value), and the most likely value of f_{RH}, f_{μ}=$\mu/N_{cluster}$ in the HM bin (very similar results are obtained for the LM bin).

Figure 3.6 shows the observed fraction of radio halos (dots) together with the results of the Monte Carlo simulations (shadowed regions) in the HM bin (left panel) and in the LM bin (right panel). We show the measured fraction of cluster with radio halos and the results of the Monte Carlo analysis in cases *(i)* (red and black dots and shadowed regions) and *(ii)* (green dots and shadowed regions). For a clearer visualization in Fig. 3.6, for case *(ii)* we only show the results obtained by assuming $M_{lim} = (7, 8, 9) \times 10^{14} M_{\odot}$. Figure 3.6 shows that, in the HM bin, the observed f_{RH} is always greater than that predicted by the Monte Carlo simulations; on the contrary, in the LM bin, the observed f_{RH} is always lower than that predicted by the Monte Carlo analysis. This suggests the existence of a systematic drop of f_{RH} in low-mass systems.

In both cases *(i)* and *(ii)*, we found that the value of M_{lim} that gives the most significant result and maximizes the drop of f_{RH} between the two mass bins is $M_{lim} \approx 8 \times 10^{14} M_{\odot}$, for which $f_{RH} \simeq 30\%$ (40%) in the LM bin and $f_{RH} \simeq 79\%$ (79%) in the HM bin in case *(i)* (in case *(ii)*). For $M_{lim} \approx 8 \times 10^{14} M_{\odot}$ the observed

Case no.	M_{lim} ($10^{14}\,M_{\odot}$)	N_{RH} (HM)	$N_{cluster}$ (HM)	N_{RH} (LM)	$N_{cluster}$ (LM)	f_{RH} (HM)	f_{RH} (LM)	f_{μ} (HM)	Z (HM)
(i)	6	24	50	0	7	48%	0%	42%	2.49
	7	16	28	8	29	57%	28%	42%	2.29
	8	11	14	13	43	79%	30%	42%	3.17
	9	5	6	19	51	83%	37%	41%	2.07
	10	4	4	20	53	100%	38%	40%	2.21
(ii)	6	27	50	1	7	54%	14%	49%	2.10
	7	17	28	11	29	60%	38%	49%	1.76
	8	11	14	17	43	79%	40%	49%	2.50
	9	5	6	23	51	83%	45%	49%	1.72
	10	4	4	24	53	100%	45%	48%	1.93

Table 3.2: The four clusters with suspect diffuse radio emission are considered as non-radio halo clusters in the upper panel (*i*) and as radio halo clusters in the lower panel (*ii*).

f_{RH} in the two mass bins differs from that obtained by the Monte Carlo analysis at $\sim 3.2\sigma$ in case *(i)* and $\sim 2.5\sigma$ in case *(ii)*. This means that the chance probability of the observed drop of f_{RH} is $< 7.4 \times 10^{-4}$ *(i)* and $< 5.7 \times 10^{-3}$ *(ii)*.

Based on this analysis, we conclude that there is statistical evidence for a drop of the fraction of radio halos in galaxy clusters at smaller masses. A similar conclusion was obtained using X-ray selected clusters (Cassano et al. 2008). However, this is the first time that such an indication is derived using a mass-selected sample and, if confirmed by the follow-up analysis of the total sample (Chapter 7), it will provide fundamental information on the origin and evolution of radio halos.

3.5.2 Radio halo–merger connection

In this Section we investigate the connection between the presence or absence of radio halos in clusters and the cluster dynamical status (merger or relaxed). Following Cassano et al. (2010b), in Fig. 3.7 we show the cluster morphological parameters, derived in Section 3.4 for the 50 clusters in the sample with available *Chandra* data, in three diagrams: $c - w$, $c - P_3/P_0$, and $w - P_3/P_0$. Vertical and horizontal dashed lines are taken from Cassano et al. (2010b); these lines represent the median value of each parameter, and were used to separate radio halo clusters ($w > 0.012$, $c < 0.2$, and $P_3/P_0 > 1.2 \times 10^{-7}$) from non-radio halo clusters ($w < 0.012$, $c > 0.2$, and $P_3/P_0 < 1.2 \times 10^{-7}$) clusters. Here we use these lines as a reference to compare our measurements with previous published results[4]. Figure 3.7 shows that radio halo clusters (red dots) can be separated from clusters without radio halo (black dots) in the morphological diagrams: radio halos are associated with dynamically disturbed clusters, while the vast majority of clusters without Mpc-scale diffuse radio

---

[4] Cassano et al. (2010b) derived these lines on a smaller redshift range ($0.2 - 0.35$); however, there is no clear indication of an evolution of P_3/P_0 and w with z (e.g. Weißmann et al. 2013).

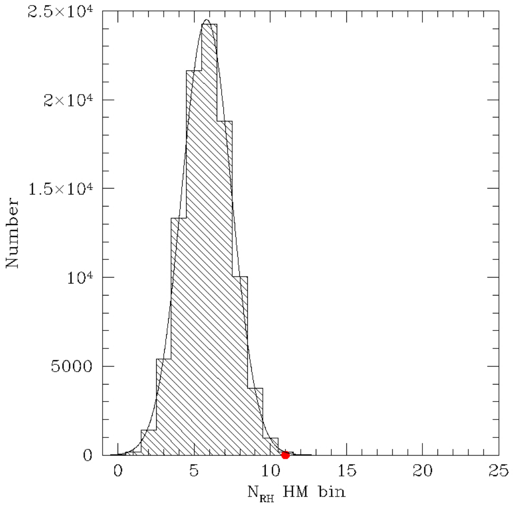

Figure 3.5: Distribution of the number of radio halos in the HM bin ($M > M_{lim} = 8 \times 10^{14} M_{\odot}$) after 10^5 Monte Carlo trials. The red point indicates the observed number of radio halos in the HM bin.

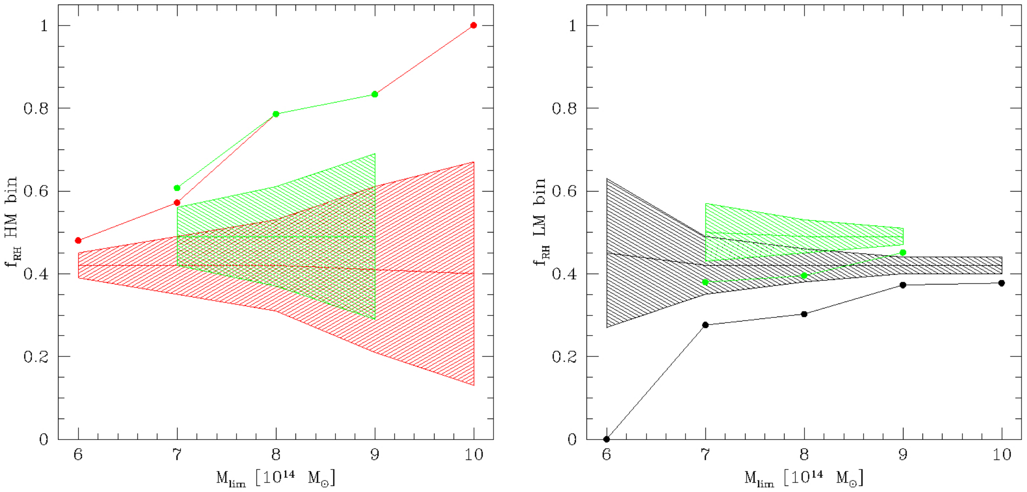

Figure 3.6: Observed fraction of radio halos f_{RH} (dots) compared to the value predicted by the Monte Carlo simulations (shadowed regions) in the HM bin (left panel) and in the LM bin (right panel) as a function of the limiting mass M_{lim}. Red dots and shadowed region and black dots and shadowed region refer to the case in which the four clusters with suspect diffuse emission are considered as non-radio halo clusters. In both panels, the green dots and the green shadowed regions show the case in which the suspect clusters are considered as radio halo clusters.

emission are relaxed. About 80% of the clusters in the HM bin of our sample are mergers, and this explains why radio halos are fairly common in this bin (Section 3.5.1). The only radio halo cluster that always falls in the region of relaxed clusters is A1689; actually, it has been shown that this cluster is undergoing a merger event at a very small angle with the line of sight (Andersson & Madejski 2004), therefore its morphological parameters are likely biased due to projection effects. We note that clusters with relics and without radio halos (blue dots) are also located in the regions of dynamically disturbed systems, in line with literature observations (e.g. de Gasperin et al. 2014) and with the idea that relics are related to merger-driven shocks (Brunetti & Jones 2014, for review).

We note that at least ten merging clusters of our sample do not host radio halos. The existence of massive and merging systems without radio halos is well known (Cassano et al. 2013, and references therein) and not surprising, given the current theoretical picture for the origin of halos. If radio halos are due to turbulence acceleration of relativistic electrons during cluster mergers they should have a typical lifetime of $\sim 1-2$ Gyr (Brunetti et al. 2009; Miniati 2015), which is smaller, but of the same order of the merger time-scale (see Cassano et al. 2016, for a comparison between the radio halo lifetime and the merger timescale). However, the generation of turbulence, its cascading from large to small scales and its dissipation take some time, corresponding to "switch-on" and "switch-off" phases that span a substantial fraction of Gyr. This produces a partial "decoupling" between X-rays and radio properties, as during these phases radio halos would appear underluminous or absent, whereas the host cluster would appear disturbed in the X-rays (e.g. Donnert et al. 2013). An additional possibility is that some of the dynamically disturbed systems host radio halos with very steep spectra that are not easily detectable at our observing frequencies (Cassano et al. 2006, 2012). The fraction of these very steep spectrum halos should increase at smaller masses. In fact, the great majority of merging clusters without radio halos belong to the LM bin, which might support the idea that in these cases (or some of them) the energy provided by the merger is not sufficient to generate radio halos emitting at the observing frequencies. This second possibility is expected to contribute to the drop of the fraction of radio halos in less massive systems, that is observed in our sample (Section 3.5.1).

3.6 Preliminary comparison with models

The drop of the fraction of clusters hosting radio halos in less massive systems is one of the most interesting results of our analysis. Such a drop is expected in the framework of turbulent re-acceleration models (e.g. Cassano et al. 2006).

At this stage, a solid comparison between models and our observations is still premature owing to the incompleteness of the observed sample (Section 3.7). Still, with this caveat in mind, in Fig. 3.8 we compare our measurements of the occurrence of radio halos in the two mass bins (black solid line) with the formation probability

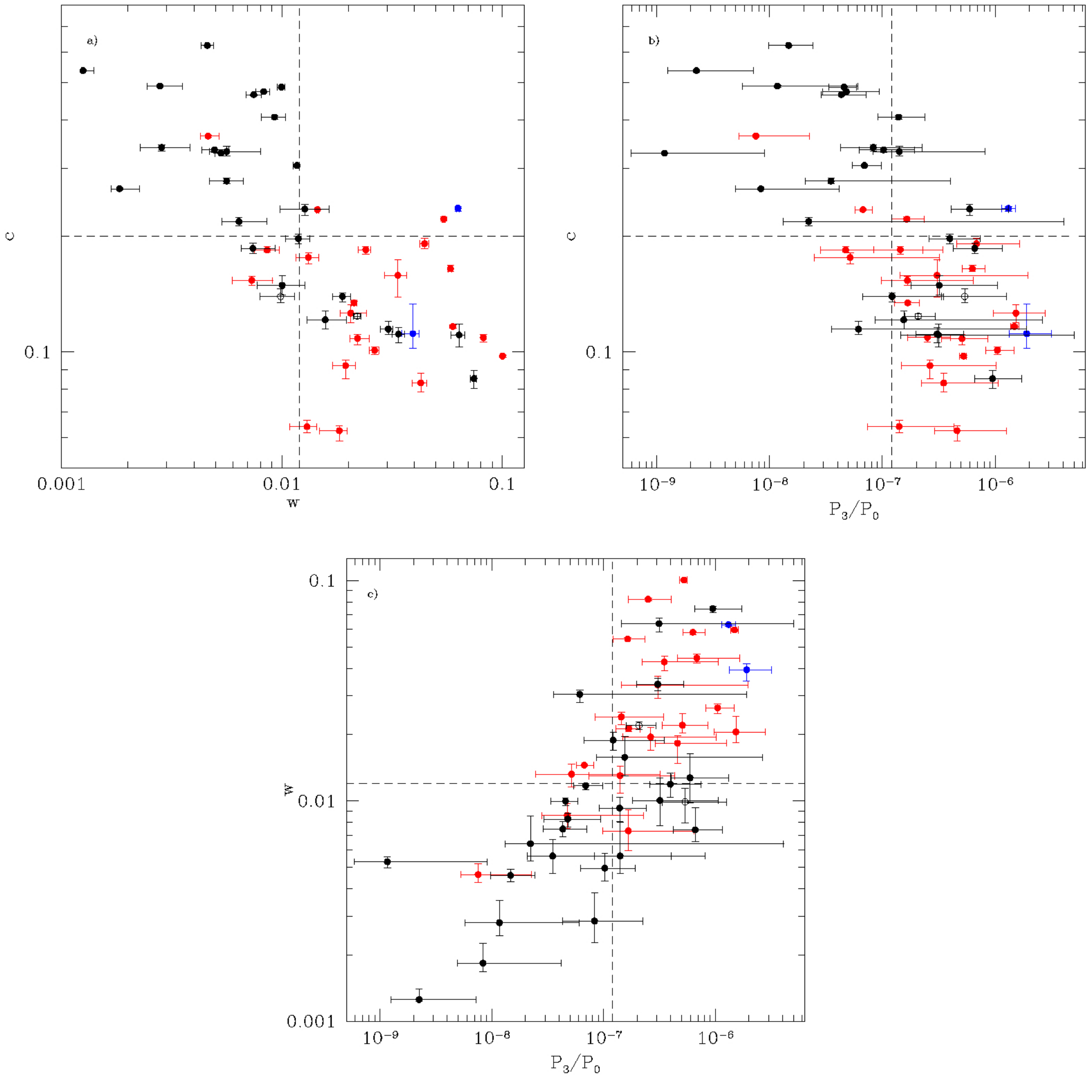

Figure 3.7: (a) $c-w$, (b) $c-P_3/P_0$, (c) $w-P_3/P_0$ diagrams. Vertical and horizontal dashed lines: $c = 0.2$, $w = 0.012$, and $P_3/P_0 = 1.2 \times 10^{-7}$. Red, black, and blue dots represent clusters with radio halos, clusters without radio halos, and clusters hosting relics (without radio halos), respectively. Black open dots are clusters with suspect diffuse emission from the NVSS.

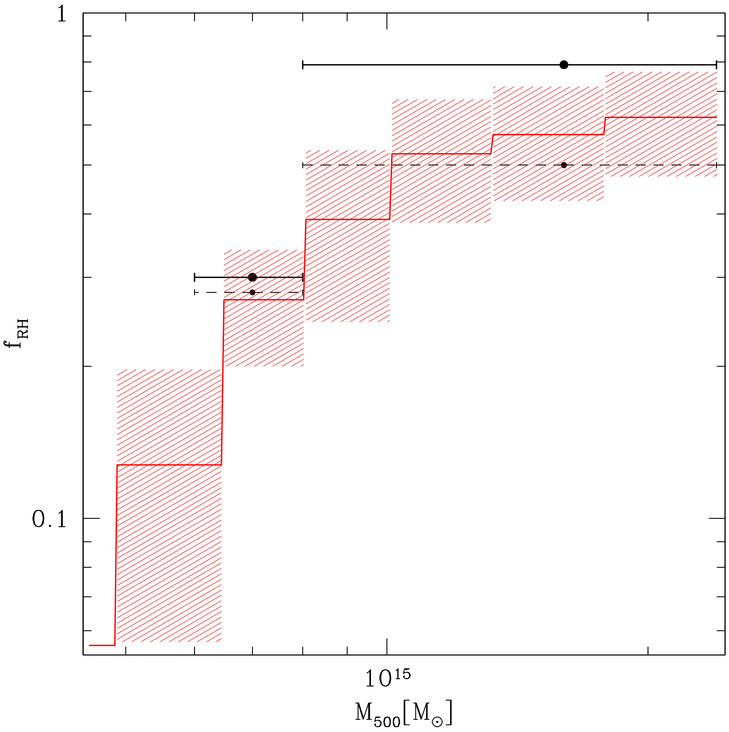

Figure 3.8: Expected fraction of clusters with radio halos with steepening frequency $\nu_s > 600$ MHz in the redshift range $0.08 < z < 0.33$ (red line and shadowed region). Calculations have been performed for the following choice of model parameters: $b = 1.5$, $\langle B \rangle = 1.9\ \mu$G (where $B = \langle B \rangle \times (M/\langle M \rangle)^b$), and $\eta_t = 0.2$ (see Cassano et al. 2012, and references therein). The observed fraction of clusters with radio halos in the two mass bins is also shown (black points with horizontal error bars). The black points with dashed error bars show f_{RH} when we exclude USSRHs (and candidate USSRHs) from the observed sample.

of radio halos derived from the turbulent re-acceleration model in its simplest form (red line). We used numerical codes available at the Institute of Radioastronomy (IRA) in Bologna, that calculate the expected fraction of clusters with radio halos with steepening frequency $\nu_s > 600$ MHz following receipts in Cassano & Brunetti (2005) (see also Section 2.1.1.1). More specifically, we assume a scaling of the magnetic field $B = \langle B \rangle \times (M/\langle M \rangle)^b$, and that a fraction $\eta_t = 0.2$ of the PdV work during mergers is channelled into magnetosonic waves. We followed the history of ~ 500 simulated clusters in the redshift range $z = 0.08 - 0.33$ and calculated the theoretical variance on the predicted formation probability by running Monte Carlo extractions, from the pool of theoretical merger trees, of subsamples of clusters of the same size of the two observed subsamples defined in Table 3.2 (using $M_{lim} = 8 \times 10^{14} M_\odot$). Despite the crude approximations adopted in these models, where B and the acceleration parameters are considered constant in a fixed aperture radius of 500 kpc (e.g. Cassano et al. 2006, 2012), we find an overall agreement between the observed and predicted behaviour of f_{RH} with the cluster mass.

The model slightly underestimates f_{RH} in the high-mass bin. There might be two main reasons for this: 1) the use of the Press & Schechter formalism, which is well known to underestimate the merging rate, and hence the number density, of very massive systems; and 2) the fact that the model predictions do not include radio halos with very steep radio spectra, i.e. those with steepening frequency $\nu_s \lesssim 600$ MHz. As an example in Fig. 3.8 (black dashed lines) we show the effect on the observed statistics induced by removing from the sample USSRHs (labelled "*US*" in Table 7.1) and candidate USSRHs (labelled "*c*" in Table 7.1), for which we do not know the detailed spectral shape.

3.7 Sample completeness

As explained in Section 3.2, in the calculation of the occurrence of radio halos we included only clusters with available radio information about the presence/absence of radio halos: 21/21 clusters in the low-z sample ($z < 0.2$) and 36/54 in the high-z ($z > 0.2$) sample. Considering that the PSZ1 catalogue (Planck Collaboration et al. 2014a) is complete at $\sim 90\%$ in the low-z sample and at $\sim 80\%$ in the high-z sample (see Fig. 3.1), we can estimate a completeness of our sample (which takes into account both the completeness in mass and in the radio information) of $\sim 63\%$[5]. Eighteen clusters in the high redshift range ($z > 0.2$) still lack radio information: 17 with $M < 8 \times 10^{14} M_\odot$ and one with $M > 8 \times 10^{14} M_\odot$. Even in the extreme and unlikely case where all the missing clusters with $M < 8 \times 10^{14} M_\odot$ host a radio halo and the one with $M > 8 \times 10^{14} M_\odot$ is a non-radio halo cluster, a hint of drop in the fraction of radio halos between the two mass bins would still remain. Therefore, we can reasonably conclude that the evidence for such a drop cannot be completely

---

[5] This is estimated as $\frac{21+36}{(21/0.9)+(54/0.8)} \sim 63\%$

driven by biases deriving from the incompleteness of the sample.

During this PhD program, we observed these 18 clusters with the JVLA at 1.5 GHz and with the GMRT at 330 and/or 610 MHz in order to complete the radio information of the sample and perform the statistical analysis of a highly complete ($> 80\%$) mass-selected sample of clusters of galaxies. The radio data analysis of these new observations is presented in Chapter 4, results are presented in Chapter 5 and 6 and the study of the statistical properties of the total sample is presented in Chapter 7.

Chapter 4

Completing the sample: data analysis

The most remarkable outcome of the analysis described in Chapter 3 is the first evidence for a drop of the fraction of clusters with radio halos at low masses. Interestingly, such a drop is predicted by models that derive the formation probability of radio halos as a function of the cluster mass in the context of the turbulent re-acceleration scenario (Sec. 3.6). Nevertheless, this result, as well as a detailed statistical analysis of the sample, is limited by the lack of radio information for a number of clusters. In particular, the main limitations are:

- the incompleteness of the high-z subsample. Indeed 18 clusters (33%) at $0.2 < z < 0.33$ lack radio observations (Section 3.7).
- 7 out of 21 low-z clusters lack deep pointed radio observations in order to firmly establish the possible presence of diffuse emission that, so far, has been assessed based on the NVSS reprocessing only (Section 3.3).

To overcome these limitations we observed the 18 high-z clusters with the GMRT at 610 MHz (project codes 26_021 and 27_025, P.I. R. Cassano) ad with the JVLA in C array at 1.5 GHz (project code 14B-190, P.I. R. Cassano) and we further observed the 7 low-z clusters with the GMRT at 330 MHz (project code 29_001, P.I. V. Cuciti) and with the JVLA in D array at 1.5 GHz (project code 15B-135, P.I. V. Cuciti). We choose to observe high-z clusters with the GMRT at 610 MHz to be consistent with the approach of the GRHS (Venturi et al. 2007, 2008; Kale et al. 2013, 2015). This choice turns out to be the best compromise between sensitivity to the extended emission and resolution to discriminate the contribution of compact sources at those redshifts. At the same time, we observed low-z clusters with the GMRT at 330 MHz to ensure a good *uv*-coverage at the short baselines to detect relatively nearby Mpc-scale sources which have large angular size. At low redshift the resolution of the GMRT at 330 MHz still allows to separate compact sources from the diffuse emission. With the same considerations we decided to observe high-z clusters with the JLVA in C array and low-z clusters in D array. In total, we analysed radio data for 25 clusters. Among these 25 clusters, 16 have archival X-ray *Chandra* data that we used to investigate their dynamical status. The clusters that we analysed, their properties and the available radio and X-ray observations are listed in Table 4.1. In this Chapter we describe the radio data analysis that we performed in order to complete the radio information of the sample and the X-ray data analysis carried out to derive the dynamical information about these clusters.

Table 4.1

cluster name	RA	Dec	z	M_{500} ($10^{14} M_\odot$)	radio data	X-ray data
A56	00 33 50.4	−07 47 28	0.30	6.20	JVLA C^a	XMM
A2813	00 43 27.4	−20 37 27	0.29	9.16	JVLA C^a	*Chandra*
A2895	01 18 11.1	−26 58 23	0.23	6.15	JVLA C^a	*Chandra*
A3041	02 41 22.1	−28 38 13	0.23	6.12	JVLA C^a	*Chandra*
A220	01 37 19.5	+07 56 16	0.33	6.74	JVLA C^a	–
A384	02 48 13.9	−02 16 32	0.24	6.38	JVLA C^a, GMRT 610 MHz^c	XMM
ZwCl 1028.8+1419	10 31 28.2	+14 03 34	0.31	6.11	GMRT 610 MHz^d	–
RXC J1322.8+3138	13 22 48.8	+31 39 17	0.31	6.63	GMRT 610 MHz^d	XMM
A1733	13 27 03.7	+02 12 15	0.33	7.05	GMRT 610 MHz^d	*Chandra*
PSZ1 G019.12+3123	16 36 29.4	+03 08 51	0.28	7.08	GMRT 610 MHz^c	XMM
MACS J2135-010	21 35 12.1	−01 02 58	0.33	7.57	GMRT 610 MHz^c	*Chandra*
A2355	21 35 22.5	+01 23 26	0.23	6.92	JVLA C^a, GMRT 610 MHz^c	*Chandra*
RXC J2051.1+0216	20 51 08.0	+02 15 55	0.32	6.13	JVLA C^a, GMRT 610 MHz^c	XMM
A2472	22 41 50.6	+17 31 43	0.31	6.15	JVLA C^a	XMM
PSZ1 G139.61+24.20	06 22 13.9	+74 41 39	0.27	7.09	JVLA C^a, GMRT 610 MHz^{d,i}	*Chandra*
A1443^S	12 01 27.7	+23 05 18	0.27	7.74	JVLA C+D^m, GMRT 610^d&330^l&150^p MHz	*Chandra*
RXCJ 0510.7-0801	05 10 47.9	−08 01 06	0.22	7.36	GMRT 610 & 240 MHz	*Chandra*
A402	02 57 41.1	−22 09 18	0.32	7.21	GMRT 330 MHz^o	*Chandra*
A1437	12 00 22.3	+03 20 33.9	0.134	5.69	GMRT 330 MHz^f	*Chandra*
A2104	15 40 08.2	−03 18 23.0	0.153	5.91	GMRT 330 MHz^g	*Chandra*
Zwcl 2120.1+2256^S	21 22 27.1	+23 11 50.3	0.143	5.91	JVLA D^b, GMRT 330 MHz^h	*Chandra*
RXC J0616.3-2156	06 16 22.8	−21 56 43.4	0.171	5.93	JVLA DnC^b	*Chandra*
Zwcl 0634.1+4750	06 38 02.5	+47 47 23.8	0.174	6.52	JVLA D^b+B^n, GMRT 330 MHz^f	*Chandra*
A3888	22 34 26.8	−37 44 19.1	0.151	6.67	GMRT 330 MHz^e	*Chandra*
A1451	12 03 16.2	−21 32 12.7	0.199	7.32	JVLA DnC^b+B^n, GMRT 330 MHz^e	XMM

(a) project code 14B-190, PI: R. Cassano; (b) project code 15B-135, PI: V. Cuciti; (c) project code 26_021, PI: R: Cassano; (d) project code 27_025, PI: R. Cassano; (e) project code 28_066, PI: V. Cuciti; (f) project code 29_001, PI: V. Cuciti; (g) project code 05VKK01, PI: V. Kulkarni; (h) project code 23_046, PI: C: Jones; (i) project code 30_065, PI: S. Giacintucci; (l) project code 23_020. PI A. Bonafede; (m) project code 13A-268, PI: A. Babul, (n) project code 15A-270, PI: R. van Weeren; (o) project code 22_021, PI: G. Macario; (p) project code ddtB222, PI: V. Cuciti; ^{S} GMRT 330 MHz dataset reduced with SPAM (Section 4.2.1)

4.1 JVLA data analysis

We performed the data reduction, both calibration and imaging, of the JVLA datasets with the Common Astronomy Software Applications package (CASA, McMullin et al. 2007). The total bandwidth, from 1 to 2 GHz, is divided into 16 spectral windows, each with 64 channels of 2 MHz in width. The hybrid configurations DnC and BnA are used in order to obtain a roundish beam also for targets with southern declination

As a first step, the data were Hanning smoothed. We applied the pre-determined antenna position offset and elevation-dependent gain tables. The flux density scale was set according to Perley & Butler (2013). We determined amplitude and phase solutions for the flux calibrators in the ten central channels of each spectral window in order to remove possible time variations during the calibrator observation. These solutions were pre-applied to find the delay terms (`gaintype='K'`) and to correct for the bandpass response. We obtained the complex gain solutions for the calibrator sources (also of the phase calibrator, if present) on the full bandwidth pre-applying the bandpass and delay solutions. Finally, we applied all the calibration tables to the target field. Automatic RFI flagging was applied to the target field using the CASA task `flagdata` (`mode=tfcrop`). In the majority of the datasets, few (two–four) spectral windows were completely flagged because of the severe RFI. To reduce the size of the dataset, we averaged the 48 central channels of each spectral window to 6 channels and we averaged in time with a time bin of 15 sec.

We ran several rounds of phase-only self-calibration on the target field and a final amplitude and phase self-calibration. Manual flagging of additional data was applied by visually inspecting the solutions of the self-calibration and the residual data column of the uv-data (`corrected-model` in `plotms`). The wprojection algorithm was used to take into account the non-coplanar nature of the array. Wide band imaging is crucial when dealing with the 1 GHz bandwidth of the JVLA, therefore we used at least two (sometimes three) Taylor terms (`nterms=2-3`) to take the frequency dependence of the brightness distribution into consideration. Images up to 6144^2 pixels were needed in B array, while 2400^2 were sufficient in D array to deconvolve also bright sources outside the primary beam. The imaging process involves the use of clean masks that have been made with the `PyBDSM` package (Mohan & Rafferty 2015). For the self-calibration we used the "Briggs" weighting scheme with `robust=0` and we made final "full-resolution" (typically $\sim 35''$ in D array and $\sim 10''$ in C array) images whose properties will be reported in Table 5.1. Once the final "full-resolution" image was obtained, we subtracted all the sources outside a square of $30'$ side centred on the pointing position form the *uv*-data to reduce the size of the clean image and make the imaging process faster. Then, in order to highlight the possible diffuse emission, we subtracted all the discrete sources. For this purpose, we produced high resolution images excluding the baselines sensitive to the emission on scales larger than ~ 250 kpc (`uvrange`$\gtrapprox 2-3$ klambda depending on the cluster redshift). The clean components of the sources detected in the high resolution images were subtracted from the visibilities. With the new dataset we produced low resolution images, using higher values for the `robust` parameter and/or tapering down the long baselines to increase the sensitivity to the diffuse emission.

Images were corrected for the primary beam attenuation. The absolute flux scale uncertainties are assumed to be within 2.5% (Perley & Butler 2013).

For two clusters, A1451 and Zwcl 0634.1+4750, in addition to the proprietary JVLA D array observations, we reduced archival JVLA B array data belonging to a project mainly aimed at studying magnetic fields in galaxy clusters through Faraday rotation measurements of polarised background sources (project code 15A-270, P.I. R. van Weeren). After a separate calibration and self-calibration, we combined the B and D array observations. Unfortunately the pointings did not coincide exactly and this severely affected the quality of the combined image, especially around bright sources away from the phase centre. In fact, the primary beam response at the position of those sources is different and this leads to considerable differences in their apparent fluxes between the two observations. To overcome this problem, we subtracted those sources from the *uv*-data and then we combined the datasets. In particular, we performed the subtraction of those sources separately for each spectral window. This is particularly important for sources that are close to the border of the primary beam because the size of the primary beam depends on the frequency, hence the flux density of those sources is considerably different in different spectral windows. The combined B+D array images have a "full resolution" of $\sim 6''$.

4.2 GMRT data analysis

The GMRT observations listed in Table 4.1 were carried out using an observing bandwidth of 32 MHz subdivided into 256 channels [1]. During the first part of the PhD project we reduced GMRT datasets with AIPS, then, after acquiring the expertise on the CASA data reduction, necessary to handle JVLA datasets, we started using CASA also for the GMRT, mainly to take advantage of the wide field imaging and of the advanced flagging techniques. Specifically, we reduced the observations of RXC J1322.8+3138, PSZ1 G019.12+3123, RXC J2051.1+0216, PSZ1 G139.61+24.20, A1443, RXC J0510.7-0801 and A402 with AIPS and those of A384, Zwcl 1028.8+1419 A1733, MACS J2135-010, A2355, A1437, A2104, Zwcl 2120.1+2256, RXC J0616.3-2156, Zwcl0634.1+4750, A3888 and A1451 with CASA. Regardless of the software we used, the calibration procedure is essentially the same and it is outlined in the following. The flux density scale was set following Scaife

---

[1] Only A2104 was observed with the old GMRT setup, namely with the simultaneous observation in two bands, the upper side band and the lower side band, each 16 MHz wide.

& Heald (2012). The bandpass was corrected using the flux density calibrators. As a first step we obtained amplitude and gain corrections for the primary calibrators in few central neighbour channels free of radio-frequency interference (RFI); these solutions were applied before determining the bandpass in order to remove possible time variations of the gains during the observation. Once we applied the bandpass, gain solutions for all the calibrator sources on the full range of channel were determined and transferred to the target source. Automatic removal of RFI was performed with the CASA task `flagdata` (`mode=rflag`) or with the AIPS task `RFLAG`. Further manual editing of the data was performed with the CASA tasks `plotms` and `flagdata` (`mode=manual`) or with the AIPS tasks `UVFLG`, `WIPER` and `SPFLG`. The central channels were averaged to a smaller number of channels each $1-2$ MHz wide to reduce the size of the dataset without introducing significant bandwidth smearing within the primary beam. A number of phase-only self-calibration rounds was carried out to reduce residual phase variations. A final amplitude and phase self-calibration was applied. We applied further manual editing to the data, flagging bad self-calibration solutions and visually inspecting the residual uv-data. Wide field imaging was implemented to account for the non-coplanarity of the baselines. In particular we used the wprojection algorithm in CASA, while in AIPS we subdivided the field of view in tens of facets (the exact number of facets depends on the frequency, the resolution and the presence of bright sources). The facets were imaged separately, with a different phase centre, and then recombined. In CASA, wide band imaging (`mode=mfs`, `nterms=2`) was also used to consider the combination of the sources spectral index and primary beam attenuation. To deal with the bright sources in the field of view that typically reduce the dynamic range of the image we adopted the so called "peeling" technique. Specifically, in CASA, we subtracted the components of all the imaged field, except the source that we want to peel. We shifted the phase center of the visibilities on the position of the source, thus creating a dataset containing only that source and centred on its position. This dataset is imaged and self calibrated several times to obtain direction dependent amplitude and phase solutions for that source. Then the peeled source is subtracted from the uv-data and the phase center is shifted back on the pointing coordinates. In AIPS, a similar procedure is implemented in the task `PEELR`, except that `PEELR` does not subtract the "peeled" sources.

We used the "Briggs" weighting scheme with `robust=0` (both for AIPS and CASA) throughout the self-calibration and we produced final "full-resolution" images whose properties are listed in Table 5.1. We subtracted all the sources outside the central $\sim 30'$ to reduce the size of the images and facilitate the imaging process. We then subtracted all the compact sources. First we made high resolution images excluding the baselines sensitive to the emission on scales larger than ~ 250 kpc (`uvrange`$\gtrapprox 2-3$ klambda depending on the cluster redshift). We subtracted the clean components of the sources detected in the high resolution images and we used the new dataset to produced low-resolution images by using different weighting schemes and/or tapering down the long baselines. Low resolution images, where the contribution of the compact sources has been subtracted, are more sensitive to the extended low surface brightness emission and thus are suitable to evaluate the presence of sources such as radio halos or relics. Images were corrected for the primary beam response. The residual calibration errors are within 10% (e.g. Chandra et al. 2004).

4.2.1 SPAM

Two of the GMRT datasets (marked with *"S"* in Table 4.1) have been processed with the Source Peeling and Atmospheric Modelling (SPAM) package. Here we provide a brief description of the SPAM pipeline, we refer to Intema et al. (2009), Intema (2014) and Intema et al. (2017) fore more details.

SPAM is an AIPS-based, semi-automated pipeline that uses the ParselTongue interface (Kettenis et al. 2006) to access AIPS tasks, files and tables from Python. The pipeline consists of two main steps: the pre-processing part that converts the raw data into pre-calibrated visibility datasets for all the observed pointings and the main pipeline which converts pre-calibrated visibilities into self-calibrated continuum images.

The aim of the first step is to obtain the instrumental calibrations for the best available primary calibrator and transfer them to the target field. The flux density scale is set according to Scaife & Heald (2012). After the flagging of the visibilities affected by severe RFI, gain solutions and bandpass solution are determined for the calibrator. The flagging, gain calibration, bandpass calibration loop is repeated several times to improve the results. The calibration solutions are transferred to the target field. In particular, the phase solutions from the calibrator are filtered to separate the instrumental and ionospheric contributions and only the instrumental phase calibration is applied to the target field. Data are averaged in time and frequency and converted to Stokes I to speed up processing. At this level, only simple clipping of excessive RFI is performed on the target visibilities.

The purpose of the main pipeline is the self-calibration. The initial phase calibration of the target field is based on a multi-point source model derived from the NVSS (Condon et al. 1998), WENSS (Rengelink et al. 1997) and VLSS (Cohen et al. 2007; Lane et al. 2014) radio source catalogues and then several runs of direction independent self-calibration are carried out. To take into account the non-coplanarity of the array, the wide field of the GMRT is divided into facets covering the primary beam and the fields around the bright sources outside the primary beam. The imaging is done using the "Briggs" weighting scheme with the AIPS `ROBUST` parameter set to -1. This slightly uniform weighting scheme produces a nearly Gaussian PSF, suppressing the broad wings typical of centrally condensed arrays such as the GMRT, at the cost of a reduced sensitivity to the large scale emission. During the self-calibration process, the excision of bad data is carried out inspecting the residual visibilities (clean components of all the facets are subtracted out) and using the Obit task `LowFRFI`[2].

The direction-dependent gain phases are obtained by peeling the brightest sources in the wide field image. The peeling phase solutions are dominated by the ionospheric contribution and represent a sparse sampling of the ionosphere over the GMRT at the time of the observation. The direction-dependent phase gains are fitted with a time-variable two-layer phase screen model that can be used to generate the antenna-based ionospheric phase delays for every position in the wide field image. Using this model, the pipeline generates the individual gain tables for each facet. The target field is re-imaged and deconvolved while applying the appropriate correction table per facet. At the end, a number of additional calibration (including an amplitude self-calibration) and flagging operations are done to solve for the residual direction-independent time and frequency calibration errors.

We re-imaged the datasets produced with SPAM to subtract the compact sources and to make low resolution images with appropriate `ROBUST` and `TAPER` parameters to increase the sensitivity to the extended emission.

4.3 Upper limits

As we will see in Section 5.3, most of the clusters that we studied do not host large scale radio emission at the sensitivity of our observations. To extract quantitative observational information from the non-detection of radio halos in our sample it is crucial to derive meaningful upper limits to the diffuse flux density of those clusters. To do that, we adopted the method of injecting fake radio halos in the *uv*-datasets. The injection technique was introduced in the GRHS (Brunetti et al. 2007; Venturi et al. 2007, 2008; Kale et al. 2013, 2015, see also Section 2.2) and it continues to be used in the literature (Russell et al. 2011; Bonafede et al. 2017; Johnston-Hollitt & Pratley 2017).

We modelled the radio halo brightness profile with an exponential law in the form:

$$I(r) = I_0 e^{-\frac{r}{r_e}}, \tag{4.1}$$

where I_0 is the central surface brightness and r_e is the e-folding radius (Orrú et al. 2007; Murgia et al. 2009). The flux density of the modelled radio halos integrated up to $3\times r_e$ is:

$$S_{RH} = 2\pi f r_e^2 I_0 \ \ \text{Jy}, \tag{4.2}$$

where r_e and I_0 are in units of arcsec and Jy/arcsec^2, respectively, and $f = 1 - 4e^{-3} = 0.8$. In order to inject Mpc scale radio halos, as reference we used $r_e = 500$ kpc/2.6 = 192 kpc, where 2.6 is the median value of the quantity r_h/r_e for the radio halos studied by both Murgia et al. (2009) and Cassano et al. (2007), with

---

[2] http://www.cv.nrao.edu/ bcotton/Obit.html

r_h being the radius of the radio halos as measured from the radio image. In the injected models, the radio halo profile was set to zero for $r > 5r_e$.

For each cluster, we chose a region in the image void of sources and clear noise pattern and we created a set of fake radio halos with different integrated flux densities (Eq. 4.2), centred on that region. To inject modelled radio halos into the datasets and image the modified dataset to infer the radio halo detection we used CASA. Specifically, we Fourier transformed the models into the MODEL_DATA column of the datasets including the wprojection algorithm to take into account the large field of view. We added the modelled radio halos to the datasets with the task `uvsub` (`reverse=true`) and, for each modified dataset, we followed the same procedures described in the previous sections to produce images optimised for the detection of the extended emission. For a given cluster mass, we started injecting a fake radio halo that would lie on the radio power–mass correlation from Cassano et al. (2013) and we reduced the injected flux density until the injected radio halo appears just as some positive residuals leading to the "suspect" of diffuse emission. The injected flux density corresponding to this marginal detection can be considered as the upper limit for that particular cluster. We did not inject the fake radio halo at the cluster center because the possible presence of some weak residual emission in the cluster field may "help" the detection of the fake radio halo, biasing our upper limit towards lower values. Indeed, faint cluster radio galaxies below the detection limit of our observations may contribute to a positive plateau in the cluster field (e.g. Farnsworth et al. 2013; Cuciti et al. 2015). An example of the injection procedure is shown in Fig. 4.1 for the cluster A220: the original image is in the upper left panel and a series of fake radio halos with decreasing flux densities is in the other panels.

4.4 X-ray data analysis

Among the clusters listed in Table 4.1, 16 have archival X-ray *Chandra* data that we analysed with the procedure described in Section 3.4. We applied the standard techniques for the data reduction implemented in the CIAO package. For the most recent observations we used CIAO 4.9 and the calibration files from CALDB 4.7.6.

We produced images in the 0.5-2 keV band and we analysed those images to get information about the dynamical properties of clusters on the radio halo scale. In particular, we analysed the X-ray surface brightness inside an aperture radius of 500 kpc, that is the region where turbulence is most likely dissipated, as discussed in Section 3.4. To study the X-ray morphology of clusters, we used the three methods described in Section 3.4: the power ratios, P_3/P_0, the centroid shift, w and the concentration parameter, c. The power ratios gives information about the presence of substructures in the surface brightness distribution, the centroid shift measures the separation between the peak and the centroid of the X-ray emission and the concentration parameter tells us how much the X-ray surface brightness is

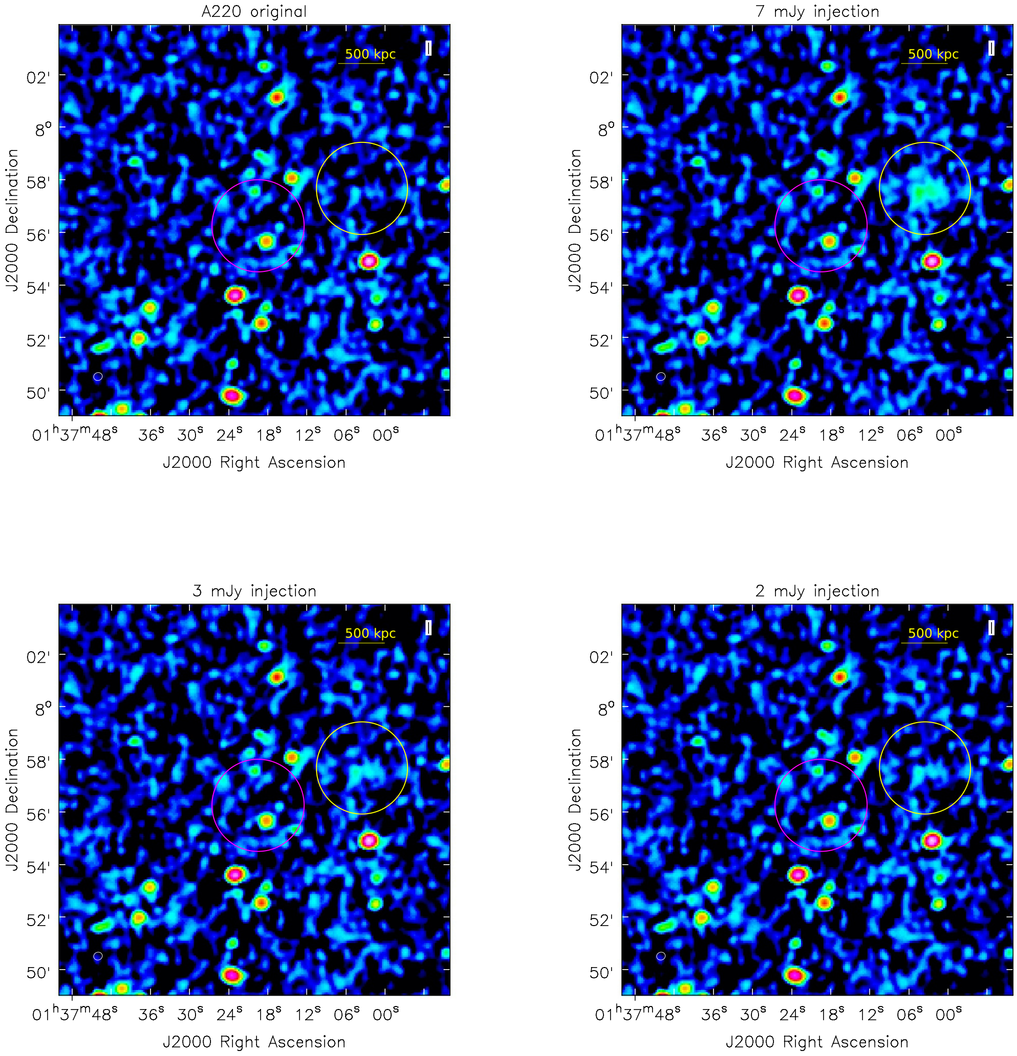

Figure 4.1: Injection of fake radio halos in the cluster A220. *Upper left*: original image. *Upper right*: injected radio halo with flux density of 7 mJy. *Lower left*: injected radio halo with flux density of 3 mJy. *Lower right*: injected radio halo with flux density of 2 mJy. The two circles have radii of 500 kpc and are centred on the cluster centre (magenta) and on the modelled radio halo (yellow). We consider 2 mJy to be the upper limit to the diffuse emission of A220.

concentrated in the cluster core.

Among the nine clusters without *Chandra* data, seven have archival *XMM-Newton* observations and two, namely A220 and ZwCl 1028.8+1419, do not have pointed X-ray observations (only the RASS image is available). While it is not possible to derive reliable dynamical information from the RASS images, *XMM-Newton* images can be used to infer the presence or absence of dynamical activity in clusters. Although we did not perform a quantitative analysis of the X-ray surface brightness distribution of the clusters with *XMM-Newton* data, in many cases, the visual inspection of the *XMM-Newton* images is efficient to deduce the merging or relaxed state of clusters, as we will show in Section 7.1.

Chapter 5

Results of the radio data analysis

The observational campaign carried out to complete the radio information of our sample led to the discovery of a number of interesting radio sources, as well as some clusters with candidate diffuse emission. At the same time, we did not detect extended emission in many of the clusters that we analysed. Still, if one manages to put stringent upper limits to the diffuse flux of clusters without radio halos, they become important statistical tools to perform population studies of galaxy clusters and to investigate the distribution and evolution of clusters in the radio power-mass (or X-ray luminosity) diagram. In this Chapter we report the results of the data analysis of the sample that we discussed in Chapter 4. For each cluster, we list telescope, frequency, time on source, "full resolution" beam and rms and detection/upper limit in Table 5.1.

More in detail, we discovered extended radio emission in five galaxy clusters (Section 5.1) and we detected some hints of diffuse emission that we can only classify as "candidate" with the currently available observations in three clusters (Section 5.2). In Section 5.3 we will describe the results of the injection procedure to derive upper limits to the diffuse flux density of clusters without radio halos. The statistical analysis of the sample will be presented in Chapter 7.

The error Δ_S associated with a flux density measurement S is calculated as:

$$\Delta_S = \sqrt{\left(rms \times \sqrt{\frac{A_s}{A_b}}\right)^2 + (\sigma_c \times S)^2}, \tag{5.1}$$

where A_s is the source area, A_b is the beam area and σ_c is the calibration uncertainty. We assume $\sigma_c \sim 2.5\%$ for the JVLA (Perley & Butler 2013) and $\sigma_c \sim 10\%$ for the GMRT (Chandra et al. 2004). Details about the general methods for the data calibration and imaging are given in the following sections.

Table 5.1: Summary of the radio data analysis

Name	telescope	ν (MHz)	Δt (min)	beam (″×″)	rms (mJy/beam)	detection
A56	JVLA C	1500	40	13.8 × 10.4	0.080	UL
A2813	JVLA C	1500	40	11.4 × 9.5	0.035	UL
A2895	JVLA C	1500	40	14.6 × 9.0	0.040	UL
A3041	JVLA C	1500	40	18.0 × 8.6	0.035	candidate RH
A220	JVLA C	1500	40	11.6 × 9.8	0.045	UL
A384	JVLA C	1500	40	13.5 × 10.4	0.035	UL
	GMRT	610	220	5.9 × 4.8	0.050	–
Zwcl1028.8+1419	GMRT	610	330	5.3 × 4.8	0.056	no RH
RXC J1322.8+3138	GMRT	610	150	5.7 × 4.4	0.060	no RH
A1733	GMRT	610	250	7.9 × 5.0	0.060	UL
PSZ1 G019.12+3123	GMRT	610	250	5.0 × 3.8	0.035	UL
MACS J2135-010	GMRT	610	300	7.8 × 5.8	0.080	UL
A2355	JVLA C	1500	40	11.6 × 10.8	0.040	UL
	GMRT	610	300	8.3 × 6.1	0.130	–
RXC J2051.1+0216	JVLA C	1500	40	14.1 × 11.5	0.050	UL
	GMRT	610	200	6.0 × 4.8	0.100	–
A2472	JVLA C	1500	40	10.5 × 10.1	0.040	UL
PSZ1 G139.61+2420	JVLA C	1500	40	10.3 × 5.1	0.030	MH
	GMRT	610	300+300	6.0 × 5.0	0.030	
	LOFAR	144	480	11.0 × 8.0	0.150	
A1443	JVLA C+D	1500	60+90	15.0 × 12.0	0.020	RH
	GMRT	610	150	5.6 × 4.2	0.050	
	GMRT	330	270	8.6 × 7.3	0.060	
	GMRT	150	240	18.7 × 14.1	1.800	
RXC J0510.7-0801	GMRT	610	330	5.4 × 4.8	0.200	no RH
	GMRT	240	330	15.7 × 13.1	1.200	no RH
A402	GMRT	330	400	13.4 × 8.6	0.100	candidate MH
	GMRT	330	380	–	–	
A1437	GMRT	330	330	9.0 × 7.4	0.400	no RH
A2104	GMRT	330	350	13.3 × 10.4	0.130	UL
Zwcl2120-1+2256	JVLA D	1500	40	33.0 × 30.3	0.075	candidate RH
	GMRT	330	250	10.0 × 9.2	0.100	
RXC J0616.3-2156	JVLA DnC	1500	40	55.4 × 19.9	0.080	UL
Zwcl 0634.1+4750	JVLA D	1500	40	35.7 × 30.7	0.045	RH
	JVLA B	1500	40	3.5 × 3.3	0.026	
	GMRT	330	170	10.0 × 9.2	0.090	
A3888	GMRT	330	260	14.6 × 8.3	0.300	RH
A1451	JVLA D	1500	40	44.4 × 17.1	0.060	RH
	JVLA B	1500	40	4.7 × 3.3	0.025	
	GMRT	330	260	11.6 × 8.1	0.095	

Notes: UL= Upper limit; RH= radio halo; MH= mini halo; no RH= no detection and no UL

5.1 Detection of diffuse emission

Among the clusters analysed in this Thesis (Chapter 4), five show clear evidence of diffuse radio emission. Specifically, we detected radio halos in A1451, Zwcl 0634.1+4750, A3888 and A1443 and a mini-halo in PSZ1 G139.61+2420. In addition, A1451 hosts a candidate radio relic at large distance from the cluster centre and Zwcl 0634.1+4750 host an interesting giant head tail radio galaxy. These two clusters will be extensively discussed in Chapter 6.

5.1.1 Radio halo in A3888

Abell 3888 (alternative names: RXC J2234.5-3744, PSZ1 G003.93-59.42) is an X-ray luminous cluster ($L_{X,500} = 6.36 \times 10^{44}$ erg/s in the 0.1–2.4 keV band, Pratt et al. 2009) at redshift $z = 0.151$ with mass $M_{500} = 6.67 \times 10^{14} M_{\odot}$ (Planck Collaboration et al. 2014a). Its dynamical status has been inconclusively studied in several papers based on *XMM-Newton* observations. Indeed, based on the centroid shift parameter and/or the power ratios, A3888 has been classified either as a relaxed (Pratt et al. 2009; Böhringer et al. 2010), disturbed (Chon et al. 2012) or intermediate (Weißmann et al. 2013) cluster. The large offset between the BCG and the X-ray peak is an indication of ongoing merging activity (Haarsma et al. 2010). Shakouri et al. (2016a) performed spectroscopic observations of 254 galaxies around A3888 and carried out a substructure analysis finding that the galaxy distribution is elongated in the East-West direction and it is bimodal along the same axis, with two subgroups of galaxies. All this evidence strongly supports the idea of an active dynamical activity. Our morphological analysis based on *Chandra* observations confirms that A3888 is a merging system (Section 7.1), with a relatively low concentration parameter and high centroid shift, although its X-ray emission is not extremely disturbed.

Hints of diffuse emission in the central region of A3888 have been detected in our re-analysis of the NVSS data (see Section 3.3). Shakouri et al. (2016b) claimed the detection of a giant radio halo in this cluster with ATCA observations in the frequency range 1.25-2.55 GHz (Fig. 5.1, top panel). In particular, they reported a radio halo flux density of 27.6 mJy at 1.4 GHz and a spectral index between 1.4 and 2.4 GHz $\alpha = -1.48$.

We detected a bright radio halo at 330 MHz with the GMRT. In Fig. 5.1 (bottom panel) we present the GMRT 330 MHz image of A3888. The overall morphology of the radio halo resembles the one described by Shakouri et al. (2016b). In particular, the two protrusions, extending towards South-West, are clearly visible in both the images if Fig. 5.1. The radio emission of the cluster is complex and characterised by the presence of many bright sources embedded in the radio halo emission. As Shakouri et al. (2016b) pointed out, source A[1] and B are head tail member galaxies,

---

[1] Source A is actually the blending of two head tail radio galaxies, clearly resolved in the ATCA

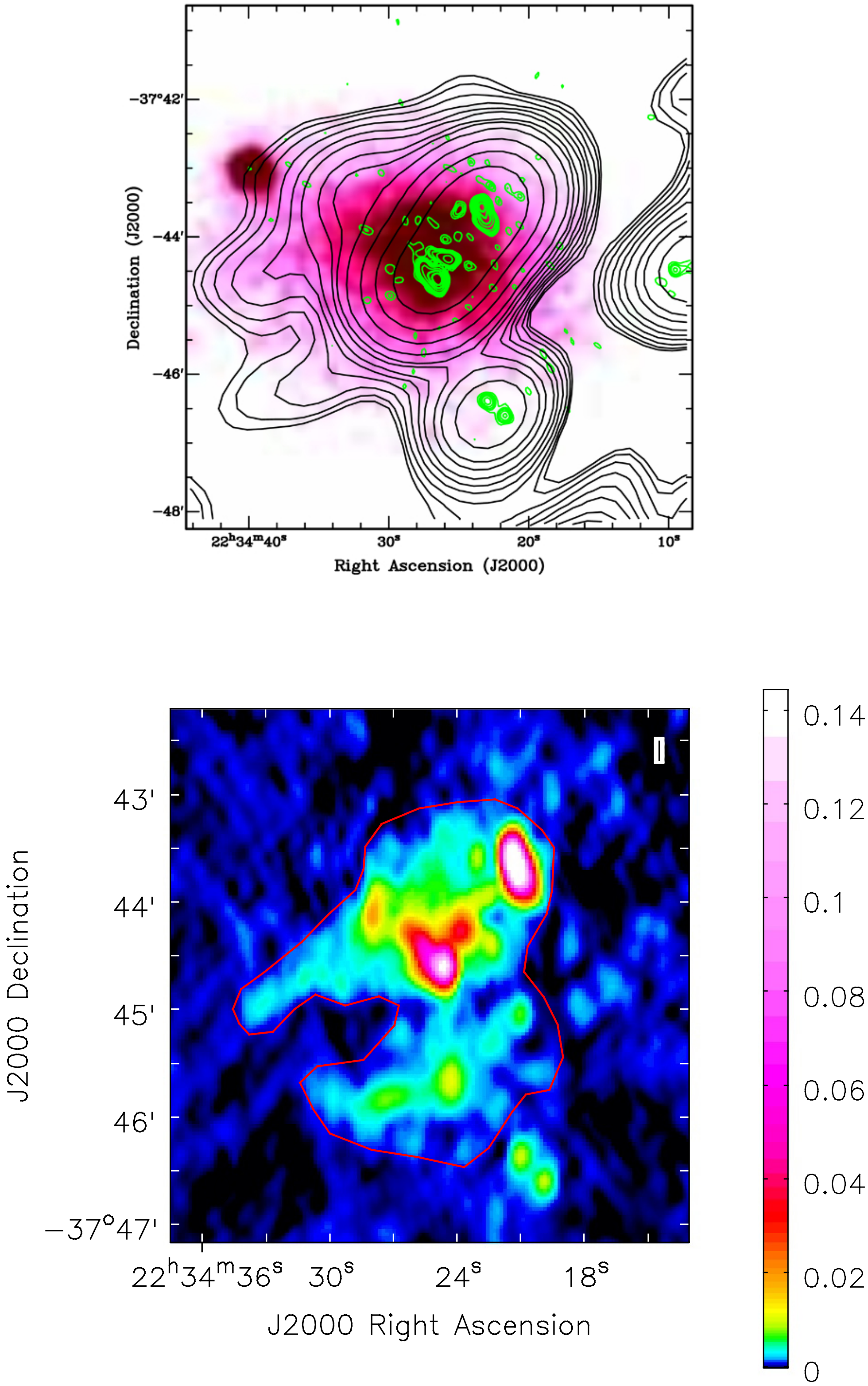

Figure 5.1: *Top*: A3888 *XMM-Newton* image with ATCA contours superimposed. Black: low resolution (beam=73″ × 58″) contours at 1.4 GHz. Green: high (beam=7″ × 8″) resolution contours at 1.4 GHz. From Shakouri et al. (2016b). *Bottom*: A3888 GMRT 330 MHz "full resolution" (14.6″ × 8.3″) image. We measured the "total" radio flux density of the cluster in the red region (see text)

while source C is a background radio galaxy. Being diffuse themselves, the subtraction of the head tail galaxies from the visibilities is very difficult. Low resolution images are not helpful in this case because it is even more difficult to separate the emission of the galaxies from the emission of the radio halo. In addition to the compact sources detected in Shakouri et al. (2016b), we detect another patch of emission (labelled E in Fig. 5.2, right panel) located North-West of source A. The superposition between the radio contours of A3888 and the optical DSS image in shown in Fig. 5.2. While source A, B and D have clear optical counterparts, the brightest part of E does not have a corresponding galaxy, thus it could be a peak of the radio halo emission.

We measured a total flux density of $\sim$ 1.29 Jy in the region highlighted in Fig.5.1 (bottom panel). In order to derive the radio halo flux density we estimated the contribution of the sources embedded in the diffuse emission and we subtracted their flux density from the total emission. We obtained a radio halo flux density $S_{330MHz} \sim 400$ mJy. Such an approach may lead to an underestimation of the flux density of the radio halo, indeed it is probable that when subtracting the contribution of the galaxies we also subtracted part of the radio halo flux density. To address this issue, we estimated the mean surface brightness of the radio halo and we calculated the amount of radio halo flux density that would lie in the galaxies regions. Thus the radio halo flux density is $S_{330MHz} \sim 450$ mJy. The LAS of the radio halo is $192'' \times 161''$ corresponding to a LLS of 505 kpc × 423 kpc.

We note that the comparison between the radio halo flux density at 330 and 1400 MHz would give a very steep spectrum ($\alpha < -1.8$), however, further analysis of the two datasets in necessary to properly investigate the spectral properties of this radio halo. Specifically, we need to match the *uv*-coverages, use an appropriate weighting scheme to reduce the differences between the two observations, subtract the galaxies contribution on the same area and estimate the radio halo flux density on the same region.

5.1.2 Radio halo in A1443

Abell 1443 (alternative names: Zwcl 1158.9+2323, RXC J1201.3+2306, PSZ1 G229.70+77.97) is a massive galaxy cluster $M_{500} = 7.74 \times 10^{14} M_{\odot}$ (Planck Collaboration et al. 2014a) at $z = 0.27$. The ROSAT Brightest Cluster Sample reports an X-ray luminosity $L_{[0.1-2.4\mathrm{keV}]} \simeq 6.2 \times 10^{14}$ erg/s. The X-ray *Chandra* image of the cluster (Fig. 5.3) reveals an elongation along the East-West direction and the presence of substructures in the gas distribution indicates a highly perturbed environment.

Bonafede et al. (2015) analysed GMRT 323 MHz observations of A1443 with the SPAM pipeline (Section 4.2.1) and they detected some diffuse emission. The cluster hosts a Γ-shaped source located at a projected distance of ∼300 kpc from

---

high resolution image (Fig. 5.1, top panel).

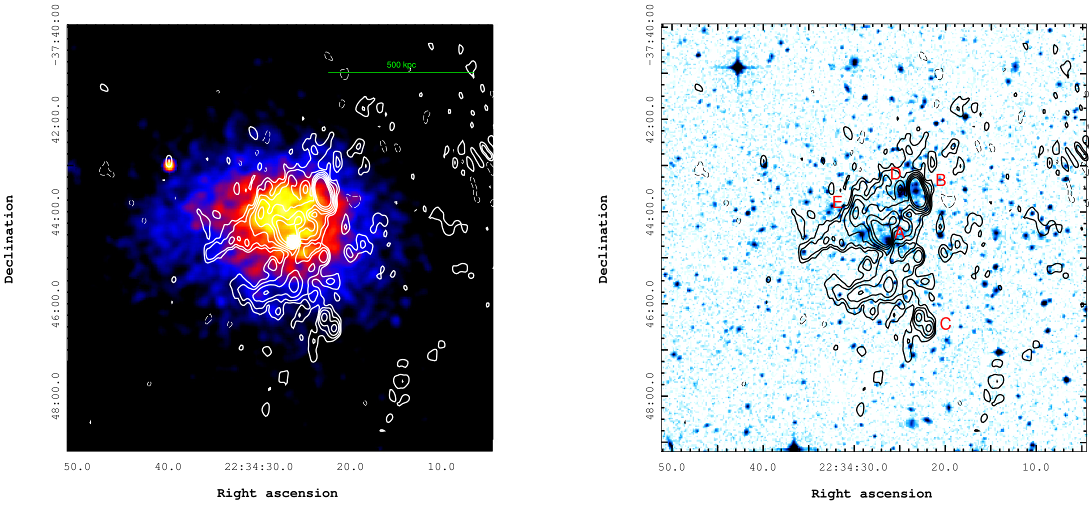

Figure 5.2: *Left*: A3888 X-ray *Chandra* image (colours) with GMRT 330 MHz contours superimposed. Contours start from 0.009 mJy/beam and are spaced by a factor 2. *Right*: Same contours as in the upper panel superimposed on the optical DSS image.

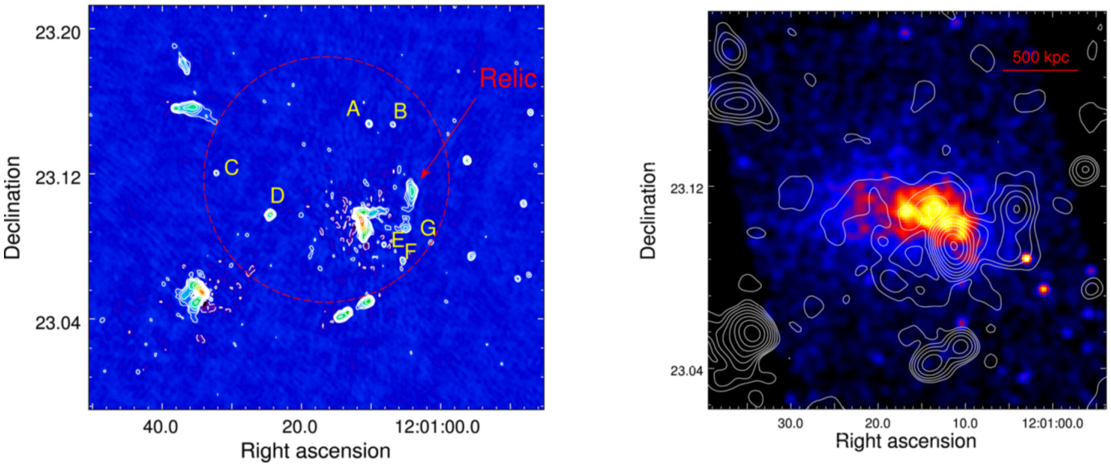

Figure 5.3: *Left panel*: A1443 GMRT 323 MHz high resolution image and contours. Contours start at 0.5 mJy/beam and are spaced by a factor of 2. The beam is $9.8'' \times 8.1''$.*Right panel*: A1443 GMRT 323 MHz low resolution contours superimposed to the X-ray *Chandra* image (colour scale) in the 0.5-7 keV energy range. Contours start at 1.1 mJy/beam and are spaced by a factor of 2. The beam is $27.4'' \times 26.7''$. Adapted from Bonafede et al. (2015).

the X-ray centre and another patch of diffuse emission is detected at ~700 kpc from the centre (Fig. 5.3, left panel). The second source can be classified as a candidate radio relic, since it is located at the edge of the X-ray cluster emission, has a typical elongated morphology and it has no visible counterpart in the Wide-field Infrared Survey Explorer (WISE) 3.4 μm image (Wright et al. 2010). Furthermore, they detected centrally located diffuse emission, with a Largest Linear Size (LLS) of $\sim$ 1.1 Mpc, that they classified as a radio halo (Fig. 5.3, right panel). The flux density of the radio halo measured by Bonafede et al. (2015) is 74.0 ± 7.6 mJy.

We analysed our 610 MHz GMRT observation of A1443 (Fig. 5.4, top right panel). While the Γ-shaped source and the candidate relic are well detected also at 610 MHz, the radio halo is only visible as patches of positive residuals with a total integrated flux density of $\sim$ 10 mJy. This could be an indication of a very steep spectrum. Therefore we analysed archival JVLA data in C and D array and we marginally detected the radio halo at 1.5 GHz (Fig. 5.4, bottom panel). The flux density measured on a region that encompasses the radio halo, the candidate relic and the Γ-shaped source is $\sim$ 102 mJy. We subtracted the contribution of the Γ-shaped source (~88 mJy) and of the candidate relic (~10 mJy) to derive the flux density of the radio halo and we obtained $S_{1.5GHz} = 3.5 \pm 0.10$ mJy, corresponding to $P_{1.4GHz} = 9.1 \pm 0.25 \times 10^{23}$ W/Hz. By matching the *uv*-coverages and weighting of the images at 330 (provided by A. Bonafede) and 1500 MHz, we estimated that the spectral index of the radio halo is $\alpha^{330MHz}_{1500MHz} \approx -1.9$. This triggered a GMRT proposal to observe A1443 at 150 MHz and confirm its ultra steep spectrum nature (project code ddtB222, P.I. V. Cuciti). We obtained 6 hours at the GMRT at 150 MHz. The dataset was processed with the SPAM pipeline. Contrary to the expectations, we did not detect any hint of diffuse emission at the cluster center with the sensitivity of the GMRT at 150 MHz ($1\sigma_{rms}$ ~2 mJy/beam).

We noticed that the 150 and 330 MHz, in Bonafede et al. (2015), observation were processed with two different versions of SPAM. Thus, in order to clarify the nature of the diffuse emission in A1443 we reprocessed all the three GMRT datasets with the last version of SPAM. The image that shows more discrepancies with respect to the old version is the one at 330 MHz; the low-resolution 330 MHz image is shown in Fig. 5.5. In particular, the total flux density of the radio halo is $\sim$ 52 mJy (to be compared with the 74 mJy found by Bonafede et al. (2015)). We note that, in the new image, the radio halo emission follows the X-ray emission better than the old image in Fig. 5.3, especially in the Southern part, where the diffuse emission has never been detected at any other frequency.

In order to estimate the spectral index of the radio halo we subtracted the discrete sources and we produced images at 330, 610 and 1500 MHz using the same *uv*-range, the appropriate weighting scheme to obtain the best possible match at various frequencies and tapering down the long baselines to obtain approximately the same resolution ($\sim 30''$). Since the subtraction of the Γ-shaped source and the relic from the *uv*-datasets is difficult, because of their diffuse nature, and disentan-

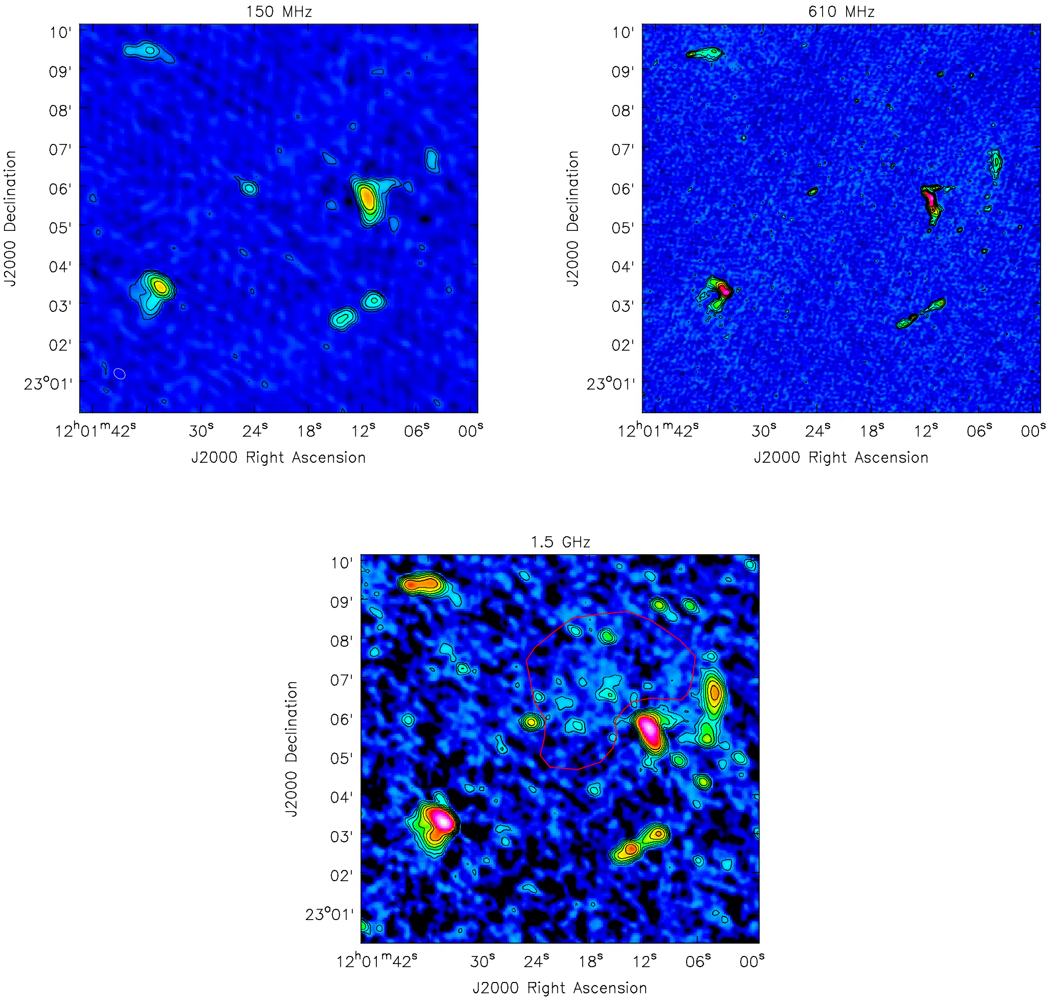

Figure 5.4: *Top left*: GMRT 150 MHz image and contours of A1443 at resolution 18.7″ × 14.1″. Contours are (3,6,12,24...)$\times\sigma_{rms}$ with $\sigma_{rms} = 1.8$ mJy/beam. *Top right*: GMRT 610 MHz image and contours of A1443 at resolution 5.6″ × 4.2″. Contours are (3,6,12,24...)$\times\sigma_{rms}$ with $\sigma_{rms} = 50\mu$Jy/beam *Bottom*: JVLA 1.5 GHz image and contours of A1443 at resolution 15.0″ × 12.0″. Contours are (3,6,12,24...)$\times\sigma_{rms}$ with $\sigma_{rms} = 20\mu$Jy/beam.

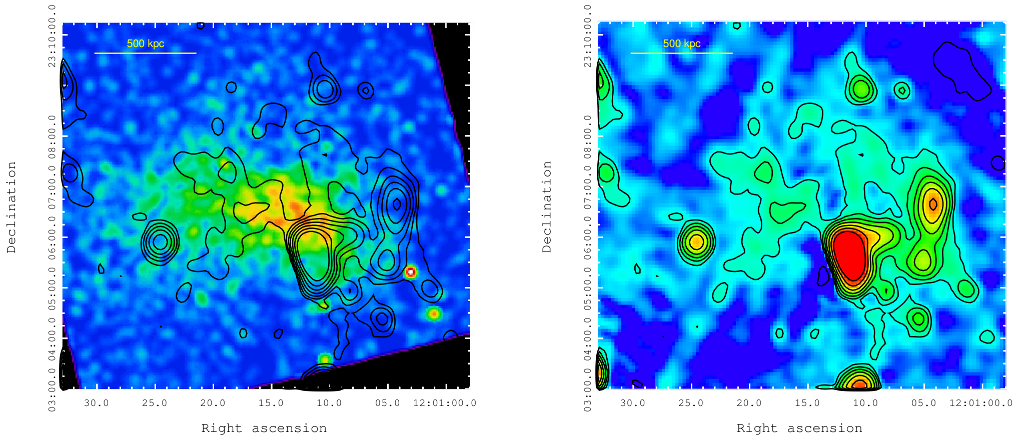

Figure 5.5: *Left*: A1443 *Chandra* image with GMRT 330 MHz contours superimposed (derived with the last version of the SPAM pipeline). Contours are the same as in the right panel. *Right*: A1443 GMRT 330 MHZ low resolution ($20.5'' \times 18.8''$) image and contours. Contours start at 0.5 mJy/beam and are spaced by a factor of 2. The rms noise of the image is 0.18 mJy/beam.

gling their emission from the radio halo emission in the Eastern part of the cluster is complicated, we measured the spectral index on the Western area (red region in Fig. 5.4, bottom panel). It is likely that with this approach we are underestimating the flux density of the radio halo, but it is fair to estimate the value of its spectral index, at least on that region. The spectrum of the radio halo in A1443 between 330 and 1500 MHz is shown in Fig. 5.6. We obtained a spectral index $\alpha_{1500MHz}^{330MHz} = -1.56 \pm 0.10$, which would still place A1443 in the class of USSRHs. Furthermore, if we -now- measure the mean radio halo surface brightness at 330 MHz and we extrapolate it at 150 MHz with a spectral index $\alpha = -1.56$, it falls below the 1σ rms noise of our GMRT 150 MHz image, making the four datasets from 150 to 1500 MHz consistent. More sensitive observations are necessary to measure the flux density of this radio halo at low frequency.

5.1.3 Mini halo in PSZ1 G139.61+2420

PSZ1 G139.61+2420 (PSZG139, hereafter), discovered by Planck, has a mass of $M_{500} = 7.09 \times 10^{14} M_{\odot}$ and it is at redshift $z = 0.27$. It has a global temperature of 7.5 keV and a low-entropy ($K_0 = 10 \pm 10$) cool core (Giacintucci et al. 2017). The high value of the concentration parameter that we derived for PSZG139 is consistent with the presence of the cool core, however, the centroid shift parameter lies at the boundary separating merging and non-merging clusters (Section 7.1). In fact, the X-ray morphology of the cluster is slightly elongated in the SE-NW direction, indicating some trace of dynamical disturbance. A deeper analysis of the X-ray surface brightness profile reveals the presence of a discontinuity around the cool core, in the NW direction. Specifically, this edge is a cold front (the

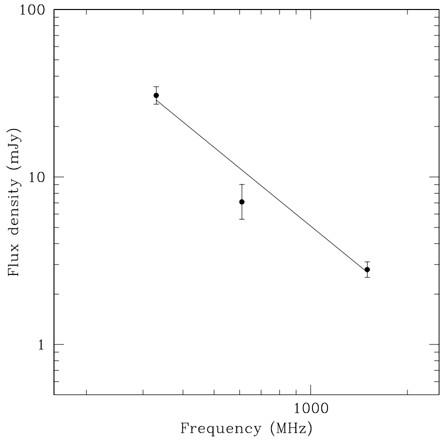

Figure 5.6: *Left*: A1443 spectrum. Flux densities are measured at 330, 610 and 1500 MHz on images made with the same *uv*-range, uniform weighting scheme and same resolution.

temperature in the upstream region is higher, Savini et al. submitted), suggesting that the cold gas in the core may be sloshing. Deeper X-ray data are necessary to investigate the presence of large scale discontinuities in this cluster.

There are two GMRT observations at 610 MHz of PSZG139: Obs. No 7380, P.I. R. Cassano and Obs No 8039, P.I. S. Giacintucci. We analysed Obs. No 7380 with the procedure described in Section 4.2 and then we combined our image with the image produced by S. Giacintucci from Obs No 8039. The combined "full resolution" image is shown in Fig. 5.7 (left panel), superimposed on the optical DSS image of the cluster field. A weak source (labelled S1) of ~ 0.4 mJy appears associated with the central galaxy. North of source S1, we detected an extended source (S2) without a clear optical counterpart and a faint point like source (S3) probably associated with a member galaxy (the redshift of the optical counterpart is not available). The flux density of S2 is ~ 2.4 mJy, while S3 is ~ 0.24 mJy. In the image with a slightly lower resolution (Fig. 5.7, right panel) the three sources are blended with a diffuse component that seems confined within the cluster core. We classify this diffuse source as a mini halo. The total extension of the diffuse emission in the East-West direction is ~ 100 kpc. We measured the total flux density inside the 3σ contours shown in Fig. 5.7 (right panel) and we subtracted the contribution of the discrete sources mentioned above, obtaining a flux for the mini halo $S_{610MHz} \sim 1.2$ mJy. The position of the X-ray cold front is roughly coincident with the edge of the radio diffuse emission, as found for other mini halos in the literature (Mazzotta & Giacintucci 2008; Giacintucci et al. 2014b,a).

In Fig. 5.8 we present the JVLA 1.5 GHz C array "full resolution" image of the central region of PSZG139 compared to the low resolution GMRT 610 MHz contours. The sources S1, S2 and S3 are detected also at 1.5 GHz, with flux densities of ~ 0.28 mJy, ~ 0.76 mJy and ~ 0.18 mJy respectively. At a similar resolution, the mini halo appears less extended towards the West at high frequency.

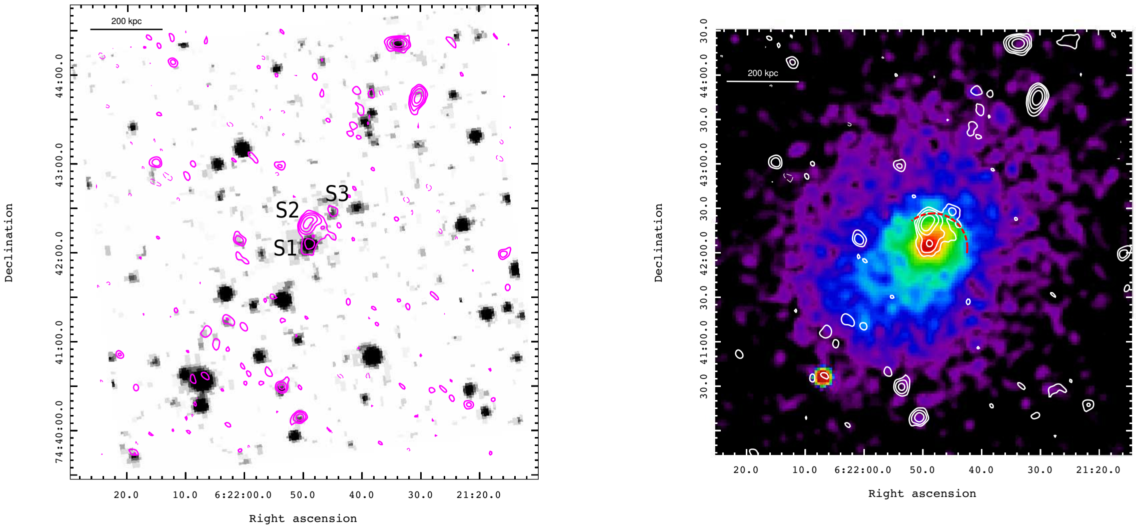

Figure 5.7: *Left*: GMRT 610 MHz "full resolution" contours of PSZG139 overlaid over the optical DSS image. Contours are $(\pm 3, 6, 9, 12...) \times \sigma_{rms}$ with $\sigma_{rms} = 30$ μJy/beam and beam=$5'' \times 6''$. The first negative contour is dashed. *Right*: GMRT 610 MHz low-resolution contours of PSZG139 overlaid over the X-ray *Chandra* image of the cluster. Contours are $(\pm 3, 6, 9, 12...) \times \sigma_{rms}$ with $\sigma_{rms} = 30$ μJy/beam and beam=$7'' \times 7''$. The first negative contour is dashed. The red dashed line represents the location of the cold front (Savini et al. submitted).

We estimated the flux density of the mini halo in the same region used for the GMRT image (3σ contours shown in Fig. 5.8) and we subtracted the contribution of the discrete sources. We obtained a flux density of the mini halo $S_{1.5GHz} \sim 0.36$ mJy, which would give a spectral index of the mini halo $\alpha_{1500MHz}^{330MHz} \approx -1.3$.

PSZG139 has been also observed with LOFAR at 144 MHz as part of a project aimed at studying the low frequency radio diffuse emission in dynamically relaxed or intermediate clusters (P.I. F. Savini). In the LOFAR image the mini halo appears much more extended, especially towards South-East (Fig. 5.9, Savini et al. submitted) and has an integrated flux density $S_{144MHz} = 38 \pm 6$ mJy. Savini et al. analysed the brightness radial profile of the emission, fitting it with an exponential form $I(r) = I_0 e^{-r/r_e}$ (Murgia et al. 2009), and found best fit values $I_0 = 13.4 \pm 0.6$ μJy/arcsec^2 and $r_e = 91.6 \pm 6.5$ kpc; this value of the radius places PSZG139 in between the typical values of giant and mini-radio halos. In order to place an upper limit to the extended emission that is detected with LOFAR but not with the GMRT at 610 MHz, we injected a simulated radio halo in the GMRT uv-dataset (Section 4.3). We modelled the fake radio halo with the parameters I_0 and r_e derived from the brightness radial profile and we created a set of fake sources with decreasing flux densities, i.e. with decreasing spectral indices. Starting from $\alpha = -1$, we lowered the value until the radio halo could not be detected any more. This analysis suggests that the diffuse source has a spectral index $\alpha = -1.7$; a similar constraint can be derived using the data at 1.5 GHz.

Clusters without evidence of major mergers showing diffuse cluster scale radio

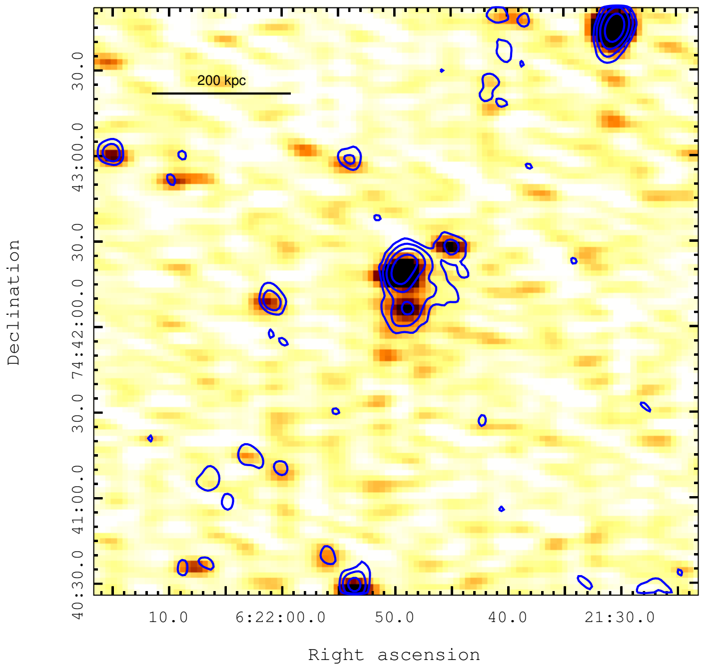

Figure 5.8: JVLA C array 10.3 × 5.1 resolution image of the center of PSZG139 with GMRT 610 MHz contours from Fig. 5.7 (right panel) overlaid.

emission are rare, still PSZG139 is not the first case (Bonafede et al. 2014b; Sommer et al. 2017; Venturi et al. 2017). In particular, some similarities can be found with the cluster A2142, where a slightly flatter spectrum diffuse emission, surrounded by cluster scale emission has been detected (Venturi et al. 2017). However, A2142 is not a cool-core cluster (Giacintucci et al. 2017) and the size, the spectrum and the radio power are those typical of giant radio halos in clusters of that mass. PSZG139 is particularly interesting because it is the first case of a cool-core cluster where a mini-halo (the diffuse component detected at higher frequencies) coexists with a diffuse emission on larger scales detected at low frequency (Savini et al. submitted). These properties may be expected in a situation where a massive cool-core cluster undergoes a minor merger. In this case the cool core would not be disrupted and the cluster may appear slightly disturbed (elongated, with relatively high values of the centroid shift) in the X-rays. At the same time, the energy dissipated on large scales may not be sufficient to generate a classical giant radio halo and the emission would appear very steep and glow up only at lower frequencies. Since minor mergers are common in cool-core clusters with evidence of gas sloshing we may expect that PSZ139 is only the first of many cases of very steep spectrum halos surrounding mini-halos that will be detected by LOFAR observations.

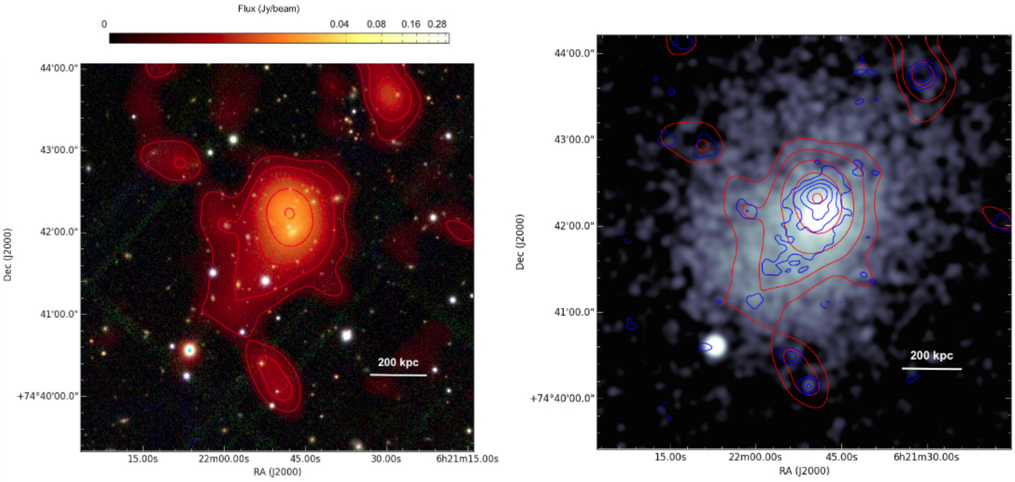

Figure 5.9: *Left*: PSZG139 optical Pan-STARRS g,r,i mosaic with low resolution ($34'' \times 26''$) 144 MHz LOFAR contours overlaid. Contours level are at $(\pm 3, 6, 12...) \times \sigma_{rms}$ with σ_{rms} = 330μJy/beam.*Right*: X-ray *Chandra* image of PSZG139 with 144 MHz LOFAR high resolution (blue) and low resolution (red) contours superimposed. Low resolution contours are the same as in the left panel. High resolution ($11'' \times 8''$) contours are $(\pm 3, 6, 12...) \times \sigma_{rms}$ with σ_{rms} = 150μJy/beam. From Savini et al. (submitted).

5.2 Clusters with candidate diffuse emission

5.2.1 Candidate radio halo in Zwcl2120-1+2256

Zwcl2120-1+2256 (PSZ1 G072.78-18.70) is one of the less massive clusters in our sample, with $M_{500} = 5.91 \times 10^{14} M_\odot$ (Planck Collaboration et al. 2014a). It is at redshift $z = 0.143$ and the information available in the literature is rather sparse. According to the morphological analysis of the X-ray surface brightness distribution, we find that Zwcl2120-1+2256 (Z2120, hereafter) sits in the intermediate region between merging and relaxed clusters. In fact, the X-ray emission of this cluster is quite interesting: it is fairly peaked at the center, however, there is a low-surface brightness "tail" extending to the South-West, which clearly indicates ongoing dynamical activity, probably driven by a minor or off-axis merger event that did not completely disrupt the core (Fig. 5.10, right panel and Fig. 5.11, right panel).

The JVLA D array image of Z2120 is shown in Fig. 5.10 (left panel). In addition to the three compact sources (labelled A, B and C) in the cluster' s central region, we detected some faint diffuse emission extending towards South-West. We subtracted the discrete sources (with the procedure outlined in Section 4.1) and we produced a low-resolution image tapering down the longest baselines. The residual emission is shown in Fig. 5.10 (right panel). It is elongated along the NE-SW axis and, interestingly, it follows the X-ray emission of the cluster, especially in the southern area. We note that, while the radio emission on top of the peak of the X-ray emission may be partly due to some residuals from the subtracted sources,

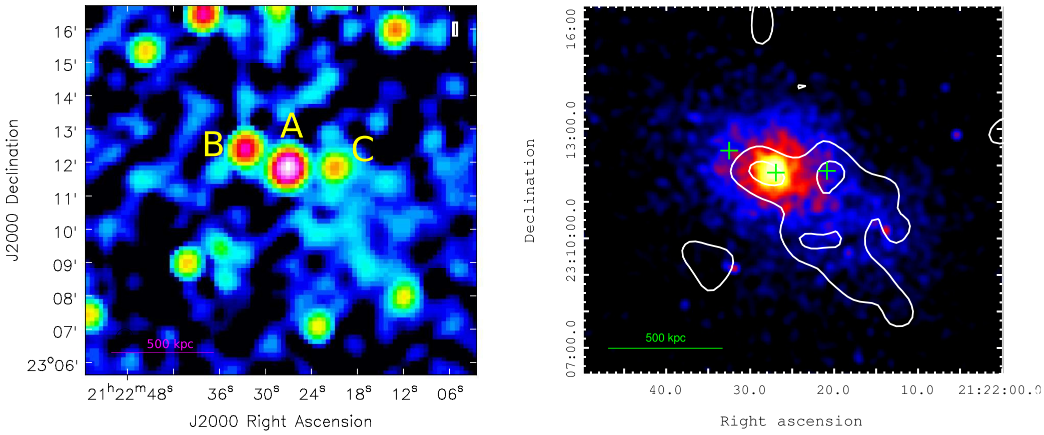

Figure 5.10: *Left*: Z2120 JVLA D array image. The resolution is $33'' \times 30''$ and the rms noise is $\sim 60 \mu$Jy/beam. *Right*: Z2120 low resolution ($55'' \times 54''$) JVLA contours after the compact sources subtraction overlaid over the X-ray *Chandra* image. Contours are drawn at $(3,6...) \times \sigma$, with $\sigma = 0.1$ mJy/beam. The first negative contour is dashed. The green crosses mark the position of the three sources at the cluster center, which have been subtracted.

the emission coincident with the low-surface brightness X-ray South-West tail is not affected by subtraction. The residual flux density measured inside the 3σ contours of Fig. 5.10 (right panel), considering also the emission in the central region of the cluster, is $S_{1.5GHz} \sim 7.7$ mJy. We classify this emission as a candidate radio halo.

A GMRT 330 MHz observation is available in the archive (P.I.:C. Jones). We reduced this dataset with the SPAM pipeline (Section 4.2.1) and then we imaged the processed data with CASA. Only some patches of diffuse emission are visible in the cluster central region on the "full resolution" image ($\sim 10''$, Fig. 5.11, left panel). In order to highlight the possible presence of diffuse emission, we subtracted the discrete sources and we tapered down the longest baselines to degrade the resolution of the image. A residual emission of ~ 46 mJy is detected at low significance level (Fig. 5.11, right panel). Remarkably, this emission is spatially coincident with the one detected at higher frequency supporting the idea of a low surface brightness emission associated to the perturbed ICM.

The tentative combination of the two datasets suggests that the diffuse emission in Z2120 has a spectral index $\alpha \approx -1.2$. We scheduled Z2120 among the LOFAR SKP Tier 1 observations in cycle 9 to investigate the nature of this diffuse emission at low frequency.

5.2.2 Candidate radio halo in A3041

Abell 3041 (alternative names: RXC J0241.3-2839, PSZ1 G222.97-65.69) is a galaxy cluster at redshift $z = 0.23$. Its mass is $M_{500} = 6.12 \times 10^{14} M_{\odot}$ (Planck Collaboration

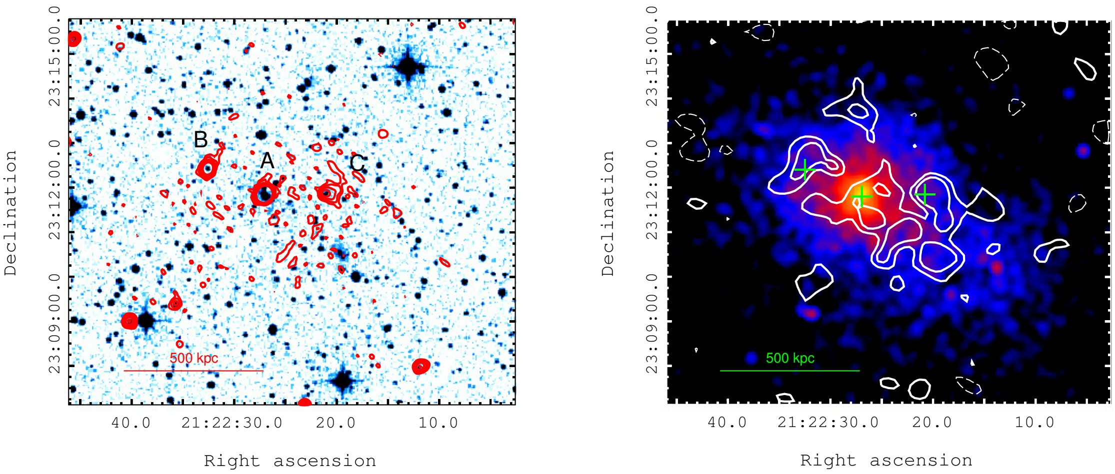

Figure 5.11: *Left*: DSS optical image if Z2120 with GMRT “full resolution” contours overlaid. Contours start at 0.1 mJy/beam and are spaced by a factor 2. The first negative contour is dashed. *Right*: Z2120 GMRT 330 MHz low resolution ($32.7'' \times 28''$) contours after the subtraction of compact sources superimposed on the *Chandra* X-ray image. Contours are (2,3,6...)$\times\sigma$, with $\sigma = 0.3$ mJy/beam. The position of the discrete sources is marked with a green cross.

et al. 2014a) and its X-ray luminosity in the [0.1-2.4] keV band is $L_{500} \simeq 3.4 \times 10^{44}$ erg/s. An X-ray *Chandra* observation of A3041 is available in the archive. Although it is very shallow (exposure time = 9 ks), we processed it and we used it to derive the morphological parameters, which place A3041 in the merging region of the morphological diagrams (Section 7.1). In Fig. 5.12 (left panel) we show a deeper *XMM-Newton* observation which better highlights the disturbed morphology of the cluster.

The cluster hosts two central radio sources, which are blended at the resolution of our C array observation ($\sim 10''$). Both have optical counterparts in the DSS optical image (Fig. 5.12, right panel). There is no available redshift for the brightest one ($\sim$ 94 mJy), while the fainter one ($\sim$ 11.2 mJy) is associated with a member galaxy (Colless et al. 2003). On the Eastern side of the cluster there is a FRII radio galaxy extending over $\sim$ 5.8 arcmin. The nucleus is located $\sim$ 5.5 arcmin from the center of A3041, and no spectroscopic redshift is available for this source. The core is detected in the 2 MASS catalogue (Skrutskie et al. 2006), with a K magnitude of 15.62. Using the $K - z$ relation by Willott et al. (2003) we estimated that the redshift of the FRII galaxy is $z = 0.42 \pm 0.16$, suggesting that it may be a background radio galaxy.

We subtracted all the discrete sources from the dataset, except for the FRII galaxy. We paid special attention to the subtraction of the two central sources. In particular, we did not adopt the usual approach of subtracting the model component derived from the high resolution image produced cutting the shortest baselines (Section 4.1), but we subtracted a model made using the whole *uv*-range. In this way, we made sure that, if there is some faint extended radio emission associated with the central sources, it is subtracted from the data that we then use to produce the low-resolution image. Also, we double checked that all the flux density of these two sources was actually included in the model components. The contours of the low-resolution image, made after an accurate source subtraction, are shown in Fig. 5.12 (left panel). A residual emission of $\sim$4.1 mJy is present in correspondence of the cluster' s X-ray peak, mostly detected at the 2σ level only. The spatial coincidence between the thermal and non-thermal emission indicates that these residuals may belong to a cluster radio diffuse source. However, the detection is marginal and we should note that even a small calibration error around the bright central source might have left some residuals showing up in the low-resolution image. We thus consider A3041 as a case of "suspect" diffuse emission. We asked and obtained uGMRT observations in the band 250-500 MHz to investigate the nature of this emission.

5.2.3 Candidate mini halo in A402

Abell 402 (alternative names: MACS J0257.6-2209, PSZ1 G210.08-60.96) is a massive ($M_{500} = 7.21 \times 10^{14} M_{\odot}$, Planck Collaboration et al. 2014a) cluster of galaxies

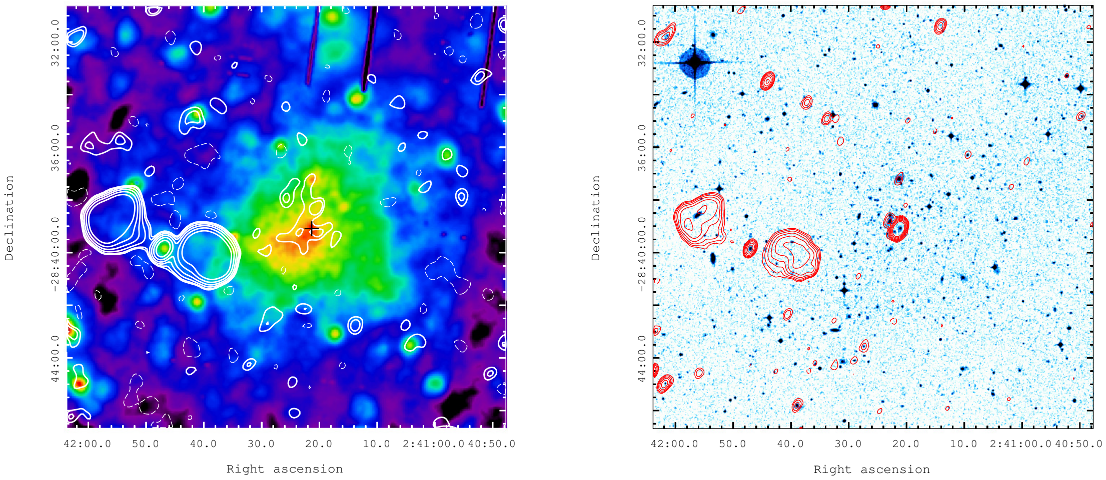

Figure 5.12: *Left*: X.ray *XMM-Newton* image of A3041 (Credits: A. Botteon) with low-resolution ($35.8'' \times 25.5''$) JVLA C array contours overlaid. Contours are $(\pm 2, 3, 6...) \times \sigma_{rms}$ with $\sigma_{rms} = 80\mu$/Jy/beam. The discrete sources in the field are subtracted, except for the region of the FRII radio galaxy. The black cross marks the position of the central brightest radio source. *Right*: "Full-resolution" JVLA C array contours (red) of A3041 superimposed on the DSS optical image. Contours start at 0.1 mJy/beam and are spaced by a factor 2. The first negative contour is dashed.

at $z = 0.32$. Its temperature within R_{2500} measured on the [0.7–7] keV band excluding the central 70 kpc region is $8.0^{+1.1}_{-0.9}$ keV (Cavagnolo et al. 2008; Giacintucci et al. 2017). Although the X-ray morphology of the cluster is fairly regular and peaked at the center, the central entropy of A402 is relatively high ($K_0 = 156 \pm 25$ keV/cm^2, Cavagnolo et al. 2009; Giacintucci et al. 2017) suggesting that some sort of dynamical activity may be taking place in this cluster, probably along the line of sight.

There are two archival GMRT 330 MHz observations available for this cluster (Obs No: 6153, P.I.: G. Macario and Obs No: 6837, P.I.:A. Bonafede). Both have been processed with the SPAM pipeline (Section 4.2.1) and both show evidence of diffuse emission at the cluster' s center. Unfortunately they have been processed with two different versions of SPAM and this challenged the combination of the *uv*-datasets. From the combination of the two images, Giacintucci et al. (2017) classified the diffuse emission in A402 as a candidate radio halo. The images of A402 are shown in Fig. 5.13. On the left panel we show the GMRT 330 MHz "full resolution" contours from Obs No 6153 (Venturi et al. in prep.). There are several diffuse sources in the cluster' s field. The most interesting one, for our purposes, is the central one, which seems to be confined in the core of the cluster, as it is typical for radio mini halos (Mazzotta & Giacintucci 2008; Giacintucci et al. 2014b). The flux density of this source, measured inside the 3σ contours shown in Fig. 5.13 (left panel) is ~12 mJy and its LAS in the East-West direction is $\sim 80''$ corresponding

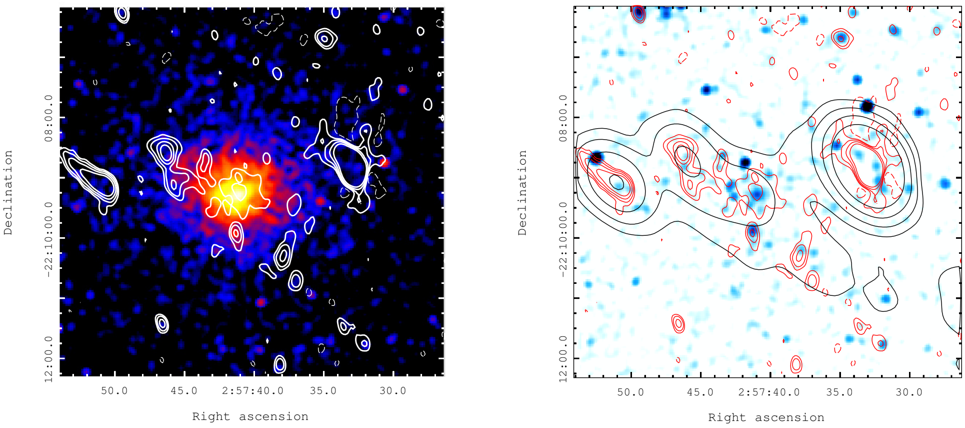

Figure 5.13: *Left*: A402 GMRT 330 MHz contours (Obs No: 6153, Venturi et al. in prep.) superimposed on the X-ray *Chandra* image of the cluster. Contours start at 0.35 mJy/beam and are spaced by a factor 2. The first negative contour is dashed. The beam is $13.4'' \times 8.6''$ and the rms noise of the radio image is ~ 0.1 mJy/beam. *Right*: DSS optical image of the field of A402 with the same contours of te left panel (red) plus the low resolution GMRT 330 MHz contours (Obs No: 6837, credits: A. Bonafede). Contours start at 3 mJy/beam and are spaced by a factor 2. The rms noise of the image is ~ 1 mJy/beam with beam=$57'' \times 42''$.

to ~ 370 kpc.

On the right panel of Fig. 5.13 we also show the low resolution contours of the same portion of the sky derived from Obs No 6837 (credits: A. Bonafede), where some diffuse emission seems to be present on a larger scale. However, the image has a fairly low sensitivity (rms noise ~ 1 mJy/beam with beam=$57'' \times 42''$) and it is not clear how much the discrete sources in the cluster' s field (which have not been subtracted) contribute to the extended emission.

The diffuse radio source at the center of A402 deserves further investigation: higher resolution images would be useful to evaluate the contribution of compact sources and more sensitive low resolution images are needed in order to establish the extension and the nature of the diffuse emission.

5.3 Non detections and upper limits

Most of the clusters analysed in this work do not host diffuse radio emission. Specifically, we did not detect cluster scale radio emission in the 17 clusters listed in Table 5.2. The images of these clusters are shown in Fig. 5.14 to 5.30. Following the procedure described in Section 4.3, we used the injection method to infer an upper limit to the diffuse flux density of these clusters. Placing upper limits on the non-detections is fundamental to analyse the populations of galaxy clusters, including their distribution in the radio power-mass diagram. Historically, those studies were performed at 1.4 GHz because the bulk of the radio information in the literature was based on VLA L-band observations. In order to promptly compare our results with previous studies, we derived the upper limits at 1.4 GHz for clusters with available JVLA L band observations and we scaled the upper limit to 1.4 GHz, assuming a spectral index $\alpha = -1.3$, for clusters with GMRT 330 or 610 MHz data (Table 5.2) only.

In general, the possibility to place deep upper limits is related to the quality of the images in terms of sensitivity, density of the inner *uv*- coverage and presence of bright sources with residual calibration errors. In line with the results from Venturi et al. (2008), we found that the presence of radio halos with flux densities $\gtrsim 10$ mJy can be safely established with GMRT 610 MHz observations, while fake radio halos of 5-10 mJy appear in the images as positive residuals that would lead to the suspect of diffuse emission and can be thus considered as upper limits. The values of the upper limits obtained with the JVLA range from 2 to 5 mJy, depending on the quality of the observations and on the presence of bright sources in the field, as stated earlier. We put one of the deepest limit with the D array observation of RXC J0616.3-2156 (2 mJy), indeed the D configuration of the JVLA ensures a dense *uv*-coverage at the short baselines with respect to the C configuration and thus a better sensitivity to the extended emission.

We note the presence of some residual emission in the low-resolution source-subtracted image of A2813 (Fig. 5.15, right panel), but we believe that it is at least partly due to the subtraction of the central bright source ($S_{1.5GHz} \sim 100$ mJy). The upper limit of 5 mJy derived for A2813 (Tab. 5.2), is about two times the residual diffuse flux detected at the cluster center.

Unfortunately, we were not able to derive reliable upper limits for 4 clusters: Zwcl1028.8+1419, RXC J1322.8+3138, RXC J0510.7-0801 and A1437. The GMRT 610 MHz and 240 MHz images of RXC J0510.7-0801 are affected by the presence of a strong radio source in the field, whose sidelobes cross the cluster field even after several runs of self-calibration and peeling (Kale et al. 2015). In Fig. 5.28 we show the GMRT 610 (left panel) and 240 MHz (right panel). In the latter, patches of diffuse emission are present on the cluster area, however, it is likely that they are related to the sidelobes of the bright source in the North (not visible in the figure). The field of RXC J1322.8+3138 is dominated by an FRII radio galaxy extending over $\sim 11.5'$ close to the cluster region. This source limited the possibility of producing sensitive low-resolution images. A lot of editing was needed for the datasets of A1437 and Zwcl1028.8+1419, especially at the short baselines; this, combined with the relatively high noise level of the images, did not allow a useful upper limit to be derived.

In terms of radio power at 1.4 GHz, the majority of the upper limits is below 10^{24} W/Hz (Table 5.2), in line with earlier results. These values are significantly smaller that the typical radio power of radio halos in clusters with masses similar to

Table 5.2

cluster name	z	M_{500}	rms	beam	UL*	$P_{1.4GHz}$**
		$(10^{14} M_\odot)$	(mJy/beam)	$('' \times '')$	(mJy)	(10^{23} W/Hz)
A56$^{(C)}$	0.30	6.20	0.09	19.8×19.2	4	12
A2813$^{(C)}$	0.29	9.16	0.055	20.5×18.1	5	14
A2895$^{(C)}$	0.23	6.15	0.055	22.4×17.9	3	5
A220$^{(C)}$	0.33	6.74	0.065	27.6×26.3	2.5	9.7
A384$^{(C)}$	0.24	6.38	0.045	28.3×26.0	3	5.5
A2472$^{(C)}$	0.31	6.15	0.06	18.1×17.4	3	10
A2355$^{(C)}$	0.23	6.92	0.08	28.2×24.2	5	8.3
RXC J2051.1+0216$^{(C)}$	0.32	6.13	0.04	19.8×18.3	2	7.3
RXC J0616.3-2156$^{(D)}$	0.171	5.93	0.08	78.3×52.8	2	1.7
Zwcl1028.8+1419	0.31	6.11	0.25	18.6×16.0	–	–
RXC J1322.8+3138	0.31	6.63	0.35	19.2×17.8	–	–
A1733	0.26	7.05	0.34	34.7×27.0	7	5.3
PSZ1 G019.12+3123	0.28	7.08	0.08	21.5×18.0	7	6.3
MACS J2135-010	0.33	7.57	0.2	21.6×17.2	10	11.7
RXC J0510.7-0801$^{(a)}$	0.22	7.36	0.2	5.4×4.8	–	–
A1437	0.134	5.69	0.27	19.4×16.5	–	–
A2104	0.153	5.91	0.25	20.6×19.6	25	2.4

Notes: *Top panel*: Upper Limits (UL) derived with JVLA L-band (C) C array or (D) D array observations. *Middle panel*: UL derived with GMRT 610 MHz observations. *Bottom panel*: UL derived with GMRT 330 MHz observations. *Flux density of the UL measured at the observing frequency. **Radio power of the UL scaled at 1.4 GHz assuming a spectral index $\alpha = -1.3$. (a) Kale et al. (2015).

the range of masses in our sample. On the other hand, for the most distant clusters in our sample, at $z > 0.3$, the flux limits translate into limits to the luminosities that become significantly larger and not far from the luminosities expected for radio halos. This simply means that, in order to infer useful limits to the presence of radio halos at $z > 0.3$, higher sensitivity data or observations with more sensitive facilities are necessary (see also Section 7.3.2).

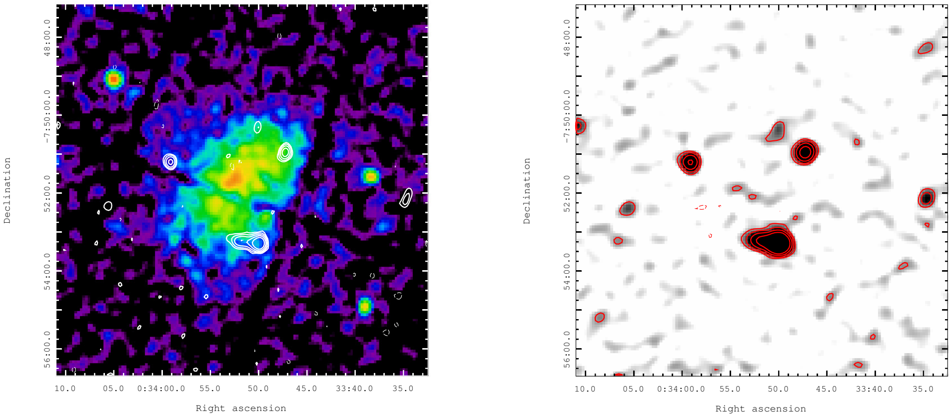

Figure 5.14: *Left*: JVLA C array "full resolution" contours superimposed on the X-ray *XMM-Newton* image of A56. Contours start at 0.25 mJy/beam and are spaced by a factor 2. The 1σ level rms noise of the radio image is 80 μJy/beam and the beam is $13.8'' \times 10.4''$. *Right*: JVLA C array low-resolution image and contours. Contours start at 0.3 mJy/beam and are spaced by a factor 2. The 1σ level rms noise of the image is 90 μJy/beam and the beam is $19.8'' \times 19.4''$.

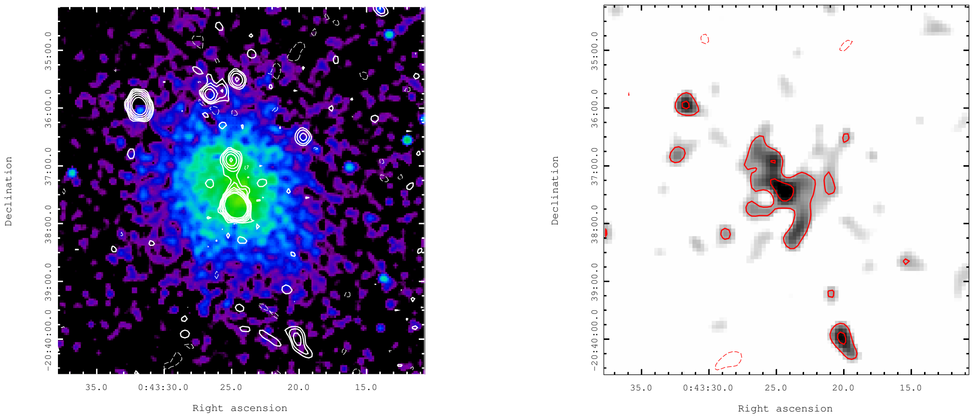

Figure 5.15: *Left*: JVLA C array "full resolution" contours superimposed on the X-ray *Chandra* image of A2813. Contours start at 0.1 mJy/beam and are spaced by a factor 2. The 1σ level rms noise of the radio image is 35 μJy/beam and the beam is $11.4'' \times 9.5''$. *Right*: JVLA C array low-resolution source-subtracted image and contours. Contours start at 0.18 mJy/beam and are spaced by a factor 2. The 1σ level rms noise of the image is 55 μJy/beam and the beam is $20.5'' \times 18.1''$.

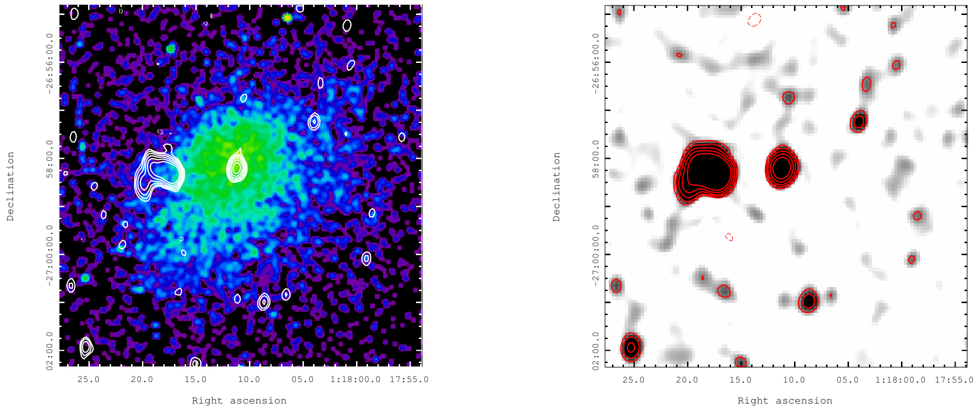

Figure 5.16: *Left*: JVLA C array "full resolution" contours superimposed on the X-ray *Chandra* image of A2895. Contours start at 0.12 mJy/beam and are spaced by a factor 2. The 1σ level rms noise of the radio image is 40 μJy/beam and the beam is $14.6'' \times 9.0''$. *Right*: JVLA C array low-resolution image and contours. Contours start at 0.18 mJy/beam and are spaced by a factor 2. The 1σ level rms noise of the image is 55 μJy/beam and the beam is $22.4'' \times 17.9''$.

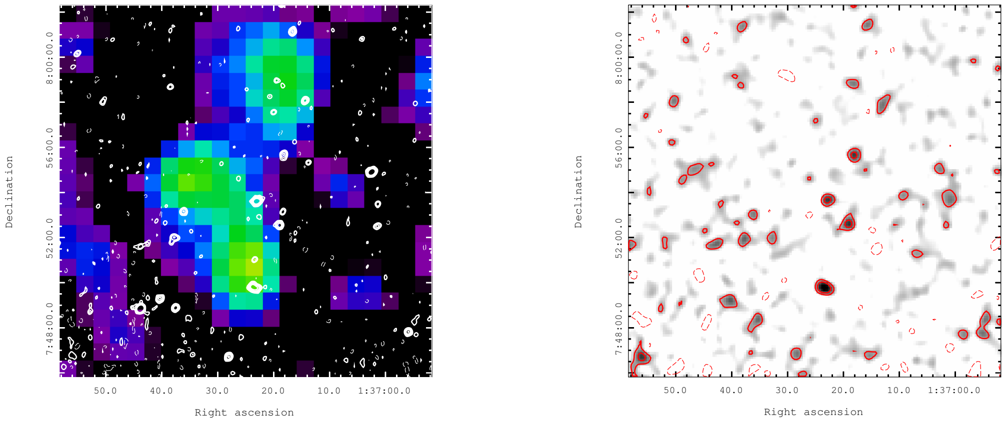

Figure 5.17: *Left*: JVLA C array "full resolution" contours superimposed on the X-ray RASS image of A220. Contours start at 0.13 mJy/beam and are spaced by a factor 2. The 1σ level rms noise of the radio image is 45 μJy/beam and the beam is $11.6'' \times 9.8''$. *Right*: JVLA C array low-resolution image and contours. Contours start at 0.2 mJy/beam and are spaced by a factor 2. The 1σ level rms noise of the image is 65 μJy/beam and the beam is $27.6'' \times 26.3''$.

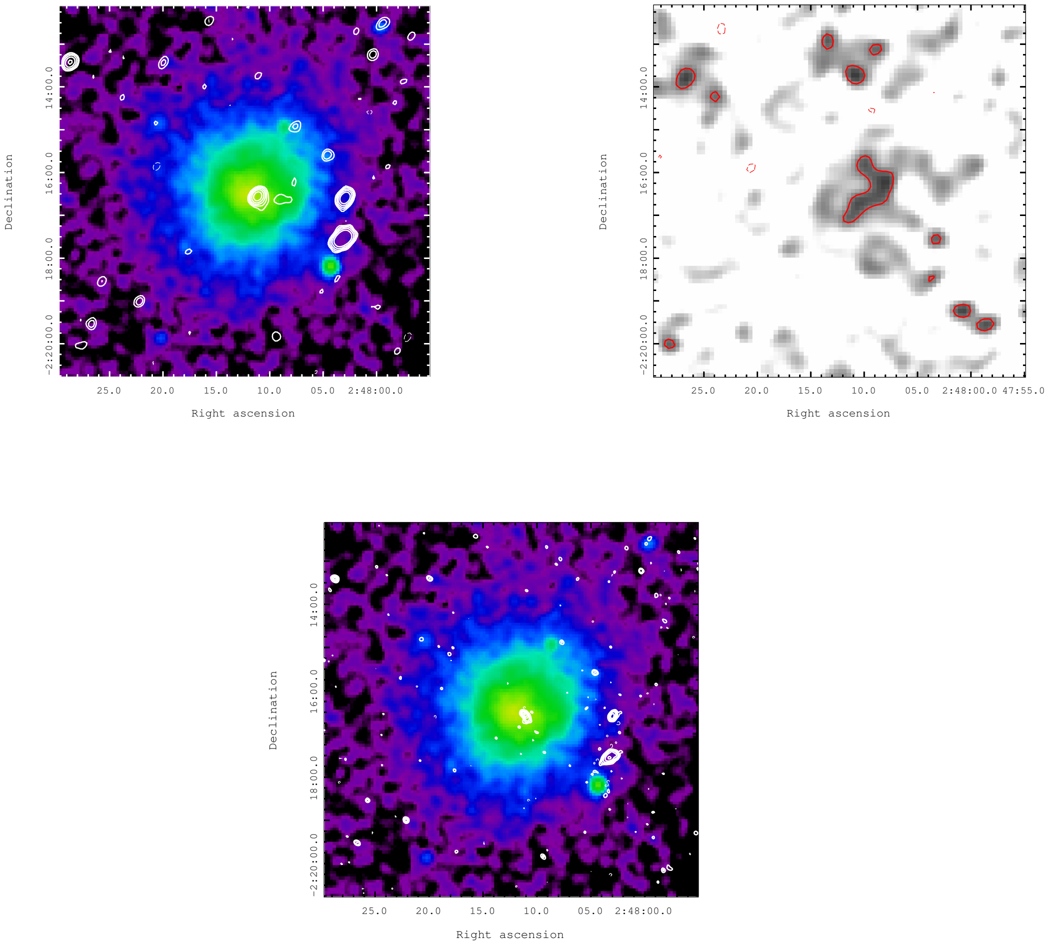

Figure 5.18: *Top left*: JVLA C array “full resolution” contours superimposed on the X-ray *XMM-Newton* image of A384. Contours start at 0.1 mJy/beam and are spaced by a factor 2. The 1σ level rms noise of the radio image is 35 μJy/beam and the beam is $13.5'' \times 10.4''$. *Top right*: JVLA C array low-resolution source-subtracted image and contours. Contours start at 0.14 mJy/beam and are spaced by a factor 2. The 1σ level rms noise of the image is 45 μJy/beam and the beam is $28.3'' \times 26.0''$. *Bottom*: GMRT 610 MHz contours overlaid on the X-ray *XMM-Newton* image. Contours start at 0.15 mJy/beam and are spaced by a factor 2. The 1σ level rms noise of the radio image is 50 μJy/beam and the beam is $5.9'' \times 4.8''$. The first negative contour is dashed.

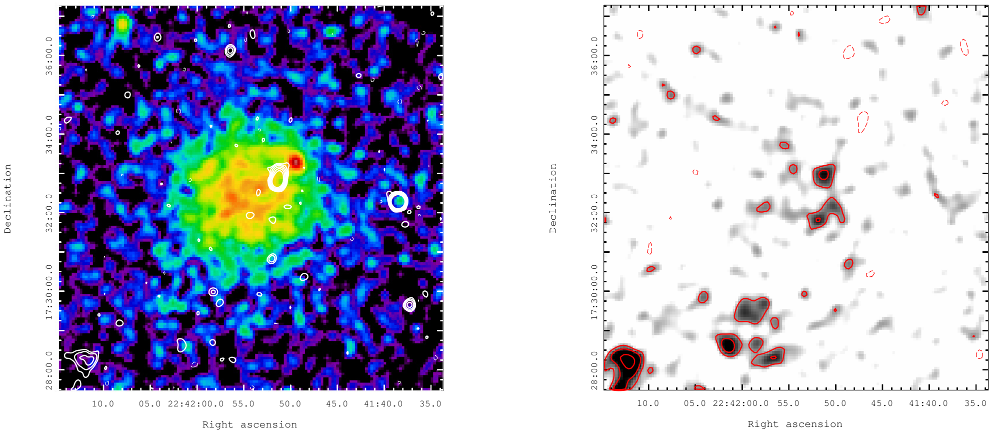

Figure 5.19: *Left*: JVLA C array “full resolution” contours superimposed on the X-ray *XMM-Newton* image of A2472. Contours start at 0.12 mJy/beam and are spaced by a factor 2. The 1σ level rms noise of the radio image is 40 μJy/beam and the beam is $10.5'' \times 10.1''$. *Right*: JVLA C array low-resolution source-subtracted image and contours. Contours start at 0.18 mJy/beam and are spaced by a factor 2. The 1σ level rms noise of the image is 60 μJy/beam and the beam is $18.1'' \times 17.4''$.

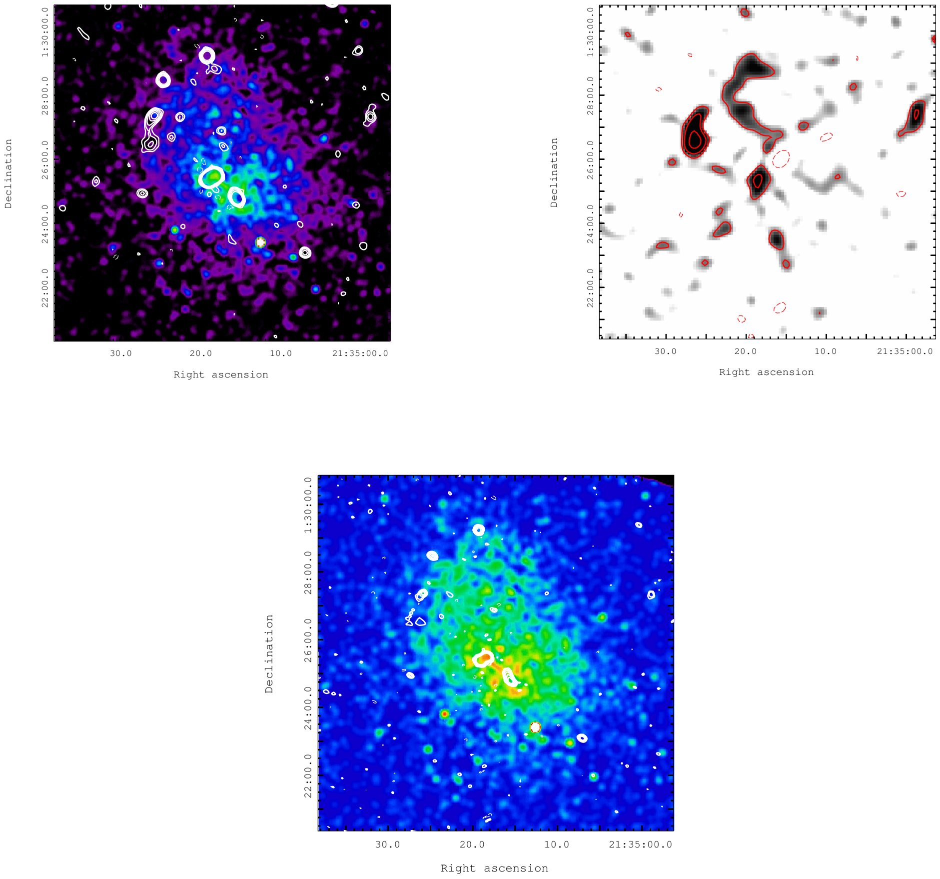

Figure 5.20: *Top left*: JVLA C array "full resolution" contours superimposed on the X-ray *Chandra* image of A2355. Contours start at 0.12 mJy/beam and are spaced by a factor 2. The first negative contour is dashed. The 1σ level rms noise of the radio image is 40 μJy/beam and the beam is $11.6'' \times 10.8''$. *Top right*: JVLA C array low-resolution source-subtracted image and contours. Contours start at 0.24 mJy/beam and are spaced by a factor 2. The first negative contour is dashed. The 1σ level rms noise of the image is 80 μJy/beam and the beam is $28.2'' \times 24.2''$. *Bottom*: GMRT 610 MHz contours overlaid on the X-ray *Chandra* image. Contours start at 0.4 mJy/beam and are spaced by a factor 2. The 1σ level rms noise of the radio image is 0.13 mJy/beam and the beam is $8.3'' \times 6.1''$. The first negative contour is dashed.

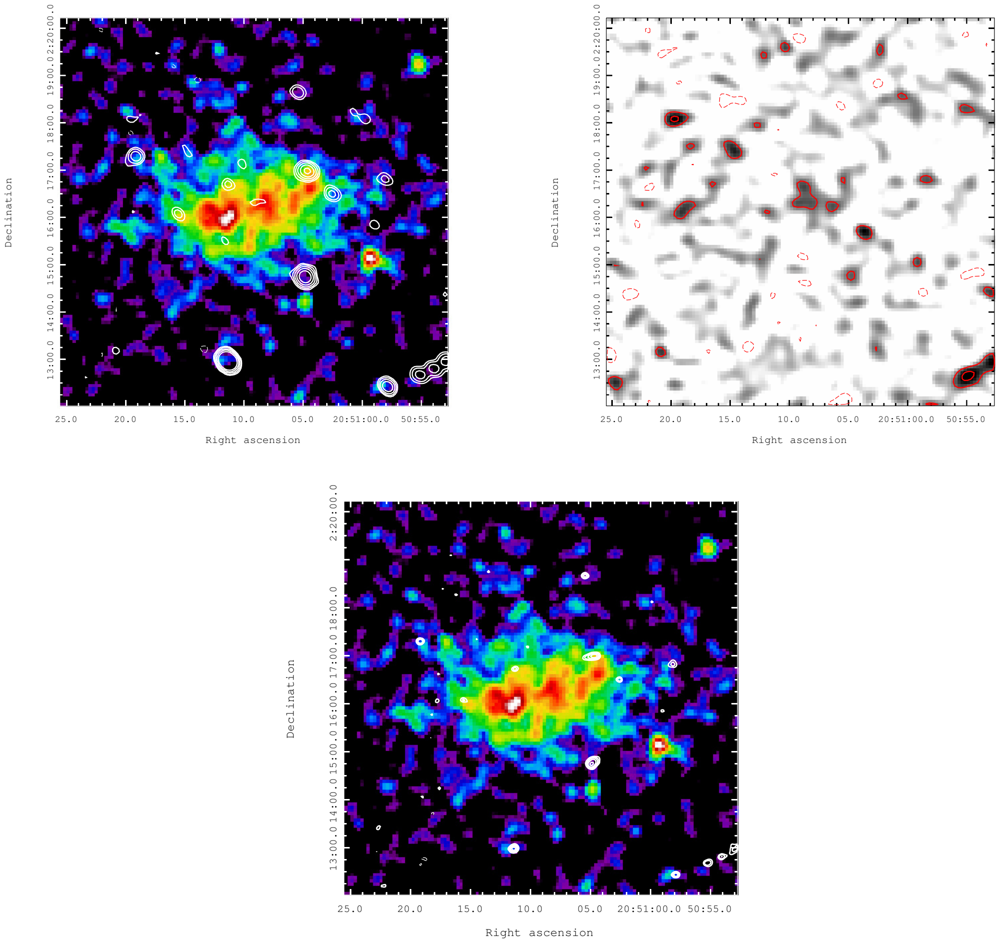

Figure 5.21: *Top left*: JVLA C array "full resolution" contours superimposed on the X-ray *XMM-Newton* image of RXC J2051.1+0216. Contours start at 0.15 mJy/beam and are spaced by a factor 2. The first negative contour is dashed. The 1σ level rms noise of the radio image is 50 μJy/beam and the beam is $14.1'' \times 11.5''$. *Top right*: JVLA C array low-resolution source-subtracted image and contours. Contours start at 0.12 mJy/beam and are spaced by a factor 2. The first negative contour is dashed. The 1σ level rms noise of the image is 40 μJy/beam and the beam is $19.8'' \times 18.3''$. *Bottom*: GMRT 610 MHz contours overlaid on the X-ray *XMM-Newton* image. Contours start at 0.3 mJy/beam and are spaced by a factor 2. The 1σ level rms noise of the radio image is 0.1 mJy/beam and the beam is $6.0'' \times 4.8''$. The first negative contour is dashed.

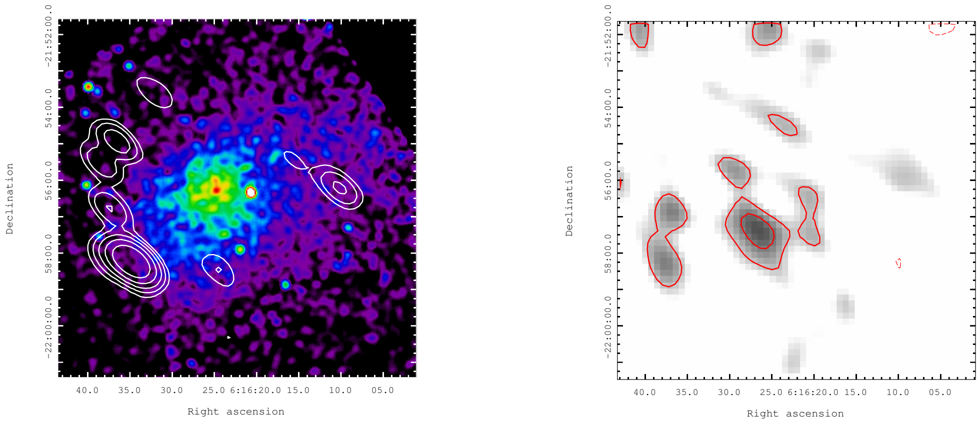

Figure 5.22: *Left*: JVLA D array "full resolution" contours superimposed on the X-ray *Chandra* image of RXC J0616.3-2156. Contours start at 0.24 mJy/beam and are spaced by a factor 2. The first negative contour is dashed. The 1σ level rms noise of the radio image is 77 μJy/beam and the beam is $55.4'' \times 19.9''$. *Right*: JVLA D array low-resolution source-subtracted image and contours. Contours start at 0.24 mJy/beam and are spaced by a factor 2. The first negative contour is dashed. The 1σ level rms noise of the image is 80 μJy/beam and the beam is $78.3'' \times 52.8''$.

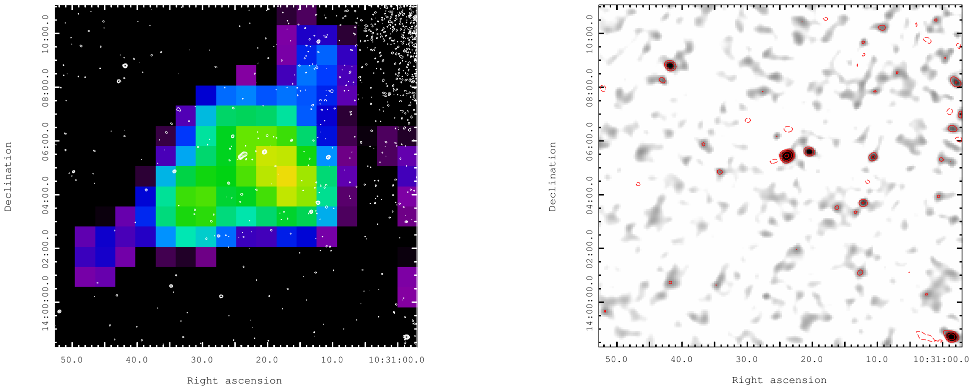

Figure 5.23: *Left*: GMRT 610 MHz "full resolution" contours superimposed on the X-ray RASS image of Zwcl1028.8+1419. Contours start at 0.18 mJy/beam and are spaced by a factor 2. The first negative contour is dashed. The 1σ level rms noise of the radio image is 56 μJy/beam and the beam is $5.3'' \times 4.8''$. *Right*: GMRT 610 MHz low-resolution image and contours. Contours start at 0.75 mJy/beam and are spaced by a factor 2. The first negative contour is dashed. The 1σ level rms noise of the image is 0.25 mJy/beam and the beam is $18.6'' \times 16.0''$.

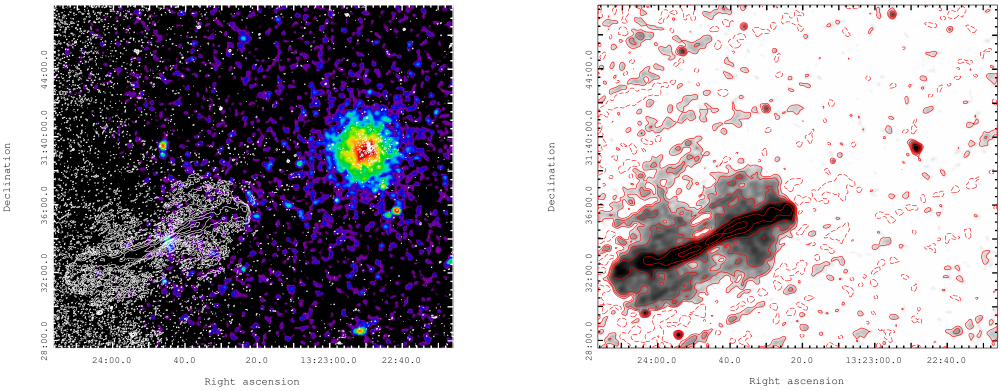

Figure 5.24: *Left*: GMRT 610 MHz "full resolution" contours superimposed on the X-ray *XMM-Newton* image of RXC J1322.8+3138. Contours start at 0.18 mJy/beam and are spaced by a factor 2. The first negative contour is dashed. The 1σ level rms noise of the radio image is 60 μJy/beam and the beam is 5.7″ × 4.4″. *Right*: GMRT 610 MHz low-resolution image and contours. Contours start at 1 mJy/beam and are spaced by a factor 2. The first negative contour is dashed. The 1σ level rms noise of the image is 0.35 mJy/beam and the beam is 19.2″ × 17.8″.

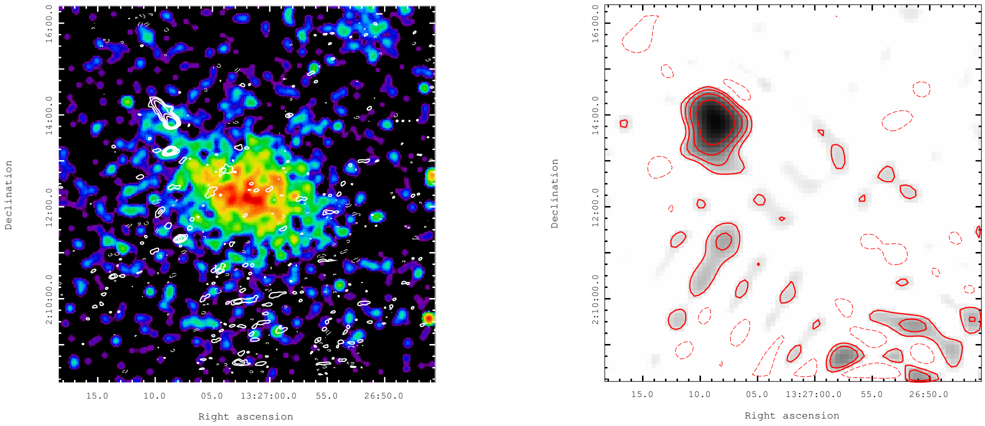

Figure 5.25: *Left*: GMRT 610 MHz "full resolution" contours superimposed on the X-ray *Chandra* image of A1733. Contours start at 0.18 mJy/beam and are spaced by a factor 2. The first negative contour is dashed. The 1σ level rms noise of the radio image is 60 μJy/beam and the beam is 5.0″ × 7.9″. *Right*: GMRT 610 MHz low-resolution image and contours. Contours start at 1 mJy/beam and are spaced by a factor 2. The first negative contour is dashed. The 1σ level rms noise of the image is 0.34 mJy/beam and the beam is 34.7″ × 27.0″.

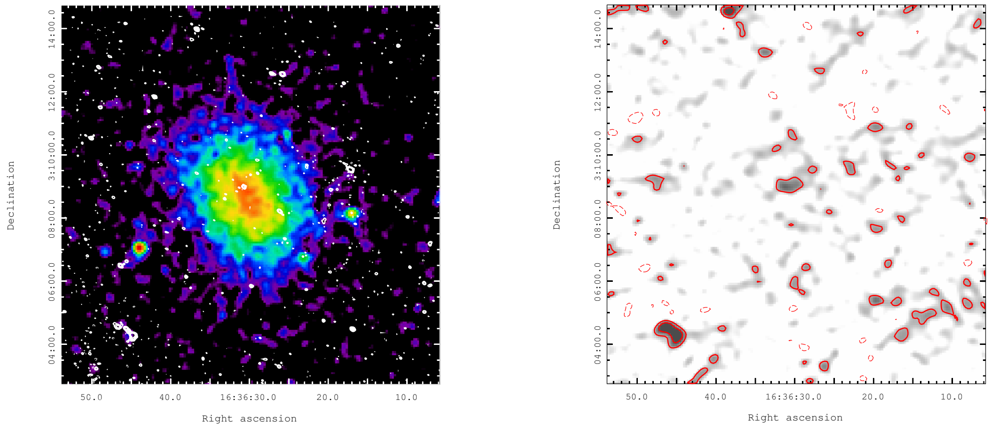

Figure 5.26: *Left*: GMRT 610 MHz "full resolution" contours superimposed on the X-ray *XMM-Newton* image of PSZ1 G019.12+3123. Contours start at 0.1 mJy/beam and are spaced by a factor 2. The first negative contour is dashed. The 1σ level rms noise of the radio image is 35 μJy/beam and the beam is $5.0'' \times 3.8''$. *Right*: GMRT 610 MHz source-subtracted low-resolution image and contours. Contours start at 0.24 mJy/beam and are spaced by a factor 2. The first negative contour is dashed. The 1σ level rms noise of the image is 80 μJy/beam and the beam is $34.7'' \times 27.0''$.

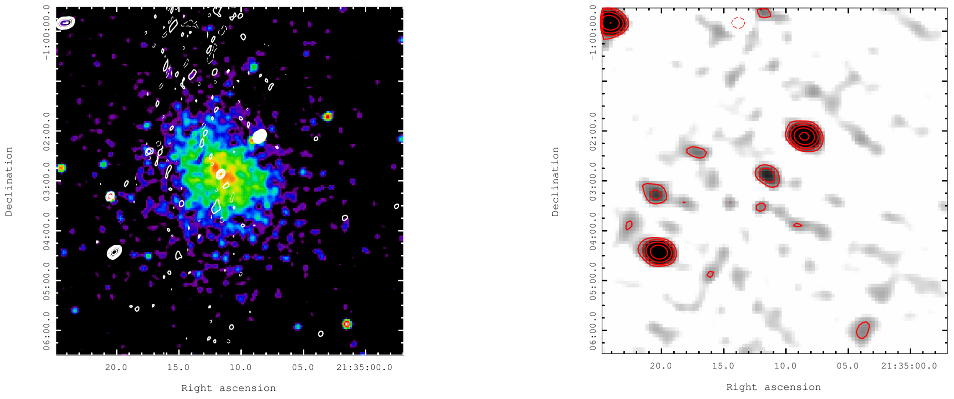

Figure 5.27: *Left*: GMRT 610 MHz "full resolution" contours superimposed on the X-ray *Chandra* image of MACS J2135-010. Contours start at 0.3 mJy/beam and are spaced by a factor 2. The first negative contour is dashed. The 1σ level rms noise of the radio image is 80 μJy/beam and the beam is $7.8'' \times 5.8''$. *Right*: GMRT 610 MHz low-resolution image and contours. Contours start at 0.6 mJy/beam and are spaced by a factor 2. The first negative contour is dashed. The 1σ level rms noise of the image is 0.2 mJy/beam and the beam is $21.6'' \times 17.2''$.

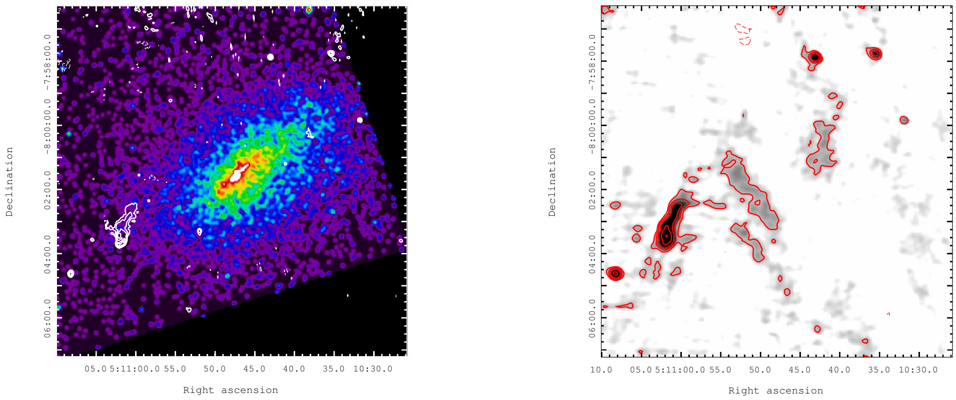

Figure 5.28: *Left*: GMRT 610 MHz "full resolution" contours superimposed on the X-ray *Chandra* image of RXC J0510.7-0801 . Contours start at 0.6 mJy/beam and are spaced by a factor 2. The first negative contour is dashed. The 1σ level rms noise of the radio image is 0.2 mJy/beam and the beam is 5.4″ × 4.8″. *Right*: GMRT 240 MHz image and contours. Contours start at 3.6 mJy/beam and are spaced by a factor 2. The first negative contour is dashed. The 1σ level rms noise of the image is 1.2 mJy/beam and the beam is 15.7″ × 13.1″.

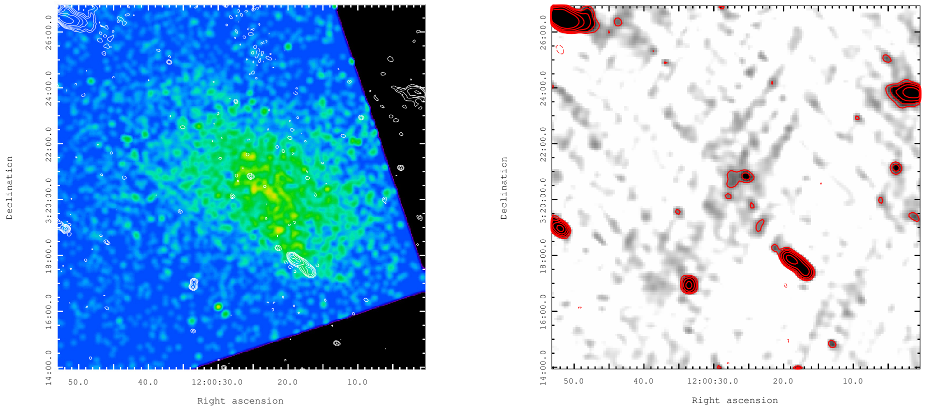

Figure 5.29: *Left*: GMRT 330 MHz "full resolution" contours superimposed on the X-ray *Chandra* image of A1437. Contours start at 0.4 mJy/beam and are spaced by a factor 2. The first negative contour is dashed. The 1σ level rms noise of the radio image is 0.13 mJy/beam and the beam is 9.0″ × 7.4″. *Right*: GMRT 330 MHz low-resolution image and contours. Contours start at 0.9 mJy/beam and are spaced by a factor 2. The first negative contour is dashed. The 1σ level rms noise of the image is 0.27 mJy/beam and the beam is 19.4″ × 16.5″.

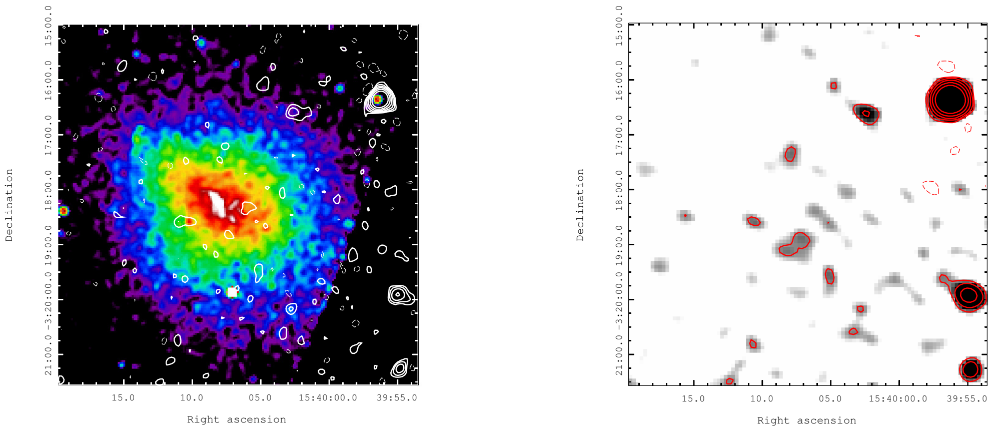

Figure 5.30: *Left*: GMRT 330 MHz "full resolution" contours superimposed on the X-ray *Chandra* image of A2104. Contours start at 0.4 mJy/beam and are spaced by a factor 2. The first negative contour is dashed. The 1σ level rms noise of the radio image is 0.13 mJy/beam and the beam is $13.3'' \times 10.4''$. *Right*: GMRT 330 MHz low-resolution image and contours. Contours start at 0.75 mJy/beam and are spaced by a factor 2. The first negative contour is dashed. The 1σ level rms noise of the image is 0.25 mJy/beam and the beam is $20.6'' \times 19.6''$.

Chapter 6

The intriguing radio emission of A1451 and Zwcl 0634.1+4750

A1451 and Zwcl 0634.1+4750 (Z0634, hereafter) are dynamically disturbed galaxy clusters at $z < 0.2$. According to the re-analysis of the NVSS datasets presented in Section 3.3, they both show hints of diffuse emission. In order to verify those marginal detections, we observed these two clusters with the GMRT at 330 MHz (project code 29_001, P.I. V. Cuciti) and with the JVLA in D array in L-band (project code 15B-035, P.I. V. Cuciti). In addition, they were observed with the JVLA in L-band in B array as part of a project mainly aimed at studying the magnetic fields in galaxy clusters through Faraday rotation measurements of polarised background sources (project code 15A-270, P.I. R. van Weeren). The radio data reduction was carried out with the procedures outlined in Chapter 4. Here we present the discovery of radio halos in both A1451 and Z0634. Moreover, we detected a candidate radio relic at large distance from the center of A1451 and an intriguing head tail (HT) radio galaxy probably interacting with a shock front in Z0634.

The results of this Chapter have been published in Cuciti et al. (2018).

6.1 Abell 1451

A1451 (alternative names: RXC J1203.2-2131, PSZ1 G288.26+39.94) is a massive ($M_{500} = 7.32 \times 10^{14} M_\odot$, Planck Collaboration et al. 2014a) and hot (13.4 keV, Valtchanov et al. 2002) galaxy cluster at redshift $z = 0.199$. The Meta-catalog of X-ray detected Clusters of Galaxies (MCXC) reports an X-ray luminosity in the $[0.1 - 2.4]$ keV band $L_{500} = 6.61 \times 10^{44} L_\odot$ (Piffaretti et al. 2011).

Although the X-ray emission of A1451 (Fig. 6.1 and Fig. 6.3) is fairly regular, several pieces of evidence support the idea of ongoing merging activity for this cluster. Indeed, the high temperature and velocity dispersion are significantly in excess with respect to the estimates derived from weak lensing data (Cypriano et al. 2004). Moreover, both the X-ray morphology and the mass distribution derived

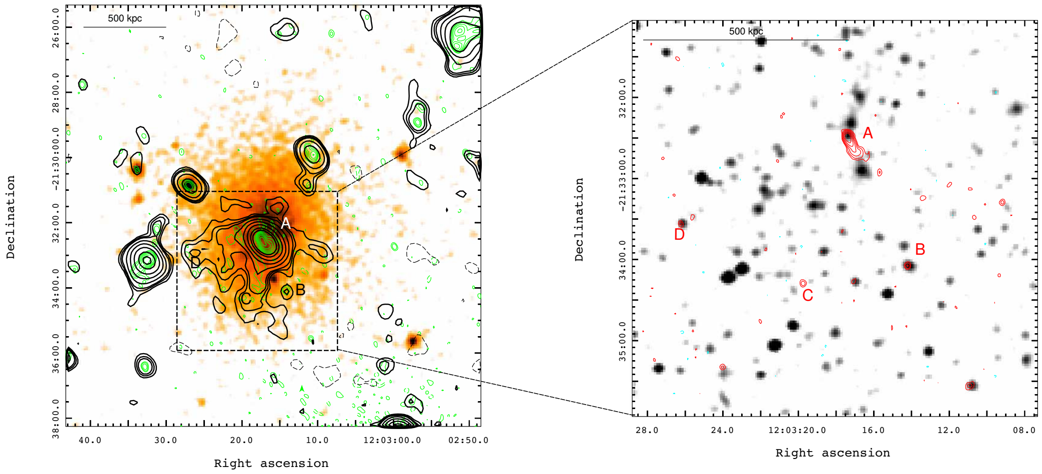

Figure 6.1: *Left*: A1451 GMRT 320 MHz full (green) and low (black) resolution contours superimposed on the X-ray *XMM-Newton* image. Low-resolution contour levels (black) are $(2, 3, 4, 8, 16, 32...) \times \sigma$ with rms noise $\sigma = 0.3$ mJy/beam and beam=$39.4'' \times 27.9''$. Full-resolution contours start at 0.3 mJy/beam and are spaced by a factor 2. The full-resolution beam is $11.6'' \times 8.1''$ The first negative contours are dashed. *Right*: JVLA B array contours (red) of the central part of the cluster superimposed on the optical DSS image. Sources are labelled A to D as in Fig. 6.3. Contours start at 0.08 mJy/ beam and are spaced by a factor 2. The beam is $4.7'' \times 3.3''$. The first negative contour is shown with a cyan dashed line.

using the distortions of the faint background galaxies (Cypriano et al. 2004) are elongated in the North-South direction. No radio diffuse emission has been detected in A1451 with ATCA 1.4 GHz observations (Valtchanov et al. 2002). On the other hand, after masking the point sources on the NVSS re-processed image, we found indication for excess of residual diffuse emission (see Section 3.3).

6.1.1 Radio halo

We analysed GMRT 330 MHz and JVLA 1.5 GHz observations of A1451. A number of discrete radio sources are visible on the cluster area in the GMRT 320 MHz full-resolution image (labelled A to D in Fig. 6.1). In particular, there is a radio galaxy at the centre of the cluster (source A), with a total flux density of ~ 80 mJy at 320 MHz and ~ 17 mJy at 1.5 GHz. The JVLA B array image (Fig. 6.1, right panel) shows that the brighter part of this source is followed by a short, low-surface-brightness tail that makes its subtraction from the *uv*-data difficult.

In addition to the individual sources, some positive residuals are visible in the full-resolution GMRT 320 MHz image (green contours in Fig. 6.1, left panel). The low-resolution image (black contours in Fig. 6.1, left panel) clearly shows the presence of extended emission, that we classify as a radio halo. The radio halo has a largest angular size (LAS) of ~ 4 arcmin in the N-S direction, corresponding to a projected largest linear size (LLS) of $\sim$750 kpc. It is mainly extended towards

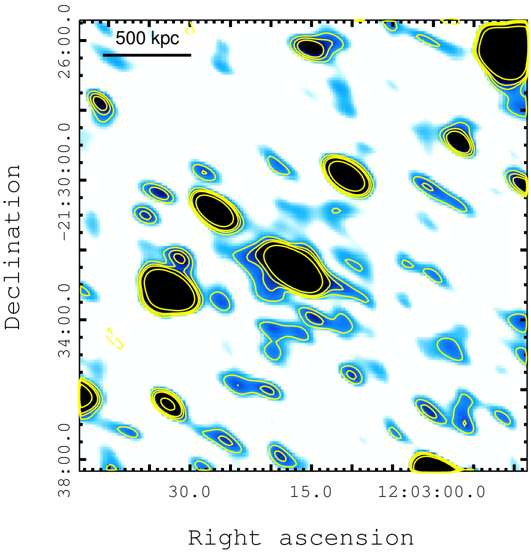

Figure 6.2: JVLA D array colour image and contours of A1451. The contour levels are $(2, 3, 4, 8, 16, 32...) \times \sigma_{rms}$ with rms noise σ_{rms} = 60μJy/beam and beam=44.4″ × 17.1″. The first negative contour is dashed.

the Southern part of the cluster. There are hints of diffuse emission also in the Northern part, both in the GMRT and JVLA images (Fig.6.2), but the surface brightness is below twice the rms noise level of the images. We measured the flux density of the radio halo on the low-resolution image (Fig. 6.1, left panel), then we subtracted the flux density of the central radio galaxy and of the three point-like sources. Specifically, we measured the flux density of the point-like sources on the full-resolution ($\sim 10''$) image, while we measured the flux density of source A on the low-resolution image, to take into account also its extended emission. We obtained a flux density for the radio halo of $S_{320MHz} \sim 22$ mJy. It is likely that, while subtracting source A, we are also subtracting part of the radio halo flux density. We measured the mean surface brightness of the central part of the radio halo (around source A) and we estimated that in the area of source A there are ~5 mJy of radio halo flux density, leading to a total flux density of the radio halo of $S_{320MHz} = 27.3 \pm 3.2$ mJy.

An equivalent procedure has been applied to measure the flux density of the radio halo at 1.5 GHz, that is, we measured the radio flux density on the whole region of the halo from the D array image (Fig. 6.2, resolution$\sim 40''$) and we subtracted the flux density of the central source, measured on the same map, and of the three point-like sources, taken from the B array image (resolution$\sim 4''$). The flux density of the radio halo is $S_{1.5GHz} = 5.0 \pm 0.5$ mJy, which corresponds to a radio power $P_{1.4GHz} = 6.4 \pm 0.7 \times 10^{23}$ W/Hz, assuming a spectral index $\alpha = -1.2$

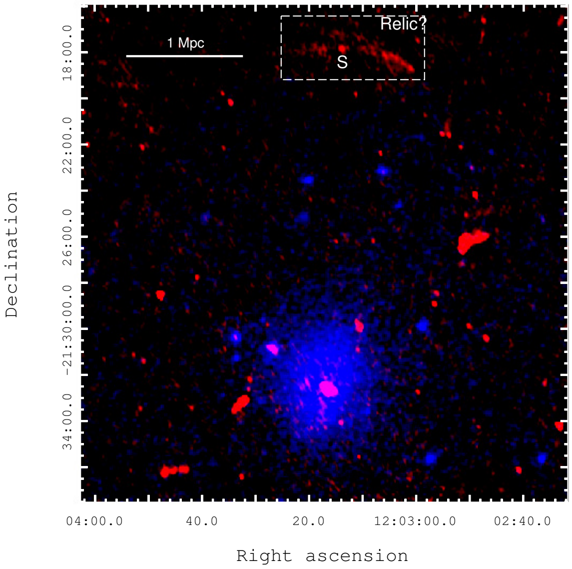

Figure 6.3: A1451 GMRT 320 MHz image (red) superimposed on the X-ray *XMM-Newton* image (blue).

for the *k-correction*. These values take into account the portion of the radio halo covered by source A.

To evaluate the spectrum of the halo between 320 and 1500 MHz (B+D array JVLA combined observations) we produced images with uniform weighting, using the common *uv*-range and tapering down to the same resolution ($\sim 20''$) and we measured the flux density of the radio halo on exactly the same region. We performed the imaging using two approaches: *i)* cleaning only inside the mask containing all the sources in the field until the residuals were approximately two times the rms noise of the image or *ii)* after that, cleaning also on the rest of the field down to two times the rms noise. Depending on how we cleaned the images and on the region where we measured the flux density of the radio halo we found values for the spectral index in the range $-1.3 \lesssim \alpha \lesssim -1.1$. In particular, we found the steepest spectral indices using approach *(ii)*. We note that a higher cleaning threshold does not yield different results; indeed, if we clean until the residuals are approximately three times the rms noise of the images, we obtain no significant difference in the flux density of the radio halo at both frequencies and using both approaches *(i)* and *(ii)*.

6.1.2 A distant relic?

In the field of A1451, we detected an elongated diffuse source located ~ 15 arcmin North of the galaxy cluster centre (Fig. 6.3), both at 320 MHz and in the JVLA D

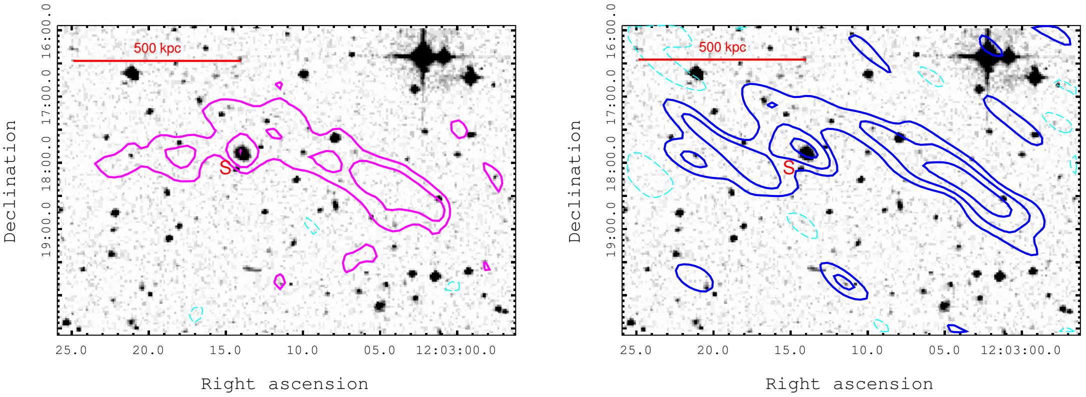

Figure 6.4: GMRT 320 MHz (*left*) and JVLA D array 1.5 GHz (*right*) contours of the relic in A1451 superimposed on the optical DSS image. *Left*: radio contours starts at 0.6 mJy/beam and are spaced by a factor 2. The first negative contour is shown with a cyan dashed line. The rms noise of the radio image is ∼ 0.2 mJy/beam with a beam of $23.3'' \times 18.0''$. *Right*: radio contours starts at 0.18 mJy/beam and are spaced by a factor 2. The first negative contour is shown with a cyan dashed line. The rms noise of the radio image is ∼ 60μJy/beam with a beam of $44.4'' \times 17.1''$.

array 1.5 GHz image (Fig. 6.4). A zoom on this source, superimposed on the optical Digitized Sky Survey (DSS) image, is shown in Fig. 6.4. If assumed to be at the redshift of the cluster, this source is ∼ 3 Mpc away from the cluster centre. Its LAS in the E-W direction is ∼ 6.5 arcmin, which would correspond to a LLS∼ 1.3 Mpc. A point-like radio source with a clear optical counterpart (labelled S in Fig. 6.4) is embedded in the diffuse emission. With the same procedure used for the radio halo, we measured the flux density of the point-like source from high-resolution images and we subtracted it from the flux density measured on the diffuse source area, obtaining a flux density of 35.5 ± 5.3 mJy at 320 MHz and 9.0 ± 0.5 mJy at 1.5 GHz.

To evaluate the spectral index of this extended source between 320 MHz and 1.5 GHz (D array observation), we used uniform weighting, the common *uv*-range and we convolved the images to the same resolution (50″). The integrated spectral index of this source is $\alpha = -1.1 \pm 0.1$. The resolution of these observations does not allow a reliable analysis of a possible spectral index gradient along the N-S axis. Conversely, the data allow us to conclude that there is no evidence of a spectral index gradient along the E-W axis, as expected in the case of an active source in S refurbishing the extended emission. The radio power of the diffuse emission at 1.4 GHz is $P_{1.4GHz} = 1.13 \pm 0.06 \times 10^{24}$ W/Hz, assuming a spectral index $\alpha = -1.1$ for the *k-correction*.

The elongated and arc-like morphology of the source detected North of A1451 (Fig. 6.4), together with its spectral index and location suggest that it could be a radio relic. This source would follow the radio-luminosity–mass correlation found by de Gasperin et al. (2014) for radio relics. However, if it is at the cluster redshift, its projected distance from the cluster centre is $\sim$ 3 Mpc, which would make it the most distant relic from the cluster centre ever detected (Vazza et al. 2012; de Gasperin et al. 2014). The virial radius of A1451 is $R_v \sim 2.5$ Mpc [1], moreover weak lensing studies show that its mass distribution is elongated in the N-S direction (see Fig. 3 in Cypriano et al. 2004), thus supporting the idea that we would be observing a radio relic located in the cluster's most external regions.

The candidate radio relic in A1451 might be associated to an external shock, rather than a merger shock (Section 1.5.4). Although accretion/external shocks are typically stronger than merger shocks, the energy flux that they dissipate is very low, because they develop in regions where the gas density is low and this makes them very difficult to detect, unless they encounter and re-accelerate some clouds of relativistic plasma during their propagation. For instance, the candidate relic in A1451 could be instigated by an external shock that propagates through the lobes of a dead radio galaxy (Enßlin & Gopal-Krishna 2001). Source S (Fig. 6.4) might be responsible for the presence of such ghost plasma. Unfortunately no spectroscopic redshift is available for this source. The 2 MASS catalogue (Skrutskie et al. 2006) reports a K_s magnitude of 15.03. Using the $K_s - z$ relation by Willott et al. (2003) we estimated that the redshift of source S is $z = 0.3 \pm 0.1$, which does not exclude the possibility that it is close to the cluster redshift. We note that this scenario is in agreement with the fact that the candidate relic is well below the LLS–cluster-centre distance correlation by de Gasperin et al. (2014). Such a correlation has been found for double radio relics, associated to merger-driven shocks. In case of shocks crossing a pre-existing cloud of relativistic plasma, the size of the relic is determined by the size of that cloud which, in general, is expected to extend much less than the surface crossed by external shocks.

Clearly, another possibility is that this source is a background giant radio galaxy, although the lack of a significant spectral gradient along the E-W direction disfavours this hypothesis.

Future studies on the polarisation properties of this object are necessary to establish its nature.

6.2 Zwcl0634.1+4750

Little is known in the literature about Zwcl0634.1+4747 (alternative names: PSZ1 G167.64+17.63, CIZA J0638.1+4747, RX J0638.1+4747). It is at redshift $z = 0.174$ and the MCXC catalogue reports an X-ray luminosity in the $[0.1 - 2.4]$ keV band $L_{500} = 4.72 \times 10^{44} L_{\odot}$ (Piffaretti et al. 2011). The mass within R_{500} estimated by

---

[1] To derive the virial radius, R_v, we converted M_{500} to M_{vir}, by assuming an NFW profile (e.g. Navarro et al. 1997) for the dark matter halos and the concentration-mass relation in Duffy et al. (2008).

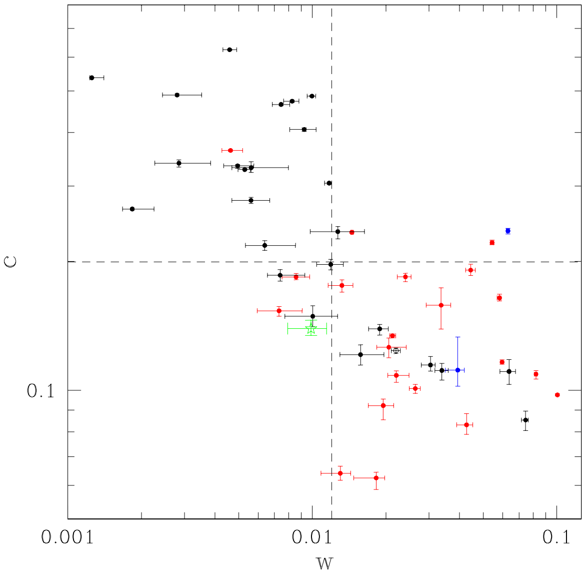

Figure 6.5: $c - w$ morphological diagram where Z0634 is marked with a green star. Red dots are radio halo clusters, black dots are non-radio halo clusters and blue dots are clusters with relics.

Planck Collaboration et al. (2014a) is $M_{500} = 6.52 \times 10^{14} M_{\odot}$. The X-ray *Chandra* image (Fig. 6.6, left panel) shows evidence of a non-relaxed dynamical state, indeed there are substructures in the X-ray surface brightness distribution and the morphology of the cluster is elongated to the East-West direction. The analysis of the X-ray *Chandra* archival data carried out in Chapter 3, confirms that Z0634 lies in the merging region of the morphological diagrams (Fig. 6.5).

We observed Z0634 with the GMRT at 330 MHz and with the JVLA in D configuration at 1.5 GHz. The JVLA D array image of Z0634 is shown in Fig. 6.6 (left panel). The cluster hosts diffuse, centrally located radio emission that we classify as a radio halo. Two head-tail radio galaxies are present in the cluster field, one located North of the radio halo (labelled HT in Fig. 6.6) and one located at the S-E edge of the cluster (source C in Fig. 6.6). While source C has the typical morphology and spectral properties of many HT radio galaxies found in clusters (e.g. O'Dea & Owen 1986; Giacintucci & Venturi 2009; Owen et al. 2014), the radio galaxy named HT has some unusual characteristics. The radio halo and the HT are described in the following subsections.

6.2.1 Radio halo

The radio halo in Z0634 extends over ~ 600 kpc in the E-W direction and follows the morphology of the X-ray emission of the cluster (Fig. 6.6, left panel). The two HT radio galaxies, HT and C, are difficult to subtract from the *uv*-data, thus we measured the radio halo flux density on an area that avoids these two sources.

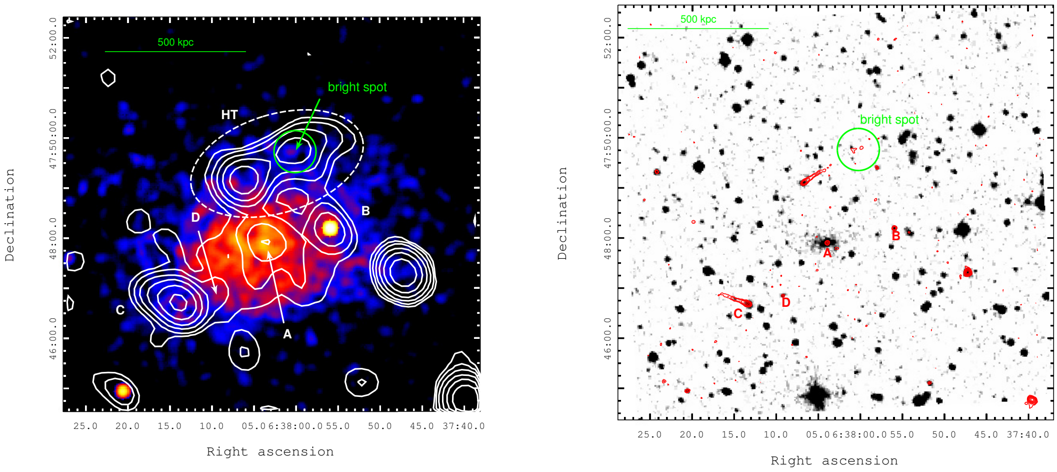

Figure 6.6: *Left*: Z0634 JVLA D array 1.5 GHz contours (white) superimposed on the X-ray *Chandra* image. Radio contours starts at 0.12 mJy/beam and are spaced by a factor 2. The rms noise of the radio image is $\sim 45\mu$Jy/beam with a beam of $35.7'' \times 30.7''$. *Right*: JVLA B array contours (red) superimposed on the optical DSS image. Contours starts at 0.09 mJy/beam and are spaced by a factor 2. The beam is $3.5'' \times 3.3''$.

Still, there are three sources (labelled A, B and D in Fig. 6.6) embedded in the radio halo emission. The high-resolution ($\sim 3''$) JVLA B array image (Fig. 6.6, right panel) reveals that they are point-like sources, so their flux density, measured from the B array image ($\sim$ 1.4 mJy in total), can be safely subtracted from the measurement on the radio halo region. We obtained a flux density of the radio halo $S_{1.5GHz} = 3.3 \pm 0.2$ mJy, corresponding to a radio power $P_{1.4GHz} = 3.1 \pm 0.2 \times 10^{23}$ W/Hz, assuming a spectral index $\alpha = -1.2$ for the *k-correction*.

The flux density of the radio halo at 320 MHz, after the subtraction of the point sources mentioned above, is $S_{320MHz} = 20.3 \pm 2.7$ mJy. We note that in the low-resolution GMRT 320 MHz image (Fig. 6.7) the radio halo does not extend to the HT and source C, thus we can reasonably exclude that we have lost a substantial part of the radio halo emission by avoiding those regions in the measurement of the radio halo flux density. To evaluate the spectral index of the radio halo, we produced images at 320 and 1500 MHz (B+D array JVLA observations) with uniform weighting and using the same *uv*-range and resolution ($\sim 20''$) and we measured the flux density of the radio halo on the same area. As done for A1451, we performed the imaging with two approaches: *i)* cleaning only inside the mask that contains all the sources in the field or *ii)* after that, cleaning also on the rest of the field down to two times the rms noise. We found that the spectral index of the radio halo ranges from -1 to -1.3, depending on where we measure the flux densities and how we clean the images (α is steeper in case *(ii)*). We obtained similar results setting the threshold at three times the rms noise in the cleaning process.

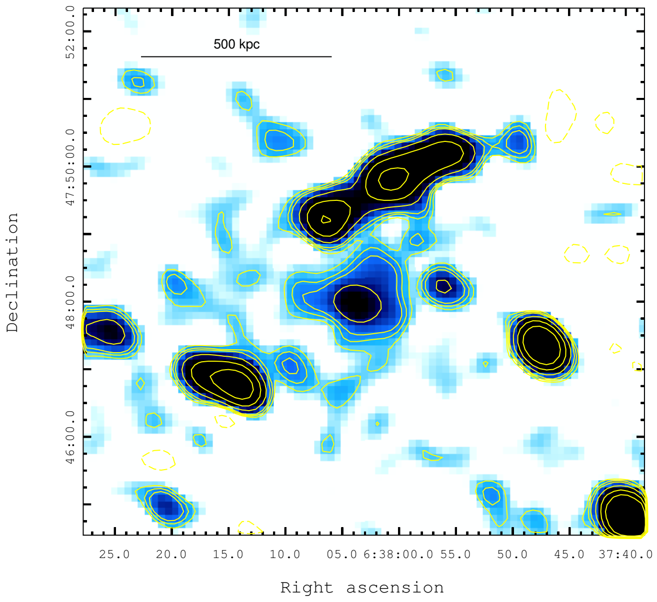

Figure 6.7: GMRT 330 MHz colour image and contours of Z0634. The contour levels are $(2, 3, 4, 8, 16, 32...) \times \sigma_{rms}$ with $\sigma_{rms} = 0.25$ mJy/beam. The resolution is $30.5'' \times 23.0''$. The first negative contour is dashed.

6.2.2 Head tail

The "head" of the HT radio galaxy is located $\sim 110''$ NE from the cluster X-ray centroid (i.e. at a projected distance of ~ 330 kpc). This bright nucleus is followed by a lower-surface-brightness tail that extends in the SE-NW direction (Fig.6.6). Considering the 3σ contours of the GMRT 320 MHz image (shown in Fig. 6.9), the angular extension of the HT is ~ 3.5 arcmin, corresponding to ~ 600 kpc at the cluster redshift (Fig.6.8, left panel). Its linear extension decreases to ~ 400 kpc at 1.5 GHz (Fig.6.8, right panel), measured from the 3σ contours of the B+D array image. The total flux density of the HT at 320 MHz is 42.5 ± 4.3 mJy, while it is 8.9 ± 0.3 mJy at 1.5 GHz. Interestingly, the radio surface brightness of the HT does not decrease regularly along the tail as it is typical for similar radio galaxies. There is a spot of higher surface brightness, roughly at half the total length, visible at both frequencies. After this spot, on the Western side, the tail is brighter than before the spot (Fig.6.8).

To make the spectral index map of the HT, we used the spectral windows 6 and 7 of the JVLA B+D dataset and we produced JVLA and GMRT images with uniform weighting and common uv-range and convolved them to the same resolution ($15''$). We blanked those pixels that in the GMRT 320 MHz image have values below two times the rms noise (~ 0.25 mJy/beam) in order to take into account the extension of the tail at low frequency as much as possible. However, given the poor S/N and

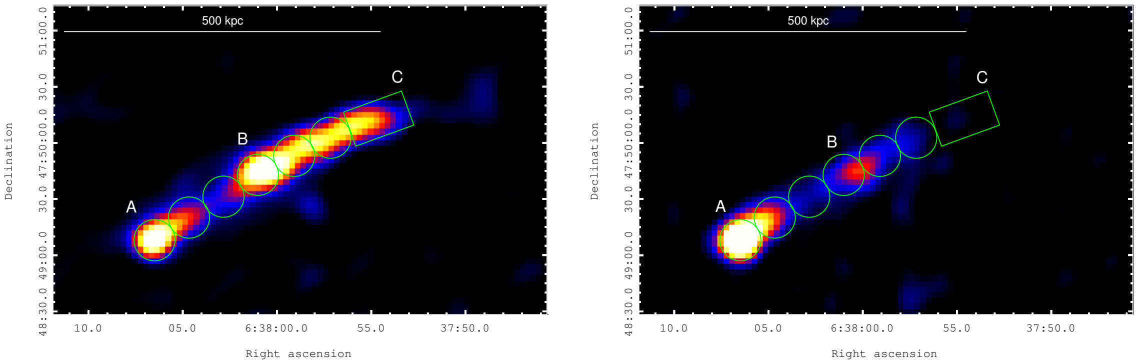

Figure 6.8: GMRT 320 MHz (*left*) and JVLA B+D array 1.5 GHz (*right*) colour images. Both are convolved with a $15'' \times 15''$ beam. The green regions mark the areas where we calculated the spectral index to trace its evolution along the tail.

the large errors associated with the spectral index (Fig. 6.9), we will not consider the westernmost part of the tail in our analysis. As shown in Fig. 6.9, we found that the spectral index between 320 MHz and 1.5 GHz steepens with the distance from the nucleus, from $\alpha \sim -0.6$ to $\alpha \sim -2.5$. We also note that the bright spot is steeper that the Eastern (initial) part of the tail.

In order to understand if the spectral index steepening along the tail is consistent with pure radiative ageing of the electrons, we attempt to extract both the spectral index and the surface brightness with distance. We selected six circular regions along the tail and a final rectangular one (Fig.6.8). The size of the circular regions is $\sim$ 1.5 times the beam area. We selected a larger rectangular area on the last portion of the tail that is only marginally visible at 1.5 GHz in order to have a better S/N. We did not consider the very last part of the tail (West of C in Fig. 6.8, left) because it is only visible at 320 MHz with a poor S/N.

The radio surface brightness and the spectral index show an unusual evolution along the tail (Fig. 6.10). In the first part of the tail (A→B) the brightness progressively declines and the spectral index steepens, as expected due to radiative losses of a population of relativistic electrons that have been accelerated in the head of the radio galaxy (in A). In the presence of synchrotron and IC losses only, the (emitted) break frequency scales with time and distance from the core (from which particles have been released) as:

$$\begin{aligned}\nu_b(\mathrm{GHz}) = 2.6\frac{\tau(\mathrm{Gyr})^{-2}B(\mu\mathrm{G})}{(B(\mu\mathrm{G})^2 + B_{CMB}(\mu\mathrm{G})^2)^2} \propto \\ \propto \frac{(\eta\sin\theta_O\sigma_v)^2}{B^3_{CMB}}\frac{\psi}{(\frac{\psi^2}{3}+1)^2}d_\perp^{-2}\end{aligned}, \qquad (6.1)$$

where τ is the radiative age of the electrons, $d_\perp$ is the projected distance from the

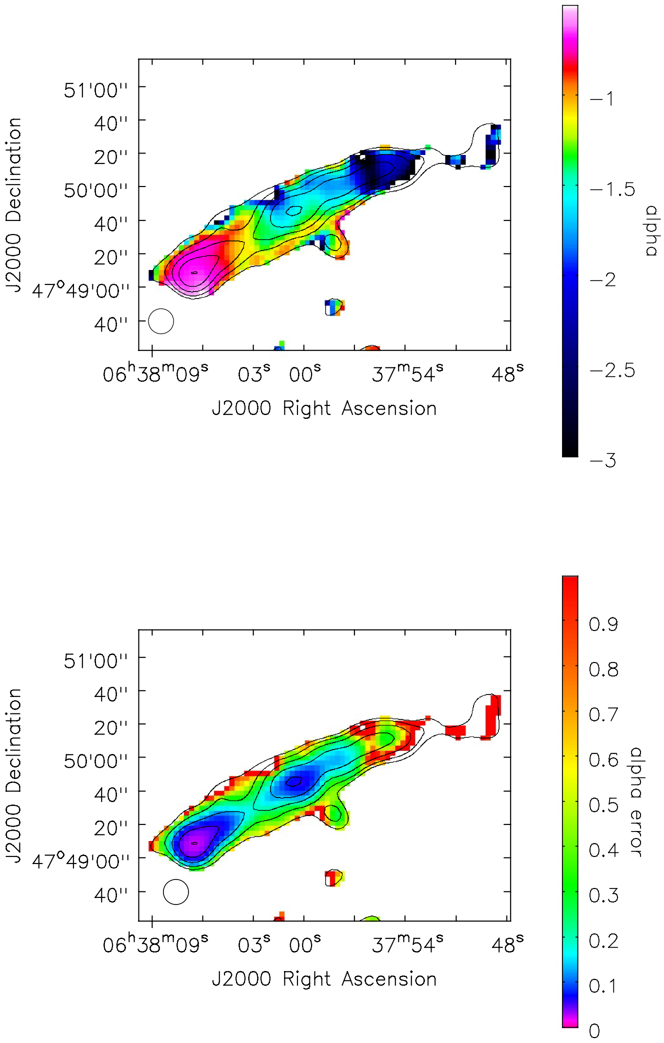

Figure 6.9: Spectral index map (*top*) and associated spectral index error map (*bottom*) of the HT in Z0634 between 320 MHz and 1.5 GHz at resolution 15″ × 15″. GMRT 320 MHZ contours of the image used to make the spectral index map are drawn in black. Contours levels start from 0.42 mJy/beam and are spaced by a factor 2.

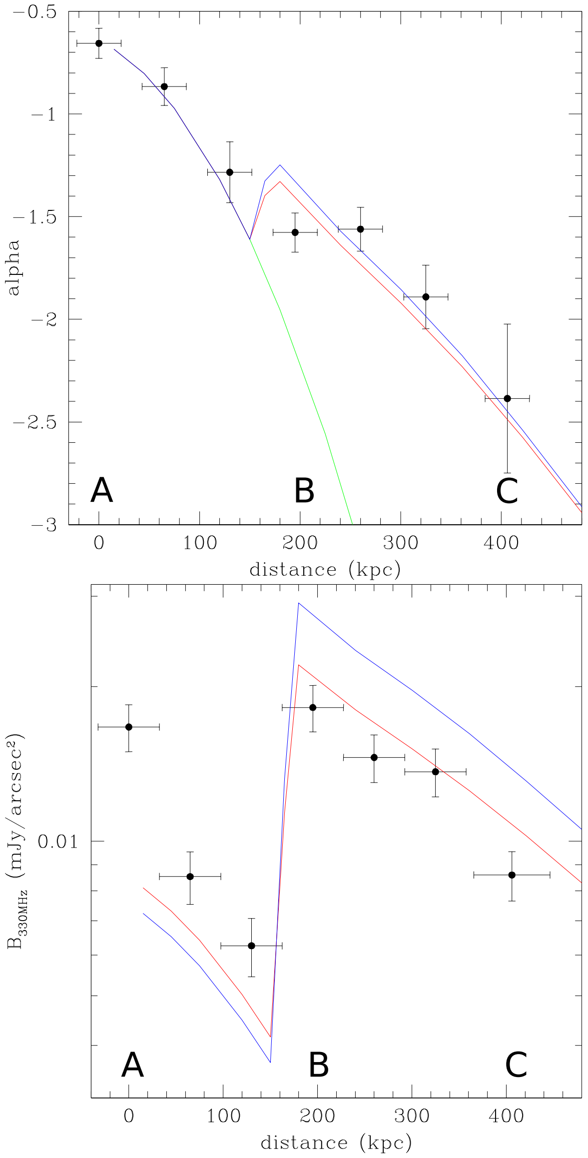

Figure 6.10: *Top*: spectral index of the HT vs. distance from the "head". The green line is the classical model of synchrotron ageing of a population of electrons that have been accelerated in the "head". The injection spectrum is assumed to match the spectrum in the head of the tail. *Bottom*: radio surface brightness vs. distance; model normalisation (K_e) is chosen to best illustrate the comparison with the data. A, B and C refer to Fig. 6.9. In both panels the model parameters are: $\mathcal{M} = 1.7$, $\theta_{SO} = \pi/2$, $a = 1$, $c_S = 1330$ km/s, $\sigma_v = 1400$ km/s, $\psi(t = 0) = 1$, $\eta \sin\theta_O = 1$, with $\theta_O = 60°$ and $\theta_{SO} = 90°$, $\Gamma = 5/3$ (red line) and $\Gamma = 4/3$ (blue line).

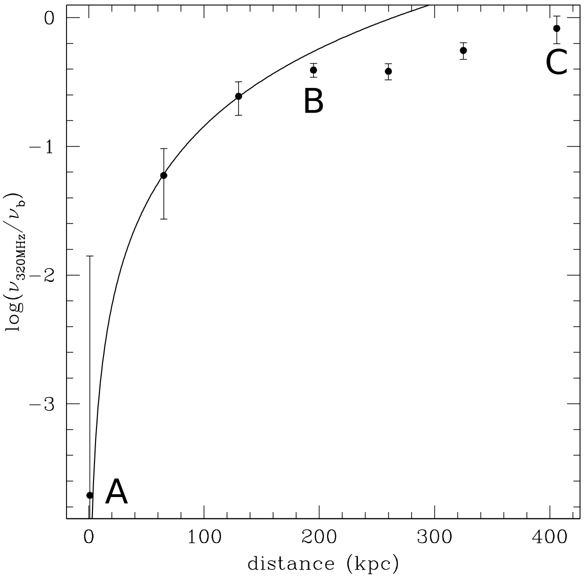

Figure 6.11: ν_{320MHz}/ν_b vs. distance from the "head" of the HT galaxy. The line represents $\nu_b \propto d^{-2}$. For display purposes the curve is normalised to the third data point.

core, B_{CMB} is the equivalent magnetic field of the CMB, σ_v is the velocity dispersion of the cluster ($\sigma_v \sim 1400$ km/s, estimated from the virial mass and radius) and $\eta\sigma_v \sin\theta_O$ is the (projected) velocity of the head. We note that $\eta \sin\theta_O$ combines two unknowns: the velocity of the HT and the inclination of its orbit. In Eq. 6.1, we introduced the quantity $B = \psi B_{cmb}/\sqrt{3}$, where ψ parametrises the magnetic field of the tail. For $\psi = 1$, the electrons emitting at the observing frequencies in a magnetic field B are in the situation of minimum radiative losses and consequently maximum lifetime. The break frequency evaluated from the spectral index measured between 330 and 1500 MHz and assuming a JP (Jaffe & Perola 1973) synchrotron spectral shape and an injection spectrum $\alpha_{inj} = -0.6$ (Fig. 6.9), is shown in Fig. 6.11 as a function of the projected distance.

In the simplest interpretation, the fact that the break frequency scales with d^{-2} between A and B (Fig. 6.11) suggests that adiabatic losses and strong variations of B do not play an important role at this stage, otherwise a faster increase of ν_1/ν_b would be observed. More quantitatively, in Fig. 6.10 (upper panel) we show the comparison between the observed spectral index and the spectral index expected in the case of IC and synchrotron losses in the reference case $\psi = 1$ and $\eta sin\theta = 1$. Also in this case, a simple scenario of pure radiative losses in the region A–B can explain the data. We note that there is degeneracy in the parameters: from Eq. 6.1, one finds that the same match can be obtained with different choices of the parameters η and ψ, that is, B, and θ_O under the condition $\eta^2 \sin^2\theta_O \frac{\psi}{(\psi^2/3+1)^2} = 9/16$.

In B (Fig. 6.8), the surface brightness is boosted up by a factor of 3.5-4 (Fig. 6.10), while the spectral index stops declining and remains almost constant for

~ 100 kpc, corresponding to ~ 60 Myr (if we consider $\eta \sin\theta_O = 1$) [2]. Then, from B to the end of the tail (C), both the surface brightness and the spectral index of the tail begin again to decrease and steepen, respectively. The possibility that we are seeing two HT radio galaxies chasing each other is excluded by the B array image (Fig. 6.6, right panel), where the bright spot is resolved and appears as part of the diffuse emission of the tail, with no indication of any compact/nuclear component. Moreover, the spectral index in B is very steep and inconsistent with that of synchrotron radiation from a young plasma. On the other hand, the properties of the tail suggest that around region B, the electrons in the tail are currently experiencing re-energisation and possibly that the magnetic field in the tail is also amplified.

6.2.2.1 A model to explain the observed properties of the HT

A mechanism that may explain the observed properties of the HT in the ICM is the interaction between a shock and the radio tail (e.g. Pfrommer & Jones 2011; de Gasperin et al. 2017). A schematic view is illustrated in Fig. 6.12. The HT galaxy is travelling outward from the cluster centre with an angle θ_O to the line of sight. A shock front impacts the tail first and gets to the point B where we are currently observing it. When the shock passes through the tail the adiabatic compression re-energises a population of aged electrons and increases the magnetic field strength. All this leads to an increase of the synchrotron brightness in B and affects the observed spectral properties. In the downstream region (B→C) the electrons cool down again in the new magnetic field, but the ageing time has to be computed from the time of the shock passage and it no longer depends on the velocity of the tail. Of course, the dynamics of the HT–shock interaction can be very complicated and would require ad hoc simulations that are beyond the scope of this Thesis. For example, the shock crossing may change the inclination of the shocked portion of the tail, implying that projection effect may play an important role. In addition, after the shock passage, the tail may experience some expansion together with the gas downstream, and adiabatic expansion may induce a strong spectral steepening in the tail at later stages due to adiabatic losses and the decline of the magnetic field.

The system is complicated and unfortunately our observations cannot constrain all model parameters. Here we only show that, in the case of a weak shock travelling at a large angle with respect to the plane of the sky, this scenario has the potential to explain the observed properties of the tail.

The evolution of the electron spectrum in the tail assuming radiative losses and

---

[2] We point out that these values are only indicative, since they depend on the sampling adopted in Fig. 6.8

compression (expansion) is (Kaiser et al. 1997; Enßlin & Gopal-Krishna 2001):

$$\frac{\partial N}{\partial t}=\frac{\partial}{\partial\gamma}\left\{N\left[\frac{4\sigma_T}{3m_ec}\left(\frac{B^2}{8\pi}+\frac{B^2_{CMB}}{8\pi}\right)\gamma^2+\frac{1}{3}\frac{\dot{V}}{V}\gamma\right]\right\}, \tag{6.2}$$

where the first term on the right accounts for radiative (synchrotron and IC) losses and the second term for adiabatic compression or expansion ($\dot{V}/V$ is the rate of compression/expansion).

If electrons are continuously injected in the core of the HT at a constant rate and with an initial energy distribution $N(\gamma,0)=k_e\gamma^{-\delta}$ (with γ between γ_{min} and γ_{max} such that $\gamma_{min} << \gamma_r << \gamma_{max}$, γ_r being the typical energy of the electrons emitting at 330 and 1400 MHz) and if we define the compression factor with time $C_t = V_0/V(t)$, the magnetic field will evolve with time according to $B(t)=B(0)C_t^{2a/3}$, where $a=1$ in the case of isotropic compression/expansion and the solution of Eq. 6.2 is :

$$N(\gamma,t)=K_eC_t^{\frac{\delta+2}{3}}\gamma^{-\delta}\left(1-\frac{\gamma}{\gamma_{*t}}\right)^{\delta-2}, \tag{6.3}$$

where

$$\gamma_{*t}^{-1}=\frac{\sigma_tB^2_{CMB}}{6\pi m_ec}\int_0^t dx\left(1+\frac{\psi_x^2}{3}\right)\left(\frac{C_x}{C_t}\right)^{\frac{1}{3}}, \tag{6.4}$$

where we have introduced the quantity

$$\psi_t=\frac{B_0}{B_{CMB}/\sqrt{3}}C_t^{\frac{2a}{3}}, \tag{6.5}$$

Here we assume $\psi(t=0)=1$, i.e. the case where radiative losses of electrons emitting at a given frequency in a given magnetic field are minimised.

Following Enßlin & Gopal-Krishna (2001), we assume three phases: (i) an initial phase where electrons simply age ($t \leq t_1$), (ii) a phase where the shock compresses the tail ($t_1 \leq t \leq t_2$, where $t_2 - t_1 = \Phi/(\mathcal{M}c_s)$, Φ is the thickness of the tail, c_s is the sound speed and $\mathcal{M}$ is the Mach number), and (iii) a new phase of cooling of the electrons after shock passage ($t > t_2$). Under this assumptions the compression factor is

$$\begin{cases} C_t = 1 & t \leq t_1 \\ C_t = 1+(C_{t_2}-1)\dfrac{t-t_1}{t_2-t_1} & t_1 < t \leq t_2 \\ C_t = C_{t_2} = \dfrac{(\Gamma+1)\mathcal{M}^2}{(\Gamma-1)\mathcal{M}^2+2} & t > t_2 \end{cases}. \tag{6.6}$$

Γ is the adiabatic index of the gas into the tail. If the plasma is relativistic, then $\Gamma=4/3$, while $\Gamma=5/3$ in the case where most of the energy of the plasma in the tail is contributed by thermal gas. The resulting synchrotron emissivity is:

$$J(\nu,t)=\frac{e^3\sqrt{3}}{m_ec^2}\int_0^{\frac{\pi}{2}}d\theta(\sin^2\theta)B\int d\gamma N(\gamma,t)x\int_x^\infty K_{5/3}(z)dz, \tag{6.7}$$

where $x = \dfrac{4\pi m_e c\nu}{3eB\sin\theta\gamma^2}$ and $K_{5/3}(z)$ is the 5/3 modified Bessel function.

Given the geometry in Fig. 6.12, the conversion from time to projected distance is given by

$$\begin{cases} d_\perp = \eta\sigma_v \sin\theta_O t & t \le t_2 \\ d_\perp = c_S\mathcal{M}\dfrac{\sin\theta_O}{\cos\left(\theta_{SO}+\theta_O-\frac{\pi}{2}\right)}(t-t_2) & t > t_2 \end{cases}, \tag{6.8}$$

where $\eta\sigma_v$ is the velocity of the head of the tail. We assume $\eta\sin\theta_O = 1$, and the velocity dispersion of the cluster $\sigma_v = 1400$ km/s. The synchrotron brightness as a function of projected distance is:

$$I(\nu, d_\perp) = \frac{1}{2\pi}\int_{d_\perp} \frac{J(\nu, r(t))rdr}{\sqrt{r^2 - d_\perp^2}}, \tag{6.9}$$

where the integral is done along the tail intercepted by the line of sight.

The model parameters are: the velocity of the HT (η), the magnetic field (ψ), the normalisation of the electron spectrum (K_e), the geometry of the problem (θ_O, θ_{SO}) and the shock Mach number ($\mathcal{M}$). In Fig. 6.10 we show the model results[3] assuming $\mathcal{M} = 1.7$ and $\theta_O = 60°$, thus the velocity of the tail is $v = \sigma_v/\sin 60° \approx 1600$ km/s. We compare the model with the data, focusing on the spatial behaviour of the synchrotron spectral index and of the synchrotron brightness. Given the number of model parameters and the uncertainties on the dynamics of the interaction between the tail and the shock, a full extrapolation of the model parameters is not meaningful at this stage. However, from Fig. 6.10, we can conclude that the proposed scenario can naturally explain the observations both in the upstream region (A→B), where the electrons generated in the core simply age and in the downstream region (B→C) after the shock passage.

We assumed a weak shock with Mach number < 2, similar to most shocks detected in galaxy clusters (e.g. Markevitch & Vikhlinin 2007; Markevitch 2010; Botteon et al. 2017). In addition, a constraint on the shock Mach number can be derived from the observed jump of the synchrotron brightness across the shock, that is, by the ratio of the downstream and upstream brightness, I_d/I_u; I_d and I_u are given by Eq. 6.9 evaluated at time $= t_2$ and t_1, respectively. An upper limit to the expected brightness jump can be easily derived by assuming that energy losses during the compression phase can be neglected, i.e. the re-energization due to compression is faster than energy losses of the emitting electrons. In this case, if we assume a power-law spectrum of electrons, $N(\gamma) \propto \gamma^{-\delta}$, the ratio $I_d/I_u = C_{t_2}^{2\delta/3+1} l_d/l_u$ (e.g. Markevitch et al. 2005) where l_d and l_u are the downstream and upstream thickness intercepted by the line of sight, respectively. For reference, this gives $I_d/I_u = C_{t_2}^{2\delta/3+1}$ and $= C_{t_2}^{2\delta/3}$ in the situation of shock travelling at small and

---

[3] We note that for a given magnetic field ψ the normalisation of the synchrotron brightness depends on the normalisation of the electron spectrum, K_e (Eq. 6.3), that is a free parameter

large angles to the plane of the sky, respectively. Thus the maximum Mach number for $\Gamma = 5/3$ (for $\Gamma = 4/3$ the limit is more stringent) of a shock travelling at a large angle to the plane of the sky is:

$$\mathcal{M} \leq \left(\frac{3}{4\left(\frac{I_u}{I_d}\right)^{\frac{3}{2\delta}} - 1} \right)^{\frac{1}{2}} , \tag{6.10}$$

which gives $\mathcal{M} \leq 1.58$ by assuming the observed brightness jump $I_d/I_u \sim 4$ and a spectrum of the emitting electrons $\delta = 3.5$ (around the energy of the emitting electrons in the region B); the allowed Mach number is slightly larger when radiative losses during compression are properly included (see Fig. 6.10) [4].

We also note that no shock is clearly visible at the position B in the currently available X-ray image, suggesting that if a shock is present it should be weak and/or moving in a direction that is significantly inclined with respect to the plane of the sky.

6.3 The "Underluminous" radio halos in A1451 and Z0634

Compared to the current radio power–mass scaling relations (Cassano et al. 2013; Martinez Aviles et al. 2016), the radio halos in A1451 and Z0634 are underluminous, being $\sim 6-7$ times below the correlation [5] (Fig. 6.13). Since these radio halos are very faint, a reliable characterisation of their morphology and spectrum is challenging with the current observations. Nonetheless, the spectral information is crucial to understand the origin of these sources.

6.3.1 Spectrum of the radio halos

The measurement of the spectral indices of A1451 and Z0634 is challenging because our GMRT and JVLA observations may have different capabilities of recovering such extended faint radio emission. We used the method of injecting fake radio halos into the datasets (Section 4.3). In fact, an important outcome of the studies involving the

---

[4] We point out that given the observed spectrum and the Mach numbers used in our calculations, even in the case $\Gamma = 5/3$ (in this case particles inside the HT will be shocked) the process of shock acceleration is subdominant with respect to compression.

[5] One possibility is that the SZ-based mass of A1451 and Z0634 is overestimated, as expected for a substantial projection along the line of sight, although their elongation on the plane of the sky may disfavour this hypothesis. We compared the mass of A1451, estimated from the weak lensing analysis (Sereno & Ettori 2017) with the mass derived by Planck Collaboration et al. (2014a), finding that they are consistent.

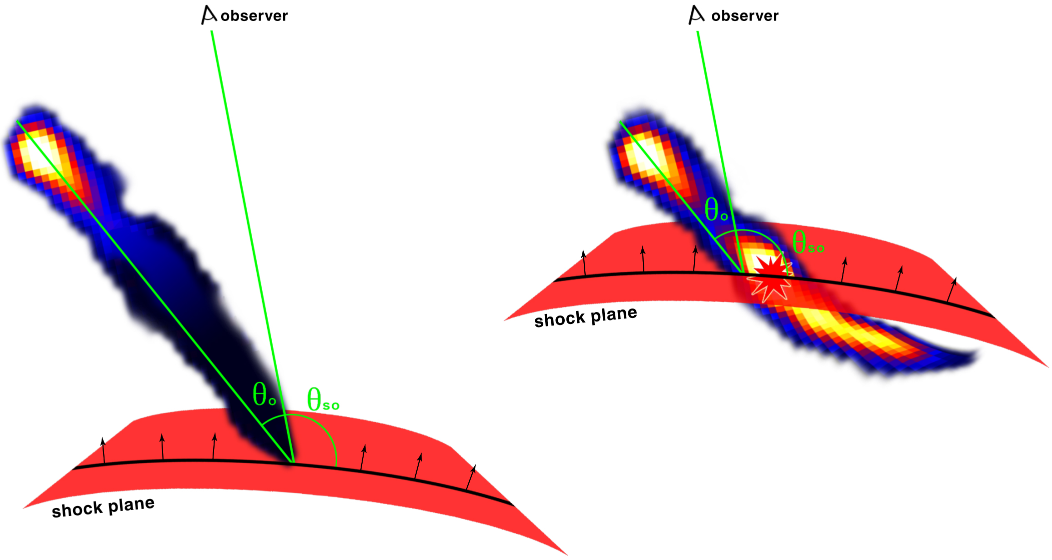

Figure 6.12: Cartoon of the interaction between the shock front and the HT. Before the interaction (*left*) the surface brightness of the HT progressively declines from the head to the tail. The right panel represents the current situation: the shock has passed through the last part of the tail that appears brighter because of the re-energisation undergone by the electrons. The bright spot is where the tail is currently shocked. The shock passage also caused the bending of the tail in the direction parallel to the shock itself.

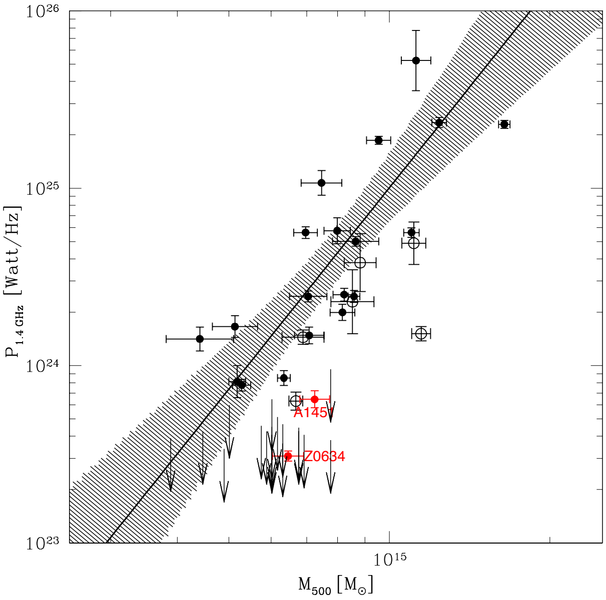

Figure 6.13: Distribution of clusters in the $P_{1.4GHz} - M_{500}$ diagram. Different symbols indicate giant radio halos (black filled dots), ultra steep spectrum radio halos (black empty dots) and upper limits (black arrows) belonging to the Cassano et al. 2013 sample. The red dots represent the two clusters presented in this paper. The best fit relation for giant radio halos (black line) and the 95% confidence level (shadowed region) from Cassano et al. (2013) are shown.

injection of modelled radio halos is that the injected flux density is at least partly lost and this effect becomes more important for faint flux densities (e.g. Venturi et al. 2008). Therefore this warns that part of the flux of the radio halos in A1451 and Z0634 may not be properly recovered by our GMRT and JVLA observations. The decline of the recovered flux depends on a combination of sensitivity of the observations, density of the inner *uv*-coverage and image fidelity of the dataset (Venturi et al. 2008; Kale et al. 2013, 2015). Thus the amount of flux losses might be different for different observations and this effect needs to be taken into account to evaluate the spectral index of such faint radio halos.

The procedure to model and inject the fake radio halos into the datasets is the one described is Section 4.3, except that here we reduced the injected flux density until the recovered flux of the fake radio halo was similar to that of the radio halo observed at the cluster centre. In addition, here we also changed the value of r_e in Eq. 4.1 (Section 4.3) for the injected halos to reproduce the extension of the halos in A1451 and Z0634. In practice, for these two clusters, we used the injection technique to find the modelled radio halos (in terms of flux density and size) that, once injected in the datasets and imaged, reproduce the radio halos observed at the cluster center at best.

Since the main aim of these injections is to check the reliability of the measured spectral indices of the two radio halos presented here, the images have been done minimising the differences between the two datasets as much as possible. In particular, we used the common *uv*-range and we tapered down to the same resolution ($\sim 20''$). We also used uniform weighting to minimise the difference in the *uv*-sampling. We performed the imaging with two approaches: *(i)* cleaning only inside the mask containing all the sources or *(ii)* cleaning inside the mask and also cleaning deeply on the rest of the field. In general, we found that the rms noise of the final image improves in case *(ii)*, but the recovered flux of the injected radio halos is significantly lower (from 10 to 40%) than in case *(i)*, such effect being more prominent for faint injected flux densities.

In line with the findings of Venturi et al. (2008) and Kale et al. (2013, 2015), for both clusters, if we inject the flux density of a radio halo that lies on the radio luminosity-mass correlation, both interferometers are able to recover the great majority of its flux density. However, when reducing the injected flux, in order to match the observed one, the fraction that is recovered decreases. Specifically, we found that our GMRT observations generally recover a higher fraction of the flux density of faint injected radio halos, assuming a spectral index $\alpha \leq -1.2$. This different performance can be explained by the different inner *uv*-coverage. Indeed, the full-track GMRT observation ensures a denser *uv*-sampling with respect to the snapshot JVLA observation (Fig. 6.14, left and right, respectively). For both A1451 and Z0634, in order to recover, in the fake halo, the same flux density that we find in the halo at the cluster centre at both frequencies, we need to inject a radio halo with a spectral index $\alpha \approx -1$. Unfortunately, a fully reliable estimate of the spectral index of these radio halos is prevented by the fact that the flux density of such faint diffuse emission can change significantly depending on where we measure it and how we perform the imaging (see Sects. 6.1.1 and 6.2.1). Nevertheless, the analysis based on the injections allows us to exclude the presence of radio halos with spectra significantly steeper than $\alpha \approx -1.3$ in A1451 and Z0634. Moreover, the injection procedure allows us to estimate the size of the halos: we found that injected halo models with $r_e \sim 140$ kpc and $r_e \sim 130$ kpc (Section 4.3) match the observed extension of the radio halos in A1451 and Z0634 when the recovered fluxes match the observed ones.

The results of the injections suggest that, even in the worst case, the true flux density of the radio halos can be underestimated by our observations at most by a factor of 1.8 (A1451) and 2.2 (Z0634) at 1.5 GHz, meaning that both the radio halos would be still $4-5$ times below the $P_{1.4GHz} - M_{500}$ correlation from Cassano et al. (2013). We also note that at these flux levels, the morphology of the injected halos that is recovered from the maps may differ from that of the injected models. For this reason it is impossible to firmly establish weather the halo in A1451 extends only in the Southern region or if there is some emission extending also in the Northern part.

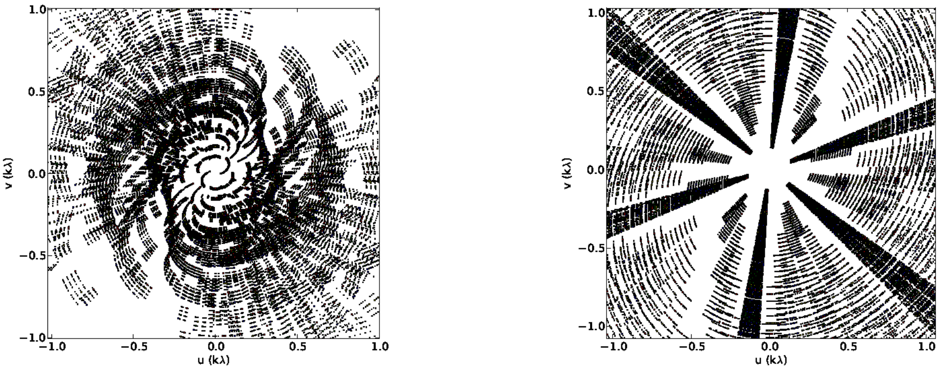

Figure 6.14: Inner *uv*-coverage of the GMRT 320 MHz observation (*left*) and of the JVLA D array observation (*right*) of Z0634.

6.3.2 Comparison with the current $P_{1.4GHz} - M_{500}$ correlation

As discussed in Chapter 2, previous statistical analysis of 30-40 galaxy clusters, have shown that their radio properties on the Mpc scale have a bimodal distribution: either they host giant radio halos following the correlation between the cluster mass (or X-ray luminosity) and the radio luminosity, or they do not show diffuse radio emission at the sensitivity level of current observations (e.g. Cassano et al. 2013). This bimodality is connected to the dynamical state of clusters, with radio halo clusters undergoing merging events and non-radio halo clusters being generally relaxed. Since its discovery, it was proposed that a bimodal segregation results from the fact that the period of time that clusters spend in the region between the limits and the correlation is smaller than the time they spend on the correlation or in a much fainter state (e.g. Brunetti et al. 2009; Donnert et al. 2013). In general, this implies that the increase of the statistics, as that provided by our sample of 75 clusters, would lead to the discovery of an increasing number of underluminous radio halos, sitting in the region between the correlation and the upper limits, which essentially sets the sensitivity of current observations. For illustrative purposes, we show in Fig. 6.13 the position of A1451 and Z0634 compared to the 95% confidence level region filled by giant radio halos in Cassano et al. (2013). Our sample allows a unique statistical assessment of the distribution of clusters in the radio power-mass diagram and of the occurrence of radio halos in clusters. These topics will be extensively discussed in Chapter 7, here we anticipate that 29 radio halos are found in this sample; 6 of them (excluding USSRHs, see Section 7.3) sit in the region between the current radio-mass correlations and the upper limits. Although these underluminous halos are statistically subdominant, their presence confirms that the increase of the statistics allows to populate the region below the correlation in the radio-mass diagram, which also leads to an apparent increase of the scatter of such correlation toward lower luminosities. In fact there are reasons to expect a fairly large scatter in the scaling relation between the radio halo power and the cluster masses. This is not only due to the fact that in larger samples an increasing number of clusters in the transition between the correlation and a much fainter state can be observed, but also to the superposition of different intermediate radio halo states that are generated by the complex hierarchy of merger events.

For example, one possibility proposed in the literature for underluminous radio halos is that they may have ultra steep spectra, resulting from less energetic merger events (smaller masses or minor mergers in massive systems) or in the case of higher-redshift clusters, where IC losses become severe compared to synchrotron losses (Cassano et al. 2006; Brunetti et al. 2008; Cassano et al. 2010a). Underluminous radio halos in transition between the correlation and the upper limits, i.e. radio halos in the very early or very late stages of their lifetime, are also expected to be underluminous and have particularly steep spectra (Donnert et al. 2013). Regarding A1451 and Z0634, these scenarios are disfavoured by the evidence that they do not host radio halos with very steep spectra (Sect. 6.3.1).

On the other hand, these two radio halos may originate from minor mergers where the bulk of the turbulence is generated and dissipated in small volumes. The fact that the X-ray morphology of these two clusters is not extremely disturbed may suggest that they are undergoing minor mergers. In this case, the bulk of the turbulence may be generated and dissipated in small volumes resulting in relatively flat radio spectra, despite the relatively low amount of energy involved in the merger events. If this is the case, the statistical analysis of the point to point X-ray radio surface brightness distribution of the radio halos of our sample may reveal a different radio-X-ray scaling in these systems with respect to typical giant radio halos. Alternatively, they could be “off-state” halos where the emission is primarily maintained by the continuous injection of secondary electrons of hadronic interactions in the ICM. Possible detections of “off-state” radio halos have been reported in the literature (e.g. Brown et al. 2011; Bonafede et al. 2014a). The relatively flat spectra ($\alpha \approx -1$, Section 6.3.1) and the small sizes of these two newly discovered radio halos would be in line with both these scenarios.

Chapter 7

Statistical analysis

The main aim of this Thesis is to obtain a sample of galaxy clusters with complete radio information to study their radio properties in connection with their dynamics and mass. To do that, we selected our sample from the Planck SZ cluster catalogue (Planck Collaboration et al. 2014a), which has been briefly described in Section 3.1. It is a highly complete catalogue of galaxy clusters and, thanks to the tight correlation between the SZ signal and the cluster mass, it offers the possibility of building almost mass-selected samples of clusters. Moreover, simulations show that the SZ selection is weakly affected by the dynamical status of clusters, thus suggesting that it should be more representative of the clusters population. In Section 3.2 we discussed the criteria adopted to select our galaxy clusters sample from the Planck catalogue. To summarise, we selected clusters with:

- $z = 0.08 - 0.33$
- $M_{500} \gtrsim 6 \times 10^{14}\, M_{\odot}$ [1]
- $\delta > -40^{\circ}$ at $z < 0.2$ and $\delta > -31^{\circ}$ at $z > 0.2$

The cut in cluster mass is mainly driven by the fact that the radio-mass scaling is very steep (Cassano et al. 2013; Martinez Aviles et al. 2016; Duchesne et al. 2017) and radio halos in clusters less massive than $\approx 6 \times 10^{14} M_{\odot}$ and typical redshift $z \approx 0.2$ would be too faint to derive stringent constraints from our observations. Our sample consists of 75 clusters, whose properties are listed in Table 7.1. The mass and redshift distributions of the clusters are shown in Fig. 7.1. The redshift distribution is rather uniform, except for the very low-redshift tail, where the volume of the Universe is too small to host such massive objects. The mass distribution is peaked around the mass cut of the sample and then it declines with mass (Press & Schechter 1974). Only few clusters with $M_{500} \gtrsim 9 \times 10^{14} M_{\odot}$ are present in the Universe at these redshifts.

---

[1] $M_{500} \geq 5.7 \times 10^{14}\, M_{\odot}$ at $z < 0.2$ and $M_{500} \geq 6 \times 10^{14}\, M_{\odot}$ at $z > 0.2$.

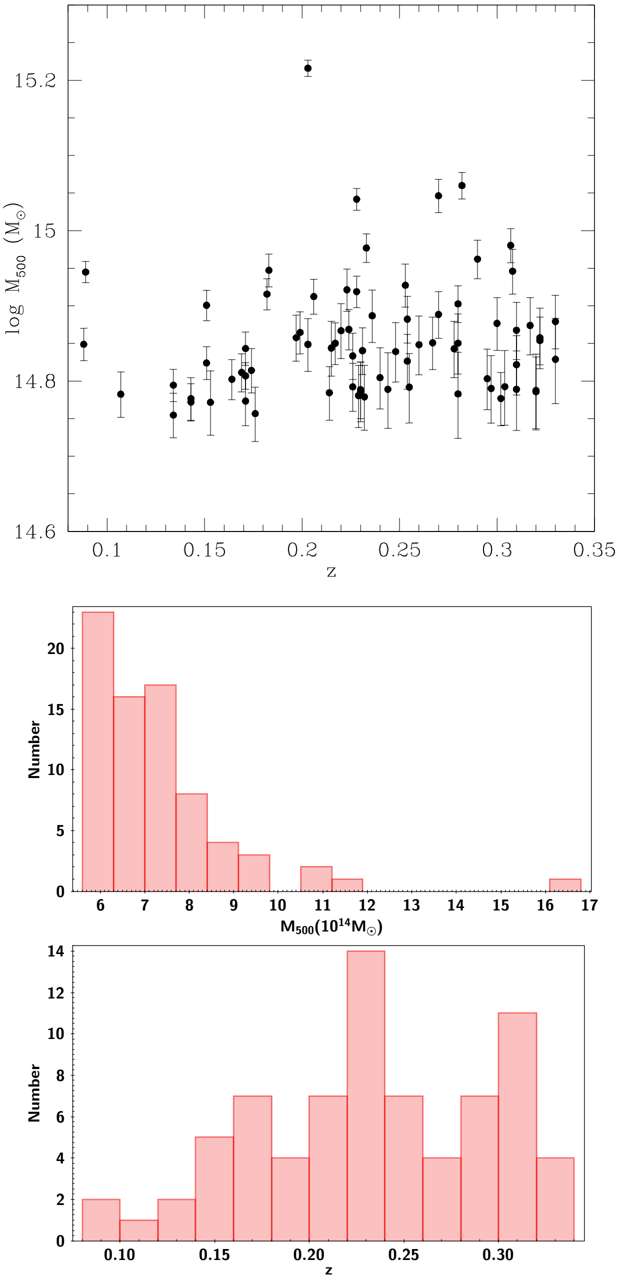

Figure 7.1: *Top*: Distribution of the clusters of our sample in the $M_{500} - z$ diagram. *Middle*: Mass distribution. *Bottom*: redshift distribution.

Table 7.1: Total sample clusters properties

Cluster name	RA	DEC	z	M_{500} (10^{14} $M_\odot$)	R_{500} (kpc)	Radio info	$P_{1.4GHz}$ (10^{24} W Hz^{-1})	R_H (kpc)
A1437	12 00 22.3	+03 20 33.9	0.134	5.69	1200	no RH*	-	-
A2345	21 27 06.8	−12 07 56.0	0.176	5.71	1190	UL^{40}	< 0.38	-
A2104	15 40 08.2	−03 18 23.0	0.153	5.91	1200	UL*	< 0.19	-
Zwcl 2120.1+2256	21 22 27.1	+23 11 50.3	0.143	5.91	1200	RH(c)*	-	-
RXC J0616.3-2156	06 16 22.8	−21 56 43.4	0.171	5.93	1200	UL*	< 0.17	-
A1413	11 55 18.9	+23 24 31.0	0.143	5.98	1220	MH^{5}	-	-
A1576	12 37 59.0	+63 11 26.0	0.302	5.98	1160	UL^{6}	< 0.64	-
A2697	00 03 11.8	−06 05 10.0	0.232	6.01	1190	UL^{2}	< 0.41	-
Z5247	12 33 56.1	+09 50 28.0	0.229	6.04	1190	$\mathrm{RH(c)}^{7}$	-	-
Zwcl 0104.9+5350	01 07 54.0	+54 06 00.0	0.107	6.06	1240	RH^{8}	1.62	465^{e}
RXC J0142.0+2131	01 42 02.6	+21 31 19.0	0.280	6.07	1170	UL^{6}	< 0.45	-
A1423	11 57 22.5	+33 39 18.0	0.214	6.09	1200	UL^{2}	< 0.38	-
ZwCl 1028.8+1419	10 31 28.2	+14 03 34.0	0.310	6.11	1160	no RH*	-	-
A3041	02 41 22.1	−28 38 13.0	0.230	6.12	1190	RH(c)*	-	-
RXC J2051.1+0216	20 51 08.0	+02 15 55.0	0.320	6.13	1150	UL*	< 0.73	-
A2472	22 41 50.6	+17 31 43.0	0.310	6.15	1160	UL*	< 1.0	-
A2895	01 18 11.1	−26 58 23.0	0.230	6.15	1190	UL*	< 0.5	-
RXC J1314.4-2515	13 14 28.0	−25 15 41.0	0.244	6.15	1190	$\mathrm{RH}^{1,US(c)}$	0.68	300
A2537	23 08 23.2	−02 11 31.0	0.297	6.17	1170	UL^{2}	< 0.45	-
A68	00 37 05.3	+09 09 11.0	0.255	6.19	1190	UL^{7}	< 0.42	-
A56	00 33 50.4	−07 47 28.0	0.300	6.20	1170	UL*	< 1.2	-
A1682	13 06 49.7	+46 32 59.0	0.226	6.20	1200	$\mathrm{RH(c)}^{2}$	-	-
A1132	10 58 19.6	+56 46 56.0	0.134	6.23	1240	$\mathrm{RH}^{32,US}$	0.16	349
RXJ1720.1+2638	17 20 10.1	+26 37 29.5	0.164	6.34	1240	MH^{9}	-	-
A781	09 20 23.2	+30 26 15.0	0.295	6.36	1180	UL^{2}	< 0.36	-
A384	02 48 13.9	−02 16 32.0	0.240	6.38	1210	UL*	< 0.55	-
A2218	16 35 51.6	+66 12 39.0	0.171	6.41	1240	RH^{3}	0.44	187
A3411	08 41 55.6	−17 29 35.7	0.169	6.48	1250	RH^{10}	0.27	277
Zwcl 0634.1+4750	06 38 02.5	+47 47 23.8	0.174	6.52	1250	RH*	0.31	245
RXC J1322.8+3138	13 22 48.8	+31 39 17.0	0.310	6.63	1190	no RH*	-	-

A3888	22 34 26.8	−37 44 19.1	0.151	6.67	1260	RH^{*,39}	1.90	432
A3088	03 07 04.1	−28 40 14.0	0.254	6.71	1220	UL^{2}	< 0.43	-
A220	01 37 19.5	+07 56 16.0	0.330	6.74	1190	UL*	< 0.97	-
A2667	23 51 40.7	−26 05 01.0	0.226	6.81	1240	MH^{33}	-	-
A521	04 54 09.1	−10 14 19.0	0.248	6.91	1240	RH^{11,US}	1.45	585^{e}
A2355	21 35 22.5	+01 23 26.0	0.230	6.92	1240	UL*	< 0.83	-
A2631	23 37 40.6	+00 16 36.0	0.278	6.97	1230	UL^{2}	< 0.41	-
A1914	14 26 03.0	+37 49 32.0	0.171	6.97	1280	RH^{12}	5.62	541^{e}
RXC J1504.1-0248	15 04 07.7	−02 48 18.0	0.215	6.98	1330	MH^{13}	-	-
A1733	13 27 03.7	+02 12 15.0	0.260	7.05	1240	UL*	< 0.53	-
A520	04 54 19.0	+02 56 49.0	0.203	7.06	1270	RH^{14}	2.45	441^{e}
A478	04 13 20.7	+10 28 35.0	0.088	7.06	1320	MH^{15}	-	-
A773	09 17 59.4	+51 42 23.0	0.217	7.08	1260	RH^{14}	1.48	514^{e}
PSZ1 G019.12+3123	16 36 29.4	+03 08 51.0	0.280	7.08	1230	UL*	< 0.6	-
PSZ1 G139.61+24.20	06 22 13.9	+74 41 39.0	0.270	7.09	1210	MH^{33}	-	-
A1351	11 42 30.8	+58 32 20.0	0.322	7.14	1210	RH^{16}	9.30	494^{e}
A115	00 55 59.5	+26 19 14.0	0.197	7.21	1280	no RH^{14}	-	-
A402	02 57 41.1	−22 09 18.0	0.320	7.21	1220	MH ^{34}	-	-
A1451	12 03 16.2	−21 32 12.7	0.199	7.32	1290	RH*	0.64	360
RXCJ 0510.7-0801	05 10 47.9	−08 01 06	0.220	7.36	1280	no RH^{35}	-	-
PSZ1 G205.07-6294	02 46 27.5	−20 32 5.29	0.310	7.37	1240	no RH^{p}	-	-
A2261	17 22 17.1	+32 08 02.0	0.224	7.39	1280	RH^{36}	0.68	618
RXCJ2003.5-2323	20 03 30.4	−23 23 05.0	0.317	7.48	1240	RH^{1}	10.71	666^{e}
A2552	23 11 26.9	+03 35 19.0	0.300	7.53	1250	RH(c)^{7}	-	-
MACS J2135-010	21 35 12.1	−01 02 58.0	0.330	7.57	1240	UL*	< 1.17	-
A3444	10 23 50.8	−27 15 31.0	0.254	7.62	1270	MH^{7,33}	-	-
S780	14 59 29.3	−18 11 13.0	0.236	7.71	1290	MH^{7,33}	-	-
A1443	12 01 27.7	+23 05 18.0	0.270	7.74	1270	RH^{37,US*}	0.91	480
A2204	16 32 45.7	+05 34 43.0	0.151	7.96	1340	MH^{15}	-	-
A1758a	13 32 32.1	+50 30 37.0	0.280	7.99	1280	RH^{17}	5.75	600^{e}
A209	01 31 53.0	−13 36 34.0	0.206	8.17	1330	RH^{1}	1.99	676^{e}
A665	08 30 45.2	+65 52 55.0	0.182	8.23	1340	RH^{3}	2.51	527^{e}
A1763	13 35 17.2	+40 59 58.0	0.228	8.29	1320	no RH^{2}	-	-
RXC J1514.9-1523	15 14 58.0	−15 23 10.0	0.223	8.34	1330	RH^{18}	2.39	680^{e}
A1835	14 01 02.3	+02 52 48.0	0.253	8.46	1320	MH^{19}	-	-

A2142	15 58 16.1	+27 13 29.0	0.089	8.81	1420	RH$^{24,38,US(c)}$	0.19	442
A1689	13 11 29.5	−01 20 17.0	0.183	8.86	1380	RH$^{20,US(c)}$	0.95	282^{e}
A1300	11 31 56.3	−19 55 37.0	0.308	8.83	1310	RH$^{21,US(c)}$	3.80	435^{e}
A2813	00 43 27.4	−20 37 27.0	0.290	9.16	1340	UL*	< 1.4	-
A2390	21 53 34.6	+17 40 11.0	0.234	9.48	1380	RH^{36}	3.10	400
A2744	00 14 18.8	−30 23 00.0	0.307	9.56	1350	RH^{14}	17.40	890
A2219	16 40 21.1	+46 41 16.0	0.228	11.01	1450	RH^{12}	5.63	728^{e}
PSZ1 G171.96-40.64	03 12 57.4	+08 22 10.0	0.270	11.13	1440	RH$^{22,US(c)}$	4.90	600^{e}
A697	08 42 53.3	+36 20 12.0	0.282	11.48	1190	RH^{2,US}	1.51	574^{e}
A2163	16 15 46.9	−06 08 45.0	0.203	16.44	1680	RH^{23}	22.90	1034^{e}

RH = Radio Halo, MH = Mini-Halo, UL = Upper Limit, M=merger, R= relaxed. [1] Venturi et al. (2007), [2] Venturi et al. (2008), [3] Giovannini & Feretti (2000), [4] Bonafede et al. (2009), [5] Govoni et al. (2009), [6] Kale et al. (2013), [7] Kale et al. (2015) , [8] van Weeren et al. (2011), [9]Giacintucci et al. (2014b), [10]van Weeren et al. (2013), [11]Brunetti et al. (2008), [12]Bacchi et al. (2003), [13]Giacintucci et al. (2011a), [14]Govoni et al. (2001), [15] Giacintucci et al. (2014a), [16] Giacintucci et al. (2009), [17]Giovannini et al. (2006), [18]Giacintucci et al. (2011b), [19]Murgia et al. (2009), [20]Vacca et al. (2011), [21]Reid et al. (1999), [22]Giacintucci et al. (2013), [23]Feretti et al. (2001), [24]Farnsworth et al. (2013), [26]Cassano et al. (2013), [28]Pratt et al. (2005), [29]Weißman et al. (2013a), [30]Owers et al. (2011), [31]Girardi et al. (2006), [32]Wilber et al. (2018), [33]Giacintucci et al. (2017), [34]Venturi et al., in prep., [35]Kale et al. (2015), [36]Sommer et al. (2017), [37]Bonafede et al. (2015), [38]Venturi et al. (2017), [39]Shakouri et al. (2016b), [40](Bonafede et al. 2017) [p]Ferrari et al. (private communication), e clusters with available measure of the e-folding radius.

7.1 Characterization of the dynamical properties

A common approach to characterise the dynamical properties of galaxy clusters is the analysis of the X-ray surface brightness distribution. In this respect, the great majority of the clusters of our sample has pointed X-ray (*Chandra* or *XMM-Newton*) observations; only two clusters out of 75, namely A220 and Zwcl1028.8+1419, do not have pointed X-ray observations (only the RASS image is available). In order to derive information about the dynamical properties of the clusters of our sample, we estimated the morphological parameters concentration (c), centroid shift (w) and power ratios (P_3/P_0) for the 63 clusters with available X-ray *Chandra* data as described is Section 3.4 (Tab 7.2). The distributions of the morphological parameters are shown in Fig 7.2, both for all the clusters (black) and for two mass bins containing the same number of objects (the mass separating the two bins is $M_{500} = 7 \times 10^{14} M_{\odot}$). We do not find a significant dependence of the morphological parameters on the cluster mass, in line with other recent results (Rossetti et al. 2017; Lovisari et al. 2017). We note that, while the w and P_3/P_0 distributions are broad and show a single peak, we can identify a second peak in the c distribution, similar, to some extent, to what has been found using X-ray selected samples of clusters (Cavagnolo et al. 2009; Pratt et al. 2010; Rossetti et al. 2017), although with much lower significance. This hint of bimodality in the c distribution of mass-selected clusters might be interpreted as the existence of a critical value of the concentration parameter beyond which the cooling time rapidly decreases in the central regions and the cluster develops a cool core and appears highly concentrated in the X-rays. We mention that such a trend in the c distribution has not been found in larger Planck SZ-selected samples (Rossetti et al. 2017; Andrade-Santos et al. 2017). Unfortunately the comparison with our result is not straightforward, owing to the different regions where the concentration parameter is evaluated in these works. This deserves a follow-up comparison.

The most efficient way to characterize the dynamical properties of clusters is the combination of two morphological parameters, at least. In this Section we focus on the combination between c and w, which has been shown to be the most robust approach to distinguish between merger and relaxed clusters (Lovisari et al. 2017). Fig. 7.3 shows the distribution of the 63 clusters of our sample with available X-ray *Chandra* data in the $c-w$ morphological diagram. The number of clusters in this plot is almost twice the numbers used in Cassano et al. (2010b) and Cassano et al. (2013). As expected, c and w are anti-correlated and the level of dynamical disturbance increases going from the top left to the bottom right corner of the diagram. Defining a meaningful threshold between relaxed and merging clusters in the $c-w$ morphological diagram is not trivial. Lovisari et al. (2017) has recently established the dynamical status of 150 galaxy clusters from the ESZ Planck catalogue (Planck Collaboration et al. 2011c) by visually inspecting their *XMM-Newton* images. The results of the visual inspection have been then combined with a number of mor-

Table 7.2: Dynamical properties of clusters

name	c	w (10^{-2})	P3/P0 (10^{-7})	dynamics (parameters)	dynamics (visual inspection)
A2631	0.116	5.970	14.850	M[1]	M
A2219	0.134	2.127	1.681	M[1]	M
A2744	0.101	2.637	10.500	M[1]	M
A1758a	0.109	8.217	2.515	M[1]	M
RXCJ2003.5-2323	0.062	1.824	4.602	M[1]	M
A1300	0.191	4.442	6.847	M[1]	M
A773	0.184	2.403	1.445	M[1]	M
A209	0.176	1.321	0.518	M[1]	M
A520	0.097	10.050	5.259	M[1]	M
A521	0.108	2.204	5.090	M[1]	M
A697	0.153	0.731	1.668	M[1]	M
A1351	0.083	4.272	3.506	M$\surd$	M
A665	0.164	5.826	6.311	M$\surd$	M
A1689	0.363	0.463	0.076	R$\surd$	M*
A1143	0.221	5.432	1.646	M$\surd$	M
A2142	0.234	1.451	0.674	R$\surd$	m
A2218	0.184	0.858	0.474	M$\surd$	m
A1443	0.108	3.530	12.890	M$\surd$	M
A3411	0.092	1.949	2.647	M$\surd$	M
RXC J1514.9-1523	0.064	1.301	1.411	M$\surd$	M
A2390	0.304	1.171	0.694	R[1]	m
A1132	0.111	3.386	3.059	M$\surd$	M
Zwcl 0634.1+4750	0.139	0.988	5.375	M$\surd$	M
Zwcl 0104.9+5350	0.088	5.693	0.604	M$\surd$	M
A3888	0.163	2.447	0.877	M$\surd$	M
A2261	0.334	0.494	1.026	R[1]	m
PSZ1 G171.96-40.64	0.144	2.318	1.086	M$\surd$	M
PSZ1 G139.61+24.20	0.362	1.348	0.193	R$\surd$	m
RXC J1504.1-0248	0.624	0.459	0.147	R[1]	R
A1835	0.486	0.996	0.458	R$\surd$	R
A478	0.328	0.529	0.012	R$\surd$	R
A1413	0.265	0.183	0.084	R$\surd$	m
S780	0.473	0.827	0.480	R[1]	R
A2204	0.537	0.125	0.022	R$\surd$	R
RXJ1720.1+2638	0.489	0.279	0.117	R$\surd$	R
A3444	0.465	0.745	0.433	R$\surd$	R
A2667	0.406	0.926	1.395	R[1]	m
A402	0.323	1.249	1.350	R$\surd$	R
A2104	0.123	2.198	2.082	M$\surd$	M
A1733	0.133	4.219	2.674	M$\surd$	M
A2355	0.075	4.879	7.495	M$\surd$	M
A2631	0.121	1.574	1.550	M[1]	M
A781	0.111	6.374	3.143	M[1]	M
RXC J0142.0+2131	0.186	0.738	6.625	M[2]	m
A1423	0.331	0.562	1.413	R[1]	M
A2537	0.278	0.561	0.351	R[1]	M
A3088	0.339	0.284	0.833	R[2]	R
A1576	0.235	1.271	5.950	R[2]	M
A1763	0.139	1.885	1.222	M$\surd$	M
A68	0.149	1.004	3.199	M$\surd$	M
A1437	0.085	7.450	9.505	M$\surd$	M
RXC J0616.3-2156	0.115	3.042	0.614	M$\surd$	M
A2895	0.161	4.271	4.851	M$\surd$	M
RXC J0510.7-0801	0.134	2.346	2.171	M$\surd$	M
MACS J2135-010	0.138	1.188	4.073	M$\surd$	M
A2813	0.172	0.311	1.230	R$\surd$	m
A115	0.236	6.305	13.140	M$\surd$	M
A2345	0.112	3.932	19.090	M$\surd$	M
A2552	0.218	0.639	0.222	R$\surd$	M
Zwcl 2120.1+2256	0.197	1.189	3.961	M$\surd$	m
Z5247	0.158	3.362	3.061	M$\surd$	M
A1682	0.126	2.054	15.320	M[1]	M
A3041	0.099	3.342	13.620	M$\surd$	M
A56	-	-	-	-	M
A2697	-	-	-	-	R
RXC J1314.4-2515	-	-	-	-	M
A1451	-	-	-	-	M
RXC J2051.1+0216	-	-	-	-	M
RXC J1322.8+3138	-	-	-	-	m
A384	-	-	-	-	R
PSZ1 G019.12+3123	-	-	-	-	m
A2472	-	-	-	-	m
PSZ1 G205.07-6294	-	-	-	-	M

Notes – Upper panel: clusters with available X-ray *Chandra* data. $\surd$ this Thesis; [1] Cassano et al. (2010b); [2] Cassano et al. (2013); * based on optical studies performed by Andersson & Madejski (2004). Lower panel: clusters with available *XMM-Newton* data.

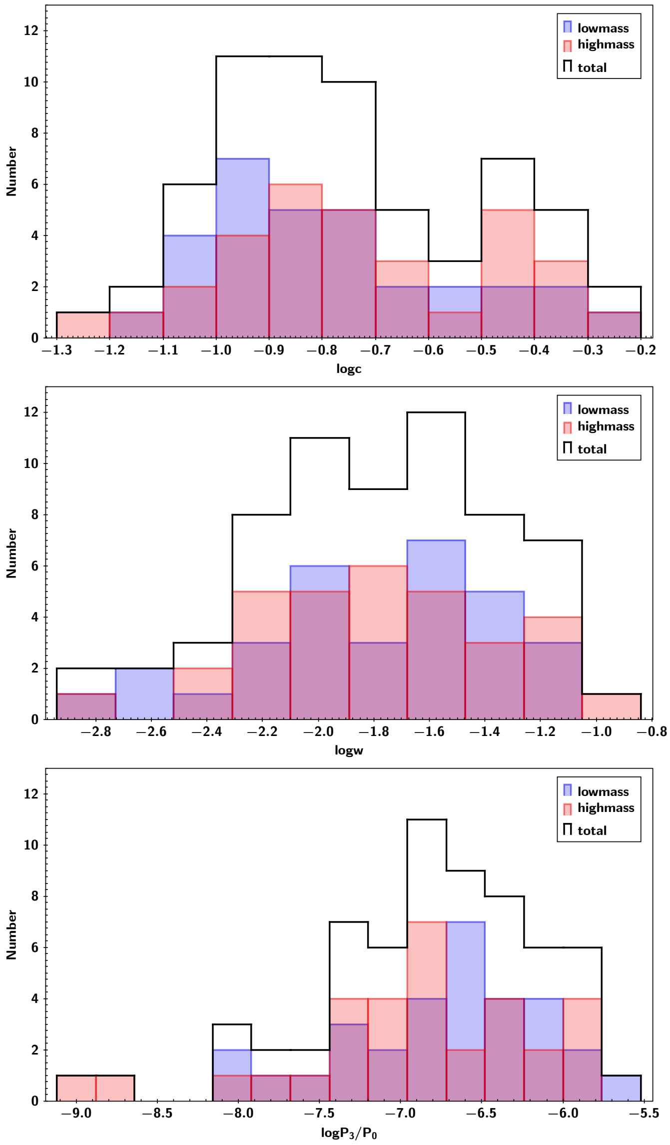

Figure 7.2: concentration parameter (*top*), centroid shift (*middle*) and power ratios (*bottom*) distribution of the clusters with available X-ray *Chandra* data

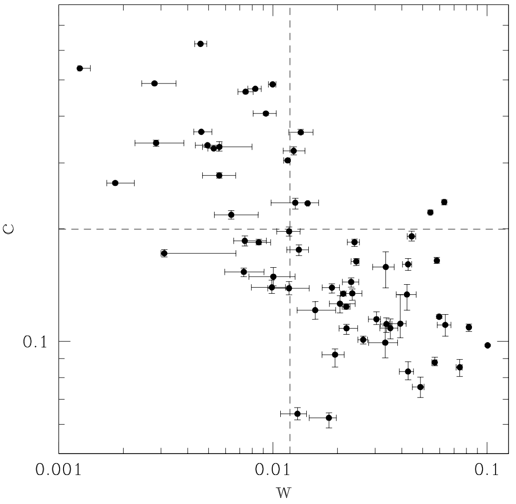

Figure 7.3: $c - w$ morphological diagram. Black lines are adapted from Cassano et al. (2010b) and are $c = 0.2$ and $w = 0.012$.

phological parameters, including c, w and P_3/P_0, to determine the threshold values between merging and relaxed clusters. They found that among the clusters with a clear dynamical classification (not "intermediate" cases) $\sim 40\%$ are relaxed and $\sim 60\%$ are merging. Similar fractions have been obtained for mass-selected samples using cool core vs non-cool core clusters as indication of relaxed systems and non relaxed systems (Rossetti et al. 2017; Andrade-Santos et al. 2017). Unfortunately, we cannot simply adopt the threshold found in Lovisari et al. (2017) because the parameters are measured within different apertures. Indeed, as mentioned in Section 3.4, we focused on the apertures adopted in Cassano et al. (2010b) that have been selected to constrain cluster dynamics on scales similar to radio halos. Still, we note that the classification of merging and relaxed clusters based on the lines derived by Cassano et al. (2010b) to separate radio halo and non-radio halo clusters actually gives similar results. Indeed $\sim$40% of our clusters lie on the upper left panel of Fig. 7.3. This suggests that, although those lines where not derived to distinguish merging from relaxed clusters, they still give reasonable statistical information on the dynamics of clusters. The dynamical classification of the clusters of our sample, based on the morphological diagram $c - w$, is reported in Table 7.2 (column 5).

In addition, we visually classified each cluster on the basis of the X-ray *Chandra* image (Table 7.2, column 6). In particular, we identified three classes of clusters marked with "M", "m" or "R" in Table." M" represents clusters where the merging status is clear from the distribution of the X-ray surface brightness and from the presence of substructures, "R" represents relaxed clusters with circular X-ray morphology and peaked cores and "m" indicates intermediate cases, where the morphology is fairly regular, sometimes with a peaked core, but with substructures or features in the X-ray distribution indicating a more complex situation. The two methods of classification are entirely consistent for clusters lying at the corners of the $c - w$ morphological diagram, while there is some discrepancy for objects lying in the central region, where clusters should be classified as relaxed according to the morphological parameters, but our visual inspection reveals some hints of disturbance.

Among the 12 clusters of our sample without available *Chandra* data, 10 have archival *XMM-Newton* data. We classified the dynamical status of these clusters by visually inspecting their *XMM-Newton* images (Fig. 7.4) and we report these classifications in the bottom panel of Table 7.2. We could not infer the dynamical status of the two clusters without pointed X-ray observations.

Based on the analysis of the morphological parameters of the 63 clusters with available *Chandra* data we estimate a fraction of merging clusters of $\sim 66\%$. Among the same 63 clusters, we identify almost the 85% of merging (M and m) clusters by visual inspecting the X-ray *Chandra* images. We find a similar result extending the visual approach to the clusters with *XMM-Newton* observations. The fraction of merging clusters derived from *our* visual inspection is larger than that found by Lovisari et al. (2017). Although the visual classification is subjective, the point here is that among fairly relaxed clusters there are some systems showing minor disturbances that are not caught by morphological parameters. These might be minor mergers, to which the cool core survives, but the X-ray distribution shows edges or irregularities. Alternatively, there may be signatures of disturbance on larger scales with respect to the radius adopted to measure the parameters, such as surface brightness substructures in the cluster outskirts. Still, we believe that the information from the visual inspection of the X-ray images of clusters can be useful when interpreting their radio properties (Section 7.2).

7.2 Properties of radio halos

In this PhD project we built the largest mass-selected sample of galaxy clusters with deep radio observations available to date. Thanks to the work done in this Thesis (Chapter 5 and 6), the radio data analysis of the sample is complete and each cluster has at least one pointed observation from which we can derive information about the presence or absence of radio diffuse emission. We summarize below the diffuse sources detected in our sample (references are given in Table 7.1):

- 29 (∼38%) clusters host radio halos, 8 of them are USSRHs or candidate USSRHs
- 7 (∼10%) clusters have radio relics, 5 of them also have radio halos (and have been already counted above), 2 are without radio halos
- 10 (∼13%) clusters have mini halos

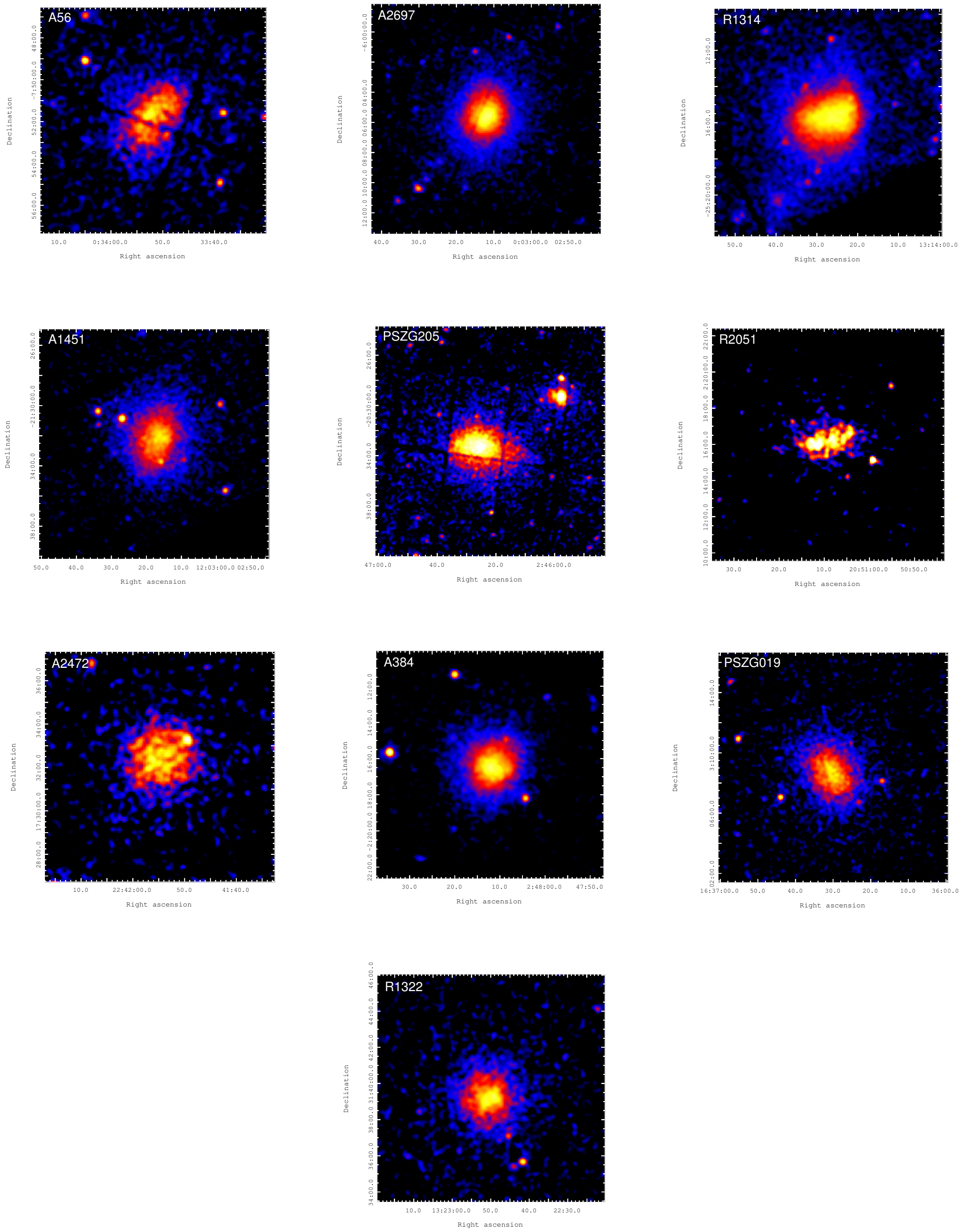

Figure 7.4: *XMM-Newton* images of the clusters without available *Chandra* data.

Table 7.3: Properties of the added clusters

Name	z	M_{500} (10^{14} $M_{\odot}$)	$P_{1.4GHz}$ (10^{24} W Hz^{-1})	R_{500} (kpc)	R_{H} (kpc)
CL0016+16	0.541	8.67	5.01	1190	460^{e}
A545	0.154	4.43	1.41	1098	393^{e}
Coma	0.023	5.29	0.76	1217	339
A2256	0.058	6.34	0.85	1280	502^{e}
Bullet	0.296	12.41	23.44	1478	582^{e}
A2255	0.081	5.19	0.81	1190	528^{e}
A2319	0.056	8.59	2.45	1420	510^{e}
MACSJ0717.5+3745	0.548	11.24	52.48	1299	560
A1995	0.319	5.15	1.66	1090	345^{e}
MACSJ1149.5+2223^{US}	0.544	8.55	2.29	1180	512
El Gordo	0.870	8.79	26.0	1050	632^{e}
A746	0.232	5.56	3.07	1150	826
PSZ1 G285.0-2307	0.390	8.57	1.72	1259	230
MACSJ0949.8+1708	0.380	8.22	1.70	1250	360
MACSJ1752.0+4440	0.366	6.96	12.2	1188	468
MACSJ0553.4+3342	0.431	9.39	6.88	1278	488
A754^{US}	0.054	6.68	0.63	1310	510^{e}
A2034^{US}	0.113	5.85	0.48	1160	400
RXCJ 1115.8+0129	0.350	6.36	0.47	1160	–
A2645	0.251	5.02	0.59	1110	–
A267	0.230	4.95	0.34	1110	–
RXJ0439.0+0715	0.244	5.75	0.46	1160	–
A611	0.288	5.85	0.43	1150	–
A2146	0.234	3.85	0.39	1020	–
RXC J2228.6+2037	0.365	7.82	0.95	1210	–

Notes – Upper panel: radio halos from Cassano et al. (2013); Middle panel: radio halos from Martinez Aviles et al. (2016); Bottom panel: upper limits from Cassano et al. (2013). e clusters with available measure of the e-folding radius.

Moreover, we found candidate diffuse emission in 6 clusters, one is a candidate mini halo and 5 are candidate radio halos. 28 (∼37%) clusters do not show any hint of diffuse emission at the sensitivity of current observations. Combining our work with the work done by Venturi et al. (2008), Kale et al. (2013) and Kale et al. (2015) for the GRHS and Bonafede et al. (2017) we have upper limits for 22 clusters. Being obtained with similar techniques (Section 4.3), the upper limits from the literature are comparable with those derived in this Thesis.

In the following we will focus on radio halos. The sample is mainly devoted to derive the occurrence of cluster-scale radio emission in connection with cluster dynamics and mass. Additionally, the wealth of information from this sample can be useful to investigate scaling relations between thermal and non-thermal properties of galaxy clusters. However, the study of scaling relations using only our sample is difficult because of the small range of cluster masses (Fig. 7.1). For this reason, to study the scaling relations, we will include, as an extension to our sample, a subsample based on Cassano et al. (2013) and Martinez Aviles et al. (2016), containing clusters at higher redshift and/or smaller masses. The additional clusters are listed in Table 7.3. Radio powers in Tables 7.1 and 7.3 are calculated as:

$$P_{1.4GHz} = 4\pi D_L^2 S_{1.4GHz} (1+z)^{-(\alpha+1)} \tag{7.1}$$

where D_L is the luminosity distance of the cluster, $S_{1.4GHz}$ is the flux density of the radio halo at 1.4 GHz and $(1+z)^{-(\alpha+1)}$ is the k-correction factor (with $S_\nu \propto \nu^\alpha$). When α is unknown, we assume $\alpha = -1.3$. All the radio powers in this sample are measured at 1.4 GHz, except the ones of RXC J1514.9-1523 and MACSJ0949.8+1708. To consider the large uncertainty on the spectral index of those two radio halos, that have been measured only at 330 MHz, we associated an error of 30% to their radio power at 1.4 GHz.

For each cluster, the radius within which the density is 500 times the critical density of the Universe at that redshift, R_{500}, is calculated from M_{500} by assuming an NFW profile (e.g. Navarro et al. 1997) for the dark matter halos and the concentration-mass relation in Duffy et al. (2008).

The size of radio halos is another parameter that will be used in this Thesis. It is commonly measured from the 3σ isophotes of the radio maps. However, this approach may be affected by the sensitivity of the radio images. Indeed, the radio halo brightness decreases with increasing distance from the center of the cluster, eventually falling below the detection limit of the observation. An obvious drawback of this approach is, for example, that fainter radio halos would appear smaller for a given sensitivity of the observations. An unbiased estimate of the size of radio halos can be obtained by fitting the azimuthally averaged brightness profile with an exponential law in the form $I(r) = I_0 e^{r/r_e}$, where I_0 is the central brightness and r_e is the e-folding radius, i.e. the radius at which the brightness is equal to I_0/e (Orrú et al. 2007; Murgia et al. 2009). This approach faces some problems as well: the presence of discrete sources embedded in the diffuse emission induces systematics in

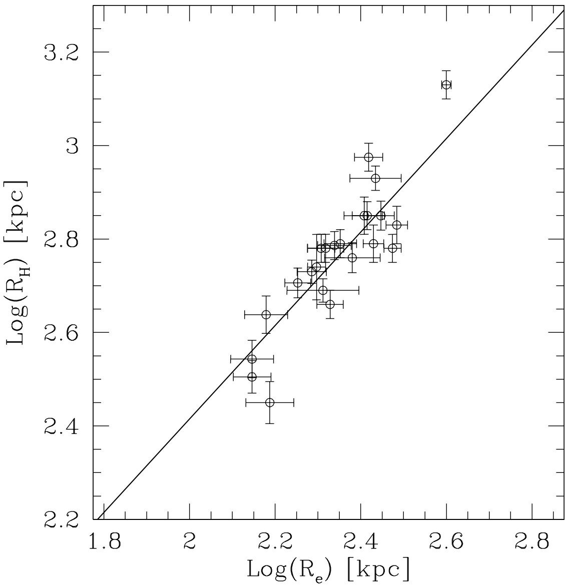

Figure 7.5: R_H vs r_e for the clusters that have both the measurements available. The black line is $R_H = 2.6 \times r_e$.

the fitting procedures, many radio halos are not azimuthally symmetric and, in the case of faint halos, the fit is anchored on a few data points (e.g. Fig. 3 in Murgia et al. 2009)) and, consequently, the brightness profile is essentially "extrapolated" from the central regions. In addition, the fitting procedure requires the analysis of the radio images, which we do not have for several clusters from the literature. Here, we adopt the following procedure to derive the radius of radio halos (R_{radio}) without introducing significant biases:

- we estimated the e-folding radius for the clusters marked with e in Table 7.1 and 7.3.
- For the other clusters we estimated the radius of the radio halo as $R_H = \sqrt{R_{max} \times R_{min}}$, where R_{max} and R_{min} are the minimum and maximum radii of the 3σ surface brightness isocontours (e.g. Cassano et al. 2007; Giacintucci et al. 2017).

We estimated R_H also for the radio halos that have the measurement of r_e and we found a good correlation between the two quantities, being $R_H \approx 2.6 \times r_e$ (Fig. 7.5), this suggests that there are no significant statistical biases introduced by mixing the two techniques. Since we will use the radii to estimate the emissivity of radio halos (see Section 7.3), for clusters having both the measurements we adopted the minimum between R_H and $2.6 \times r_e$. This is a good choice for the following reasons: 1) when $R_H < 2.6 \times r_e$ the radio power is measured inside R_H. At the same time, in the cases with $R_H > 2.6 \times r_e$, the emissivity calculated inside

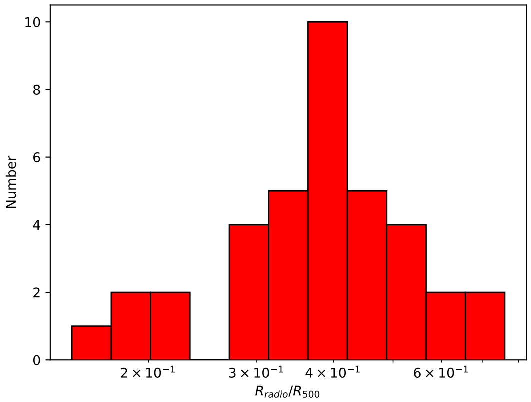

Figure 7.6: Distribution of the radio halos radii. Te five clusters lying on the left tail, separated from the main distribution are: A3411, Z0634, A2218, PSZG285 and A1689.

R_H would be underestimated as compared to the other clusters because it is likely that the luminosity integrated between $2.6 \times r_e$ and R_H is just a small fraction of the total radio halo luminosity ($S = 2\pi f r_e^2 I_0$, where $f = 1 + e^{-r'}(-a-1) > 0.8$ for $r' > 3 \times r_e$).

We show the distribution of the radii of radio halos (with respect to R_{500} of each cluster) in Fig. 7.6. The majority of radio halos are distributed around $R_{radio}/R_{500} = 0.35 - 0.5$, then there are a few clusters in a tail of slightly larger R_{radio}/R_{500} (A2163, A2744, A746 and El Gordo) that are well known to be the among the largest radio halos known today. On the other hand, there are five radio halos that are about two times smaller than the typical radio halos and have $R_{radio}/R_{500} = 0.2$, they are in the clusters Z0634, A3411, A1689, PSZG205 and A2218. Interestingly, the size of these five radio halos roughly coincides with the threshold value between radio halos and mini halos ($R_H \approx 0.2 \times R_{500}$ defined by Giacintucci et al. (2017), indicating that they could be objects with intermediate properties.

7.2.1 Radio halo – merger connection

It is widely accepted that radio halos are preferentially found in merging clusters (e.g. Cassano et al. 2010b, 2012; Bonafede et al. 2015, see also Section 3.5.2). In this context, our sample offers the opportunity to assess the radio halo merger connection with unprecedented statistics. Fig. 7.7 shows the three morphological diagrams $c - w$, $c - P_3/P_0$ and $w - P_3/P_0$, where radio halo clusters are quite well separated from non-radio halo clusters, with the former lying on the merging region and the latter lying on the relaxed region of the diagrams. Mini halos are included among the clusters without radio halos in Fig. 7.7 (black dots) and they all lie in the regions of relaxed systems. According to the morphological parameters

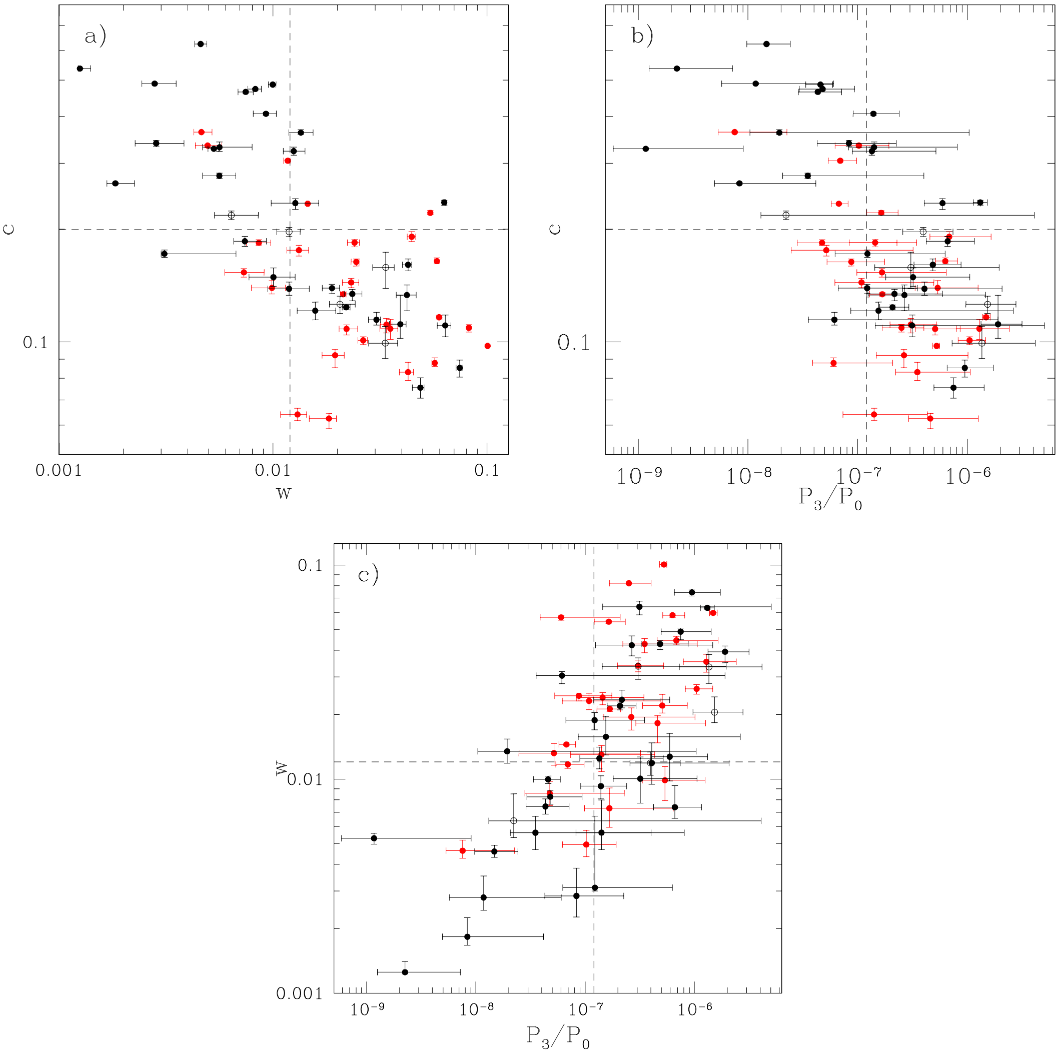

Figure 7.7: a) $c - w$, b) $c - P_3/P_0$, c) $w - P_3/P_0$ morphological diagrams for the clusters of our sample with available X-ray *Chandra* data. Vertical and horizontal dashed lines are adapted from Cassano et al. (2010b) and are: $c = 0.2$, $w = 0.012$, and $P_3/P_0 = 1.2 \times 10^{-7}$. Red and black dots represent clusters with radio halos and clusters without radio halos, respectively

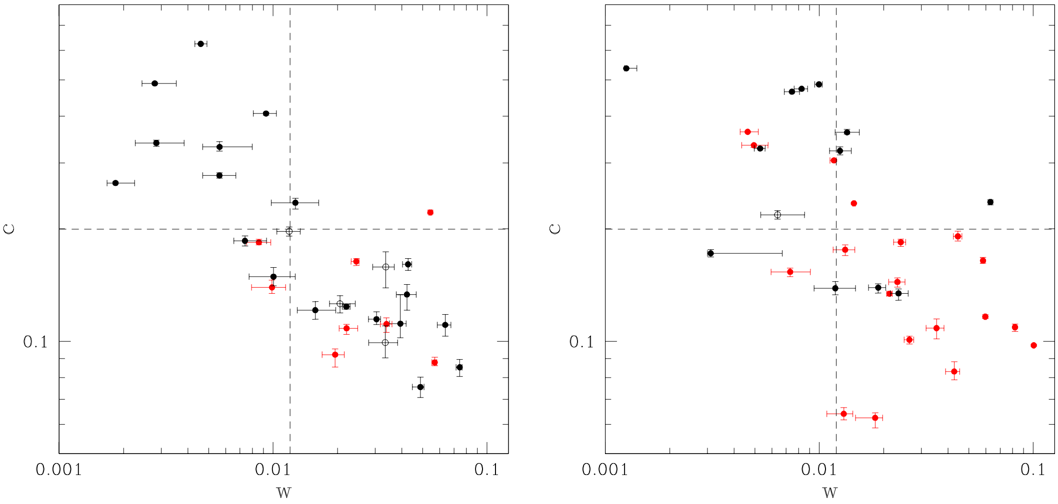

Figure 7.8: $c-w$ diagram for low mass (*left*) and high mass (*right*) clusters. Symbols are the same as in Fig. 7.7.

classification and considering that A1689 is a merging system with the merger occurring along the line of sight (Andersson & Madejski 2004), the 90% of radio halos is hosted by merging clusters, while only the 10% is found in relaxed systems. This is the first time that striking evidence for a connection between mergers and radio halos is found in a large and mass-selected sample of galaxy clusters. Such a connection becomes even more evident considering that: (i) among the 3 relaxed systems hosting a radio halo, A2142 ($c = 0.234$, $w = 1.451$) is a nearby massive minor merging system hosting multiples Mpc-scale cold fronts (Markevitch et al. 2000; Owers et al. 2011; Rossetti et al. 2013) and (ii) the remaining two systems that are relaxed from the morphological parameters and host radio halos are A2390 ($c = 0.304$, $w = 1.171$) and A2261 ($c = 0.334$, $w = 0.494$) that, however, would not be classified as relaxed according to our visual inspection, since they show signatures of ongoing dynamical activity. A further information contained in Fig.7.7 is that $\sim$ 60% of merging clusters hosts a radio halo. This is another important result being achieved for the first time using a mass-selected sample of galaxy clusters. It confirms previous studies (e.g. Cassano et al. 2013; Bonafede et al. 2017) and suggests that mergers are not the unique players in the formation of radio halos (see Brunetti & Jones 2014, for a discussion on the many ingredient and complexity of the problem). One player is the mass of the clusters that sets the amount of energy released during merger events.

To investigate the role of the cluster mass in the radio halo merger connection, we split the sample into two mass bins with the same number of clusters (separated by $M_{500} = 7 \times 10^{14} M_{\odot}$). We show the $c-w$ diagrams for the two mass bins in Fig. 7.8. We focus on c and w because, as we mentioned earlier, they are the most robust parameters to define the dynamical status of clusters and they are also determined with much higher accuracy with respect to the power ratios. An important information can be derived from Fig. 7.8: the fraction of merging clusters without radio halo is ∼20% in high mas systems, while it is ∼65% in low mass objects. It is the first time that an increase of the fraction of merging clusters without radio halos at smaller masses can be claimed from statistical grounds. This evidence can be interpreted in the framework of turbulent re-acceleration models as the consequence of the fact that massive and merging systems form radio halos emitting up to high frequency, while merging event in low mass cluster may not induce enough turbulence to accelerate particles up to the energies necessary to emit radiation at GHz frequency. These clusters are the best candidate to search for USSRHs (e.g. Cassano et al. 2012). In this respect, we asked and obtained uGMRT time in the 250-500 MHz band to observe 4 of the merging clusters without radio halos and we obtained 8 hours with LOFAR at 140 MHz to observe A1763, the most massive merging cluster without radio halo in our sample. Furthermore, we note that the 3 clusters with radio halos that appear dynamically relaxed from the morphological parameters are all in the high-mass bin. This suggests that, while minor mergers in massive clusters may be sufficient to generate radio halos even though the X-ray morphology of the cluster does not look extremely disturbed, low mass-systems need major mergers introducing a large amount of turbulent energy in the ICM to accelerate electrons and produce radio diffuse emission.

For the sake of completeness, we mention that ∼ 50% of relaxed clusters in our sample host a mini halo.

7.3 Radio power-mass correlation

It is well know that the radio luminosity of giant radio halos correlates with the mass of the host clusters (Basu 2012; Cassano et al. 2013; Martinez Aviles et al. 2016; Duchesne et al. 2017). In this Section we use the findings of this Thesis to investigate and update such correlation.

In Fig. 7.9 (left panel) we show radio power, $P_{1.4GHz}$, vs mass, M_{500}, for all the clusters of our sample hosting radio halos and USSRHs and having upper limits to the diffuse emission. Since the mass range of our sample is too small to study the possible correlation with the radio power of radio halos, we added the radio halos and the upper limits from Cassano et al. (2013) and Martinez Aviles et al. (2016) (Table 7.3) to our sample. We will refer to the sum of our sample and this extension as the “extended sample”. We are aware that the addition of a sub-sample of clusters without a well defined selection function, as opposed to our original sample, may add systematics to the derived correlation (e.g. Mantz et al. 2010). At the same time, the extended sample allows us to study the radio power-mass relation in a lager mass range and with larger statistics. In particular we will use 47 radio halos (11 of which are USSRHs or candidate) and 30 upper limits (upper limits will be used in Section 7.3.1). We stress that the extended sample is not a statistical sample, therefore it will not be used to derive the fraction of clusters with radio halos (Section 7.5).

To investigate the correlation between the radio power of radio halos and the mass of the host clusters we followed the procedure outlined in Cassano et al. (2013). Specifically, we fit a power-law relation in the log-log space by adopting the BCES-bisector linear regression algorithm (Akritas & Bershady 1996) which treats the variables symmetrically and takes measurement errors in both variables into account. We fitted the observed $P_{1.4GHz} - M_{500}$ data points with a power-law in the form:

$$\log\left(\frac{P_{1.4GHz}}{10^{24.5}\mathrm{Watt/Hz}}\right) = B\,\log\left(\frac{M_{500}}{10^{14.9}\,M_{\odot}}\right) + A \tag{7.2}$$

where A and B are the intercept and the slope of the correlation, respectively.

Considering $Y{=}\log\frac{P_{1.4GHz}}{10^{24.5}}$ and $X{=}\log\frac{M_{500}}{10^{14.9}}$, and having a sample of N data points (X_i, Y_i) with errors $(\sigma_{X_i}, \sigma_{Y_i})$ the raw scatter of the correlation can be estimated as:

$$\sigma^2_{raw} = \frac{1}{N-2}\sum_{i=0}^{N} w_i (Y_i - BX_i - A)^2 \tag{7.3}$$

where

$$w_i = \frac{1/\sigma_i^2}{(1/N)\sum_{i=0}^{N} 1/\sigma_i^2} \quad \text{and} \quad \sigma_i^2 = \sigma_{Y_i} + B^2\sigma^2_{Y_i} \tag{7.4}$$

Since we are dealing with a limited sample, we obtain a sampled regression line that can deviate from the true (unknown) regression line. To evaluate the 95% confidence region of the best-fit relation, i.e. the area that has the 95% probability of containing the "true" regression line, we calculated the 95% confidence interval of the mean value of Y, $\langle Y\rangle$. For a given X, this is $\langle Y\rangle \pm \Delta Y$, where:

$$\Delta Y = \pm 1.96\sqrt{\left[\sum_{i=0}^{N}\frac{(Y_i - Y_m)^2}{N-2}\right]\left[\frac{1}{N} + \frac{(X - X_m)^2}{\sum_{i=0}^{N}(X_i - X_m)^2}\right]} \tag{7.5}$$

where $Y_m = BX_i + A$ and $X_m = \sum_{i=0}^{N} X_i/N$ for each observed X_i.

The result of the fitting procedure applied to the extended sample is shown in Fig. 7.9 (right panel). The slope of the correlation is $B = 4.73 \pm 0.70$, the intercept is $A = 0.025 \pm 0.079$ and the scatter is $\sigma_{raw} = 0.44$ if we exclude USSRHs. The best-fit relation has the same slope, but a lower normalization ($A = 0.089 \pm 0.075$) and a larger scatter ($\sigma_{raw} = 0.54$) when we include USSRHs. This arises from the steepness of their spectra, since USSRHs are significantly less luminous than typical radio halos at 1.4 GHz.

7.3.1 On the radio bimodality of galaxy clusters

The radio luminosity-mass correlation found in the previous section is steeper with respect to the one derived by e.g. Cassano et al. (2013) or Martinez Aviles et al.

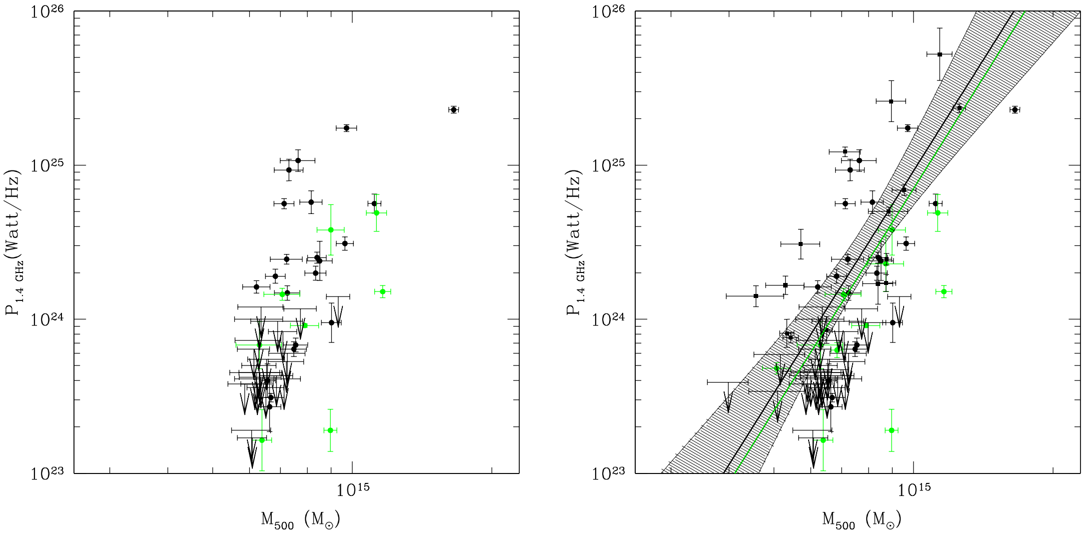

Figure 7.9: *Left*: $P_{1.4GHz} - M_{500}$ diagram for the clusters of our sample. Black dots are radio halos, arrows are upper limits and green dots are USSRHs or candidate USSRHs. *Right*: Distribution of clusters in the $P_{1.4GHz} - M_{500}$. Black dots are radio halos belonging to our sample, black squares are radio halos belonging to the extended sample, arrows are upper limits and green dots are USSRHs or candidate USSRHs. Best-fit relation to radio halos only (black line and shadowed region) and to both radio halos and USSRHs (green line).

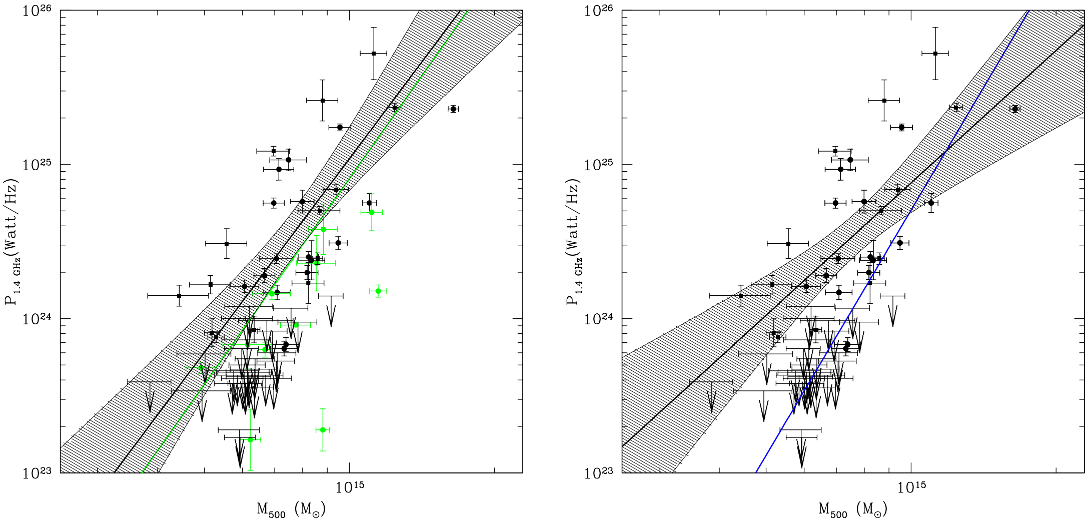

Figure 7.10: *Left*: distribution of clusters in the $P_{1.4GHz} - M_{500}$. Black dots are radio halos belonging to our sample, black squares are radio halos belonging to the extended sample, arrows are upper limits and green dots are USSRHs or candidate USSRHs. Best-fit relation to radio halos only (black line and shadowed region) and to both radio halos and USSRHs (green line). *Right*: Same distribution as in left panel. The best fit relation including only radio halos derived with the EM regression method is shown with its 95% confidence region (black line and shadowed region). The blue line is best-fit relation to radio halos plus upper limits.

(2016) (Section 2.2.5), owing to the presence of few radio halos lying on the region of the upper limits. The extended sample that we are using to investigate the correlation is almost twice the size of the Cassano et al. (2013) sample. As we mentioned in Section 6.3, the increased statistics has allowed the discovery of radio halos underlying the correlation found by Cassano et al. (2013). Some of them are or might be USSRHs, generated during less energetic merger events and/or at higher redshift. Alternatively, they could be "off-state" halos where the emission is essentially maintained by the continuous injection of secondary electrons of hadronic interactions in the ICM. Underluminous radio halos could also be observed in clusters in the very early or very late stage of merging activity, when the radio halo is lighting up or switching off. Another possibility is that they are smaller than the giant radio halos lying on the Cassano et al. (2013) correlation. Small radio halos may be generated during minor mergers where turbulence is dissipated in a small fraction of the cluster volume only. In this case, it is reasonable to expect that they have a synchrotron emissivity ($\propto$ radio power/R_H^3) similar to that of larger radio halos, but they are less luminous simply because the total luminosity is produced inside a smaller volume. In this respect, we showed in Section 7.2 that five clusters host radio halos that are a factor 2 smaller than typical radio halos (in R_{radio}/R_{500}). Since their luminosity is generated in a much smaller volume, their radio power cannot be directly compared to the power of giant radio halos. Also, their radio power cannot be directly compared to the upper limits because upper limits are derived using $R_{radio} = 500$ kpc by choice (that is about $R_{radio}/R_{500} \sim 0.4$ for the typical masses and redshift in our sample). Therefore, we removed them from the radio luminosity mass diagram and we performed the fit again. The result is shown in Fig. 7.10 (left panel). The slope of the correlation, excluding USSRHs, is $B = 4.17 \pm 0.59$, the intercept is $A = 0.12 \pm 0.074$ and the scatter is $\sigma_{raw} = 0.45$. The values obtained including USSRHs are $B = 4.43 \pm 0.60$, $A = -0.035 \pm 0.77$ and $\sigma_{raw} = 0.53$. The correlation is still steeper than that obtained by Cassano et al. (2013), while it is consistent with the finding of Martinez Aviles et al. (2016). As we expected, given the significant increase of the statistics, the scatter of the correlation is larger with respect to Cassano et al. (2013), as a consequence of the complex superposition of different radio halo stages and type of merging events.

We consider the correlation found excluding the USSRHs as the reference case. In fact, because of their steep spectra, USSRHs have radio luminosities at 1.4 GHz systematically lower than the typical luminosities of radio halos at that frequency (see Fig. 7.9 and 7.10) and this may induce systematics in the correlations (see also Cassano et al. 2013).

For clusters with $M_{500} \gtrsim 5.5 \times 10^{14} M_\odot$ we found that almost all the upper limits (except two) are below the 95% confidence region of the correlation, confirming the bimodal behaviour of massive galaxy clusters in the radio power mass diagram.

To further investigate the radio bimodality of clusters in the $P_{1.4GHz} - M_{500}$ diagram, we made use of another method of regression analysis, based on the Expectation Maximization (EM) algorithm, that is implemented in the ASURV package (Isobe et al. 1986) and deals with upper limits as "censored data". This method allows to study the effect of the upper limits on the correlation and to investigate the presence of a bimodality. We applied the EM regression algorithm to the radio halos and to the radio halos plus upper limits. The resulting best fits are shown in Fig. 7.10. All the upper limits but one lie well below the correlation; most importantly, the correlation that includes the upper limits (blue line) is much steeper than the best fit relation to radio halos only and has a different normalization. This analysis suggests that radio halos and upper limits belong to two distinct populations of galaxy clusters: those hosting radio halos lie on the correlation, those without radio halos occupy a different region of the diagram.

We note that the two fitting methods, BCESS and EM, give different best fit relations. We point out that the reference method to study the correlation parameters (slope and normalization) is the BCESS regression (Isobe et al. 1986, 1990; Cassano et al. 2013), while EM is necessary to investigate the role of upper limits.

7.3.2 The role of redshift

Similarly to what has been found in the radio power-X-ray luminosity diagram (Brunetti et al. 2007, 2009; Kale et al. 2015), the two populations, radio halos and upper limits, in the radio luminosity-mass plot from Cassano et al. (2013) are separated with a region in between that is less populated (see Section 2.2.5). The bimodal distribution of clusters in the radio power-mass (or X-ray luminosity) diagram has been interpreted as the consequence of the fact that the time scale of the radio halo evolution (amplification and suppression of the synchrotron emission) is smaller than both the radio halo life time and the time that clusters spend as non-radio halo systems (Brunetti et al. 2009; Donnert et al. 2013). This separation seems less clear in our sample (Fig. 7.10). On one hand, we have already mentioned that the increased statistics is expected to lead to the discovery of radio halos in the transition region that are currently switching on or off. On the other hand, we should point out that the redshift range we are analysing here is much larger than that analysed by e.g. Cassano et al. (2013). This implies that our upper limits, that are similar in terms of flux limits, span a broader range of luminosity distances and thus a larger range of radio powers, since $P_R \propto D_L^2$ (see also Section 5.3). In order to assess the presence of a clear separation between radio halos and upper limits it is necessary to compare detections and non-detections at similar luminosity distance. Therefore, we split the extended sample into two bins with similar luminosity distance. In particular, in Fig. 7.11, we show the radio power-mass diagram for clusters at $z = 0.1 - 0.2$ (left panel) and at $z = 0.2 - 0.3$ (right panel). These redshift bins roughly coincide with those of our statistical sample, still, with the extension, we are adding a few lower mass or lower declination clusters.

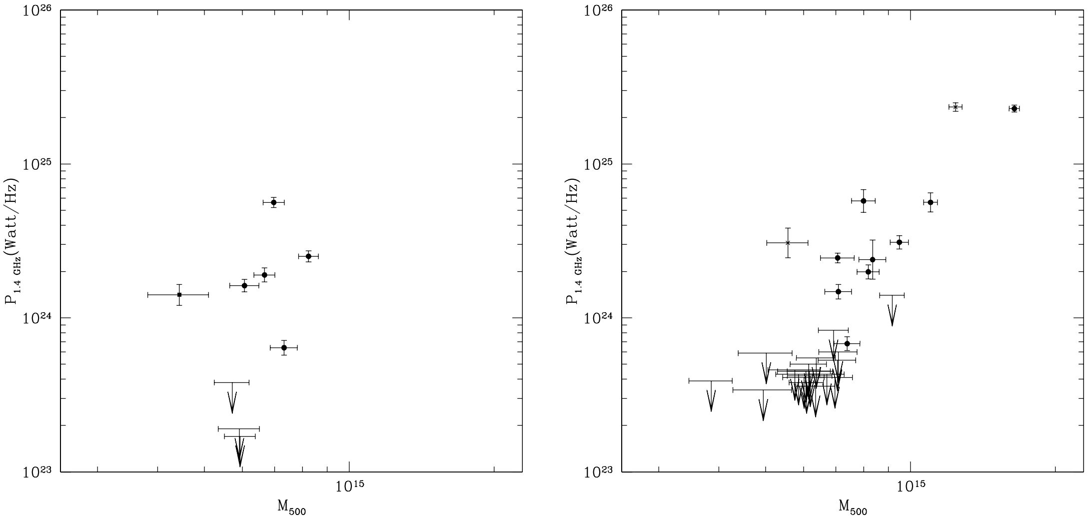

Figure 7.11: $P_{1.4GHz}$ vs M_{500} for clusters in the redshift range $0.1-0.2$ (*left*) and $0.2-0.3$ (*right*). Symbols are the same as in Fig.7.10. USSRHs are not shown.

At low redshift the statistics is scarce, still the few available upper limits are clearly below all detections. At higher redshift there is only one radio halo close to the region of the upper limits, in line with the scenario outlined above. Fig. 7.11 (right panel) highly resembles the diagram published in Cassano et al. (2013), in fact the redshift ranges are similar and the observations from which the upper limits have been derived are similar, as well.

7.4 Emissivity versus mass

To study the distribution of the clusters in the radio power mass diagram we removed the smallest radio halos, whose size significantly deviates from the distribution of the sizes of the radio halos in the extended sample (Fig. 7.6). More generally, the different emitting volumes of radio halos may drive a significant fraction of the scatter in the $P_{1.4GHz} - M_{500}$ diagram. Therefore, one possibility to remove this effect is to look at the emissivities, instead of the radio luminosities.

Murgia et al. (2009) compared the emissivities of giant radio halos with those of mini halos. They found that the emissivity does not change significantly among radio halos, whereas mini halos have much higher emissivities than radio halos. Our extended sample allows to look at the emissivities in radio halos improving the statistics by a factor three with respect to Murgia et al. (2009). In addition, we can study, for the very first time, the distribution of radio halos and upper limits in the emissivity-mass diagram and investigate the presence of a possible bimodality.

The emissivity of radio halos is calculated as $\frac{P_{1.4GHz}}{R^3_{radio}} \times \sqrt{\frac{R_{min}}{R_{max}}}$, where R_{radio}, R_{min}

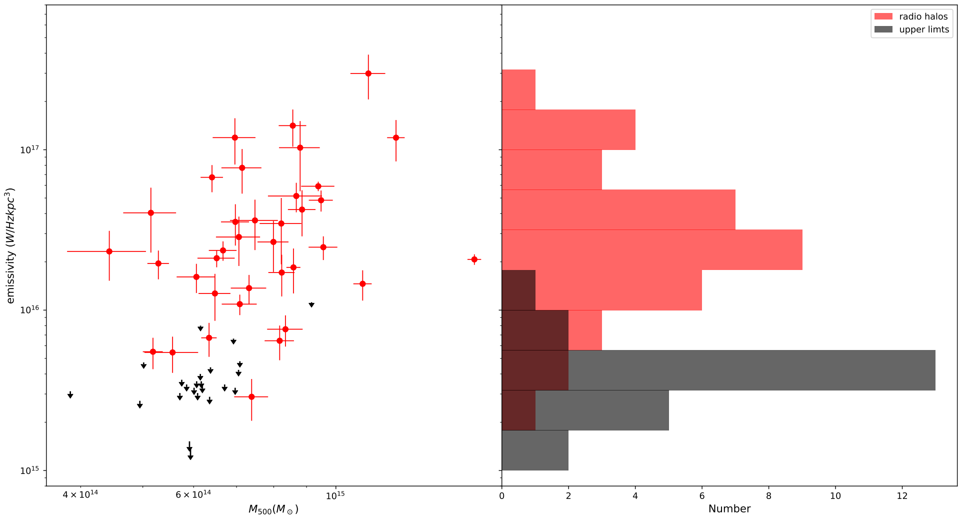

Figure 7.12: Distribution of clusters belonging to the extended sample in the emissivity–M_{500} diagram. Red dots are radio halos, black arrows are upper limits. Only upper limits at $z < 0.3$ are shown.

and R_{max} are defined as in Section 7.2 and $\sqrt{\frac{R_{min}}{R_{max}}}$ accounts for the ellipticity of radio halos; for the upper limits $R_{radio} = 500$ kpc.

The emissivity vs mass diagram for the clusters of the extended sample is shown in Fig. 7.12, together with the distribution of the emissivity of radio halos and upper limits. Upper limits at $z > 0.3$ are not taken into consideration in this plot, because they are not suitable to be directly compared to the distribution of radio halos due to the sensitivity of our observations, as discussed in Section 4.3. Also, USSRHs are not shown as their emissivity would be systematically below that of the other radio halos. For the sake of completeness, in Fig. 7.13 we show the same plot for both radio halos and upper limits at $z < 0.3$ in the statistical sample. The emissivity of radio halos is broadly distributed around $\sim 3 \times 10^{16}$ W/Hz kpc^{-3}, while upper limits lie almost ten times below and are peaked around $\sim 4 \times 10^{15}$ W/Hz kpc^{-3}. Interestingly, the five small radio halos in Fig. 7.6, which we excluded from the radio luminosity vs mass analysis, are all consistent or above the peak of the emissivity distribution, indicating that their radio power is below the radio power of giant radio halos simply because it is emitted from a smaller volume. The large scatter of the emissivity distribution of radio halos might be contributed by the uncertainties in the measurement of the radii of radio halos. However, a large fraction of the scattering is likely due to the intrinsic scatter in radio halos with similar spectrum. This is naturally expected as different clusters may have different distributions of the magnetic fields and different number density of seed particles to re-accelerate.

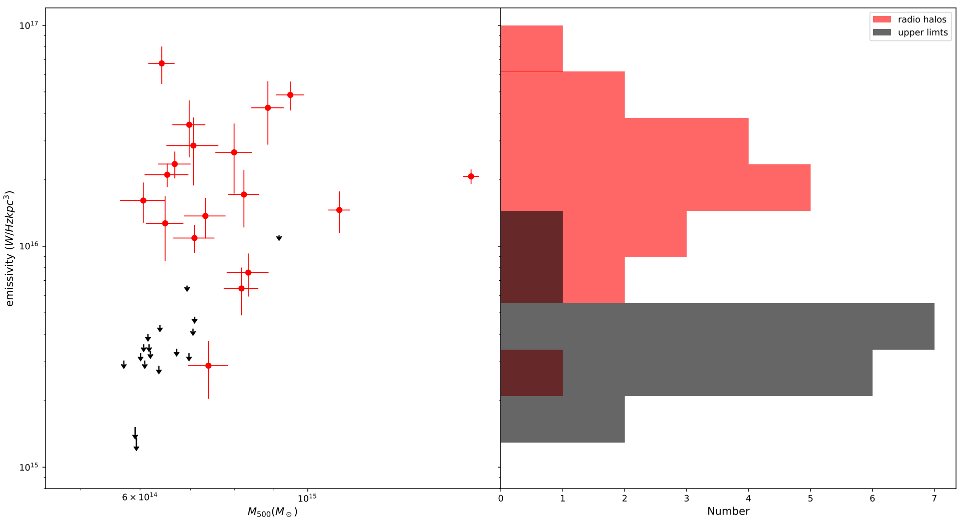

Figure 7.13: Distribution of clusters belonging to the statistical sample and having $z < 0.3$ in the emissivity–M_{500} diagram. Red dots are radio halos, black arrows are upper limits.

For the first time, after removing the systematics from the spectrum (USSRHs are excluded) and the scattering from different emitting volumes (emissivities), we are now able to estimate that this intrinsic scatter is about a factor 10 (Fig. 7.12 and 7.13).

Most importantly, for the first time, we discovered that clusters have a bimodal distribution in emissivity (Fig. 7.12 and 7.13), with upper limits obtained for non radio halo clusters sitting about ten times below the typical emissivity of radio halos. We stress that this result is unaffected by biases, since the bimodal distribution is clear also in the statistical sample (Fig. 7.13). This is a way to look at the bimodality of galaxy clusters that is complementary to that of the radio power-mass distribution. This way is probably even more straightforward as it is not affected by the scattering that is induced by the different volumes of radio halos.

7.5 Occurrence of radio halos

The aim of this section is to determine the occurrence of radio halos as a function of the cluster mass in our mass-selected sample of galaxy clusters and compare our results with the expectations of the turbulent re-acceleration model. We have already performed a similar analysis considering a sub-sample of clusters that had available radio information about the possible presence of diffuse emission at the beginning of this PhD project (Section 3.5.1). We showed that the fraction of clusters with radio halos increases with the mass of the host clusters and, most importantly, we found, for the first time, that the fraction of radio halos drops from high to low mass clusters, as predicted by models based on the turbulent re-acceleration scenario. However, that result could be biased because of the incompleteness of the radio information, indeed there was a relatively high number of clusters (18 out of 75) that were not included in the analysis because they did not have any deep radio observation (see Section 3.7).

Now that, at the end of the PhD program, we have observed these remaining 18 clusters with the GMRT and/or the JVLA, we can update this study deriving, for the very first time, the occurrence of radio halos in a complete mass-selected sample of galaxy clusters. To do that, we focus on the statistical sample (Table 7.1) without considering the additional clusters from Cassano et al. (2013) and Martinez Aviles et al. (2016).

The great majority of the galaxy clusters with radio upper limits are below the 95 percent confidence level spanned by the radio power-mass correlation (Fig. 7.10); we classify these clusters as non-radio halos. In a few cases, clusters are classified as non-radio halo from the literature using deep radio observations; although no upper limits were derived, we classified also these cases as non-radio halos. However, there are two upper limits consistent with the correlation in our sample, and four clusters for which we were not able to derive upper limits due to problems in the observations. Moreover there are five candidate radio halos in the sample. These 11 clusters have uncertain classification. We will consider two cases: a "reduced sample", which does not include the uncertain cases at all and the total sample with a guess about the presence of diffuse emission in the uncertain clusters.

Following the procedure adopted in Section 3.5.1, we split the sample into two mass bins and measured the fraction of clusters with radio halos, f_{RH}, in the low-mass bin (LM, $M < M_{lim}$) and in the high-mass bin (HM, $M > M_{lim}$). In particular, we used $M_{lim} = 8 \times 10^{14} M_{\odot}$, since we showed that it is the value of limiting mass giving the most significant result (Section 3.5.1). With this partition we have:

- 60 clusters in the LM bin, among which 10 host radio halos, 4 host USSRHs, 3 host radio halos with R_H/R_{500} ~0.2 and 11 have uncertain classification (5 candidate radio halos and 6 clusters without solid upper limit).

- 15 clusters in the HM bin, 7 of which have radio halos, 4 have USSRHs and one has a radio halo with R_H/R_{500} ~0.2.

Having defined these mass bins, the fraction of clusters with radio halos in the HM bin is $f_{RH} = \frac{12}{15} = 80\%$, whereas, in the LM bin, $f_{RH} = \frac{17}{49} = 35\%$ if we consider the "reduced" sample and it is $f_{RH} = \frac{22}{60} = 37\%$ in the total sample. For the total sample, we assumed that candidate radio halos actually host radio halos and clusters without good upper limits do not host radio halos. We point out that a random assignment of radio halos among the 11 uncertain clusters would lead to almost equal results.

As in Section 3.6, we used numerical codes based on Cassano & Brunetti (2005) to derive the expected probability of forming radio halos as a function of the cluster mass in the framework of turbulent re-acceleration models (see Sections 2.1 and 3.6 for more details). We calculated the theoretical formation probability of radio halos with steepening frequency ν_s >600 MHz and ν_s >140 MHz as a function of the cluster mass in the redshift range $z = 0.08 - 0.33$ (Fig. 7.14). The uncertainties in the model (red and blue shadowed regions) are calculated with Monte Carlo extraction from the large number of theoretical merger trees and take into account the statistical error introduced by the limited size of our observed sample. The value of ν_s >600 MHz can be considered as a reference frequency for both VLA 1.4 GHz and GMRT 610 MHz observations, that constitute the great majority of the available radio observations for the clusters of our sample. However, some of the USSRHs observed in our sample may have ν_s <600 MHz, in that case, they should be "counted" as radio halos only in the comparison with model expectations with ν_s >140 MHz. Therefore we will derive the fraction of radio halos both considering USSRHs as radio halo clusters and as non-radio halos clusters.

The theoretical model for the formation of radio halos fixes the size of the emitting volume at $R_H = 500$ kpc (Section 2.1, Cassano & Brunetti 2005; Cassano et al. 2006), that corresponds to $R_{radio}/R_{500} \sim 0.4$ for the typical masses of our cluster sample. This is consistent with the average/typical sizes of radio halos in our sample. On the other hand, the theoretical volume is a factor 6-8 larger than the volume of the five small radio halos in our sample ($R_{radio}/R_{500} \sim 0.2$, Fig. 7.6). If turbulence is generated in a smaller volume V_t, as in the case of the small radio halos, the theoretical procedure followed by Cassano & Brunetti (2005) would assume that this turbulence is redistributed into a fixed volume $V_H = \frac{4}{3}\pi(500\text{kpc})^3$ causing a decline of the particle acceleration efficiency ($\chi \propto (V_t/V_H)^2$) and consequently a steepening of the spectrum of the halo ($\nu_s \propto \chi^2$). Therefore, in the comparison between models and observations, we shall consider small radio halos as non radio halos or, alternatively, as USSRHs.

The fraction of clusters with radio halos in the two mass bins that we use to compare with model expectations are shown in Table 7.4: in the upper panel we consider the total sample whereas, in the lower panel, we exclude clusters with uncertain classification ("reduced sample"). In both cases (total or "reduced" sample) we consider three possibilities: A) small radio halos and USSRHs are non radio clusters, B) small radio halos are non radio halo clusters whereas USSRHs are, C) both small radio halos and USSRHs are considered as radio halo clusters.

In general, we found that the fraction of radio halos is higher in the HM bins than in the LM bins, ranging from $\sim$ 50% to $\sim$ 80% in the HM bin and from $\sim$ 20% to $\sim$ 35% in the LM bin. We thus confirmed the existence of a drop in f_{RH} at low mass systems with a complete ($\gtrsim$ 80% mass completeness) mass-selected sample of galaxy clusters. We show the comparison between the predicted and observed fraction of radio halos as a function of mass in Fig. 7.14. We note that the difference

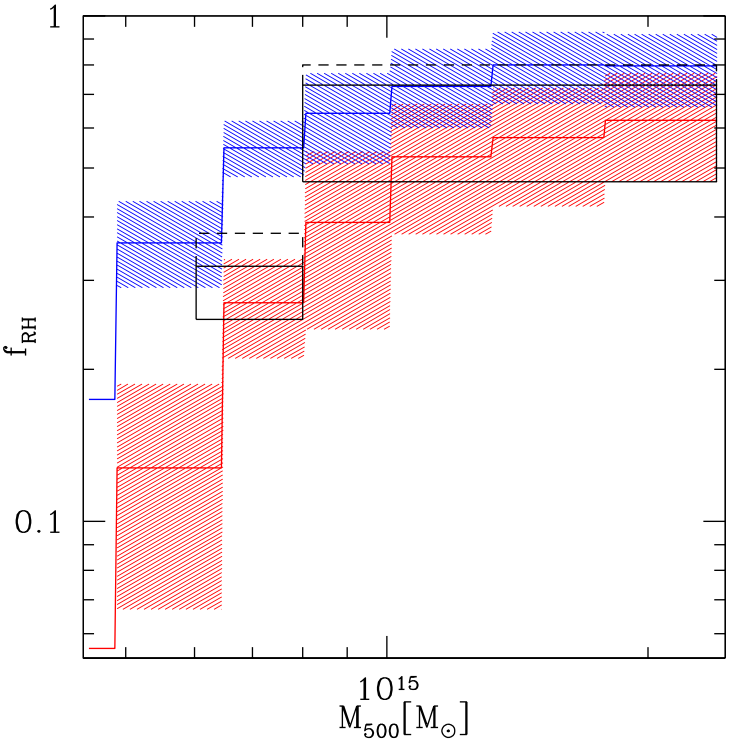

Figure 7.14: Expected fraction of clusters with radio halos with steepening frequency $\nu_s > 600$ MHz and $\nu_s > 140$ MHz in the redshift range $0.08 < z < 0.33$ (red and blue lines and shadowed regions, respectively). Calculations have been performed for the following choice of model parameters: $b = 1.5$, $\langle B \rangle = 1.9$ μG (where $B = \langle B \rangle \times (M/\langle M \rangle)^b$), and $\eta_t = 0.2$ (see Cassano et al. 2012, and references therein). The observed fraction of clusters with radio halos in the two mass bins is overlaid and refers to the total sample (black rectangles). The solid lines range from case A to B (Table 7.4), while the dashed line includes case C.

Table 7.4: Observed fraction of radio halos

	A		B		C	
	f_{RH}(LM)	f_{RH}(HM)	f_{RH}(LM)	f_{RH}(HM)	f_{RH}(LM)	f_{RH}(HM)
total sample	$\frac{15}{60} = 0.25$	$\frac{7}{15} = 0.47$	$\frac{19}{60} = 0.32$	$\frac{11}{15} = 0.73$	$\frac{22}{60} = 0.37$	$\frac{12}{15} = 0.80$
reduced sample	$\frac{10}{49} = 0.20$	$\frac{7}{15} = 0.47$	$\frac{14}{49} = 0.29$	$\frac{11}{15} = 0.73$	$\frac{17}{49} = 0.35$	$\frac{12}{15} = 0.80$

Notes - A: small radio halos and USSRHs are non radio clusters; B: small radio halos are non radio halo clusters, USSRHs are radio halo clusters; C: small radio halos and USSRHs are considered as radio halo clusters.

between the total and the "reduced" samples in terms of f_{RH} is marginal (Table 7.4), thus, in Fig. 7.14, we focus on the total sample, for clarity. In spite of the basic assumption adopted in the model there is a remarkable agreement between the observed fraction of clusters with radio halos in the two mass bins and the model expectation.

The observed fraction of radio halos in the LM bin, when USSRHs and small radio halos are taken into account (case C in Table 7.4), is in between the models with $\nu_s > 600$ MHz and $\nu_s > 140$ MHz. This is consistent with the fact that a fraction of known USSRHs (at least the steepest ones) have steepening frequency $\nu_s < 600$ MHz and are not "counted" as radio halos in the model with $\nu_s > 600$ MHz. At the same time, the discrepancy between the model predictions for $\nu_s > 140$ MHz and the observed fraction of radio halos in the LM bin implies that a number of radio halos in low mass clusters should be discovered with future low frequency observations.

Our results provide strong support to the current view for the formation of radio halos that is based on particle acceleration driven by cluster merger turbulence.

Furthermore, we point out that models like the one in Fig. 7.14 take into account the formation of galaxy clusters and (under their assumptions) calculate the generation of turbulence, the particle acceleration and the emerging synchrotron spectrum self consistently. These models are anchored to the observed mass distribution function of clusters (Press & Schechter 1974) and to the rate of mergers that is predicted by the standard ΛCDM model and consequently the fact that the occurrence of radio halos declines at smaller masses implies that an increasing number of merging systems are predicted to be non-radio halo clusters when observed at frequencies > 600 MHz. This is exactly what we found in Section 7.2.1. At the same time, however, the same models predict that a fraction of these mergers will generate radio halos that glow up at lower frequencies (e.g. Cassano et al. 2006, 2010a, 2012, see also Fig. 7.14). Consequently, we expect that a large fraction of the merging systems in our sample that do not show radio halos (or that show only faint residual cluster-scale emission) at the GMRT and JVLA will be USSRHs that can be detected by future low frequency (e.g. LOFAR) observations.

Chapter 8

Summary and conclusions

The study of the statistical properties of radio halos in galaxy clusters has became increasingly important in the last decade; it is a powerful tool to unveil the connection and evolution of radio halos with cluster dynamics and test the theoretical models for their origin of the diffuse synchrotron emission in galaxy clusters.

The ambitious aim of this Thesis was to carry out a large statistical study, in the radio and X-ray bands, of the first complete mass-selected sample of galaxy clusters to obtain solid constraints on the connection between radio halos and the dynamics and mass of the host clusters. This is a major step forward in this field.

With this goal in mind, we extracted 75 clusters with $M_{500} \gtrsim 6 \times 10^{14} M_{\odot}$ and $0.08 < z < 0.33$ from the Planck SZ catalogue (PSZ1, Planck Collaboration et al. 2014a). This sample is more than 80% complete in mass. Thanks to the observational campaign (with the GMRT and the JVLA) and the data analysis carried out during this PhD program, this is the largest and most complete mass-selected sample of galaxy clusters with adequate radio information about the possible presence of diffuse emission available to date. Therefore, this sample allows the assessment of the statistical properties of radio halos is galaxy clusters with unprecedented statistics.

Beyond the statistical study of radio halos, the large number of data analysed in this Thesis also yielded many by-products, including the discovery of mini halos, radio relics and peculiar radio galaxies in our clusters.

We summarize below the main results of this Thesis.

8.1 Discovery of radio halos

During this Thesis we analysed numerous clusters without previous information in the radio band. As a consequence, we discovered a number of radio halos and candidate radio halos.

- **A1451 and Z0634**
  In Chapter 6 we reported on the discovery of new radio halos in A1451 and

Z0634 with GMRT 330 MHz and JVLA D and B array observations. With radio powers $P_{1.4GHz} = 6.4 \pm 0.7 \times 10^{23}$ W/Hz and $P_{1.4GHz} = 3.1 \pm 0.2 \times 10^{23}$ W/Hz, respectively, they are both underluminous with respect to the radio power-mass correlation in Cassano et al. (2013). Underluminous radio halos are statistically subdominant in the population of radio halos, however, they constitute an important piece of the puzzle, as their occurrence provides information on the evolution of these sources. Contrary to theoretical expectations for very young ("switching on") or very old ("switching off") radio halos, the halos in A1451 and Z0634 do not have steep spectra. We estimated that the spectral index of these radio halos is $-1.3 \lesssim \alpha \lesssim -1.0$. Based on their small size, compared to the typical size of radio halos in clusters with similar masses, we proposed that they might be generated during minor mergers, where turbulence has been dissipated in smaller volumes. This possibility complicates the theoretical scenario for the formation of radio halos and deserves future theoretical work on the diffusion and transport of turbulence in the ICM. The results on the clusters A1451 and Z0634 have been published in Cuciti et al. (2018).

- **A3888 and A1443**
  During the PhD, two radio halos in clusters belonging to our sample (A3888 and A1443) have been discovered and published by other authors. We observed these clusters, as part of our observational campaign, and we derived complementary information allowing an assessment of the spectral and morphological properties of these targets.
  The radio halo in A3888 has been discovered by Shakouri et al. (2016b) with ATCA observations at 1.25-2.55 GHz. We observed it at 330 MHz with the GMRT and we detected a bright radio halo ($S_{330MHz} = 450$ mJy) with a complex morphology (Section 5.1.1), highly resembling the one described by Shakouri et al. (2016b). The combination of the two datsets suggests that the radio halo has a very steep spectrum.
  Bonafede et al. (2015) detected a radio halo in A1443 with GMRT 330 MHz observations. In Section 5.1.2, we analysed GMRT 610 MHz and JVLA 1.5 GHz observations of A1443, finding indication of a possible steep spectrum. Therefore, we observed this cluster with the GMRT also at 150 MHz and we reprocessed all the GMRT datasets (including the one in Bonafede et al. (2015)) with the same procedure. We found that the spectrum of the radio halo is $\alpha \sim -1.65$, placing it in the rare class of USSRHs.

- **Candidate diffuse emission in Z2120 and A3041**
  We detected cluster scale suspect diffuse emission in two merging clusters: Z2120 (with GMRT 330 MHz and JVLA D array observations) and in A3041 (with JVLA C array data). These sources have been discussed in Sections 5.2.1 and 5.2.2. They are faint and only detected as positive residual emission

at 2-3 sigma level, however, their spatial coincidence with the X-ray emission of the clusters, suggests that they could be connected to the ICM.
The residuals in Z2120 are seen in both observations at 330 and 1500 MHz and the tentative combination of the two datasets suggests the presence of very steep spectrum emission. Therefore, an observation of Z2120 has been scheduled among the LOFAR SKP Tier 1 observations in cycle 9. We also obtained uGMRT observations at 250-500 MHz to follow-up A3041.

8.2 Interesting by-products

- **Candidate relic in A1451**
  We detected an elongated diffuse source ~ 15 arcmin North of the center of A1451, that we classified as a candidate radio relic (Section 6.1.2). This source has a radio power $P_{1.4GHz} = 1.13 \pm 0.06 \times 10^{24}$ W/Hz and a spectral index between 330 and 1500 MHz $\alpha = -1.1 \pm 0.1$. If this source is at the cluster redshift, its projected distance from the cluster center is ~ 3 Mpc, which would be the largest distance measured for relics. We proposed that this relic could be the result of an accretion/external shock propagating through some clouds of relativistic plasma, similarly to other cases (e.g. van Weeren et al. 2017); the presence of a compact source embedded in the diffuse emission supports this scenario.

- **A shocked head tail radio galaxy in Z0634**
  We discovered a long head tail radio galaxy with peculiar characteristics in the cluster Z0634 (Section 6.2.2). The spectral index between 320 and 1500 MHz steepens from the head to the tail (from $\alpha = -0.65$ to $\alpha = -2.4$), however this steepening is not consistent with a purely radiative ageing of electrons. Moreover, there is a spot of high surface brightness along the tail and the second part of the tail, after the spot, is brighter than the first part, before the spot. We showed that the interaction of this radio galaxy with a weak shock ($\mathcal{M} \lesssim 2$) moving toward the outskirts of the cluster can explain the observed properties. We note that evidence for interactions between head tails and weak shocks and gas motions in the ICM of dynamically active clusters are becoming common thanks to low frequency studies with LOFAR (Shimwell et al. 2016; Wilber et al. 2018; de Gasperin et al. 2017). These mechanisms are likely to affect the life-cycle of relativistic particles in the ICM and deserve future theoretical studies.

- **Mini halo in PSZG139**
  In Section 5.1.3, we presented the discovery of a ~ 100 kpc sized mini halo in the core of PSZG139 with GMRT 610 MHz observations and JVLA C array observations at 1.5 GHz. An edge of the mini halo roughly coincides with a cold front detected with X-ray *Chandra* data, as observed in other mini halos

in the literature. The spectral index of the mini halo is $\alpha_{1500MHz}^{330MHz} \sim -1.3$. A recent LOFAR 140 MHz follow-up of this cluster revealed the presence of radio emission extending on larger scales. We estimated that the spectra index of such emission is $\alpha \sim -1.7$. PSZG139 is the first cool-core cluster where a mini halo at high frequency coexists with larger scale emission at low frequency. This can be interpreted as the results of a minor merger that did not destroy the core and dissipated a relatively low amount of energy on large scale, generating synchrotron emission with very steep spectrum.

- **Candidate mini halo in A402**
  Two GMRT 610 MHz observations of A402 are available in the archive. We found that both these observations show the presence of diffuse emission in the central region of the cluster, although on slightly different scales (Section 5.2.3). In the most sensitive image, the emission appears confined in the core of the cluster, as typical of mini halos. The other image reveals some diffuse emission extending on larger scales, but, given the low sensitivity, the contribution of the discrete sources is unclear. Therefore, we classified the central radio emission in A402 as a candidate mini halo.

8.3 Statistical analysis of the sample

Our total sample consists of 75 clusters. Now that the data analysis is completed, each cluster of the sample has at least one pointed observation from which we can derive information about the possible presence of diffuse emission. For clusters without radio halos we derived upper limits to their diffuse radio luminosity. Furthermore, 73 clusters, out of 75, have pointed X-ray (*Chandra* or *XMM-Newton*) observations that can be used to infer their dynamical status. To do that, we analysed the X-ray surface brightness distribution of clusters with available *Chandra* data and we derived the morphological parameters (concentration, centroid shift and power ratios) that are powerful diagnostics of the presence of dynamical disturbance. For clusters with only *XMM-Newton* data we inferred their dynamical status from the visual inspection of the images. We discussed the results of the morphological analysis in Section 7.1. According to the morphological parameter classification, the fraction of merging clusters in our sample is $\sim 60\%$, in line with recent studies of mass-selected samples.

We summarize the main steps and results from the statistical analysis of the radio halo properties in our sample below.

- **First step on the statistical analysis**
  As a first step, in Chapter 3, we focused on the analysis of a subsample of 57 clusters with available radio information in the literature (plus our NVSS reprocessing). Although not complete, at that time (2015) this was by far the largest sample of galaxy clusters selected in mass. This sample allowed

us to carry out a first study of the statistics of radio halos in mass-selected clusters. In order to study the occurrence of radio halos as a function of the cluster mass, we split the sample into two mass bins and we measured the fraction of clusters with radio halos in the two bins separately. For the very first time, we showed that the fraction of clusters with radio halos increases with increasing the host cluster mass. Most importantly, the fraction of radio halos drops from $\approx 80\%$ in high mass clusters to $\approx 30\%$ in low mass systems, in line with the expectations from turbulent re-acceleration models.
Using X-ray Chandra data, available for 50, out of 57, clusters, we confirmed that radio halo clusters are merging systems while non-radio halo clusters are relaxed, highlighting the role of merger in the formation of radio halos.
The results of the first step of the statistical analysis have been published in Cuciti et al. (2015).

- **Analysis of the total sample**
  After the completion of the radio information (Chapeters 5 and 6), we performed the statistical analysis of the radio properties on the total sample in Chapter 7.

  We studied scaling relations between the radio luminosity of radio halos and the mass of the host clusters in Section 7.3. In order to maximize the range of masses spanned by clusters and to further increase the statistics, we combined our sample with an extended sample of radio halos from the literature that allowed us to add a number of clusters at smaller masses and higher redshifts. The total number of clusters (with radio halos and with upper limits to the radio halo luminosity) is about twice the one used by e.g. Cassano et al. (2013). The correlation is steeper and has a larger scatter with respect to previous finding from Cassano et al. (2013). We confirmed theoretical expectations predicting that USSRHs should be underluminous. The increased scatter makes scaling relations more complex to interpret, however, this is a natural consequence of the increased statistics (and removal of the possible observational biases) in the complex scenario where the halo luminosity is powered by scattered merger events that generate a variety of intermediate states.

  A fundamental piece of information that we investigated is the possible presence of a radio bimodal behaviour of galaxy clusters. Once the scatter, induced by the broad redshift distribution of the clusters in our sample and by the different sizes of radio halos, is removed (Sections 7.3.1 and 7.3.2), we found that clusters tend to have a bimodal behaviour in the radio power-mass diagram, with radio halos following the correlation and upper limits lying below the scaling relation. The measured occurrence of clusters in the region between radio halos and limits in the radio power-mass diagram can be used in future studies to constrain the life-time of radio halos and the timescale of

switch-on/off of radio halos.
For the first time, we investigated the distribution of clusters in the radio emissivity-mass diagram (Section 7.4), finding a clear bimodal behaviour between radio halos and upper limits. This finding is unaffected by statistical biases (e.g. X-ray selection, mass incompleteness); in fact a bimodal behaviour in radio emissivity is clear also when we limit the analysis to our mass-selected sample. The fact that clusters with similar masses have different non-thermal properties, opens the possibility of putting fundamental constraints on the time evolution and origin of radio halos.

Similarly to previous studies we found that the bimodal behaviour of clusters is strengthened by the separation of those clusters in the dynamical status, indeed the 90% of radio halos is hosted by merging clusters, while only the 10% is found in relaxed systems.

With the same procedure adopted during the first step of the analysis, we studied the occurrence of radio halos as a function of the cluster mass (in the range $6 - 20 \times 10^{14} M_{\odot}$), this time, in a complete mass-selected sample of galaxy clusters (Section 7.5). We confirmed the presence of a drop in the fraction of radio halos in lower mass clusters. Specifically, the fraction of radio halos in the high mass bin is $\approx 80\%$, whereas it is $\approx 30\%$ in the low mass bin. We compared this result with the expected probability of forming radio halos, derived in the framework of turbulent re-acceleration models. The agreement between the predicted and the observed fraction of radio halos as a function on the mass is remarkable. Interestingly, we also found that the fraction of merging systems without radio halos that are firmly detectable in our GMRT and JVLA observations increases in clusters with smaller masses, in line with theoretical models. As an unavoidable consequence of these models we should expect that a large fraction of these merging clusters without radio halos in our sample should show diffuse emission at low frequency. LOFAR and MWA observation will test this prediction.
The statistical analysis of the total sample will be presented in a forthcoming paper (Cuciti et al. in prep.).

This PhD project was ambitious and yielded new constraints on the evolution of radio halos and on their connection with cluster dynamics that will be a long-standing reference for theoretical and interpretative efforts in the field. The increased complexity of the radio properties of galaxy clusters, that emerged from this work, paved the way to future, more detailed, theoretical studies. The results of this Thesis provide a a legacy value for the future, for two main reasons: 1) this sample is an unique starting point to search for USSRHs with lo frequency observations (LOFAR, MWA, SKA) and 2) the derived statistical properties will constitute the linchpin to anchor future studies (up to high redshift and down to small masses) with more sensitive facilities (uGMRT, LOFAR, SKA). This work, combined with future *studies will provide unique diagnostics for our understanding of the non-thermal emission in galaxy clusters.*

Bibliography

Abell, G. O. 1957, AJ, 62, 2

Ackermann, M., Ajello, M., Albert, A., et al. 2014, ApJ, 787, 18

Ackermann, M., Ajello, M., Albert, A., et al. 2016, ApJ, 819, 149

Ackermann, M., Ajello, M., Albert, A., et al. 2015, ApJ, 812, 159

Ackermann, M., Ajello, M., Allafort, A., et al. 2010, ApJ, 717, L71

Ajello, M., Costamante, L., Sambruna, R. M., et al. 2009, ApJ, 699, 603

Ajello, M., Rebusco, P., Cappelluti, N., et al. 2010, ApJ, 725, 1688

Akamatsu, H. & Kawahara, H. 2013, PASJ, 65, 16

Akritas, M. G. & Bershady, M. A. 1996, ApJ, 470, 706

Andersson, K. E. & Madejski, G. M. 2004, ApJ, 607, 190

Andrade-Santos, F., Jones, C., Forman, W. R., et al. 2017, ApJ, 843, 76

Angulo, R. E., Springel, V., White, S. D. M., et al. 2012, MNRAS, 426, 2046

Asai, N., Fukuda, N., & Matsumoto, R. 2004, ApJ, 606, L105

Asai, N., Fukuda, N., & Matsumoto, R. 2007, ApJ, 663, 816

Ascasibar, Y. & Markevitch, M. 2006, ApJ, 650, 102

Bacchi, M., Feretti, L., Giovannini, G., & Govoni, F. 2003, A&A, 400, 465

Bartelmann, M., Meneghetti, M., Perrotta, F., Baccigalupi, C., & Moscardini, L. 2003, A&A, 409, 449

Basu, K. 2012, MNRAS, 421, L112

Bauer, F. E., Fabian, A. C., Sanders, J. S., Allen, S. W., & Johnstone, R. M. 2005, MNRAS, 359, 1481

Bell, A. R. 1978a, MNRAS, 182, 147

Bell, A. R. 1978b, MNRAS, 182, 443

Bernardi, G., Venturi, T., Cassano, R., et al. 2016, MNRAS, 456, 1259

Best, P. N., von der Linden, A., Kauffmann, G., Heckman, T. M., & Kaiser, C. R. 2007, MNRAS, 379, 894

Bîrzan, L., Rafferty, D. A., McNamara, B. R., Wise, M. W., & Nulsen, P. E. J. 2004, ApJ, 607, 800

Blasi, P. 2001, Astroparticle Physics, 15, 223

Blasi, P. & Colafrancesco, S. 1999, Astroparticle Physics, 12, 169

Bleem, L. E., Stalder, B., de Haan, T., et al. 2015, ApJS, 216, 27

Böhringer, H., Pratt, G. W., Arnaud, M., et al. 2010, A&A, 514, A32

Böhringer, H., Schuecker, P., Guzzo, L., et al. 2004, A&A, 425, 367

Bonafede, A., Brüggen, M., van Weeren, R., et al. 2012, MNRAS, 426, 40

Bonafede, A., Cassano, R., Brüggen, M., et al. 2017, MNRAS, 470, 3465

Bonafede, A., Feretti, L., Giovannini, G., et al. 2009a, A&A, 503, 707

Bonafede, A., Feretti, L., Murgia, M., et al. 2010, A&A, 513, A30

Bonafede, A., Giovannini, G., Feretti, L., Govoni, F., & Murgia, M. 2009b, A&A, 494, 429

Bonafede, A., Intema, H., Brüggen, M., et al. 2015, MNRAS, 454, 3391

Bonafede, A., Intema, H. T., Brüggen, M., et al. 2014a, ApJ, 785, 1

Bonafede, A., Intema, H. T., Brüggen, M., et al. 2014b, MNRAS, 444, L44

Bonafede, A., Vazza, F., Brüggen, M., et al. 2013, MNRAS, 433, 3208

Borgani, S., Murante, G., Springel, V., et al. 2004, MNRAS, 348, 1078

Botteon, A., Gastaldello, F., & Brunetti, G. 2017, ArXiv e-prints [1707.07038]

Botteon, A., Gastaldello, F., Brunetti, G., & Dallacasa, D. 2016a, MNRAS, 460, L84

Botteon, A., Gastaldello, F., Brunetti, G., & Kale, R. 2016b, MNRAS, 463, 1534

Bourdin, H., Mazzotta, P., Markevitch, M., Giacintucci, S., & Brunetti, G. 2013, ApJ, 764, 82

Bravi, L., Gitti, M., & Brunetti, G. 2016, MNRAS, 455, L41

Brown, S., Emerick, A., Rudnick, L., & Brunetti, G. 2011, ApJ, 740, L28

Brown, S. & Rudnick, L. 2011, MNRAS, 412, 2

Brüggen, M., Bykov, A., Ryu, D., & Röttgering, H. 2012, Space Sci. Rev., 166, 187

Brüggen, M., Ruszkowski, M., Simionescu, A., Hoeft, M., & Dalla Vecchia, C. 2005, ApJ, 631, L21

Brunetti, G. 2003, in Astronomical Society of the Pacific Conference Series, Vol. 301, Matter and Energy in Clusters of Galaxies, ed. S. Bowyer & C.-Y. Hwang, 349

Brunetti, G. & Blasi, P. 2005, MNRAS, 363, 1173

Brunetti, G., Blasi, P., Reimer, O., et al. 2012, MNRAS, 426, 956

Brunetti, G., Cassano, R., Dolag, K., & Setti, G. 2009, A&A, 507, 661

Brunetti, G., Giacintucci, S., Cassano, R., et al. 2008, Nature, 455, 944

Brunetti, G. & Jones, T. W. 2014, International Journal of Modern Physics D, 23, 1430007

Brunetti, G. & Lazarian, A. 2007, MNRAS, 378, 245

Brunetti, G., Rudnick, L., Cassano, R., et al. 2013, A&A, 558, A52

Brunetti, G., Setti, G., Feretti, L., & Giovannini, G. 2001, MNRAS, 320, 365

Brunetti, G., Venturi, T., Dallacasa, D., et al. 2007, ApJ, 670, L5

Brunetti, G., Zimmer, S., & Zandanel, F. 2017, MNRAS, 472, 1506

Buote, D. A. 2001, ApJ, 553, L15

Buote, D. A. & Tsai, J. C. 1995, ApJ, 452, 522

Burns, J. O., Sulkanen, M. E., Gisler, G. R., & Perley, R. A. 1992, ApJ, 388, L49

Carlstrom, J. E., Holder, G. P., & Reese, E. D. 2002, ARA&A, 40, 643

Cassano, R. & Brunetti, G. 2005, MNRAS, 357, 1313

Cassano, R., Brunetti, G., Giocoli, C., & Ettori, S. 2016, A&A, 593, A81

Cassano, R., Brunetti, G., Norris, R. P., et al. 2012, A&A, 548, A100

Cassano, R., Brunetti, G., Röttgering, H. J. A., & Brüggen, M. 2010a, A&A, 509, A68

Cassano, R., Brunetti, G., & Setti, G. 2006, MNRAS, 369, 1577

Cassano, R., Brunetti, G., Setti, G., Govoni, F., & Dolag, K. 2007, MNRAS, 378, 1565

Cassano, R., Brunetti, G., Venturi, T., et al. 2008, A&A, 480, 687

Cassano, R., Ettori, S., Brunetti, G., et al. 2013, ApJ, 777, 141

Cassano, R., Ettori, S., Giacintucci, S., et al. 2010b, ApJ, 721, L82

Cavagnolo, K. W., Donahue, M., Voit, G. M., & Sun, M. 2008, ApJ, 682, 821

Cavagnolo, K. W., Donahue, M., Voit, G. M., & Sun, M. 2009, ApJS, 182, 12

Cavaliere, A. & Fusco-Femiano, R. 1976, A&A, 49, 137

Chandra, P., Ray, A., & Bhatnagar, S. 2004, ApJ, 612, 974

Chernyshov, D. O., Dogiel, V. A., & Ko, C. M. 2012, ApJ, 759, 113

Chon, G., Böhringer, H., & Smith, G. P. 2012, A&A, 548, A59

Clarke, T. E. & Ensslin, T. 2006, Astronomische Nachrichten, 327, 553

Cohen, A. S., Lane, W. M., Cotton, W. D., et al. 2007, AJ, 134, 1245

Colless, M., Peterson, B. A., Jackson, C., et al. 2003, ArXiv Astrophysics e-prints [astro-ph/0306581]

Condon, J. J., Cotton, W. D., Greisen, E. W., et al. 1998, AJ, 115, 1693

Cuciti, V., Brunetti, G., van Weeren, R., et al. 2018, A&A, 609, A61

Cuciti, V., Cassano, R., Brunetti, G., et al. 2015, A&A, 580, A97

Cypriano, E. S., Sodré, Jr., L., Kneib, J.-P., & Campusano, L. E. 2004, ApJ, 613, 95

Dallacasa, D., Brunetti, G., Giacintucci, S., et al. 2009, ApJ, 699, 1288

Dasadia, S., Sun, M., Sarazin, C., et al. 2016, ApJ, 820, L20

de Gasperin, F., Intema, H. T., Shimwell, T. W., et al. 2017, Science Advances, 3, e1701634 de Gasperin, F., van Weeren, R. J., Brüggen, M., et al. 2014, MNRAS, 444, 3130

Dennison, B. 1980, ApJ, 239, L93

Diaferio, A. 1999, MNRAS, 309, 610

Diaferio, A., Geller, M. J., & Rines, K. J. 2005, ApJ, 628, L97

Dolag, K., Schindler, S., Govoni, F., & Feretti, L. 2001, A&A, 378, 777

Dolag, K., Vazza, F., Brunetti, G., & Tormen, G. 2005, MNRAS, 364, 753

Donnert, J., Dolag, K., Brunetti, G., & Cassano, R. 2013, MNRAS, 429, 3564

Donnert, J., Dolag, K., Brunetti, G., Cassano, R., & Bonafede, A. 2010, MNRAS, 401, 47

Drury, L. O. 1983, Reports on Progress in Physics, 46, 973

Duchesne, S. W., Johnston-Hollitt, M., Offringa, A. R., et al. 2017, ArXiv e-prints [1707.03517]

Ebeling, H., Edge, A. C., Allen, S. W., et al. 2000, MNRAS, 318, 333

Eckert, D., Gaspari, M., Vazza, F., et al. 2017, ApJ, 843, L29

Eckert, D., Jauzac, M., Vazza, F., et al. 2016, MNRAS, 461, 1302

Eckert, D., Molendi, S., & Paltani, S. 2011, A&A, 526, A79

Enßlin, T., Pfrommer, C., Miniati, F., & Subramanian, K. 2011, A&A, 527, A99

Ensslin, T. A., Biermann, P. L., Klein, U., & Kohle, S. 1998, A&A, 332, 395

Enßlin, T. A. & Gopal-Krishna. 2001, A&A, 366, 26

Enßlin, T. A. & Röttgering, H. 2002, A&A, 396, 83

Fabian, A. C. 1994, ARA&A, 32, 277

Fabian, A. C., Sanders, J. S., Ettori, S., et al. 2000, MNRAS, 318, L65

Farnsworth, D., Rudnick, L., Brown, S., & Brunetti, G. 2013, ApJ, 779, 189

Feretti, L., Giovannini, G., Govoni, F., & Murgia, M. 2012, A&A Rev., 20, 54

Feretti, L., Orrù, E., Brunetti, G., et al. 2004, A&A, 423, 111

Fujita, Y., Ohira, Y., & Yamazaki, R. 2014, ApJ, 789, 67

Fusco-Femiano, R., Dal Fiume, D., Feretti, L., et al. 1999, ApJ, 513, L21

Fusco-Femiano, R., Landi, R., & Orlandini, M. 2007, ApJ, 654, L9

Fusco-Femiano, R., Orlandini, M., Brunetti, G., et al. 2004, ApJ, 602, L73

Gastaldello, F., Wik, D. R., Molendi, S., et al. 2015, ApJ, 800, 139

Geller, M. J., Diaferio, A., Rines, K. J., & Serra, A. L. 2013, ApJ, 764, 58

Giacintucci, S., Markevitch, M., Brunetti, G., et al. 2014a, ApJ, 795, 73

Giacintucci, S., Markevitch, M., Cassano, R., et al. 2017, ApJ, 841, 71

Giacintucci, S., Markevitch, M., Venturi, T., et al. 2014b, ApJ, 781, 9

Giacintucci, S. & Venturi, T. 2009, A&A, 505, 55

Giacintucci, S., Venturi, T., Macario, G., et al. 2008, A&A, 486, 347

Giovannini, G., Feretti, L., & Stanghellini, C. 1991, A&A, 252, 528

Giovannini, G., Feretti, L., Venturi, T., Kim, K.-T., & Kronberg, P. P. 1993, ApJ, 406, 399

Giovannini, G., Tordi, M., & Feretti, L. 1999, NewA, 4, 141

Gitti, M., Brunetti, G., Feretti, L., & Setti, G. 2004, A&A, 417, 1

Gitti, M., Brunetti, G., & Setti, G. 2002, A&A, 386, 456

Govoni, F., Murgia, M., Feretti, L., et al. 2005, A&A, 430, L5

Govoni, F., Murgia, M., Feretti, L., et al. 2006, A&A, 460, 425

Haarsma, D. B., Leisman, L., Donahue, M., et al. 2010, ApJ, 713, 1037

Hanisch, R. J. 1982, A&A, 111, 97

Hasselfield, M., Hilton, M., Marriage, T. A., et al. 2013, JCAP, 7, 008

Hitomi Collaboration, Aharonian, F., Akamatsu, H., et al. 2016, Nature, 535, 117

Hlavacek-Larrondo, J., Allen, S. W., Taylor, G. B., et al. 2013, ApJ, 777, 163

Hoang, D. N., Shimwell, T. W., Stroe, A., et al. 2017, MNRAS, 471, 1107

Intema, H. T. 2014, SPAM: Source Peeling and Atmospheric Modeling, Astrophysics Source Code Library

Intema, H. T., Jagannathan, P., Mooley, K. P., & Frail, D. A. 2017, A&A, 598, A78

Intema, H. T., van der Tol, S., Cotton, W. D., et al. 2009, A&A, 501, 1185

Isobe, T., Feigelson, E. D., Akritas, M. G., & Babu, G. J. 1990, ApJ, 364, 104

Isobe, T., Feigelson, E. D., & Nelson, P. I. 1986, ApJ, 306, 490

Jaffe, W. J. 1977, ApJ, 212, 1

Jaffe, W. J. & Perola, G. C. 1973, A&A, 26, 423

Jeltema, T. E., Canizares, C. R., Bautz, M. W., & Buote, D. A. 2005, ApJ, 624, 606

Jeltema, T. E. & Profumo, S. 2011, ApJ, 728, 53

Johnston-Hollitt, M. & Pratley, L. 2017, ArXiv e-prints [1706.04930]

Kaiser, C. R., Dennett-Thorpe, J., & Alexander, P. 1997, MNRAS, 292, 723

Kaiser, N. 1986, MNRAS, 222, 323

Kale, R., Dwarakanath, K. S., Bagchi, J., & Paul, S. 2012, MNRAS, 426, 1204

Kale, R., Venturi, T., Giacintucci, S., et al. 2015, A&A, 579, A92

Kale, R., Venturi, T., Giacintucci, S., et al. 2013, A&A, 557, A99

Kang, H., Ryu, D., & Jones, T. W. 2012, ApJ, 756, 97

Kempner, J. C. & Sarazin, C. L. 2001, ApJ, 548, 639

Keshet, U., Markevitch, M., Birnboim, Y., & Loeb, A. 2010, ApJ, 719, L74

Kettenis, M., van Langevelde, H. J., Reynolds, C., & Cotton, B. 2006, in Astronomical Society of the Pacific Conference Series, Vol. 351, Astronomical Data Analysis Software and Systems XV, ed. C. Gabriel, C. Arviset, D. Ponz, & S. Enrique, 497

Krymskii, G. F. 1977, Akademiia Nauk SSSR Doklady, 234, 1306

Lacey, C. & Cole, S. 1993, MNRAS, 262, 627

Lane, W. M., Cotton, W. D., van Velzen, S., et al. 2014, MNRAS, 440, 327

Lecoanet, D., Parrish, I. J., & Quataert, E. 2012, MNRAS, 423, 1866

Liang, H., Hunstead, R. W., Birkinshaw, M., & Andreani, P. 2000, ApJ, 544, 686

Łokas, E. L., Prada, F., Wojtak, R., Moles, M., & Gottlöber, S. 2006a, MNRAS, 366, L26

Łokas, E. L., Wojtak, R., Gottlöber, S., Mamon, G. A., & Prada, F. 2006b, MNRAS, 367, 1463

Lovisari, L., Forman, W. R., Jones, C., et al. 2017, ApJ, 846, 51

Macario, G., Markevitch, M., Giacintucci, S., et al. 2011, ApJ, 728, 82

Macario, G., Venturi, T., Brunetti, G., et al. 2010, A&A, 517, A43

Mantz, A., Allen, S. W., Ebeling, H., Rapetti, D., & Drlica-Wagner, A. 2010, MNRAS, 406, 1773

Markevitch, M. 2010, ArXiv e-prints [1010.3660]

Markevitch, M., Gonzalez, A. H., David, L., et al. 2002, ApJ, 567, L27

Markevitch, M., Govoni, F., Brunetti, G., & Jerius, D. 2005, ApJ, 627, 733

Markevitch, M., Ponman, T. J., Nulsen, P. E. J., et al. 2000, ApJ, 541, 542

Markevitch, M., Sarazin, C. L., & Vikhlinin, A. 1999, ApJ, 521, 526

Markevitch, M. & Vikhlinin, A. 2007, Phys. Rep., 443, 1

Martinez Aviles, G., Ferrari, C., Johnston-Hollitt, M., et al. 2016, A&A, 595, A116

Maughan, B. J., Giles, P. A., Rines, K. J., et al. 2016, MNRAS, 461, 4182

Maughan, B. J., Jones, L. R., Pierre, M., et al. 2008, MNRAS, 387, 998

Mazzotta, P. & Giacintucci, S. 2008, ApJ, 675, L9

McMullin, J. P., Waters, B., Schiebel, D., Young, W., & Golap, K. 2007, in Astronomical Society of the Pacific Conference Series, Vol. 376, Astronomical Data Analysis Software and Systems XVI, ed. R. A. Shaw, F. Hill, & D. J. Bell, 127

McNamara, B. R. & Nulsen, P. E. J. 2007, ARA&A, 45, 117

McNamara, B. R. & Nulsen, P. E. J. 2012, New Journal of Physics, 14, 055023

Miniati, F. 2003, MNRAS, 342, 1009

Miniati, F. 2014, ApJ, 782, 21

Miniati, F. 2015, ApJ, 800, 60

Miniati, F., Ryu, D., Kang, H., & Jones, T. W. 2001, ApJ, 559, 59

Mohan, N. & Rafferty, D. 2015, PyBDSM: Python Blob Detection and Source Measurement, Astrophysics Source Code Library

Mohr, J. J., Fabricant, D. G., & Geller, M. J. 1993, ApJ, 413, 492

Motl, P. M., Hallman, E. J., Burns, J. O., & Norman, M. L. 2005, ApJ, 623, L63

Murgia, M., Govoni, F., Feretti, L., et al. 2004, A&A, 424, 429

Murgia, M., Govoni, F., Markevitch, M., et al. 2009, A&A, 499, 679

Nagai, D. 2006, ApJ, 650, 538

Narayan, R. & Medvedev, M. V. 2001, ApJ, 562, L129

Norris, R. 2010, in Bulletin of the American Astronomical Society, Vol. 36, American Astronomical Society Meeting Abstracts #215, 1127

O'Dea, C. P. & Owen, F. N. 1986, ApJ, 301, 841

O'Hara, T. B., Mohr, J. J., Bialek, J. J., & Evrard, A. E. 2006, ApJ, 639, 64

Orrú, E., Murgia, M., Feretti, L., et al. 2007, A&A, 467, 943

Ota, N., Nagayoshi, K., Pratt, G. W., et al. 2014, A&A, 562, A60

Owen, F. N., Rudnick, L., Eilek, J., et al. 2014, ApJ, 794, 24

Owers, M. S., Nulsen, P. E. J., & Couch, W. J. 2011, ApJ, 741, 122

Owers, M. S., Nulsen, P. E. J., Couch, W. J., et al. 2014, ApJ, 780, 163

Parekh, V., van der Heyden, K., Ferrari, C., Angus, G., & Holwerda, B. 2015, A&A, 575, A127

Perley, R. A. & Butler, B. J. 2013, ApJS, 204, 19

Peterson, J. R. & Fabian, A. C. 2006, Phys. Rep., 427, 1

Petrosian, V. 2001, ApJ, 557, 560

Petrosian, V. & East, W. E. 2008, ApJ, 682, 175

Pfrommer, C. & Enßlin, T. A. 2004, A&A, 413, 17

Pfrommer, C., Enßlin, T. A., & Springel, V. 2008, MNRAS, 385, 1211

Pfrommer, C. & Jones, T. W. 2011, ApJ, 730, 22

Pfrommer, C., Pakmor, R., Simpson, C. M., & Springel, V. 2017, ApJ, 847, L13

Pfrommer, C., Springel, V., Enßlin, T. A., & Jubelgas, M. 2006, MNRAS, 367, 113

Piffaretti, R., Arnaud, M., Pratt, G. W., Pointecouteau, E., & Melin, J.-B. 2011, A&A, 534, A109

Pizzo, R. F., de Bruyn, A. G., & Brentjens, M. A. 2009, in Astronomical Society of the Pacific Conference Series, Vol. 407, The Low-Frequency Radio Universe, ed. D. J. Saikia, D. A. Green, Y. Gupta, & T. Venturi, 241

Planck Collaboration, Ade, P. A. R., Aghanim, N., et al. 2014a, A&A, 571, A29

Planck Collaboration, Ade, P. A. R., Aghanim, N., et al. 2015, A&A, 581, A14

Planck Collaboration, Ade, P. A. R., Aghanim, N., et al. 2014b, A&A, 571, A20

Planck Collaboration, Ade, P. A. R., Aghanim, N., et al. 2011a, A&A, 536, A8

Planck Collaboration, Ade, P. A. R., Aghanim, N., et al. 2011b, A&A, 536, A11

Planck Collaboration, Aghanim, N., Arnaud, M., et al. 2011c, A&A, 536, A10

Poole, G. B., Fardal, M. A., Babul, A., et al. 2006, MNRAS, 373, 881

Pratt, G. W., Arnaud, M., Piffaretti, R., et al. 2010, A&A, 511, A85

Pratt, G. W., Croston, J. H., Arnaud, M., & Böhringer, H. 2009, A&A, 498, 361

Press, W. H. & Schechter, P. 1974, ApJ, 187, 425

Rajpurohit, K., Hoeft, M., van Weeren, R. J., et al. 2018, ApJ, 852, 65

Raymond, J. C. & Smith, B. W. 1977, ApJS, 35, 419

Reimer, A., Reimer, O., Schlickeiser, R., & Iyudin, A. 2004, A&A, 424, 773

Rengelink, R. B., Tang, Y., de Bruyn, A. G., et al. 1997, A&AS, 124, 259

Rephaeli, Y. & Gruber, D. 2002, ApJ, 579, 587

Rephaeli, Y., Gruber, D., & Blanco, P. 1999, ApJ, 511, L21

Rephaeli, Y., Sadeh, S., & Shimon, M. 2005, in Background Microwave Radiation and Intracluster Cosmology, ed. F. Melchiorri & Y. Rephaeli, Vol. 2005937974, 57

Riseley, C. J., Scaife, A. M. M., Wise, M. W., & Clarke, A. O. 2017, A&A, 597, A96

Rossetti, M., Eckert, D., De Grandi, S., et al. 2013, A&A, 556, A44

Rossetti, M., Gastaldello, F., Eckert, D., et al. 2017, MNRAS, 468, 1917

Rossetti, M., Gastaldello, F., Ferioli, G., et al. 2016, MNRAS, 457, 4515

Rossetti, M. & Molendi, S. 2004, A&A, 414, L41

Röttgering, H., Afonso, J., Barthel, P., et al. 2011, Journal of Astrophysics and Astronomy, 32, 557

Röttgering, H., van Weeren, R., Brüggen, M., et al. 2013, Astronomische Nachrichten, 334, 333

Röttgering, H. J. A., Wieringa, M. H., Hunstead, R. W., & Ekers, R. D. 1997, MNRAS, 290, 577

Rudnick, L., Delain, K. M., & Lemmerman, J. A. 2006, Astronomische Nachrichten, 327, 549

Rudnick, L. & Lemmerman, J. A. 2009, ApJ, 697, 1341

Russell, H. R., van Weeren, R. J., Edge, A. C., et al. 2011, MNRAS, 417, L1

Ruszkowski, M. & Begelman, M. C. 2002, ApJ, 581, 223

Ryu, D., Kang, H., Hallman, E., & Jones, T. W. 2003, ApJ, 593, 599

Sanchis, T., Łokas, E. L., & Mamon, G. A. 2004, MNRAS, 347, 1198

Santos, J. S., Rosati, P., Tozzi, P., et al. 2008, A&A, 483, 35

Sarazin, C. L. 1988, X-ray emission from clusters of galaxies

Sarazin, C. L. 2002, in Astrophysics and Space Science Library, Vol. 272, Merging Processes in Galaxy Clusters, ed. L. Feretti, I. M. Gioia, & G. Giovannini, 1–38

Scaife, A. M. M. & Heald, G. H. 2012, MNRAS, 423, L30

Scaife, A. M. M., Oozeer, N., de Gasperin, F., et al. 2015, MNRAS, 451, 4021

Schlickeiser, R., Sievers, A., & Thiemann, H. 1987, A&A, 182, 21

Sereno, M. & Ettori, S. 2017, MNRAS, 468, 3322

Shakouri, S., Johnston-Hollitt, M., & Dehghan, S. 2016a, MNRAS, 458, 3083

Shakouri, S., Johnston-Hollitt, M., & Pratt, G. W. 2016b, MNRAS, 459, 2525

Shimwell, T. W., Luckin, J., Brüggen, M., et al. 2016, MNRAS, 459, 277

Shimwell, T. W., Markevitch, M., Brown, S., et al. 2015, MNRAS, 449, 1486

Sijbring, L. G. 1993, A radio continuum and HI line study of the perseus cluster

Skrutskie, M. F., Cutri, R. M., Stiening, R., et al. 2006, AJ, 131, 1163

Sommer, M. W. & Basu, K. 2014, MNRAS, 437, 2163

Sommer, M. W., Basu, K., Intema, H., et al. 2017, MNRAS, 466, 996

Springel, V., Frenk, C. S., & White, S. D. M. 2006, Nature, 440, 1137

Subramanian, K., Shukurov, A., & Haugen, N. E. L. 2006, MNRAS, 366, 1437

Sutherland, R. S. & Dopita, M. A. 1993, ApJS, 88, 253

Thierbach, M., Klein, U., & Wielebinski, R. 2003, A&A, 397, 53

Tingay, S. J., Goeke, R., Bowman, J. D., et al. 2013, PASA, 30, e007

Tribble, P. C. 1989, MNRAS, 238, 1247

Vacca, V., Murgia, M., Govoni, F., et al. 2012, A&A, 540, A38

Valtchanov, I., Murphy, T., Pierre, M., Hunstead, R., & Lémonon, L. 2002, A&A, 392, 795

van Haarlem, M. P., Wise, M. W., Gunst, A. W., et al. 2013, A&A, 556, A2

van Weeren, R. J., Andrade-Santos, F., Dawson, W. A., et al. 2017, Nature Astronomy, 1, 0005

van Weeren, R. J., Brunetti, G., Brüggen, M., et al. 2016, ApJ, 818, 204

van Weeren, R. J., Intema, H. T., Lal, D. V., et al. 2014, ApJ, 786, L17

van Weeren, R. J., Röttgering, H. J. A., Brüggen, M., & Hoeft, M. 2010, Science, 330, 347

Vazza, F. & Brüggen, M. 2014, MNRAS, 437, 2291

Vazza, F., Brüggen, M., van Weeren, R., et al. 2012, MNRAS, 421, 1868

Vazza, F., Brunetti, G., & Gheller, C. 2009, MNRAS, 395, 1333

Vazza, F., Dolag, K., Ryu, D., et al. 2011, MNRAS, 418, 960

Vazza, F., Jones, T. W., Brüggen, M., et al. 2017, MNRAS, 464, 210

Vazza, F., Tormen, G., Cassano, R., Brunetti, G., & Dolag, K. 2006, MNRAS, 369, L14

Ventimiglia, D. A., Voit, G. M., Donahue, M., & Ameglio, S. 2008, ApJ, 685, 118

Venturi, T. 2011, Mem. Soc. Astron. Italiana, 82, 499

Venturi, T., Giacintucci, S., Brunetti, G., et al. 2007, A&A, 463, 937

Venturi, T., Giacintucci, S., Dallacasa, D., et al. 2008, A&A, 484, 327

Venturi, T., Giacintucci, S., Dallacasa, D., et al. 2013, A&A, 551, A24

Venturi, T., Giovannini, G., & Feretti, L. 1990, AJ, 99, 1381

Venturi, T., Rossetti, M., Brunetti, G., et al. 2017, A&A, 603, A125

Vogt, C. & Enßlin, T. A. 2005, A&A, 434, 67

Wayth, R. B., Lenc, E., Bell, M. E., et al. 2015, PASA, 32, e025

Weißmann, A., Böhringer, H., Šuhada, R., & Ameglio, S. 2013, A&A, 549, A19

Wen, Z. L. & Han, J. L. 2013, MNRAS, 436, 275

Wik, D. R., Hornstrup, A., Molendi, S., et al. 2014, ApJ, 792, 48

Wik, D. R., Sarazin, C. L., Finoguenov, A., et al. 2011, ApJ, 727, 119

Wik, D. R., Sarazin, C. L., Zhang, Y.-Y., et al. 2012, ApJ, 748, 67

Wilber, A., Brüggen, M., Bonafede, A., et al. 2018, MNRAS, 473, 3536

Willott, C. J., Rawlings, S., Jarvis, M. J., & Blundell, K. M. 2003, MNRAS, 339, 173

Willson, M. A. G. 1970, MNRAS, 151, 1

Wright, E. L., Eisenhardt, P. R. M., Mainzer, A. K., et al. 2010, AJ, 140, 1868

Yuan, Z. S., Han, J. L., & Wen, Z. L. 2015, ApJ, 813, 77

Zandanel, F., Pfrommer, C., & Prada, F. 2014, MNRAS, 438, 124

Zhuravleva, I., Churazov, E., Schekochihin, A. A., et al. 2014, Nature, 515, 85

ZuHone, J. A., Brunetti, G., Giacintucci, S., & Markevitch, M. 2015, ApJ, 801, 146

ZuHone, J. A., Markevitch, M., Brunetti, G., & Giacintucci, S. 2013, ApJ, 762, 78

Zwicky, F. 1937, ApJ, 86, 217